

OPTICAL SPECTROSCOPY OF HIGHLY EXCITED
GROUP III NITRIDES

By

THEODORE J. SCHMIDT

Bachelor of Science

North Dakota State University

Fargo, North Dakota

1992

Submitted to the Faculty of the
Graduate College of the
Oklahoma State University
in partial fulfillment of
the requirements for
the Degree of
DOCTOR OF PHILOSOPHY
December, 1998

Thesis
1994D
S3548

COPYRIGHT

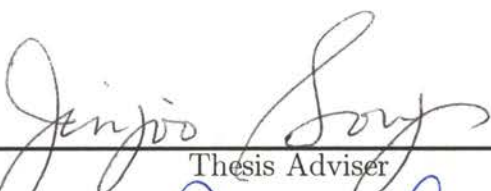
By

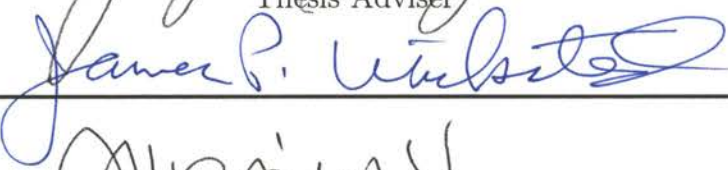
Theodore John Schmidt

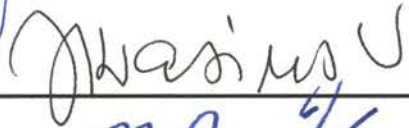
December, 1998


OPTICAL SPECTROSCOPY OF HIGHLY EXCITED
GROUP III NITRIDES

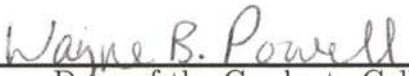
Thesis Approved:



Thesis Adviser








Dean of the Graduate College

ACKNOWLEDGEMENTS

I wish to express my sincere gratitude to my thesis advisor, Dr. Jin-Joo Song, for her support and guidance during my years of research at Oklahoma State University. Her advising style has helped me to become an independent researcher while still managing to keep me from going too far astray. I wanted for nothing in performing my research in her lab, and I thank her for the innumerable opportunities she provided me. I would also like to thank the other members of my committee, Dr. Robert Hauenstein, Dr. Jerzy Krasinski, and Dr. James Wicksted for their help and guidance.

I am indebted to Dr. Wei Shan for his guidance and technical conversations during my earlier years. I would also like to thank all the members of Dr. Song's group, past and present, whom I was fortunate enough to work with: Dr. X. H. Yang, Dr. Bahman Taheri, Dr. Seon-Ju Hwang, Dr. Gil-Han Park, Dr. Yong-Hoon Cho, Dr. Arthur Fischer, Brian Little, and Serge Bidnyk. I feel I benefited greatly from working in a large and culturally diverse group, both from a scientific and a political standpoint. The advice, support, differences, and comradery of the members of this research group made daily life continually entertaining.

I would like to thank my football coaches at North Dakota State University, Bruce Saum and Rocky Hagar, for their help in motivating me to be my best and for instilling in me the importance of discipline and teamwork. Without their motivation during my early college years, this chapter of my life would have never begun.

I would like to thank my mother and father for providing me with the constant love and support I needed to pursue and achieve my goals in life. I thank my sons, Jonathan and Christian, whose birth this past February brought about a sudden and complete change in my view of the world and my place in it. And last, but certainly

not least, my wife of nearly six years, Shelly, who has put up with being a student's wife from the beginning. I thank her for her patience. It is for Jonathan, Christian, and Shelly that I finally bring this long chapter of my life to a close.

PUBLICATIONS AND PRESENTATIONS

The following scientific publications were generated from the research contained in this thesis:

- *Amplification path length dependence studies of stimulated emission from optically pumped InGaN/GaN multiple quantum wells*, T.J. Schmidt, S. Bidnyk, Y.H. Cho, A.J. Fischer, J.J. Song, S. Keller, U.K. Mishra, and S.P. DenBaars, MRS Internet J. Nitride Semicond. Res. (submitted for publication).
- *Stimulated emission in thin GaN films in the temperature range of 300 K to 700 K*, S. Bidnyk, B.D. Little, T.J. Schmidt, Y.H. Cho, J. Krasinski, B. Goldenberg, W.G. Perry, M.D. Bremser, and R.F. Davis, J. Appl. Phys. (to be published, February 2) (1999).
- *Room temperature deep ultraviolet stimulated emission from $Al_xGa_{1-x}N$ thin films grown on sapphire*, T.J. Schmidt, Y.H. Cho, J.J. Song, and W. Yang, Appl. Phys. Lett. (to be published, January 11) (1999).
- *Near-threshold gain mechanisms in GaN thin films in the temperature range of 20 K to 700 K*, S. Bidnyk, T.J. Schmidt, B.D. Little, J.J. Song, B. Goldenberg, W.G. Perry, M.D. Bremser, and R.F. Davis, Appl. Phys. Lett. (to be published, January 4) (1999).
- *Stimulated emission characteristics of InGaN/GaN multiple quantum wells: Excitation length and excitation density dependence*, T.J. Schmidt, S. Bidnyk, Y.H. Cho, A.J. Fischer, J.J. Song, S. Keller, U.K. Mishra, and S.P. DenBaars, Appl. Phys. Lett. (to be published, December 21) (1998).

- *Pump-probe spectroscopy of band tail states in metalorganic chemical vapor deposition-grown InGaN*, T.J. Schmidt, Y.H. Cho, G.H. Gainer, J.J. Song, S. Keller, U.K. Mishra, and S.P. DenBaars, Appl. Phys. Lett. **73**, 1892 (1998).
- *Energy selective optically pumped stimulated emission from InGaN/GaN multiple quantum wells*, T.J. Schmidt, Y.H. Cho, G.H. Gainer, J.J. Song, S. Keller, U.K. Mishra, and S.P. DenBaars, Appl. Phys. Lett. **73**, 560 (1998).
- *Study of stimulated emission in InGaN/GaN multi-quantum wells in the temperature range of 175 K to 575 K*, S. Bidnyk, Y.H. Cho, T.J. Schmidt, J.J. Song, S. Keller, U.K. Mishra, and S.P. DenBaars, Mat. Res. Soc. Symp. Proc. **512**, 199 (1998).
- *High-temperature stimulated emission studies of MOCVD-grown GaN films*, S. Bidnyk, T.J. Schmidt, J. Krasinski, and J.J. Song, SPIE Conf. Proceedings Series **3419**, 35 (1998).
- *Large optical nonlinearities in the band gap region of GaN thin films grown by MOCVD on sapphire*, T.J. Schmidt, Y.C. Chang, and J.J. Song, SPIE Conf. Proceedings Series **3419**, 61 (1998).
- *High-temperature stimulated emission in optically pumped InGaN/GaN multi-quantum wells*, S. Bidnyk, T.J. Schmidt, Y.H. Cho, G.H. Gainer, J.J. Song, S. Keller, U.K. Mishra, and S.P. DenBaars, Appl. Phys. Lett. **72**, 1623 (1998).
- *Large optical nonlinearities near the bandgap of GaN thin films*, T.J. Schmidt, J.J. Song, Y.C. Chang, B. Goldenberg, and R. Horning, Appl. Phys. Lett. **72**, 1504 (1998).
- *Study of surface-emitted stimulated emission in GaN*, S. Bidnyk, T.J. Schmidt, G.H. Park, and J.J. Song, Appl. Phys. Lett. **71**, 729 (1997).
- *Optical processes in GaN and its related heterostructures*, J.J. Song, A.J. Fischer, T.J. Schmidt, S. Bidnyk, and W. Shan, Nonlinear Optics **18**, 269 (1997).

- *Recent progress in optical studies of wurtzite GaN grown by metalorganic chemical vapor deposition*, W. Shan, T.J. Schmidt, X.H. Yang, J.J. Song, and B. Goldenberg, Inst. Phys. Conf. Ser. **145**, 1151 (1996).
- *Optical properties of MG-GaN, GaN/AlGaN SCH structures, and GaN on ZnO substrates*, H. Morkoc, W. Kim, O. Atkas, A. Salvador, A. Botchkarev, D.C. Reynolds, M. Smith, G.D. Chen, J.Y. Lin, H.X. Jiang, T.J. Schmidt, X.H. Yang, W. Shan, J.J. Song, B. Goldenberg, C.W. Litton, and K. Evans, Mat. Res. Soc. Symp. Proc. **395**, 527 (1996).
- *Spectroscopic studies of GaN grown by metalorganic chemical vapor deposition*, W. Shan, J.J. Song, T.J. Schmidt, X.H. Yang, and B. Goldenberg, TWN Proceedings (1996).
- *Room-temperature stimulated emission in GaN/AlGaN separate confinement heterostructures grown by molecular beam epitaxy*, T.J. Schmidt, X.H. Yang, W. Shan, J.J. Song, A. Salvador, W. Kim, O. Atkas, A. Botchkarev, and H. Morkoc, Appl. Phys. Lett. **68**, 1820 (1996).
- *Optical properties of wurtzite GaN grown by low-pressure metalorganic chemical vapor deposition*, W. Shan, T.J. Schmidt, X.H. Yang, J.J. Song, and B. Goldenberg, J. Appl. Phys. **79**, 3691 (1996).
- *Optical studies of epitaxial GaN based materials*, J.J. Song, W. Shan, T.J. Schmidt, X.H. Yang, A.J. Fischer, S.J. Hwang, B. Taheri, B. Goldenberg, R. Horning, A. Salvador, W. Kim, O. Aktas, A. Botchkarev, and H. Morkoc, SPIE Conf. Proceedings Series **2693**, 86 (1996).
- *Above room temperature near ultraviolet lasing from an optically pumped GaN film grown on sapphire*, X.H. Yang, T.J. Schmidt, W. Shan, J.J. Song, and B. Goldenberg, Appl. Phys. Lett. **66**, 1 (1995).

- *Temperature dependence of interband transitions in GaN grown by low-pressure metalorganic chemical vapor deposition*, W. Shan, T.J. Schmidt, X.H. Yang, S.J. Hwang, J.J. Song, and B. Goldenberg, Appl. Phys. Lett. **66**, 985 (1995).
- *Pressure-dependent photoluminescence study of wurtzite GaN*, W. Shan, T.J. Schmidt, R.J. Hauenstein, J.J. Song, and B. Goldenberg, Appl. Phys. Lett. **66**, 3492 (1995).

The research conducted towards this thesis was presented at the following scientific conferences:

- *Nonlinear optical spectroscopy of band tail states in highly excited InGaN*, T.J. Schmidt, Y.H. Cho, S. Bidnyk, J.J. Song, S. Keller, U.K. Mishra, and S.P. DenBaars, **3625-7**, SPIE Photonics West, January 25-29, San Jose, California (1999).
- *Comparative study of near-threshold stimulated emission mechanisms in GaN, InGaN, and InGaN/GaN multiquantum wells*, S. Bidnyk, T.J. Schmidt, and J.J. Song, **3625-8**, SPIE Photonics West, January 25-29, San Jose, California (1999).
- *Amplification path length dependence studies of stimulated emission from optically pumped InGaN/GaN multiple quantum wells*, T.J. Schmidt, S. Bidnyk, Y.H. Cho, A.J. Fischer, J.J. Song, S. Keller, U.K. Mishra, and S.P. DenBaars, **G25243**, Mat. Res. Soc. Fall Meeting, November 30- December 4, Boston, Massachusetts (1998).
- *Pump-probe spectroscopy of band tail states in MOCVD-grown InGaN*, T.J. Schmidt, Y.H. Cho, J.J. Song, S. Keller, U.K. Mishra, and S.P. DenBaars, **ThQQ4**, OSA/ILS-XIV Annual Meeting, October 4-9, Baltimore, Maryland (1998).
- *Stimulated emission studies of the group III nitrides over the temperature range 10 K to 700 K*, S. Bidnyk, T.J. Schmidt, J.J. Song, S. Keller, U.K. Mishra, and S.P. DenBaars, **ThQQ5**, OSA/ILS-XIV Annual Meeting, October 4-9, Baltimore, Maryland (1998).
- *Optical characterization of GaN, InGaN, and InGaN/GaN multiple quantum wells grown by metalorganic chemical vapor deposition*, Y.H. Cho, T.J. Schmidt, S. Bidnyk, G.H. Gainer, J.J. Song, S. Keller, and S.P. DenBaars, 5th Wide Bandgap Semiconductor Workshop, August 4-7, St. Louis, Missouri (1998).

- *Stimulated emission studies of MOCVD-grown GaN and InGaN structures*, J.J. Song, S. Bidnyk, T.J. Schmidt, Y.H. Cho, S. Keller, S.P. DenBaars, and W. Yang, 5th Wide Bandgap Semiconductor Workshop, August 4-7, St. Louis, Missouri (1998).
- *Large optical nonlinearities in the bandgap region of GaN thin films grown by MOCVD on sapphire*, T.J. Schmidt, J.J. Song, and Y.C. Chang, **3419-11**, SPIE Asia Pacific Symposium on Optoelectronics, July 9-11, Taipei, Taiwan (1998).
- *High temperature stimulated emission studies of MOCVD-grown GaN films*, S. Bidnyk, C.K. Choi, T.J. Schmidt, J.S. Krasinski, and J.J. Song, **3419-06**, SPIE Asia Pacific Symposium on Optoelectronics, July 9-11, Taipei, Taiwan (1998).
- *Large optical nonlinearities near the bandgap of MOCVD-grown GaN thin films*, T.J. Schmidt, J.J. Song, Y.C. Chang, R. Horning, and B. Goldenberg, **QFH4**, IQEC 98, May 3-8, San Francisco, California (1998).
- *Characterization of InGaN/GaN lasing structures for high temperature device applications*, S. Bidnyk, Y.H. Cho, T.J. Schmidt, J.J. Song, S. Keller, U.K. Mishra, and S.P. DenBaars, **CWD2**, CLEO 98, May 3-8, San Francisco, California (1998).
- *High-temperature stimulated emission in optically pumped InGaN/GaN multiple quantum wells*, S. Bidnyk, Y.H. Cho, T.J. Schmidt, J.J. Song, S. Keller, U.K. Mishra, and S.P. DenBaars, **F4.11**, MRS Spring Meeting, April, San Francisco, California (1998).
- *Energy selective optically pumped blue stimulated emission in InGaN/GaN multiple quantum wells*, T.J. Schmidt, Y.H. Cho, J.K. Krasinski, J.J. Song, S. Keller, U.K. Mishra, and S.P. DenBaars, **G18 10**, APS March Meeting, March 16-20, Los Angeles, California (1998).

- *Study of stimulated emission in GaN thin films in the temperature range of 20 K to 700 K*, S. Bidnyk, C.K. Choi, T.J. Schmidt, J.K. Krasinski, and J.J. Song, **A18 8**, APS March Meeting, March 16-20, Los Angeles, California (1998).
- *Optical processes in GaN and its related heterostructures*, W. Shan, T.J. Schmidt, S. Bidnyk, A.J. Fischer, B.D. Little, and J.J. Song, 4th GaN Workshop, February, St. Louis, Missouri (1997).
- *Optical processes in GaN and its related heterostructures*, J.J. Song, A.J. Fischer, T.J. Schmidt, S. Bidnyk, and W. Shan, International Symposium on Quantum Structures for Photonic Applications, Sendai, Japan (1997).
- *Room temperature stimulated emission from GaN/AlGaIn separate confinement heterostructures*, T.J. Schmidt, W. Shan, J.J. Song, B. Goldenberg, R. Davis, C.H. Cheng, H. Morkoc, and G. Bulman, **G26 1**, APS March Meeting, March 18-22, St. Louis, Missouri (1996).
- *Above room temperature optically pumped lasing in GaN at 382 nm*, T.J. Schmidt, X.H. Yang, W. Shan, J.J. Song, and B. Goldenberg, Rare Earth Doped Optoelectronic Materials Workshop, June 16-17, Malibu, California (1994).

For Jonathan and Christian
that their life may be bettered by a better understanding of the world around them

TABLE OF CONTENTS

Chapter	Page
I. INTRODUCTION	1
II. GENERAL OPTICAL PROPERTIES OF HIGHLY EX- CITED SEMICONDUCTORS	6
Band Structure of Semiconductors	7
Excitons	8
Basic Theory of Excitons	9
LO-phonon Interaction	11
Exciton Related Gain Processes	12
The Electron-Hole Plasma	15
III. GENERAL PROPERTIES OF THE GROUP III NITRIDES	28
Structural	28
Optical	29
Photoluminescence	30
Absorption	31
Photoreflexion	31
Strain effects on the excitonic transitions	31
AlGa _N	32
InGa _N	33
IV. EMISSION PROPERTIES OF HIGHLY EXCITED GROUP III NITRIDES	44
Stimulated Emission from Highly Excited Ga _N	45
Cavity Formation and Lasing in Ga _N	50
Stimulated Emission from Highly Excited AlGa _N and InGa _N	53
Summary	58
V. PUMP-PROBE SPECTROSCOPY OF Ga _N THIN FILMS	74
Nondegenerate Optical Pump-Probe Absorption Spectroscopy	76
Motivation	77
Experimental Technique and Results	78
At Zero Time Delay	79

Chapter	Page
At Non-Zero Time Delay	83
Single-Beam Power Dependent Absorption Spectroscopy . . .	104
Motivation	104
Experimental Technique and Results	104
Summary	105
Nondegenerate Optical Pump-Probe Reflection Spectroscopy .	109
Motivation	109
Experimental Technique and Results	109
Summary	110
Nondegenerate Optical Pump-Probe Spectroscopy of	
InGaN Thin Films	112
Motivation	112
Experimental Technique and Results	113
Summary	115
Summary	122
VI. OPTICAL SPECTROSCOPY OF HIGHLY EXCITED In-	
GaN/GaN MULTIPLE QUANTUM WELLS	124
Temperature Dependence of SE from InGaN/GaN MQWs . .	128
Motivation	128
Experimental Technique and Results	129
Summary	132
Excitation Length Dependent Studies of Optically	
Pumped SE from InGaN/GaN MQWs	137
Motivation	137
Experimental Technique and Results	138
Summary	141
Energy Selective Optically Pumped SE Studies of In-	
GaN/GaN MQWs	147
Motivation	147
Experimental Technique and Results	148
Summary	151
Variable-Stripe Gain Spectroscopy of InGaN/GaN MQWs . .	156
Experimental Technique and Results	156
Summary	158
Nondegenerate Optical Pump-Probe Spectroscopy of	
InGaN/GaN MQWs	161
Motivation	161
Experimental Technique and Results	162
Summary	166
Summary	171
VII. SUMMARY	175

Chapter	Page
BIBLIOGRAPHY	178
APPENDIX	186
APPENDIX A - POLISHING CAVITY FACETS FOR GROUP-III NITRIDE LASER STRUCTURES . . .	187
Before You Begin	187
Squeaks	188
Adjusting the Guide Roller Position	188
Adjusting the Polishing Pressure	189
Monitoring the Sample Thickness	189
Calculating Particle Size From Mesh	190
Avoiding Cross-Contamination	190
Mounting Samples for Polishing	191
Grinding the Porous Substrate Flat	192
Gluing the Samples to the Braces	192
Polishing	193
Rough Grinding	194
70 μm diamond on steel	194
30 μm diamond on steel	194
Polishing	194
8.5 μm diamond on copper	194
3.2 μm diamond on copper	195
MasterPolish2 [®] on tin	195
Polishing the Second Cavity Facet	196
Dismounting and Cleaning Polished Samples	197
APPENDIX B - REFRACTIVE INDEX OF WURTZITE GaN	207

LIST OF FIGURES

Figure	Page
1. Low temperature emission spectra of CdS for various optical excitation levels.	19
2. Energy banding of allowed electronic levels in diamond as a function of interatomic spacing.	20
3. Schematic of excitonic dispersion curves of Wannier excitons in direct gap semiconductors.	21
4. Absorption spectrum of high purity GaAs at 1.2 K near the band edge. .	22
5. Schematic of exciton-exciton scattering recombination in direct gap semiconductors.	23
6. Emission spectra of GaN at 1.8 K as a function of optical excitation. . .	24
7. Calculated gain spectra of exciton-exciton scattering in CdS.	25
8. Band diagram of a direct gap semiconductor under the conditions of strong optical pumping.	26
9. Schematic representation of EHP gain calculation.	27
10. Wurtzite unit cell.	34
11. Stacking sequence of atomic planes in wurtzite GaN.	35
12. Band structure of wurtzite GaN.	36
13. Band structure of wurtzite GaN near zone center.	37
14. Low temperature photoluminescence from an MOCVD-grown GaN thin film.	38
15. Absorption spectra of a thin GaN epitaxial layer near the fundamental absorption edge.	39
16. 10 K photoreflexion spectrum of a high quality GaN layer.	40

Figure	Page
17. Shift in excitonic transition energies due to residual strain as measured by photoreflexion.	41
18. AlGa _N band gap as a function of Al mole fraction.	42
19. Band gap of InGa _N as a function of In mole fraction.	43
20. Edge emission and surface emission pumping geometries.	60
21. Evolution of Ga _N band edge emission with increasing optical excitation at 10 K.	61
22. Evolution of the SE from Ga _N at 10 K under the conditions of intense femtosecond optical excitation.	62
23. SE threshold of MOCVD-grown Ga _N as a function of temperature; 10 K to 375 K.	63
24. SE threshold of MOCVD-grown Ga _N as a function of temperature; 10 K to 700 K.	64
25. SE peak position of MOCVD-grown Ga _N as a function of temperature; 10 K to 700 K.	65
26. SEM micrographs of Ga _N laser cavity facets before and after mechanical polishing.	66
27. RT lasing spectra from a Ga _N layer as a function of facet treatment.	67
28. RT lasing spectrum of a Ga _N laser structure with mirrored facets illustrating single mode emission.	68
29. 10 K PL, PLE, and SE spectra of an $x = 0.17$ AlGa _N layer.	69
30. 10 K PL, PLE, and SE spectra of an $x = 0.18$ InGa _N layer.	70
31. RT emission spectra of an $x = 0.17$ and an $x = 0.26$ AlGa _N thin film as a function of increasing optical excitation.	71
32. RT dependence of emission on excitation density for an $x = 0.17$ and an $x = 0.26$ AlGa _N thin film.	72
33. Relative SE thresholds for InGa _N , Ga _N , and AlGa _N at 10 K and RT. . .	73
34. Near band edge absorption spectra of a Ga _N thin film at various temperatures.	90

Figure	Page
35. Nanosecond nondegenerate optical pump-probe absorption setup A. . . .	91
36. 10 K nondegenerate optical pump-probe absorption spectra of a GaN thin film.	92
37. RT nondegenerate optical pump-probe absorption spectra of a GaN thin film.	93
38. Magnitudes of induced transparency and absorption at 10 K and RT for a GaN thin film.	94
39. RT optical switching of a laser using a GaN switch.	95
40. Nanosecond nondegenerate optical pump-probe absorption setup B. . . .	96
41. 10 K band edge absorption spectra of a GaN thin film as a function of delay across the pump beam duration.	97
42. 10 K band edge absorption spectra of a GaN film at various delays after the pump pulse.	98
43. 10 K differential absorption spectra of a GaN thin film as a function of delay after the pump beam.	99
44. Room temperature absorption spectra of a GaN thin film as a function of delay after the pump pulse.	100
45. Room temperature differential absorption spectra of a GaN thin film as a function of delay after the pump pulse.	101
46. Effective temperature rise at 10 K of a GaN thin film as a function of time delay and excitation density.	102
47. Effective temperature rise at room temperature of a GaN thin film as a function of time delay and excitation density.	103
48. Single-beam power dependent absorption experimental setup.	107
49. 10 K single-beam power dependent absorption spectra of a GaN thin film.	108
50. 10 K pump-probe reflection spectra of a GaN thin film.	111
51. Nanosecond nondegenerate optical pump-probe absorption experimental setup C.	117
52. 10 K band edge absorption spectra of an InGaN layer for several excitation densities above and below the stimulated emission threshold.	118

Figure	Page
53. 10 K differential absorption spectra of an InGaN thin film for several excitation densities above and below the stimulated emission threshold.	119
54. Room temperature band edge absorption spectra of an InGaN thin film for several excitation densities above and below the stimulated emission threshold.	120
55. Room temperature differential absorption spectra of an InGaN thin film for several excitation densities above and below the stimulated emission threshold.	121
56. Schematic of InGaN/GaN MQW structure.	126
57. 10 K emission from InGaN/GaN MQWs as a function of increasing optical excitation.	127
58. RT stimulated emission threshold as a function of Si doping of InGaN/GaN MQWs.	133
59. Emission spectra of an InGaN/GaN MQW at 200 K, 300 K, and 450 K.	134
60. SE threshold versus temperature for an InGaN/GaN MQW.	135
61. Integrated intensity of InGaN/GaN MQW emission as a function of pump density at various temperatures.	136
62. 10 K SE spectra from an InGaN/GaN MQW showing two distinct SE peaks.	143
63. SE thresholds of SE peaks (1) and (2) as a function of excitation length for an InGaN/GaN MQW.	144
64. SE peak positions of SE peaks (1) and (2) as a function of excitation length for an InGaN/GaN MQW.	145
65. Emission intensity of SE peaks (1) and (2) as a function of optical excitation density for an InGaN/GaN MQW.	146
66. 10 K emission spectra as a function of excitation density for an InGaN/GaN MQW with Si doped GaN barriers.	153
67. SE peak position as a function of excitation photon energy for InGaN/GaN MQWs at 10 K.	154

Figure	Page
68. Optical excitation efficiency as a function of excitation photon energy for spontaneous and stimulated emission from InGaN/GaN MQWs at 10 K.	155
69. Modal gain spectra as a function of increasing optical excitation for an InGaN/GaN MQW.	159
70. Modal gain spectra and band edge of an InGaN/GaN MQW.	160
71. General optical properties of an InGaN MQW and epilayer at 10 K. . . .	167
72. Effective recombination lifetime as a function of temperature for an InGaN MQW and epilayer.	168
73. 10 K emission spectra as a function of excitation density for an InGaN MQW and epilayer.	169
74. 10 K nanosecond nondegenerate optical pump-probe spectra for an InGaN MQW and epilayer.	170
75. Summary of observed high excitation density phenomena from InGaN/GaN MQWs.	174
76. Logitech PP5D precision polishing jig.	198
77. Glue-up schematic of GaN thin films prior to mechanical polishing. . . .	199
78. Schematic of proper orientation of samples on Logitech PP5D jig mount.	200
79. Illustration of proper bracing.	201
80. Polishing GaN/SiC, part 1.	202
81. Polishing GaN/SiC, part 2.	203
82. Polishing GaN/sapphire, part 1.	204
83. Polishing GaN/sapphire, part 2.	205
84. SEM image of GaN/sapphire laser facet after mechanical polishing. . . .	206
85. Reflection and transmission spectra of a GaN thin film at RT.	210
86. RT index of refraction dispersion curves for GaN thin films on sapphire.	211

CHAPTER I

INTRODUCTION

The group III nitride semiconductors, most notably AlN, GaN, InN, and their alloys, have experienced an unprecedented amount of attention in the semiconductor world over the past half decade, due mostly to the realization of high brightness UV, blue, and green light emitting diodes (LEDs) and UV-blue cw laser diodes (LDs) based on the ternary alloy InGaN. Although most of the fundamental optical properties of the group III nitrides were known as early as the 1960s (in fact, metal-insulator-semiconductor (MIS) type structures were demonstrated to emit strong and reliable UV-blue emission and were briefly commercialized in the early 1970s [1], [2]), it took the development of p-type doping by Akasaki and Amano in 1989 [3] and the development of suitable epitaxial techniques, such as molecular beam epitaxy (MBE) and metalorganic chemical vapor deposition (MOCVD), for p-n junction light emitting devices to emerge. These advances made it possible for Shuji Nakamura and co-workers at Nichia Chemical (Japan) to develop and commercialize UV, blue, green, yellow, and white LEDs based on the ternary alloy InGaN starting in early 1994. Room temperature continuous wave (cw) operation of near-UV and blue LDs have also been demonstrated by Nichia with lifetimes in excess of 13,000 hours [4], with predictions of commercialization in 1999. With the above said, some background on the economic impact and potential uses of the group III nitrides that drive this research will now be given.

In 1996, the total world market for materials and devices based on the group III nitrides amounted to an estimated US\$227.4 million, and is forecast to exceed US\$9991.4 million by the year 2001. The principle applications are in full color

information displays and indicators, where GaN-based LEDs are expected to revolutionize medium-to-large area (> 100 inches diagonal) information displays and traffic signs by completing the tricolor red-green-blue (RGB) spectrum. These markets had a value of US\$854 million in 1996 and are expected to reach US\$1717.6 million by 2001. In addition, the allure of increased data storage has provided a strong economic pull for solid-state semiconductor LDs based on this material system. We note that the minimum spot size a laser beam can be focused to (and hence, the maximum possible resolution one can achieve with) is limited by the wavelength of the laser emission. Reducing the laser wavelength by a factor of two leads to a four-fold increase in potential data storage capacity. Therefore, by replacing conventional GaAs-based LDs (emitting in the near infrared, ≈ 780 nm) with GaN-based blue LDs, the storage capacity of CD-ROM technology can be quadrupled from around 650 Mbyte to around 2600 Mbyte per disc. This increase in storage capacity would make it possible to fit a feature length film (approximately 90 to 120 minutes long) on a conventional CD-ROM. This increase would, of course, apply to DVD technology also, further extending data storage capacity. Other applications for blue LDs include: use in laser printers, where the smaller spot size makes higher resolution printing and graphics output possible; underwater optical communications, where the blue-green optical transmission window of water can be exploited; satellite to satellite optical communication, where the use of UV lasers would exploit the absorption of UV radiation by the Earth's atmosphere to make eavesdropping from Earth impossible; applications in the medical field, where rugged and compact UV-blue lasers will find a myriad of uses, both known and presently unrealized. The market for blue semiconductor lasers is estimated to exceed US\$200 million by 2001 [5]. Other applications of interest for GaN-based light emitting devices include replacement of white-light-emitting filament lamps with white LEDs, leading to a 10-fold increase in efficiency and a three orders of magnitude increase in lifetime (from $\approx 10^3$ hours to $\approx 10^6$ hours) [6].

The uses of the group III nitrides in non-light emitting applications are also attracting a considerable amount of attention. Due to their large direct band gaps,

GaN and its alloy with AlN (AlGaN) are promising materials for the development of solar-blind detectors capable of efficiently detecting UV radiation (such as is emitted by missiles and jet engines) without a background from solar radiation (the Earth's atmosphere efficiently absorbs radiation below 290 nm). The high thermal and chemical stability, high breakdown fields, good thermal conductivity (compared to other III-V compounds and silicon), and large direct band gaps of the group III nitrides are also promising for use in high temperature and power electronics as well as microwave electronics [7].

This monograph will focus on the properties of the group III nitrides related to their light emitting device applications and their potential for use in optical switching applications. Chapter 2 starts with a general introduction to the band structure of semiconductors and the concept of excitons. It then goes on to describe excitonic interactions with other quasi-particles, including those that can result in optical gain. It concludes with a general description of electron-hole plasma (EHP) formation in semiconductors and how optical gain develops from it. Chapter 2 gives emphasis to absorption and recombination processes in semiconductors pertinent to the contents of this monograph. Chapter 3 gives a general introduction to the structural and optical properties (in the low excitation regime) of the group III nitrides that are pertinent to the following chapters. Chapter 4 starts with the emission properties of highly excited GaN thin films, providing insight into the recombination and gain processes present in GaN and how they evolve and change with increasing temperature. This section also covers the original work performed on the high temperature (up to 700 K) stimulated emission (SE) properties of GaN. It goes on to describe how optically pumped lasing and "single-mode" laser emission from GaN thin films was achieved. It concludes with the optical properties of highly excited AlGaN and InGaN thin films, concentrating on the similarities and differences in their emission properties compared to their base material, GaN. Chapter 5 takes over and describes how the absorption properties of GaN thin films evolve with increasing optical excitation, providing complimentary insight to the emission processes studied in the preceding chapter. It includes evidence of the suitability of GaN for use in optical

switching applications. It concludes with the absorption properties of highly excited InGa_N films and how they differ from those of GaN. Chapter 6 is the largest of this monograph and is devoted to the optical properties of highly excited InGa_N/GaN multiple quantum well laser structures, including the observation of SE and optical gain. Its prominence in the contents of this monograph gives evidence of the importance of these structures in current state-of-the-art blue laser diode technology. Chapter 6 includes the characterization of SE as a function of temperature and the observation of high temperature (575 K) SE. It emphasizes how the emission from these structures differs from that of GaN. This chapter also includes the results of nontraditional and innovative studies related to the highly excited optical properties of these structures, including “energy selective” SE studies, excitation length dependent SE studies, and nondegenerate optical pump-probe studies of their band tail states. The results of these studies indicate the emission mechanisms in these materials differ greatly from those of conventional direct gap semiconductors. The two appendices are devoted to: (A) the mechanical polishing procedure used to produce repeatable high quality laser cavity facets for the group III nitrides, and (B) the experimental determination of the index of refraction dispersion curves for the GaN thin films used in this work.

In the following chapters, the data will be presented in one of two conventions for defining the “color” of the photons: (1) the “color” of the photons will be expressed in terms of their photon energy, given in eV, or (2) their “color” will be expressed in terms of the photon’s wavelength, given in nm. The convention adopted for a given experiment was chosen to make the interpretation of the experimental results more intuitive and/or to satisfy the convention typically used to present data for the particular experiment. One can move between the two conventions using the simple relation:

$$E = \hbar\omega = \frac{hc}{\lambda}$$

which takes the usable form:

$$[\text{photon energy in (eV)}] \cdot [\text{photon wavelength in (nm)}] = 1239.51 \text{ (nm} \cdot \text{eV)}$$

In the near UV wavelength region of band edge emission and absorption from GaN, 1 nm corresponds to approximately 10 meV.

Pulsed optical excitation with pulse durations on the order of nanoseconds will predominantly be used for the studies presented in this monograph, as the short time scales at which the optical phenomena of interest occur (on the order of tens of picoseconds or less) make it possible to study quasi-steady state phenomena during the pulse duration and still achieve the high excitation conditions necessary for these studies. These conditions make predictions about continuous-wave (cw) operation and phenomena more direct.

CHAPTER II

GENERAL OPTICAL PROPERTIES OF HIGHLY EXCITED SEMICONDUCTORS

This chapter is devoted to the optical properties associated with highly excited semiconductors (HES). For clarity, only the optical properties related to direct gap semiconductors, particularly the phenomena exhibited by and relating to highly excited group III nitrides, will be discussed. As an introduction to the general behavior exhibited by HES, we will follow the lead of Klingshirn and Haug [8] and examine the low temperature emission spectra of CdS exposed to a wide range of optical excitation intensities. This is shown in Fig. 1 [9]. Spectrum "a" was taken under steady state band-to-band optical excitation by a high pressure Hg lamp with an excitation density (I_{exc}) of approximately 2 mW/cm². The two narrow peaks observed at 2.537 and 2.546 eV, designated as I_1 and I_2 , respectively, are attributed to the recombination of excitons (bound electron-hole states) bound to neutral acceptors and donors. The weak emission at ≈ 2.553 eV is attributed to free exciton recombination. No significant changes were observed with varying I_{exc} until I_{exc} exceeded ~ 10 kW/cm². Beyond this excitation density a new emission band was observed on the low energy side of I_2 . As I_{exc} was increased further, this new emission band broadened and shifted to longer wavelengths. Its intensity was observed to grow superlinearly with increasing I_{exc} . Depending on the experimental conditions and the particular sample, other emission lines were observed to appear and disappear with increasing I_{exc} . The features shown in Fig. 1 for CdS are general to all highly excited semiconductors in that new emission bands tend to appear in a particular semiconductor as I_{exc} is increased to sufficiently high values. Typically, the emission under investigation occurs in the band edge region of the semiconductor, suggesting the new emission bands are

due to interaction processes of excitons and/or free carriers with themselves or other quasiparticles. This leads to the basic "definition" of highly excited semiconductors as it will be used in this monograph: A HES is one in which the density of electronic excitations has been increased (*i.e.* by optical pumping) to sufficiently high values that the interaction processes between the quasiparticles in the semiconductor that can be neglected at low densities become effective (to varying degrees) and give rise to new radiative (or nonradiative) recombination processes. Some basic theoretical background pertaining to the properties of HES follows in this chapter. Emphasis is given to the properties exhibited by the group III nitrides.

Band Structure of Semiconductors

In this section the concept of energy bands in semiconductors is briefly introduced. For this purpose, we will consider a crystal constructed from atoms that are infinitely far apart from each other and see how their discrete atomic energy levels are changed as we move the atoms closer and closer together. When the atoms are far from each other the electrons are tightly bound to each atom. As we move them closer together, exchange of electrons between atoms becomes more and more probable. Consider the simplest case of two atoms, A and B. As the two atoms come closer together, their wavefunctions, Ψ_A and Ψ_B , will eventually overlap. To satisfy Pauli's exclusion principle, the states of all spin-paired electrons acquire energies which are slightly different from their values in the isolated atom. The behavior of the compound AB is then described by the linear combinations of $\Psi_A \pm \Psi_B$. The sum of the wavefunctions yields the bonding state of the compound and the difference of the wavefunctions represents the antibonding state in which the atoms repel each other. If we then extend our considerations to the case of an N atom system where the N atoms are packed within a range of interaction, 2N electrons of the same orbital can occupy 2N different states, forming a band of states rather than the discrete level exhibited by the isolated atom. The energy distribution of these states is strongly dependent on the interatomic distance of the atoms, as illustrated in Fig. 2 for the specific case of carbon atoms. As the carbon atoms are brought closer together, the

lowest energy states eventually are depressed to a minimum value and the diamond crystal is formed. In the process, some of the higher energy states (2P) merge with the band of 2S states. Because of this mixture of states, the lower energy band contains as many states as electrons. This energy band is called the *valence band* and is characterized by the fact that it is completely filled with electrons. As such, it is unable to carry a current. The higher energy band is called the *conduction band* and is characterized by the fact that it is completely devoid of electrons. As such, it also cannot carry a current. If an electron were placed in this band, it would acquire a net drift under the influence of an electric field. In the region between the two bands (the energy gap) there are no allowed states and we would not expect to find any electrons. Since the interatomic distance in a crystal is not isotropic (it varies with the crystallographic direction), one would expect the banding of states to be affected by this directional variation. This leads to complex topography of the energy gap within the unit cell of the crystal. Of course, since each unit cell is identical, the energy gap has the same minimum value in each unit cell.

An alternative approach we can use to arrive at the concept of bandstructure in crystals is to start with the picture of the atoms of the crystal already in their ordered state. We then can describe the effect this crystal lattice has on electrons in the crystal by approximating the crystal as a periodic array of potential wells. This leads us to the well known Kronig-Penney model [10], which is often solved in the one dimensional case in introductory solid-state courses. The above discussion, while qualitative, will suffice for the purposes of this chapter.

Excitons

Excitons can be considered as the excited states of the N-particle system comprising the semiconductor: As an electron from the valence band is excited to the conduction band, it can experience an attractive Coulomb potential between itself and the missing electron (which can be regarded as a positively charged particle, or hole) in the valence band. This attractive potential between the electron in the conduction band and the hole in the valence band gives rise to a hydrogen-like spectrum

with an infinite number of bound states and an ionization continuum. As such, an exciton can be defined as the lowest excited state of a pure insulating semiconductor.

Basic Theory of Excitons

Two distinct limits are used to describe the excitonic nature of a particular material. They are referred to as Frenkel excitons and Wannier excitons. In general, the Frenkel picture best describes excitons in (ionic) crystals, where the interaction between the atoms of the crystal are weak and any excitation can be considered as being localized to a given atom of the crystal. Frenkel excitons are, therefore, localized to distances on the order of, or slightly greater than, the atomic spacing of the crystal, typically 0.5-1.0 nm [11]. The localized exciton description of Frenkel, though, is not appropriate for most II-VI and III-V semiconductors, including the group III nitrides, because the interaction between individual atoms in the crystal is very strong and any elementary excitation will extend over a large number of atomic sites [12]. In this case, the excited state of the crystal is constructed by taking an electron from the valence band and placing it in the otherwise unoccupied conduction band. The complex many body-interactions between the conduction band electron and the N-1 electrons in the valence band is simplified by introducing the concept of a "hole" in the valence band left when the electron was excited to the conduction band. The electron and hole can then be bound by the Coulomb interaction between them to form a hydrogen-like system known as a Wannier exciton [13], [14].

In the above mentioned limit of Wannier excitons, where the electron and hole are separated by many atomic spacings, we can use the effective mass approximation to simplify a description of the excitonic system [13]. In this approximation, the Schrödinger equation of the two particle system can be written as:

$$\left(\frac{-\hbar^2 \nabla_e^2}{2m_e^*} - \frac{-\hbar^2 \nabla_h^2}{2m_h^*} - \frac{e^2}{\epsilon r} \right) \Psi = E\Psi \quad (1)$$

where m_e^* and m_h^* are the effective masses of the electron and hole, respectively, r is the separation between the electron and the hole, and ϵ is the dielectric constant of the material. In this formalism, the similarities to the hydrogen atom are clear. The

major differences are the effective masses used for the semiconductor system and the dielectric constant, which screens the Coulomb interaction between the electron and the hole. The solution of the Schrödinger equation gives eigenstates that include a set of bound states of energies:

$$E_n(k) = -\frac{m_r e^4}{2\hbar^2 \epsilon^2 n^2} + \frac{\hbar^2 K^2}{2(m_e^* + m_h^*)} \quad (2)$$

where $n = 1, 2, \dots, \infty$, m_r is the reduced effective mass given by $m_r^{-1} = (m_e^*)^{-1} + (m_h^*)^{-1}$, and $\hbar K$ is the momentum of the center of mass (the mass in the center of mass system is given by $M = m_e^* + m_h^*$). In the above equation, the energy (E_n) is measured with respect to the bottom of the conduction band. The excitonic spectrum, therefore, consists of a hydrogen-like system of bound states below the energy gap of the semiconductor. This is shown schematically in Fig. 3. The first term in the above equation is typically expressed as $-R_y/n^2$, where R_y is defined as the exciton Rydberg, $R_y = (m_r/m_o \epsilon_o^2) R_y^H$, $R_y^H = 13.6$ eV is the hydrogen atom Rydberg, and m_o is the rest mass of an electron.

The solution for the wavefunction can be expressed as the product of a plane wave and the hydrogenic wavefunction:

$$\Phi_{n,K}(\vec{R}, \vec{r}) = V^{-1/2} \exp(i\vec{K} \cdot \vec{R}) \Psi_n(r) \quad (3)$$

where R is the center of mass coordinate and $\Psi_n(r)$ are the hydrogenic wavefunctions for the excitonic system. The hydrogenic wavefunction of the ground state is given by:

$$\Psi(r) = (\pi a_B^3)^{-1/2} \exp(-r/a_B) \quad (4)$$

where a_B is the Bohr radius of the ground state, given by $a_B = (m_o/m_r) \epsilon_o a_B^H$. a_B^H is the Bohr orbit radius of the hydrogen atom, $a_B^H = 0.053$ nm. Fig. 4 shows a low temperature absorption spectrum of high quality GaAs near the band edge, clearly illustrating $n = 1, 2, 3$ free exciton transitions.

LO-phonon Interaction

Due to the large exciton binding energy and wide band gap nature of the materials studied in this monograph, excitons are not thermally dissociated at room temperature. As such, the Fröhlich interaction between carriers and longitudinal optical (LO) phonons has the greatest effect on the optical properties studied in this work. The Fröhlich interaction Hamiltonian describing the LO-phonon interaction in a crystal is given by [15], [16]:

$$H_F(r) = \sum_q -i \left(\frac{4\pi r_p \alpha}{\Omega} \right)^{1/2} \hbar \omega_{LO} \frac{1}{q} \exp(iq \cdot r) \left(\frac{2\omega_q}{\hbar} \right)^{1/2} Q_q \quad (5)$$

where Q_q is the canonical vibrational coordinate, ω_q is the frequency of LO-phonon mode q , Ω is the volume of the crystal, and $\hbar \omega_{LO}$ is the LO-phonon energy (approximately 92 meV for GaN). The polaron radius, r_p , and the polaron constant, α , are defined as:

$$r_p = \left(\frac{\hbar}{2m\omega_{LO}} \right)^{1/2} \quad (6)$$

and

$$\alpha = \frac{1}{r_p} \frac{1}{2\hbar\omega_{LO}^3} \frac{e^2}{4\pi\epsilon_0\epsilon_\infty} (\omega_{LO}^2 - \omega_{TO}^2) \quad (7)$$

The importance of long wavelength phonons is obvious in the $1/q$ dependence of equation (5). The strength of this interaction in a given material is often expressed by the product of α and r_p , given by the parameter $r_s = \pi^{-1/2} \alpha r_p$. GaN exhibits a significantly stronger LO-phonon interaction than is typically observed in II-VI [17] and III-V [18] semiconductor materials. This strong interaction in the group III nitrides affects the optical properties, most clearly evidenced in the temperature dependent absorption spectra, where the narrow excitonic features seen at low temperatures significantly broaden with increasing temperature due to LO-phonon intermediated dissociation. The linewidth broadening, determined by the increase

in the full width at half maximum (FWHM), of the 1s exciton state due to the interaction with one LO-phonon can be expressed by first order perturbation theory as [19]:

$$\Gamma(T) = \Gamma_{inh} + \Gamma_{LO} \left[\exp \left(\frac{\hbar\omega_{LO}}{k_B T} \right) - 1 \right]^{-1} \quad (8)$$

where Γ_{inh} is the inhomogeneous linewidth (due to extrinsic effects such as alloy fluctuations), k_B is the Boltzmann constant, and Γ_{LO} represents the strength of LO-phonon coupling. Values of Γ_{LO} for GaN obtained experimentally using femtosecond four wave mixing [20] and optical absorption [21] experiments were found to be 390 and 375 meV, respectively. These values are much larger than those for GaAs and GaAs quantum wells [18]. This is not surprising as GaN has larger electron and hole effective masses than GaAs and, hence, a much larger density of states. In contrast, the density of states of ZnSe and ZnCdSe quantum wells are comparable to that of GaN, but Γ_{LO} is still considerably smaller than that of GaN [17]. This is somewhat counter-intuitive, as the density of states of ZnSe and its polarity are comparable to those of GaN. The difference in Γ_{LO} is explained, in part, by the considerably larger optical phonon energy of GaN (approximately 92 meV) compared to that of ZnSe (30 meV). It is also possible that a larger deformation potential interaction, accounting for a significant fraction of Γ_{LO} in addition to the Fröhlich interaction, is responsible for the larger value of Γ_{LO} in GaN. In any event, linewidth broadening is seen to be more severe in GaN based systems than II-VI and conventional III-V systems.

Exciton Related Gain Processes

In this section a brief description of excitonic processes leading to optical gain in HES is given. These processes occur in a regime of moderately high excitation intensity in which excitons have not been entirely dissociated due to screening by free carriers and scattering mechanisms, but are present at densities high enough that interactions between particles becomes sufficiently high and the following recombination processes become appreciable. In these processes, only part of the energy

of the recombining exciton leave the crystal as a photon. The remaining energy is transferred to other excitations, such as free carriers, excitons, or phonons. Possible exciton related optical gain processes in HES, first introduced by Benoit à la Guillaume *et al.*[22], are given below

- ▲ Exciton-Electron recombination
- ▲ Exciton-Hole recombination
- ▲ Exciton-LO phonon recombination
- ▲ Exciton-Exciton recombination
- ▲ Excitonic molecule recombination

In exciton-electron recombination, an exciton scatters off of a free electron, losing energy and momentum to the free electron and recombining at or near $k = 0$. A similar process can occur between excitons and holes in the valence band. Exciton-LO phonon recombination involves the loss of energy and momentum of an exciton to an LO-phonon with the exciton again recombining at or near $k = 0$. Exciton-exciton recombination occurs when two excitons in the $n = 1$ hydrogen-like ground level scatter, promoting one exciton to the $n = 2$ level (or higher). The other exciton recombines at a lower energy, conserving total energy. The final possibility is that (at high excitation densities) an excitonic molecule, consisting of the bound state of two excitons [23], can decay into a free exciton and another that recombines at lower energy (conserving total energy) near $k = 0$, emitting a photon. Of the above excitonic recombination mechanisms leading to optical gain in semiconductors, only exciton-exciton scattering is pertinent to the contents of this monograph and will be discussed in more detail.

Inelastic exciton-exciton scattering manifests itself in the luminescence spectra of HES by a new emission band, which is displaced from the free exciton position by approximately one exciton binding energy (E_x^b). These new emission bands, commonly referred to as P -bands in the literature, are generally described to good approximation by:

$$\hbar\omega_{\max} = E_g - E_x^b(1 - 1/n^2); \quad n = 2, 3, 4, \dots, \infty \quad (9)$$

where, again, E_g is the band gap of the semiconductor, E_x^b is the binding energy of the exciton, and $\hbar\omega_{\max}$ is the peak energy of the P_n band. This is shown schematically in Fig. 5. The P_n lines are often broad (10-30 meV in GaN) compared to the exciton linewidths, even at low lattice temperatures. This is explained by the excitons having excess kinetic energy and results in the excitons having an effective temperature (T_x) that can be much higher than the lattice temperature (T_L). In addition, the exciton binding energy may change due to the presence of the dense excitonic gas created by the intense optical pump beam [24]. From equation 9 we see that the P -bands extend from approximately $(1 + 3/4)E_x^b$ to $2E_x^b$ below the band gap of the semiconductor (or, equivalently, from $3/4E_x^b$ to E_x^b below the excitonic resonance). Fig. 6 shows a low temperature spectrum of highly excited GaN illustrating various P_2 -lines. In addition, there is the possibility that the P -bands can extend to energies far below $E_g - 2E_x^b$ if one of the excitons is scattered high into the continuum. In this case, as the excitation increases, the bottom of the bands become filled and the unbound pairs created in the exciton-exciton scattering process must have higher and higher energies. As such, the kinetic energy ($E_{e,h}^c$) can no longer be neglected. The shift of the P -line towards lower energy can then be expressed as:

$$\hbar\Delta\omega_{\max} = -E_{e,h}^c \quad (10)$$

If we assume that the bands are elliptical and consist of only one extremum this band-filling gives a shift in the P -line maximum (with respect to the P_∞ line) of:

$$\hbar\Delta\omega_{\max} = \left[\frac{1}{m_e^*} + \frac{1}{m_h^*} \right] \frac{\hbar^2}{8} \left(\frac{3}{8\pi} \right)^{2/3} n^{2/3} \quad (11)$$

where n designates the number of free carriers per unit volume in the above equation. The exciton-exciton scattering process gives rise to a rather symmetric gain spectrum with a flat transition from gain to absorption. The maximum of the gain shifts to lower energies with increasing temperature. Fig. 7 shows calculated gain spectra for CdS at different temperatures. Only scattering to the $n = 2$ exciton state (P_2 -line emission) is considered in the calculation.

The Electron-Hole Plasma

In this section the optical properties of semiconductors in which the density of e-h pairs is so high that the bound e-h pair states (excitons) are no longer stable will be described. The e-h pairs can then form a collective state, described as an electron-hole plasma (EHP). This collective state is characterized by a phase transition at a critical temperature at which the excitons ionize as the density of electronic excitations is increased. This ionization is due to the screening of the attractive Coulombic force between the electrons and holes due to the presence of a high density of free carriers. The bound e-h pairs then become unstable and the system is said to undergo a Mott transition. The density at which this transition occurs can be estimated by the simple argument that bound states become impossible if the screening length becomes on the order of, or less than, the Bohr radius of the exciton ($k_D = 1/a_o$, where k_D is the inverse Debye-Hückel screening length and a_o is the exciton Bohr radius in the ground state). The inverse Debye-Hückel screening length is given by:

$$k_D = \left(\frac{8\pi n e^2}{\epsilon_o k_B T_p} \right) \quad (12)$$

where $k_B T_p$ is the thermal plasma energy and n is the density of free carriers. The density of free carriers at which the Mott transition occurs can then be estimated as:

$$n = \frac{\epsilon_o k_B T_p}{8\pi e^2} \left(\frac{1}{a_o} \right)^2 \quad (13)$$

We start our discussion of EHP recombination by examining the electronic states in a given band structure and show how high densities of free carriers can result in net optical gain.

The wavefunction of an electron in a given band (say the conduction band) can be written as:

$$\Psi_c(\vec{r}) = u_{c\vec{k}}(\vec{r}) \exp(i\vec{k} \cdot \vec{r}) \quad (14)$$

where $u_{c\vec{k}}(\vec{r})$ contains information on the periodicity of the semiconductor crystal lattice and \vec{k} is the crystal momentum vector. The crystal momentum vector is

quantized such that:

$$k_i = \frac{2\pi s}{L_i}; \quad i = x, y, z \quad (15)$$

where s is an integer and L_i is the length of the crystal in the i -direction. In the parabolic band approximation, the energy above the conduction band edge for a given state k is given as:

$$E(\vec{k}) = \frac{\hbar^2 k^2}{2m_c} \quad (16)$$

where m_c is the effective mass for electrons in the conduction band and $E(\vec{k})$ is measured with respect to the bottom of the conduction band. From equations (15) and (16) we can obtain an expression for the density of states per unit energy in the conduction band:

$$\rho_c(E) = \frac{1}{2\pi} \left(\frac{2m_c}{\hbar^2} \right)^{3/2} E^{1/2} \quad (17)$$

with a similar expression for the density of states per unit energy in the valence band.

At $T = 0$ the ground state of an electron system in a semiconductor is characterized by a fully occupied valence band and an empty conduction band. If an electron is excited by a photon from the valence band (state a) to the conduction band (state b), leaving behind an empty electronic state (hole) in the valence band, the total energy and momentum should be conserved (the reverse process in which an electron and hole recombine and emit a photon should also conserve energy and momentum). Since the photon momentum k_p is, in general, negligible compared to the carrier momentum, the conservation of energy and momentum equations become:

$$E_b - E_a = \hbar\omega \quad (18)$$

and

$$\vec{k}_b = \vec{k}_a + \vec{k}_p \approx \vec{k}_a \quad (19)$$

Now assume that by some means (*i.e.* by optical excitation) we prepare a semiconductor such that the states below a given level in the conduction band (E_{Fc}) are occupied and those above a certain level in the valence band (E_{Fv}) are empty. E_{Fc} and E_{Fv} are referred to as the quasi-Fermi levels of the conduction and valence

bands, respectively. This is illustrated in Fig. 8. In this condition, the semiconductor is referred to as “inverted”. At finite temperatures the electrons and holes are thermally distributed around their quasi-Fermi energies. This thermal redistribution is governed by the Fermi-Dirac law:

$$f(E) = \frac{1}{\exp[(E - E_{Fv,c})/k_B T] + 1} \quad (20)$$

This is given schematically in Fig. 9(a). Now, it can be shown [25] that the gain coefficient, $g(\omega)$, at a given temperature can be expressed as:

$$g(\omega) = \frac{\pi \omega \mu^2}{\hbar c n \epsilon_o} \int_{E_g/\hbar}^{\infty} \rho_j(\omega_o) [f_c(\omega_o) - f_v(\omega_o)] \frac{T^2 d\omega_o}{\pi [1 + (\omega - \omega_o)^2 T_2^2]} \quad (21)$$

where μ is the interband matrix element, T_2 is the carrier dephasing time, and ρ_j is the joint density of states, given by:

$$\rho_j(\omega_o) \equiv \frac{1}{2\pi^2} \left(\frac{2m_r}{\hbar} \right)^{3/2} (\omega_o - E_g/\hbar)^{1/2} \quad (22)$$

where m_r is again the reduced mass of the electron and hole. In the approximation $T_2 \rightarrow \infty$, the last term in the integrand of equation (21) becomes a delta function and the gain can be integrated to:

$$g(\omega) = \alpha_o(\omega) [f_c(\omega) - f_v(\omega)] \quad (23)$$

where $\alpha_o(\omega)$ is the loss of the unpumped system, given as:

$$\alpha_o(\omega) = \frac{\omega \mu^2 (2m_r)^{3/2}}{2\pi \hbar^3 c n \epsilon_o} (\hbar \omega - E_g)^{1/2} \quad (24)$$

It follows from equation (23) that the necessary condition for net optical gain ($g(\omega) > 0$) is:

$$f_c(\omega) - f_v(\omega) > 0 \quad (25)$$

which can be rewritten using the Fermi-Dirac function as:

$$E_{Fc} - E_{Fv} > \hbar \omega \quad (26)$$

A graphic illustration of EHP gain calculation based on equation (23) is given in Fig. 9. The gain profile is enveloped by the $E^{1/2}$ functional form of the bulk density of states given in equation (17). It is clear from Fig. 9 that optical gain exists for photons in the energy range between the reduced band gap (E'_g) and the energy separation of the quasi-Fermi energies:

$$E'_g < \hbar\omega < E_{Fc} - E_{Fv} \quad (27)$$

where $E_{Fc} - E_{Fv}$ is referred to as the chemical potential, $\mu(n, T)$. Often the quasi-Fermi energies are given with respect to their respective band edge. In this case equation (27) becomes:

$$E'_g < \hbar\omega < E'_g + E_F^e + E_F^h \quad (28)$$

where E_F^e and E_F^h represent the quasi-Fermi energies in this convention. Absorption is clearly expected for photons of energy greater than:

$$\hbar\omega > E'_g + E_F^e + E_F^h \quad (29)$$

Typically, optical gain originating from an electron-hole plasma will be observed at photon energies slightly below the *unperturbed* band gap of the material.

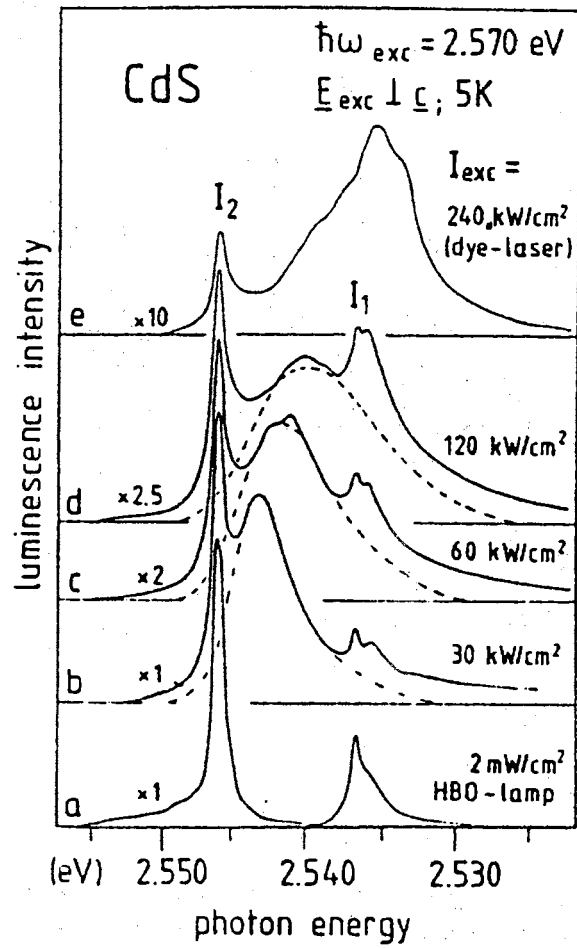


Figure 1. 5 K near band edge luminescence spectra of CdS for various optical excitation intensities. The normalization factors are given on the left side of the figure. From [9].

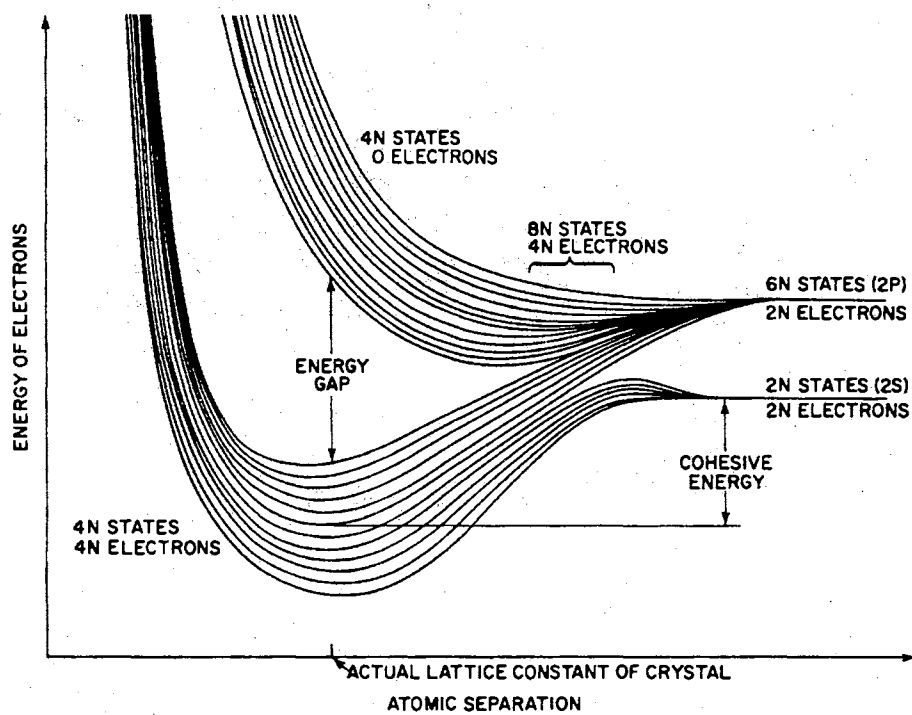


Figure 2. Energy banding of allowed electronic levels in diamond as a function of spacing between carbon atoms. From [26].

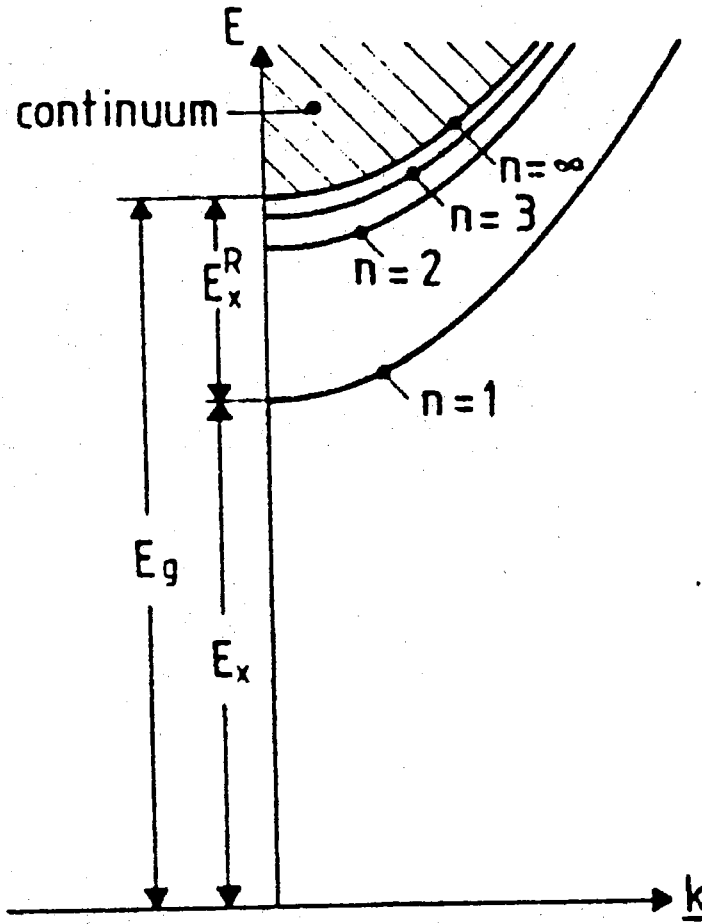


Figure 3. Schematic of the dispersion curves of Wannier excitons in direct gap semiconductors. The bound states form the discrete bands with main quantum numbers $n = 1, 2, \dots, \infty$, while the ionized states form a continuum. E_g and E_x^R represent the band gap energy and exciton Rydberg energy, respectively. The curvature of the dispersion curve gives the effective mass of the exciton. From ref. [8].

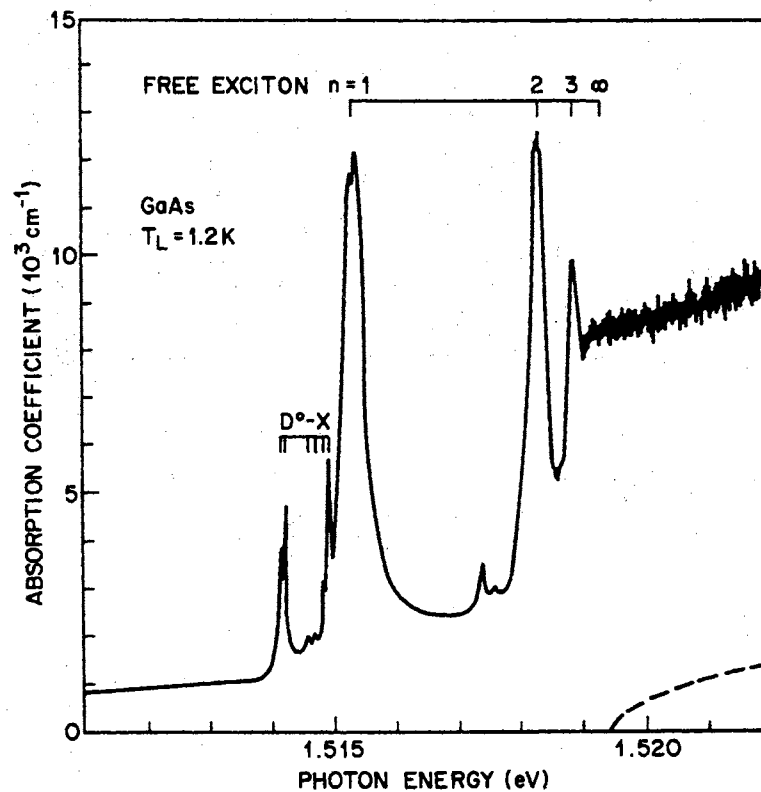


Figure 4. Absorption spectrum of high quality GaAs near the band edge at 1.2 K. The $n = 1, 2, 3$ free exciton transitions are clearly seen. Excitons bound to donors ($D^0\text{-X}$) are also indicated. From ref. [27].

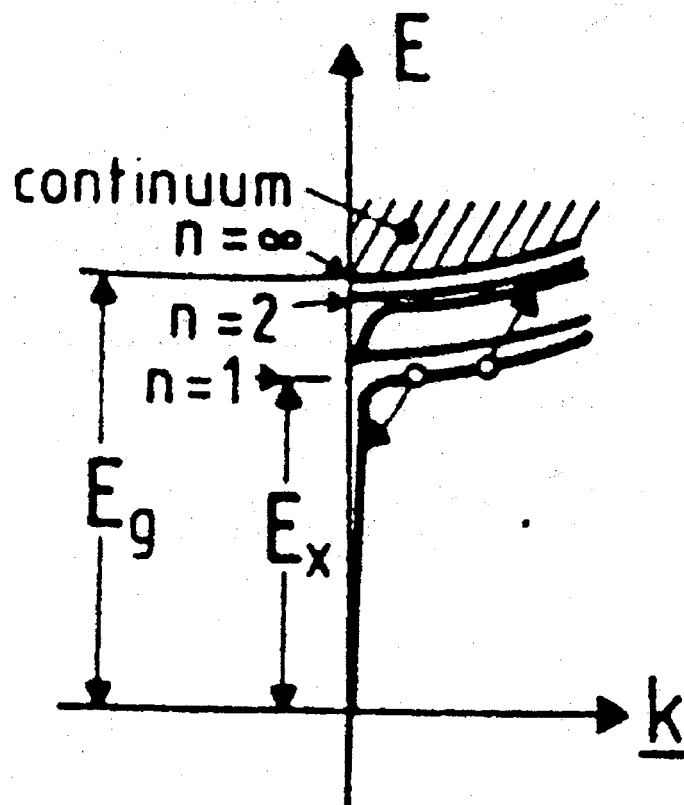


Figure 5. Schematic of inelastic exciton-exciton scattering recombination in direct gap semiconductors. E_g and E_x represent the band gap energy and the $n = 1$ free exciton energy, respectively. From ref. [8].

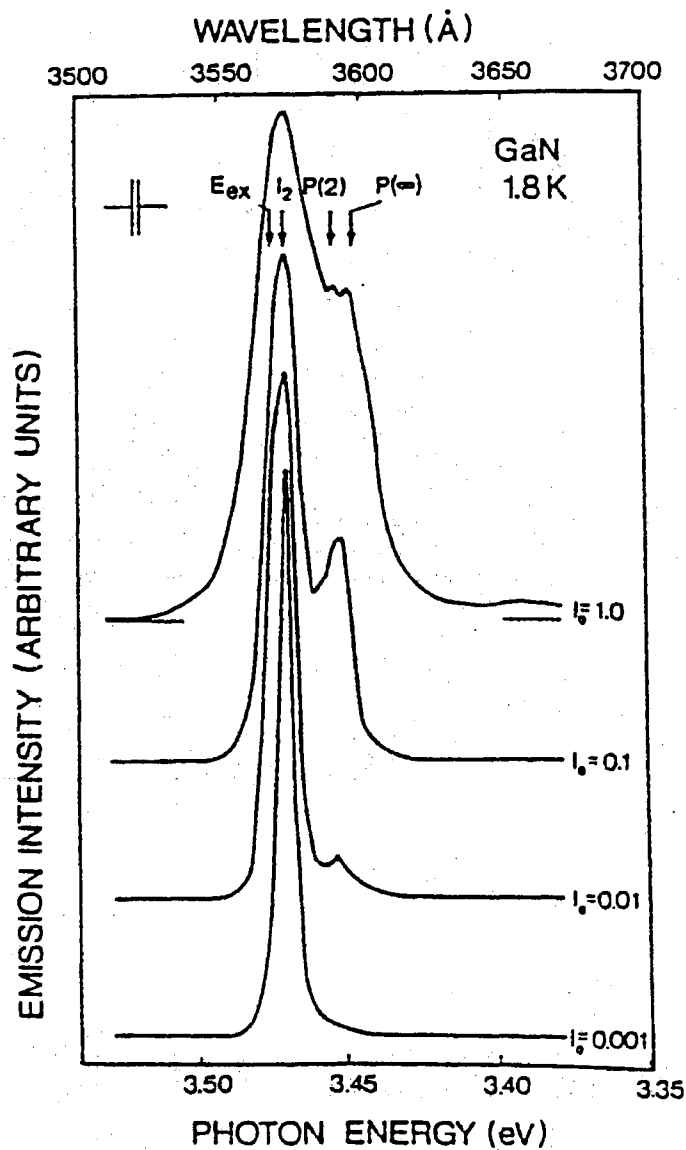


Figure 6. Emission spectra of GaN at 1.8 K as a function of optical excitation density under the conditions of ns pulsed excitation. $I_0 \approx 2.5 \text{ MW/cm}^2$. New emission lines attributed to inelastic scattering of excitons into the $n = 2$ and $n = \infty$ excited states appear with increasing optical excitation. From ref. [28].

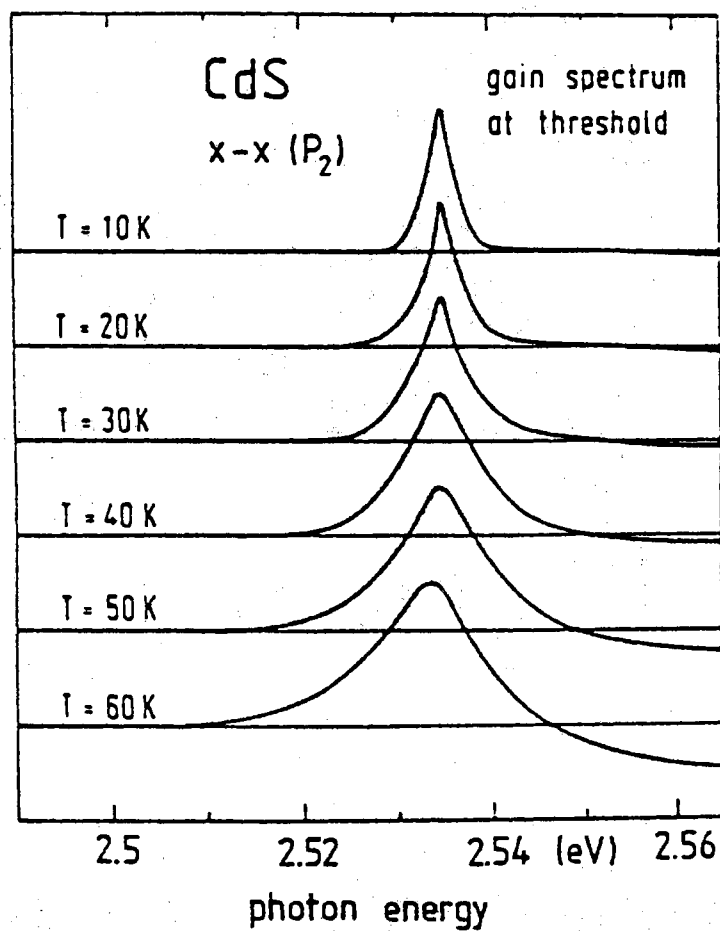


Figure 7. Calculated gain spectra of exciton-exciton scattering in CdS at different temperatures. Only transitions to the $n = 2$ exciton state (P_2 -emission) were considered in the calculation. From ref. [29].

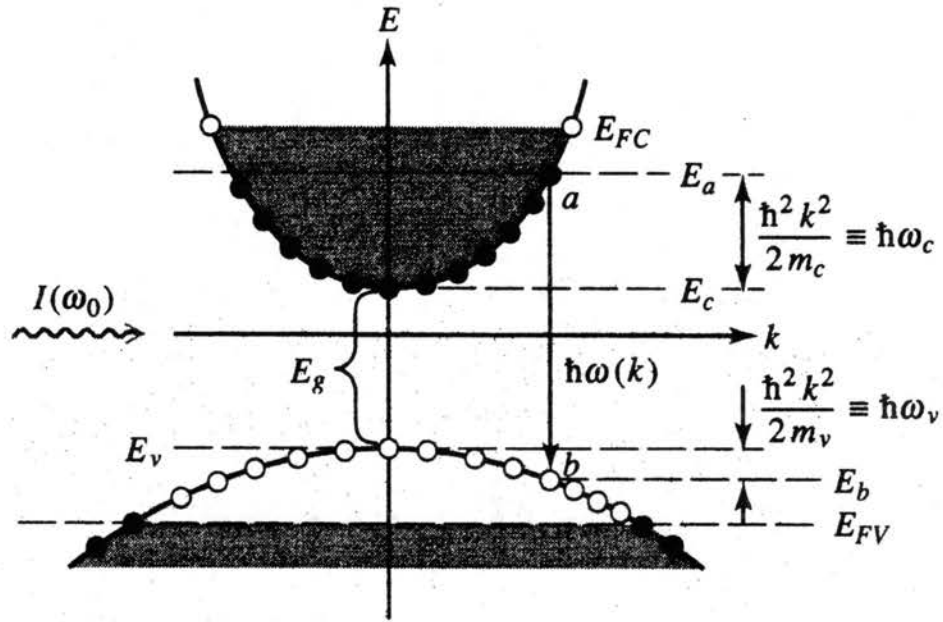


Figure 8. Band diagram of a direct gap semiconductor under the conditions of strong optical excitation leading to the formation of an EHP. An optical beam of frequency ω_o and intensity I_o is incident on a pumped semiconductor medium characterized by quasi-Fermi levels E_{Fc} and E_{Fv} . A single pair (a, b) with the same k value is shown. The induced transition $a \rightarrow b$ contributes one photon to the beam. From ref. [30].

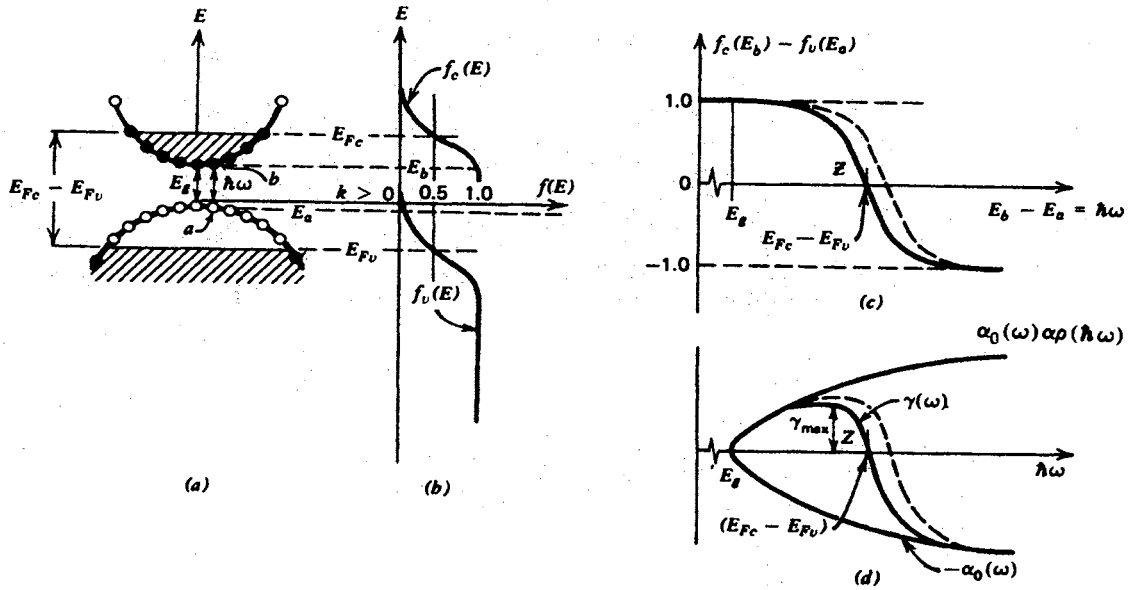


Figure 9. A graphical step-by-step construction of the gain profile, referred to here as $\gamma(\omega)$ instead of $g(\omega)$, assuming $T_2 = \infty$. The dashed curves in (c) and (d) correspond to a higher excitation level, resulting in a shift in point Z to the right which in turn results in an increase in γ_{max} and the frequency, ω_{max} , at which it occurs. $\hbar\omega = E_{Fc} - E_{Fv}$. From ref. [25].

CHAPTER III

GENERAL PROPERTIES OF THE GROUP III NITRIDES

Because several reviews of the optical properties of the group III nitrides exist in the literature (see, for example [31], [32]) where interested readers can readily find the a good synopsis of known optical properties, only those properties that are pertinent to the contents of this monograph will be given here. Since the technologically important nitride-based materials are InGaN (for blue light emitting devices) and AlGaN (for solar blind UV detectors) with moderate to low indium and aluminum concentrations, respectively, we will concentrate on the optical properties of the base material, GaN. This is also made necessary because of the large band tailing that results from the incorporation of Al and In into GaN to form AlGaN and InGaN, making the observation of fundamental optical transitions very difficult, even in state-of-the-art high quality crystals.

Structural

Like most semiconductor materials, the group III nitrides have a tetrahedrally coordinated atomic arrangement that typically results in either a hexagonal (wurtzite) or cubic (zincblende) crystal structure. In all, there are three common crystal structures shared by the group III nitrides: The wurtzite, zincblende, and rocksalt structures. The thermodynamically stable structure for bulk AlN, GaN, and InN at ambient conditions is wurtzite, although the zincblende structure has been stabilized by epitaxial growth of thin films on the (100) and (011) crystal planes of cubic crystal substrates such as Si, MgO, and GaAs. The rocksalt structure can only be induced at very high pressures. Only the structural and optical properties of the

wurtzite form of the group III nitrides will be considered in this monograph. The wurtzite crystal structure has a hexagonal unit cell, and therefore two lattice constants, designated as a and c . It contains six atoms of each type and consists of two interpenetrating hexagonal close packed sublattices (each with one type of atom), offset along the c axis by $5/8$ of the cell height ($5/8 c$). The stacking sequence of the (0001) diatomic planes is ABABAB in the $\langle 0001 \rangle$ direction. The space grouping of the wurtzite structure is $P6_3mc$ (C_{6v}^4). The wurtzite crystal structure and stacking sequence are given in Figs. 10 and 11, respectively. In its wurtzite form, AlN has a molar mass of 20.495 gm/mol. Reported lattice parameters range from 0.3111 to 0.3113 nm for a , and from 0.4978 to 0.4982 nm for c . The AlN linear thermal expansion coefficients are $\alpha_{\perp} = 5.27 \times 10^{-6} \text{ K}^{-1}$ for $T = 20 - 800 \text{ }^{\circ}\text{C}$, and $\alpha_{\parallel} = 4.15 \times 10^{-6} \text{ K}^{-1}$. The thermal conductivity of AlN is $k = 2 \text{ W/cm}\cdot^{\circ}\text{C}$ at room temperature. The dielectric constants of AlN are $\epsilon(0) = 9.14$ and $\epsilon(\infty) = 4.84$ at 300 K. GaN has a molecular weight of 83.728 gm/mol and room temperature lattice parameters of $a_o = 0.31892 \pm 0.00009 \text{ nm}$ and $c_o = 0.51850 \pm 0.00005 \text{ nm}$. The GaN linear thermal expansion coefficient is $\alpha_{\parallel} = 4.15 \times 10^{-6} \text{ K}^{-1}$ along the a -axis. The thermal conductivity of GaN is $k = 1.3 \text{ W/cm}\cdot^{\circ}\text{C}$ at room temperature, nearly equal to that of Si and about three times that of GaAs. The dielectric constant of GaN has been measured to be in the range $\epsilon(0) = 8.9$ to 9.5 at room temperature, just below that of SiC. Values reported for InN are varied due to the absence of good quality single crystal films. InN has a molar mass of 128.827 gm/mol and the lattice parameters reported in the literature range from 0.3530 to 0.4980 nm for a_o , and from 0.5960 to 0.574 nm for c_o . For a complete review of the structural properties of the group III nitrides, see, for example, ref. [31]. GaN is by far the most extensively studied of the group III nitrides, but is still in need of extensive investigation if it is to reach the level of understanding and technological status of Si and GaAs.

Optical

When GaN crystallizes in the wurtzite form, its conduction band minimum is located at the center of the Brillouin zone (Γ -point, $k = 0$) and has a Γ_7 -symmetry

with a quantum number $J_z = 1/2$. The valence band also has its maximum at the Γ -point, resulting in a direct fundamental band gap. The top of the valence band is split into three sub-bands as a result of crystal-field and spin-orbit coupling. These valence bands are conventionally referred to as the A, B, and C valence bands and are a direct result of GaN's wurtzite crystal structure. The A-band has Γ_9 -symmetry, while the B and C bands have Γ_7 -symmetry. Detailed reviews of the electronic band structure can be found in abundance in the literature. The band structure of wurtzite GaN is shown in Fig. 12. Because only the transitions associated with the lowest conduction band and uppermost valence bands in GaN near $k = 0$ are pertinent to this monograph, they are shown in detail in Fig. 13. In GaN, each valence band generates a hydrogenic series of excitonic states [33], [34]. The free exciton states in GaN are adequately described by the Wannier-Mott approximation described in the preceding chapter. The ternary compounds InGaN and AlGaN typically do not exhibit excitonic features and (spontaneous) emission is dominated by recombination from band tail states, with the depth of band tailing dependent on the Al and In concentrations as well as the growth conditions. Because of this, we will concentrate in this section only on the optical properties of GaN. This allows us to gain a better understanding of the base material without the complications presented in the ternary compounds. The optical properties of the ternary compounds will be introduced as needed later in the text.

Photoluminescence

At low temperatures, the near band edge luminescence observed from most GaN layers is dominated by a strong, narrow emission line resulting from radiative recombination of bound excitons, typically denoted as BX. In addition, one or more other features may be present originating from radiative recombination of the A and B free exciton transitions, designated as FX^A and FX^B , respectively. Typical low temperature photoluminescence spectra are shown in Fig. 14. Note that the intensity of the BX line decreases with increasing temperature at a rate much quicker than the free exciton transitions, giving evidence that the bound exciton designation is correct.

Typical lifetimes of the main PL decay are on the order of ≈ 35 ps for the free exciton transitions and ≈ 55 ps for the bound exciton transition at 10 K. These values are much shorter than the theoretically estimated values of a few nanoseconds [35]. The faster than expected decay indicates that nonradiative recombination dominates the exciton population decay.

Absorption

Three fine exciton resonances associated with the A, B, and C exciton transitions between the bottom of the conduction band and the top three valence bands have been observed in high quality GaN thin films. The excitonic resonances have been observed in absorption measurements at temperatures in excess of 400 K, illustrating the substantially large exciton binding energy of excitons in this material [21]. Typical absorption spectra from high quality GaN thin films are shown in Fig. 15. The spectrally distinct excitonic resonances seen at 10 K are seen to broaden and merge with increasing temperature, but are still observable at temperatures exceeding 400 K.

Photoreflection

Reflectivity measurements, especially photoreflectance, clearly demonstrate the signatures of the 1s A, B, and C excitonic transitions as well as the fundamental band-to-band transition [36], [37], [38]. In addition, higher order excitonic transitions can often be observed. This is demonstrated in Fig. 16.

Strain effects on the excitonic transitions

Recently, the importance of residual strain effects in GaN epilayers due to the mismatch of lattice parameters and coefficients of thermal expansion between GaN and common substrate materials has been realized [39], [40], [41], [42]. Even though strain relaxation by the formation of a large density of dislocations is known to occur in GaN, the residual strain in the layers has been shown to have a strong influence on

the exciton transition energies. This is illustrated in Fig. 17 for samples of varying thickness (and therefore varying degrees of relaxation) and different substrates (SiC and sapphire). The reflection spectra clearly show shifts of the excitonic transitions between the different samples. In general, it is difficult to determine if the dominant strain effect is due to the lattice parameter mismatch or the thermal mismatch between the GaN layer and the substrate, but it is clear from Fig. 17 that the overall effect of residual strain in GaN on sapphire is compressive, leading to an increase in the band gap energy, while the stress induced on GaN on SiC is tensile and results in a decrease in the band gap energy. From this it has been determined that the thermal expansion mismatch has the dominant effect on the energy variations of the excitonic transitions in GaN, since lattice mismatch induced strain by itself would have an opposite effect on the transition energies [43], [42], [41]. For the above reasons, it is important to compare relative energy shifts of the band edge transitions with increasing optical excitation, not just the absolute energy changes, in the pages to come. It is also important to take this into consideration when attempting to compare optical phenomena from different GaN layers, even though they may all be of exceptional quality.

AlGaN

The alloying of GaN with AlN results in the ternary compound $\text{Al}_x\text{Ga}_{1-x}\text{N}$, which is technologically important in that its (direct) band gap can be tuned from that of GaN (≈ 3.5 eV) to that of AlN (≈ 6.2 eV), covering almost the entire deep UV region of the spectrum. To first approximation, the band gap of $\text{Al}_x\text{Ga}_{1-x}\text{N}$ can be estimated to be a linear extrapolation between that of GaN and AlN. Typically this is not the case in semiconductors, and a bowing parameter, b , must be introduced. The dependence of E_g on x then becomes:

$$E_g(x) = xE_g(\text{AlN}) + (1 - x)E_g(\text{GaN}) - bx(1 - x) \quad (30)$$

where $E_g(AlN)$ and $E_g(GaN)$ designate the band gap energies of AlN and GaN, respectively, x is the aluminum mole fraction, and b is the bowing parameter. Currently there is no agreement on a suitable method for determining the mole fraction of aluminum in AlGaN films. Consequently, significant controversy exists on how the band gap changes with aluminum mole fraction. The reported values for the band gap change with aluminum mole fraction are summarized in Fig. 18. Note that the band gap is almost a linear function of x .

InGaN

The alloying of GaN with InN results in the ternary compound $In_xGa_{1-x}N$ which is technologically important for its use in near UV-blue-green light emitting devices, as its (direct) band gap can be tuned from that of GaN (≈ 3.5 eV) to that of InN (≈ 1.9 eV) by varying the indium concentration. Unlike $Al_xGa_{1-x}N$, the band gap dependence on indium mole fraction measured by a number of researchers with different growth techniques has resulted in a consistent bowing parameter of $b = 1.0$ eV in the following equation [44]:

$$E_g(x) = (1 - x)E_g(InN) + xE_g(GaN) - bx(1 - x) \quad (31)$$

where $E_g(InN)$ and $E_g(GaN)$ refer to the band gaps of InN and GaN, respectively, and x is the indium mole fraction. The consistency of reported results is illustrated in Fig. 19. A good fit of equation (31) to the experimental results is clearly seen.

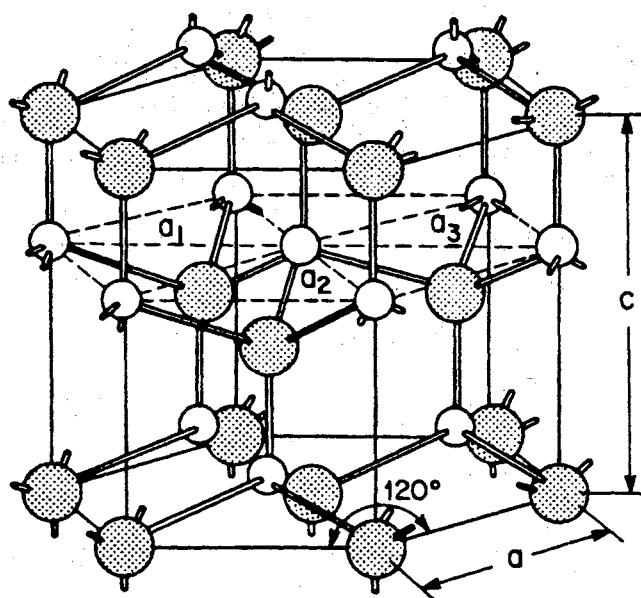


Figure 10. Schematic of the wurtzite unit cell. From [45].

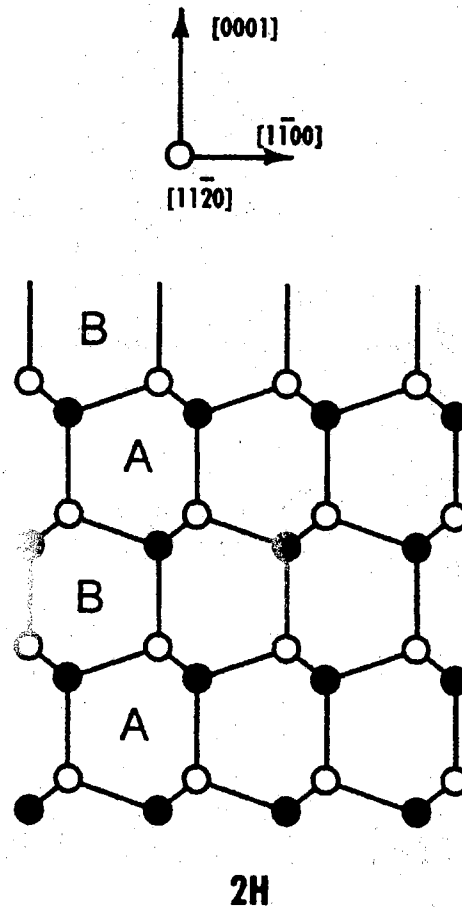


Figure 11. Stacking sequence of atomic planes in wurtzite GaN. From [46].

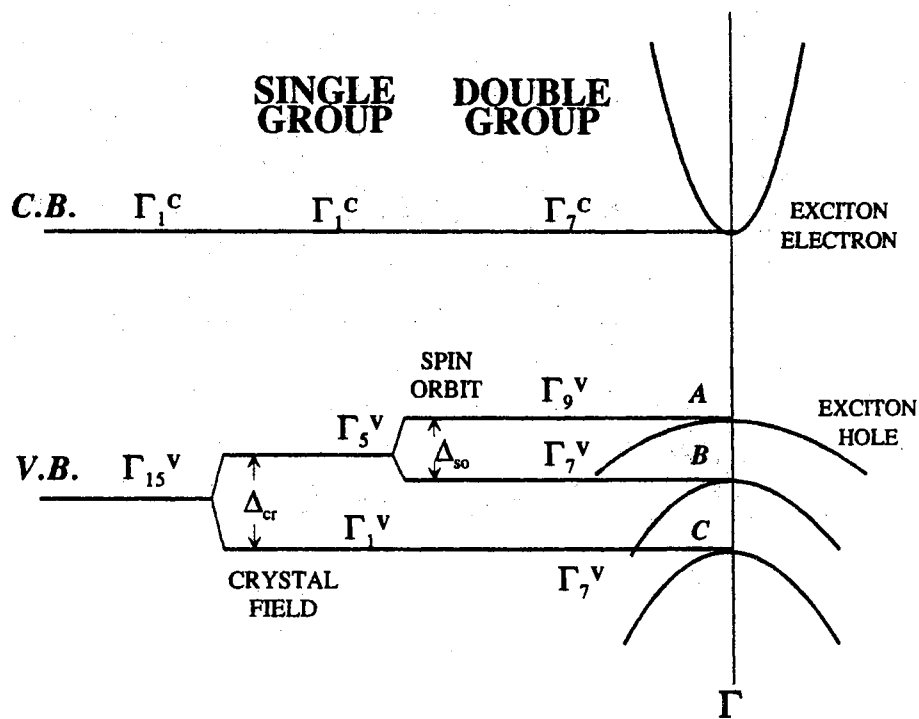


Figure 13. Structure and symmetries of the lowest conduction band and the uppermost valence bands in wurtzite GaN at the Γ point ($k \approx 0$). From [48].

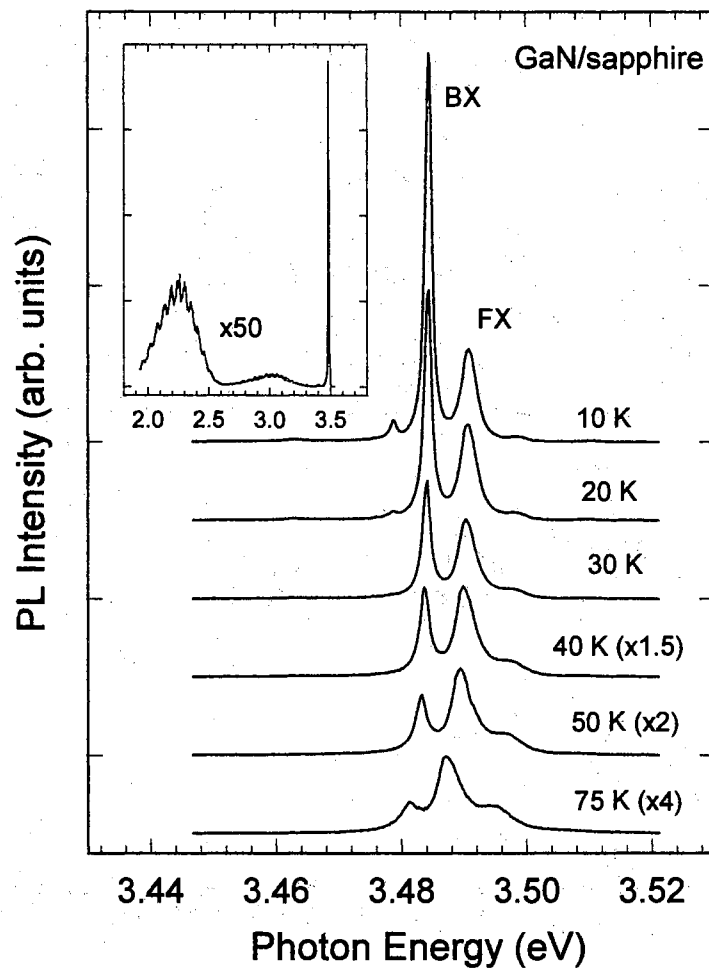


Figure 14. Low temperature near band edge PL spectra from a 7.2 μm GaN thin film grown by MOCVD on (0001) oriented sapphire. The spectra have been shifted vertically for clarity. The inset shows the 10 K PL spectrum over an expanded spectral range. Adapted from [49].

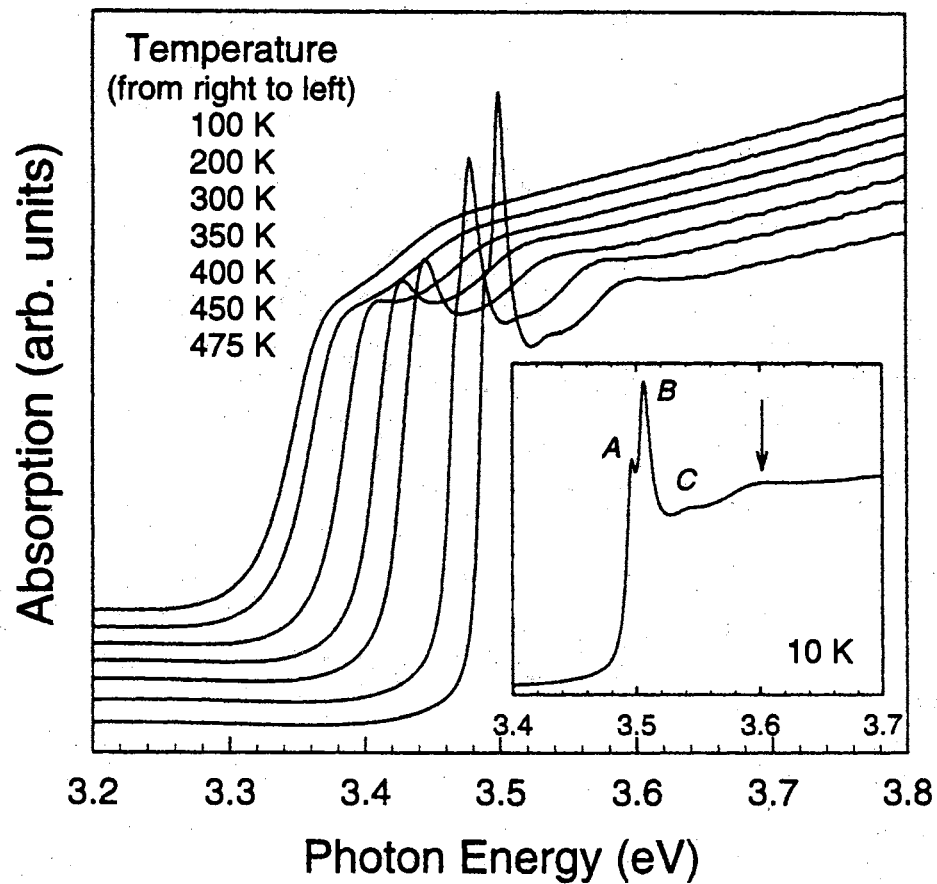


Figure 15. Absorption spectra in the vicinity of the fundamental absorption edge of a 0.38 μm GaN epitaxial layer grown on (0001) oriented sapphire by MOCVD. The curves have been vertically displaced for clarity. The inset details the near band edge exciton resonances at 10 K. The spectral feature indicated by the arrow in the inset is due to indirect exciton formation by the simultaneous creation of an exciton and an LO phonon. From [48].

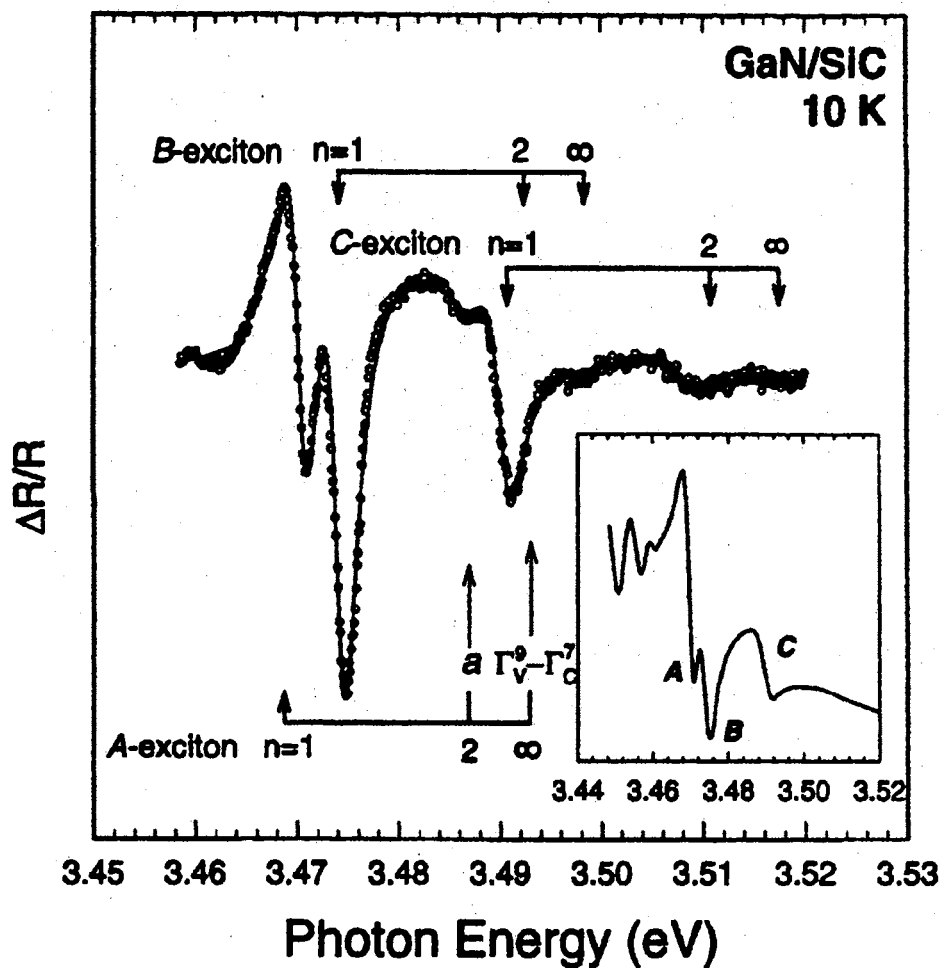


Figure 16. 10 K photoreflection spectrum from a 7.2 μm GaN epitaxial layer grown by MOCVD on (0001) oriented sapphire. The open circles represent experimental data and the solid line represents the best least squares fit to the experimental data. The A, B, and C excitonic transitions are clearly seen in the PR spectrum, as are higher order excitonic transitions. The inset shows the same for a 3.7 μm GaN epitaxial layer grown on SiC. From [36].

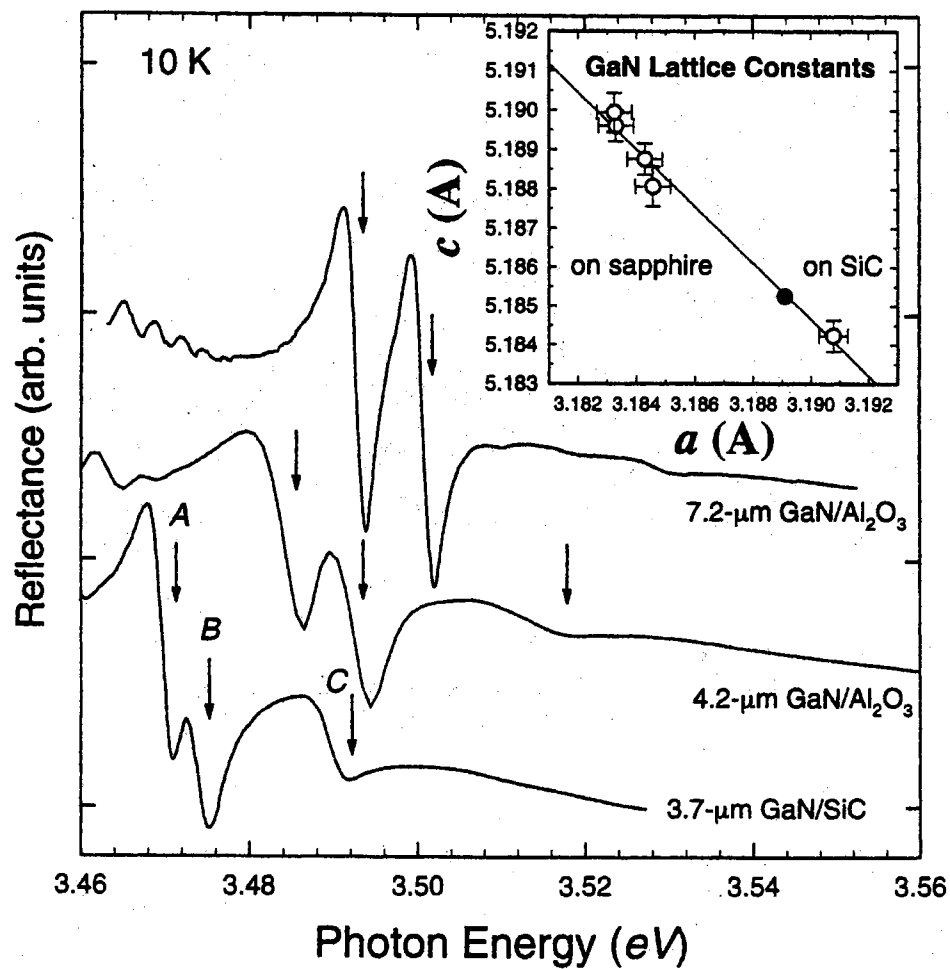


Figure 17. 10 K photoreflection spectra in the excitonic region of GaN layers of various thickness and substrate material. The curves have been vertically displaced for clarity. The inset gives the measured GaN lattice parameter in the growth direction (c-axis) versus the in-plane lattice constants (a-axis) measured by high precision X-ray diffraction. The solid circle in the inset shows the lattice constants for strain-free GaN for reference. From [48].

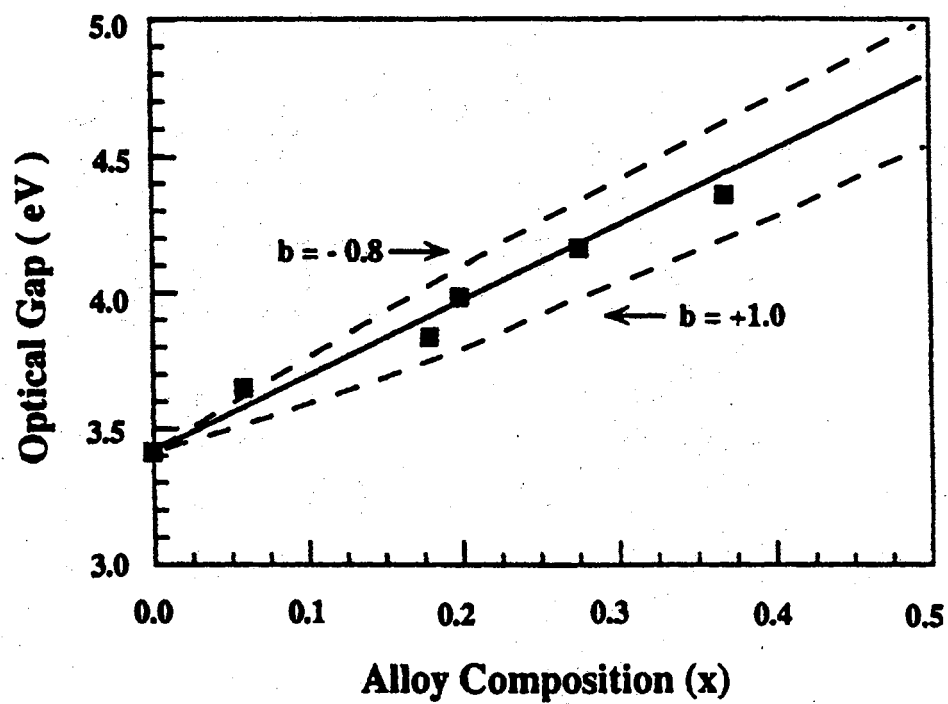


Figure 18. Band gap of $\text{Al}_x\text{Ga}_{1-x}\text{N}$ epitaxial layers as a function of alloy concentration x . The solid line represents $b = 0$ and the dashed lines represent the range of values reported in the literature. From [31].

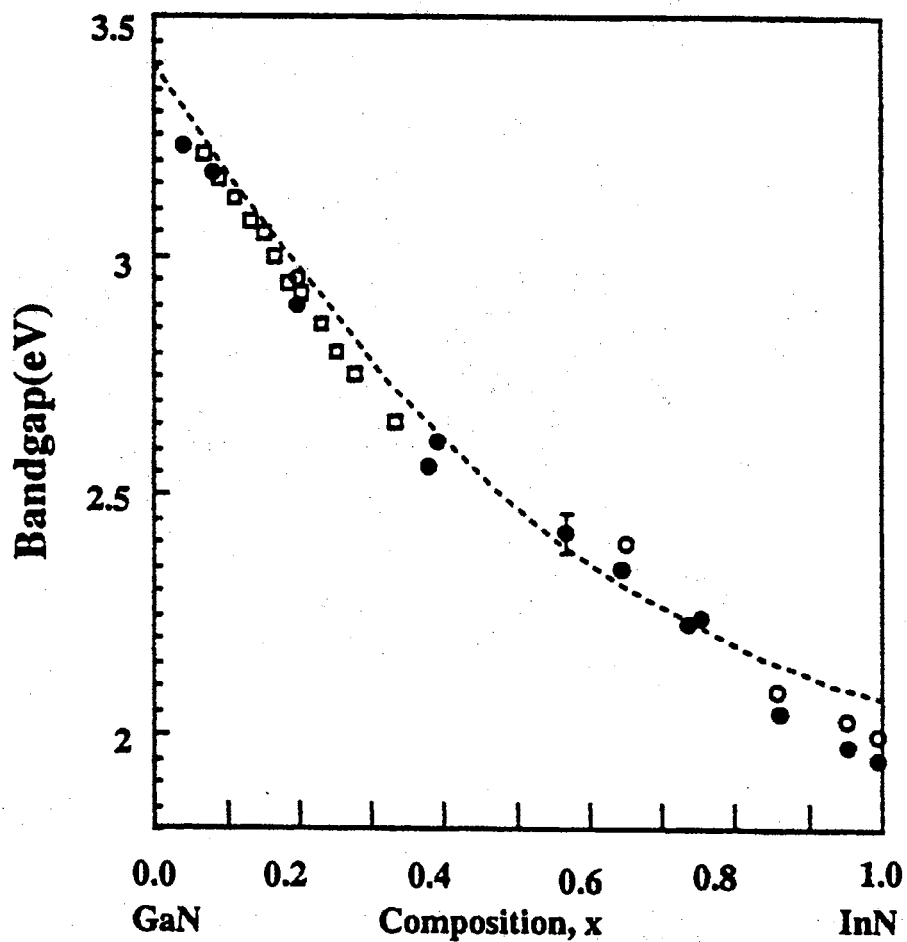


Figure 19. Band gap of $\text{In}_x\text{Ga}_{1-x}\text{N}$ epitaxial layers as a function of alloy composition x . The solid circles, open circles, and open squares represent experimental data reported in the literature. The dashed line represents the equation given in the text. From [31].

CHAPTER IV

EMISSION PROPERTIES OF HIGHLY EXCITED GROUP III NITRIDES

We will concentrate in this chapter on the emission properties of highly excited group III nitrides, with an emphasis on GaN, which is by far the most extensively studied of the group III nitrides. The alloying of GaN with moderate ($x \lesssim 0.2$) molar concentrations of Al and In to form the ternary compounds $\text{Al}_x\text{Ga}_{1-x}\text{N}$ and $\text{In}_x\text{Ga}_{1-x}\text{N}$ allows the band edge emission to be tuned over the entire near UV to blue wavelength region. In particular, InGaN is well suited for generation of light in the violet and blue spectral region, and is therefore of significant technological relevance. Because of the difficulties associated with indium incorporation into GaN, InGaN films typically exhibit significantly broader band edge transitions due to compositional fluctuations. The same is true for AlGaN films, although the difficulties in uniform Al incorporation have different origins. Because of this, we will concentrate in this section mostly on the optical properties of the base material, GaN, where the band edge transitions are significantly better behaved and can be better compared to phenomena predicted by theory. We will point out here that while GaN exhibits markedly improved optical quality over its ternary alloys, its development is still in its infancy compared to traditional III-V semiconductor technology. Because of this, its optical quality is far from that of GaAs based semiconductors. For this reason, the optical phenomena associated with highly excited GaN can vary (slightly) from sample to sample and experimental fact often cannot be quantitatively described by theory (this is often difficult even in near perfect semiconductors). Because of this, we will concentrate on the optical properties associated with highly excited GaN.

that are common to all high quality GaN layers studied and we will rely on qualitative analysis to describe the emission mechanisms common to all. This chapter will start with a description of the band edge related emission from GaN thin films as a function of increasing optical excitation. It will then describe the stimulated emission (SE) behavior of GaN as a function of temperature, most notably how the SE threshold (I_{th}) and the energy separation between the SE peak and the spontaneous emission peak change as a function of temperature. We will then use this behavior to deduce the SE mechanism(s) for the various temperatures. Next, we will describe the emission behavior as we form laser structures from GaN layers by processing the sample edges to form cavity mirrors (facets) and increase the reflectivity of the laser cavity mirrors by imposing external mirrors on the facets. The last section will describe the emission behavior of highly excited AlGaN and InGaN thin films and how their behavior compares to GaN.

Stimulated Emission from Highly Excited GaN

SE from GaN was reported as early as 1971 by Dingle *et al.* who optically pumped single crystal GaN needles using the 337 nm radiation from a nitrogen laser to achieve SE at cryogenic temperatures [50]. The report also included the observation of lasing when the needles were mechanically polished to form the cavity facets necessary for feedback and lasing to occur. Following the report by Dingle, several groups reported similar behavior and some preliminary work was done towards identifying the low temperature gain mechanisms in GaN. Although SE was reported over 25 years ago from GaN, it took the development of suitable epitaxial techniques to produce GaN thin films and heterostructures necessary for device development. In addition, the lack of a suitable lattice matched substrate for GaN significantly hindered the development of high quality single-crystal GaN thin films. Some of these issues remain today.

The GaN layers used in this work were nominally undoped epitaxial films grown by low pressure metalorganic chemical vapor deposition (MOCVD) on (0001) oriented sapphire and 6H-SiC substrates. Thin AlN buffer layers (on the order nanometers) were deposited on the substrates at 775 °C prior to the growth of GaN. The GaN layers were deposited at 1040 °C on the AlN buffer layers. These growth conditions typically result in high quality single-crystal GaN layers [51], [52]. The thickness of the GaN layers used in this work ranged from 0.8 to 7.2 μm .

Optically pumped SE studies are typically carried out in a “side-pumping” or “edge emission” geometry, where the exciting laser beam is focussed to a line on the sample surface using a cylindrical lens and the emission is collected from one edge of the sample. This geometry ensures adequate amplification path length and simulates the geometry of traditional stripe geometry laser diodes. In contrast, the sample may be excited in a “surface emission” geometry, where the exciting laser beam is focused onto the sample surface (typically in the form of a circular spot) and the emission is collected from the surface of the sample. This is often done in spontaneous emission studies where one wants to avoid the lineshape distortion caused by the reabsorption of emitted photons as they travel along the (long) amplification path in the edge emission experiments. These two geometries are shown in Fig. 20. The near UV laser radiation required to optically pump GaN above its fundamental band gap was generated by frequency doubling deep red radiation generated by an amplified dye laser pumped by the second harmonic of a Q-switched, injection seeded Nd:YAG laser. The pulse width was ≈ 4 ns FWHM and the laser operated at a repetition rate of 10 Hz. Alternately, the third harmonic (355 nm) of the Nd:YAG laser could be used directly to pump the samples. The latter system is advantageous in that the laser noise is significantly reduced but it suffers from a lack of tunability of the excitation wavelength. For this reason, both pumping systems were utilized, depending on which was more advantageous for a given experiment. Naturally, optically pumped SE and lasing is a precursor to the desired goal - current injection lasers. Optical pumping is, therefore, a valuable tool in assessing the material quality of a semiconductor and in studying its optical phenomena without the restrictions

imposed by proper junction placement, current confinement/leakage considerations, and suitable electrical contacts.

The evolution of band edge emission from GaN with increasing optical excitation is shown in Fig. 21 at 10 K. Under the conditions of low optical excitation, two distinct transitions are clearly seen, attributed to radiative recombination of bound excitons (BX) and the 1s A free exciton transition (designated as FX in the figure), as described in the preceding chapter. With increasing optical excitation, the BX transition is observed to saturate and the FX transition broadens and continues to increase. At sufficiently high excitation densities (I_{exc}), as achieved in nanosecond optical pumping experiments, a new emission peak emerges approximately 21 meV below the FX transition, grows superlinearly with increasing I_{exc} , and redshifts with increasing I_{exc} . This new (stimulated) emission peak is consistent with stimulated emission originating from inelastic exciton-exciton scattering, as described in Chapter 2. Emission originating from exciton-exciton scattering is commonly referred to as the P-line(s), and this notation will be used throughout the rest of this monograph. As we increase I_{exc} further, the P-line emission redshifts approximately 15 meV and starts to significantly broaden. If we continue to increase I_{exc} , a new emission peak shifts out of the P-line and grows superlinearly with increasing I_{exc} . This is shown in more detail in Fig. 22 for a 4.2 μm thick GaN layer grown on (0001) oriented sapphire. The data presented in the upper curve of Fig. 21 and all of Fig. 22 were taken using an amplified femtosecond laser (≈ 500 fs FWHM pulse width) to achieve the necessary high density excitation without inducing thermal damage to the excited region. This new SE peak is seen to redshift significantly with increasing I_{exc} and is attributed to stimulated recombination of an electron-hole plasma (EHP), as described in Chapter 2. The presence of the two SE mechanisms for a given I_{exc} may seem contradictory, since by definition no excitons exist when the semiconductor undergoes the EHP phase change, but can be explained quite simply by considering the different temporal evolution of the two mechanisms and the spatial distribution of I_{exc} across the excitation spot. The spectral coexistence of these two emission

mechanisms has been observed in other materials and results from the spatial and temporal separation of the excitonic and EHP recombination processes [53].

The dependence of SE threshold (I_{th}) of the first SE peak on temperature is shown in Fig. 23 for the 4.2 μm sample whose spectra are presented in Fig. 22, plotted on a semi-log scale. For temperatures less than approximately 200 K, I_{th} increases faster than exponentially with increasing I_{exc} . For temperatures greater than approximately 200 K, I_{th} is seen to increase exponentially with increasing I_{exc} . In this temperature region the dependence of I_{th} on temperature is described well by the empirical formula:

$$I_{th}(T) = I_o \exp(T/T_c) \quad (32)$$

where T_c represents the characteristic temperature of the SE threshold. A higher T_c indicates a lower sensitivity of I_{th} on temperature. The characteristic temperature for the sample shown in Fig. 23 was found to be approximately 273 K for the temperature region indicated. This value of T_c is considerably larger than that exhibited by other material systems [54], [55], and indicates that GaN is well suited for use in light emitting devices required to operate at elevated temperatures.

An interesting and exciting feature of GaN (and the group III nitrides in general) is its ability to exhibit SE for temperatures well above room temperature. Initial studies in this area were performed for temperatures up to 475 K and demonstrated the suitability of GaN for use in light emitting devices required to operate at elevated temperatures. In these initial studies, the limiting factor was the cryostat/heater system, not the GaN (the indium seals in the cryostat/heater system would melt if the temperature was increased further) [56]. In order to further study the high temperature SE behavior of GaN and to find the maximum temperature at which GaN would stimulate, a new heater system was designed and implemented by the author. This heater system was able to sustain temperatures in excess of 500 °C for extended periods of time. With this new heater system we were able to obtain SE from GaN at temperatures as high as 700 K and sustain it without degradation for several hours.

The SE threshold as a function temperature for the entire range in which SE was observed is shown in Fig. 24 for a $7.2\ \mu\text{m}$ sample grown on (0001) oriented sapphire and a $4\ \mu\text{m}$ sample grown on 6H-SiC. Similar behavior is seen for both samples as well as for the previously mentioned $4.2\ \mu\text{m}$ sample grown on sapphire. The shown behavior was observed to be a general property of state-of-the-art GaN thin films. The differences in the absolute value of I_{th} at a given temperature for the different samples results from varying degrees of dominance of non-radiative recombination channels leading to differences in the radiative recombination efficiency, but clear similarities in the behavior of all samples is clearly seen. In the extended range of temperatures from approximately 300 to 700 K, GaN is seen to exhibit a critical temperature of $T_c \simeq 172\ \text{K}$, which is significantly smaller than the value of $T_c \simeq 273\ \text{K}$ reported above for 200 to 350 K, but is still remarkably large. Further information about the mechanisms leading to SE in GaN can be obtained by measuring the emission energy of the SE peak near I_{th} relative to the spontaneous emission peak. This is shown in Fig. 25 for the entire temperature range (10 K to 700 K) in which SE was observed. In these experiments, the spontaneous emission was collected in a surface emission geometry to avoid reabsorption of the emitted photons. At low temperatures the SE is seen to originate approximately 21 meV below the 1s A free exciton emission peak. With increasing temperature the separation between SE and spontaneous peak positions increases, reaching a value of $\approx 90\ \text{meV}$ at room temperature and $\approx 200\ \text{meV}$ at 700 K. We see from Fig. 25 that the energy separation increases at a faster rate with increasing temperature past $\sim 150\ \text{K}$. We note that while excitonic features have been observed in the absorption spectra of GaN thin films at temperatures as high as 450 K [21], no excitonic features have been observed, nor are expected, at 700 K. This eliminates all excitonic gain mechanisms from consideration and leaves only one, that of an EHP (see Chapter 2). By working backwards in temperature, we see no significant change in the SE behavior (both in the I_{th} and the energy separation between spontaneous and stimulated emission change with temperature) until the temperature is reduced below ~ 150 to 200 K. Below this temperature, I_{th} is seen

to change drastically with temperature and the energy separation between spontaneous and stimulated emission changes its near linear dependence on temperature and quickly approaches one exciton binding energy (≈ 21 meV) [36]. This behavior is attributed to a shift in the SE mechanism from EHP recombination to that of inelastic exciton-exciton scattering for temperatures less than ~ 150 to 200 K. The absolute energy differences between the emission (spontaneous and stimulated) from the GaN on sapphire sample compared to the GaN on SiC sample seen in Fig. 25 is a result of residual strain in the GaN layer, as described in the previous chapter.

Cavity Formation and Lasing in GaN

Although SE from GaN has been reported by several groups, lasing in this material system had only been demonstrated in polished single-crystal GaN needles. The cavity lengths in these studies were on the order of a few hundreds of μm [50]. Optically pumped lasing in epitaxial GaN suffered from the lack of a suitable method of cavity formation, as the most common substrate material, (0001) oriented sapphire, is not cleavable. In addition, due to the chemically stable nature of GaN, standard chemical etching procedures failed to produce suitable cavity facets. New etching techniques, such as reactive ion etching (RIE), needed to be developed and refined for the group III nitrides. For this reason, a procedure for the fabrication of suitable cavity facets using mechanical polishing was developed by the author (see Appendix A). This required new mounting and polishing techniques, as the materials to be polished (GaN and sapphire) are extremely hard. In addition, the short wavelength operation of GaN placed strict requirements on the facets compared to conventional III-V lasers. For example, imperfections in the facet quality that may be acceptable at wavelengths in the red region of the spectrum could very well be detrimental to lasers emitting in the near UV region of the spectrum. The demonstration of optically pumped lasing and single-mode operation following cavity facet formation illustrated the suitability of the group III nitrides for laser diode applications and showed that high quality cavities could be formed from this material system. This work was soon repeated by a number of nitride research groups. Some

of the first reports of current injection lasing in the group III nitrides used the mechanical polishing technique for facet formation [57]. Using the mechanical polishing techniques outlined in Appendix A, we were able to obtain high quality laser facets, as illustrated in Fig. 26 for the $4.2\ \mu\text{m}$ GaN on sapphire sample described above. The improvement of the room temperature lasing spectra with increasing facet quality is shown in Fig. 27, where Fig. 27(a) shows the emission spectra for a bar-like sample simply cut from the full sample wafer with a “cavity” length of approximately $200\ \mu\text{m}$. In this case, it was possible to achieve laser action at certain spots along the length of the bar corresponding to locally smooth and parallel regions where the GaN fractured in the cutting process, thereby forming the desired cavity facets. The regions of suitable facet quality in this case are few and the resulting mode spacing is irregular and not very well defined. Fig. 27(b) shows typical spectra for the same sample after mechanical polishing of the edge facets. The sample was polished to a cavity length of approximately $200\ \mu\text{m}$ in order to directly compare it to the spectra of the bar used in Fig. 27(a). We note that the FWHM of the lasing spectrum is markedly reduced but that the mode quality is only marginally improved. This changed dramatically when dielectric mirrors were carefully glued to the facet edges, as shown in Fig 27(c), where a high reflective mirror was mounted to one facet and a 30% reflective mirror was mounted to the other, acting as an output coupler. We see a dramatic increase in the mode quality of the lasing spectra and the emission intensity was observed to increase by a factor of two after mirror coatings were applied to the facets. The mode structure caused by the $\sim 200\ \mu\text{m}$ Fabry-Pérot resonant cavity was observed to be $\approx 0.13\ \text{nm}$, with approximately every other mode dominating the spectra, as seen in Fig. 27(c). This value is very close to the calculated value of the mode spacing determined by the formula [58], [59]:

$$\Delta\lambda = \frac{\lambda_o^2}{2L(n - \lambda_o dn/d\lambda)} \quad (33)$$

where L is the cavity length, λ_o is the wavelength of one mode, $\Delta\lambda$ is the spacing of an adjacent mode, n is the index of refraction at λ_o , and $dn/d\lambda$ is the variation of

the index of refraction with wavelength. The index of refraction of MOCVD-grown GaN thin films is given as a function of wavelength in Appendix B.

With further improvements in mirroring techniques, single-mode lasing was achieved, as illustrated in Fig. 28 for the 4.2 μm sample described above with an improved mirroring scheme. In this case, one facet was again high reflective coated, but the other facet had another high reflective coating applied with a small aperture ($\approx 20 \mu\text{m}$) in the coating that acted as an output coupler. In this situation we relied on the reflectivity ($R \approx 19\%$ at 374.5 nm, see Appendix B) of the GaN-air interface to provide the feedback necessary for laser oscillation. In calculating the reflectivity (R) of the GaN/air interface at the lasing wavelength (≈ 374.5 nm), the following equation was used:

$$R(\lambda) = \left| \frac{n(\lambda) - 1}{n(\lambda) + 1} \right|^2 \quad (34)$$

where the index of refraction for the lasing wavelength, $n(374.5 \text{ nm})$, was experimentally obtained (see Appendix B). The high reflectivity in the other regions of the output facet acted as a spatial filter, cleaning up the laser emission. The aperture allowed emission to escape only if it was amplified along the path defined by the aperture. In this situation, the single-mode emission was extremely stable and repeatable, even after several months had passed. The data generated by this study gave clear evidence of lasing in epitaxially grown GaN films and helped provide the motivation to further pursue current injection lasing in GaN based materials. We will note in passing that a considerable amount of attention has been, and still is, given to 6H-SiC as a substrate for epitaxial group III nitride growth. SiC has the advantage of a better lattice match to GaN, better thermal conductivity, ease of doping for current injection devices, and is cleavable along the $\langle 11\bar{2}0 \rangle$ planes. The latter property is extremely desirable for laser diode development in that high quality cavity facets can be formed through cleaving and the process is simple compared to RIE and mechanical polishing techniques. Although good quality cavity facets could be formed by suitable cleaving techniques, this process often induced a myriad of cracks along all three of the $\langle 11\bar{2}0 \rangle$ SiC planes. These parallel cracks can act as internal cavities and severely affect the emission properties of the active layers. For

this reason, mechanical polishing techniques were extended to GaN layers grown on 6H-SiC.

Stimulated Emission from Highly Excited AlGa_xN and InGa_xN

Room temperature deep ultraviolet stimulated emission (SE) has been observed from optically pumped metalorganic chemical vapor deposition-grown Al_xGa_{1-x}N thin films. SE has been observed for Al concentrations as high as $x = 0.26$, with a resultant SE wavelength as low as 328 nm at room temperature. The results obtained for the Al_xGa_{1-x}N layers are compared with In_xGa_{1-x}N layers of comparable x values and GaN reference layers. The incorporation of Al into GaN is shown to result in Al_xGa_{1-x}N layers with similar high excitation density emission behavior as GaN, in contrast to In_xGa_{1-x}N layers, which exhibit markedly different SE behavior. The observation of room temperature SE from Al_xGa_{1-x}N layers of significant Al concentration illustrates the suitability of Al_xGa_{1-x}N based structures, not only for use in deep ultraviolet detectors, but also as a potential source of deep ultraviolet laser radiation.

The group-III nitrides, consisting of AlN, GaN, InN, and their alloys are attracting a considerable amount of scientific interest due to their large direct band gaps of 6.2, 3.4, and 1.9 eV, respectively, at room temperature (RT) in their wurtzite form, making them promising materials for the development of light emitting and detecting devices covering a spectral range unmatched in any other semiconductor system. In particular, the ternary compound Al_xGa_{1-x}N has the potential for use in light emitting devices and detectors covering nearly the entire deep ultraviolet (UV) region of the spectrum (190 - 350 nm). Applications of deep UV emitters and detectors include satellite to satellite communication shielded from Earth-based eavesdropping, remote sensing of chemical and biological contaminants, and medical applications where a compact, tunable UV laser source will find a myriad of uses, both known and presently unrealized. Despite a considerable amount of research directed towards AlGa_xN based UV photodetectors [7], very little research has been

conducted towards its use in UV laser diode development. Research conducted towards this end has only been directed at low aluminum content AlGaIn layers, whose emission wavelengths vary only slightly from that of GaN [60], [61]. We report here the observation of RT SE from optically pumped $\text{Al}_x\text{Ga}_{1-x}\text{N}$ thin films with x values as high as 26 %, putting the SE wavelengths well within the deep UV region of the spectrum (~ 328 nm). The recent demonstration of cw blue laser diodes with lifetimes in excess of 10,000 hours based on group-III nitride technology [4], combined with the observation of RT deep UV SE from $\text{Al}_x\text{Ga}_{1-x}\text{N}$ reported here, makes the prospects of extending laser diode technology into the near and deep ultraviolet region of the spectrum using this material system look promising.

The $\text{Al}_x\text{Ga}_{1-x}\text{N}$ layers used in this work were grown by low-pressure metalorganic chemical vapor deposition (MOCVD) on (0001) oriented sapphire at a temperature of 1050 °C. Prior to $\text{Al}_x\text{Ga}_{1-x}\text{N}$ growth, a thin ~ 5 nm AlN buffer layer was deposited on the sapphire at a temperature of 625 °C. Triethylgallium, triethylaluminum, and ammonia were used as precursors in the $\text{Al}_x\text{Ga}_{1-x}\text{N}$ growth. The $\text{Al}_x\text{Ga}_{1-x}\text{N}$ layer thickness was ~ 0.8 μm . The $\text{In}_{0.18}\text{Ga}_{0.82}\text{N}$ layer used for comparison was grown by MOCVD at 800 °C on a 1.8 μm thick GaN layer deposited at 1060 °C on (0001) oriented sapphire. The $\text{In}_{0.18}\text{Ga}_{0.82}\text{N}$ layer was 0.1 μm thick and was capped by a 0.05 μm GaN layer.

The $\text{Al}_x\text{Ga}_{1-x}\text{N}$ layers were optically pumped in an edge emission geometry using the second harmonic of the deep orange radiation generated by an amplified dye laser pumped by the second harmonic of a Q-switched, injection seeded Nd:YAG (~ 4 ns pulse width and 10 Hz repetition rate). The deep UV radiation (310 nm) from the dye laser was focused to a line on the sample surface using a cylindrical lens. The emission was collected from one edge of the sample, coupled into a one meter spectrometer, and spectrally analyzed using a UV enhanced, gated CCD. Photoluminescence (PL) experiments were performed using the 244 nm line of a inter-cavity doubled cw Ar^+ laser as an excitation source. PL excitation (PLE) experiments were also carried out using the quasi-monochromatic emission from a Xe lamp dispersed by a $\frac{1}{2}$ meter monochromator as the excitation source. Both

the PL and PLE experiments used a PMT in conjunction with a 1 meter double spectrometer as a detector.

Figure 29 shows a low temperature SE spectrum from an $\text{Al}_{0.17}\text{Ga}_{0.83}\text{N}$ layer superimposed on its low power cw PL peak (dashed line) and its band edge as measured by PLE (solid line). We see the spontaneous emission is Stokes shifted by approximately 2 nm from the band edge. The decrease in the PLE intensity above the band edge is a result of the decreasing intensity of the excitation source at these wavelengths. The SE originates at ≈ 340 nm at threshold and redshifts with increasing excitation density (I_{exc}). The redshift of approximately 7 nm of the SE with respect to the band edge is consistent with the behavior of GaN at elevated I_{exc} . The SE spectrum shown in Fig. 29 was taken with an excitation density twice that of the SE threshold (I_{th}), *i.e.* $I_{exc} = 2 \times I_{th}$.

Figure 30 shows the low temperature SE from an $\text{In}_{0.18}\text{Ga}_{0.82}\text{N}$ layer superimposed on its low power cw PL peak (dashed line) and its band edge as measured by PLE (solid line) for comparison. The band edge feature is most likely a result of spatial inhomogeneity of the indium composition. The SE spectrum was collected using the third harmonic (355 nm) of the Q-switched, injection seeded Nd:YAG laser as the excitation source. The PL was excited using the 325 nm line of a cw He:Cd laser. We see the spontaneous emission is Stokes shifted by more than 7 nm from the band edge. The SE originates just below the peak of the spontaneous emission (≈ 415.5 nm at threshold) and redshifts only slightly with increasing I_{exc} . The redshift of approximately 7 nm of the SE with respect to the band edge may seem to be consistent with that of the AlGa_xN layers, but differences will become clear in the following paragraphs. The SE spectrum shown in Fig. 30 was taken with $I_{exc} = 2 \times I_{th}$.

Figure 31 shows RT emission spectra for (a) the $\text{Al}_{0.17}\text{Ga}_{0.83}\text{N}$ layer described above and (b) an $\text{Al}_{0.26}\text{Ga}_{0.74}\text{N}$ layer for several excitation densities below and above I_{th} . The low power cw PL peaks are also overlaid (dashed lines) for reference. The SE emerges out of the low energy spontaneous emission wing with increasing optical excitation for both layers. The separation between spontaneous and stimulated emission

was measured to be ≈ 10.5 and 8.5 nm, respectively, for the $x = 0.17$ and $x = 0.26$ layers. The red shift of the spontaneous emission peaks seen in the nanosecond excitation spectra of Figs. 31(a) and 31(b) compared to the cw spontaneous emission peaks is due to re-absorption of the emitted photons as they propagate along the excitation path in the edge-emission experiments. The larger shift in Fig. 31(b) compared to that in Fig. 31(a) is due to a larger band tail in the $x = 0.26$ layer compared to the $x = 0.17$, a result of increased compositional fluctuations in the $\text{Al}_x\text{Ga}_{1-x}\text{N}$ layers with increasing Al composition.

Figure 32 shows the emission intensity of the spontaneous and stimulated emission peaks as a function of I_{exc} at RT. The spectral regions for the spontaneous and stimulated emission are indicated in Fig. 31 as SP and SE, respectively. The spontaneous emission is seen to increase approximately linearly with increasing I_{exc} , while SE is seen to increase in a strongly superlinear fashion with increasing I_{exc} .

A comparison between the I_{exc} dependent behavior of these $\text{Al}_x\text{Ga}_{1-x}\text{N}$ films and that of GaN and InGaN films can now be made. We first note that the Stokes shift of the SE (≈ 7 nm) with respect to the band edge exhibited by the $\text{Al}_{0.17}\text{Ga}_{0.83}\text{N}$ layer at 10 K is consistent with the SE behavior of GaN thin films at elevated temperatures and/or high I_{exc} (several times I_{th}), and is attributed to stimulated recombination of an electron-hole plasma (EHP). At low temperatures and I_{exc} close to I_{th} , GaN stimulates approximately 21 meV (≈ 2.1 nm) below the 1s A free exciton position, consistent with an exciton-exciton scattering related gain mechanism [28], [62], [63], as described in the preceding sections. The fact that the $\text{Al}_x\text{Ga}_{1-x}\text{N}$ samples do not exhibit this behavior (and gain mechanism) is not surprising, nor expected, considering no excitonic features were observed in the PLE and photoreflectance spectra of these samples. At elevated temperatures and/or I_{exc} several times I_{th} , GaN exhibits a large Stokes shift of the SE compared to the band edge, exceeding 90 meV (≈ 9.8 nm) near I_{th} at RT, as described above. In this regime, the SE is attributed to stimulated recombination of an EHP and exhibits an I_{exc}^β dependence on I_{exc} ($I_{SE} \propto I_{exc}^\beta$), where $\beta \approx 4$. We see from Figs. 31 and 32 that both $\text{Al}_x\text{Ga}_{1-x}\text{N}$ samples exhibit a large Stokes shift of the SE with respect to the

spontaneous emission (> 8 nm) and a $\beta \approx 3.5$ dependence of I_{SE} on I_{exc} , consistent with the behavior of GaN in the EHP recombination regime. We note that InGaN films typically exhibit a large Stokes shift of the SE with respect to the band edge but only a slight redshift or even a blueshift with respect to the spontaneous emission. We also note that results for InGaN layers can vary strongly from sample to sample and with different experimental conditions [64], whereas the results for GaN and $Al_xGa_{1-x}N$ layers are far more consistent from sample to sample. The unique SE behavior of $In_xGa_{1-x}N$ thin films is attributed to stimulated recombination of carriers localized by large potential fluctuations in the $In_xGa_{1-x}N$ layers due to difficulties in uniform indium incorporation [64], [65], [66], [67], [68], [69]. We note that carrier localization at potential fluctuations is not expected in $Al_xGa_{1-x}N$ thin films as it is in $In_xGa_{1-x}N$, as a spatial increase in indium content in an $In_xGa_{1-x}N$ layer will lead to a potential minimum, while a spatial increase in aluminum content in an $Al_xGa_{1-x}N$ layer will result in a potential maximum. We further note that incorporation of indium into GaN typically results in a significant decrease in I_{th} , whereas incorporation of aluminum into GaN typically results in an increase in I_{th} , as seen in Fig. 33.

Figure 33 shows the SE threshold at 10 K and RT of the $Al_xGa_{1-x}N$ samples studied here compared to the $4.2 \mu m$ GaN layer whose optical properties have been reported above and elsewhere [56], [70], [71] and the MOCVD-grown $In_{0.18}Ga_{0.82}N$ layer (of comparable alloy concentration to the $Al_{0.17}Ga_{0.83}N$ layer) described above. The SE thresholds for the $Al_xGa_{1-x}N$ and $In_xGa_{1-x}N$ samples have been normalized to the GaN SE threshold at RT (≈ 800 kW/cm²) for clarity. All samples were optically excited with the same nanosecond excitation source described above. The 10 K time-resolved PL (TRPL) effective lifetime of the main PL peak is also included in Fig. 33 to further illustrate the differences in the emission behavior of InGaN compared to GaN and AlGaN. Incorporation of In into GaN is clearly seen to result in a significant increase in the TRPL lifetime compared to GaN, as is the incorporation of Al into GaN. This is due to suppression of nonradiative channels in the alloys, and should aid in the reduction of the SE threshold. Since this trend is shared by both

InGaN and AlGaIn, one might expect their SE behavior to follow similar trends, but this is clearly seen not to be true. More than an order of magnitude decrease in I_{th} for the $\text{In}_x\text{Ga}_{1-x}\text{N}$ layer compared to the GaN layer is clearly seen, while incorporation of Al into GaN is seen to result in an increase in I_{th} with increasing Al concentration. The reason for the drastic decrease in I_{th} for InGaIn layers lies in its origin, stimulated recombination of localized states confined by spatial alloy fluctuations, and will be further explained in Chapter 5 through the use of nondegenerate pump-probe spectroscopy.

In summary, optically pumped SE has been observed at room temperatures from MOCVD-grown $\text{Al}_x\text{Ga}_{1-x}\text{N}$ films with SE wavelengths as low as 328 nm, putting the SE well within the deep UV region of the spectrum. A comparison of the SE behavior with that of MOCVD-grown GaN and $\text{In}_x\text{Ga}_{1-x}\text{N}$ thin films indicates that EHP recombination is the dominant gain mechanism in $\text{Al}_x\text{Ga}_{1-x}\text{N}$, even at 10 K. To the best of our knowledge, this is the shortest room temperature SE wavelength ever reported from a semiconductor and illustrates that $\text{Al}_x\text{Ga}_{1-x}\text{N}$ based heterostructures have an unmatched capability for extending the range of semiconductor laser diodes deep into the UV.

Summary

In this chapter we have given an overview of the emission properties of highly excited group III nitrides. All of the work presented here, with the exception of SE from InGaIn films, was the first of its kind reported in the literature. The characterization of high temperature SE in GaN films allowed us to unambiguously determine the gain mechanism in GaN thin films for temperatures exceeding ~ 200 K, that of EHP recombination. This study of the SE behavior as a function of temperature also shows a shift in the near threshold gain mechanism in the temperature range of 150-200 K. By studying the emission behavior at 10 K, we were then able to determine that inelastic exciton-exciton scattering was responsible for the dominant gain mechanism near threshold for temperatures from 10 K to ~ 200 K. Power dependent emission studies using cw, nanosecond, and amplified femtosecond pulses

allowed us to access an unprecedented large optical pumping excitation range. The results of the authors work on GaN-based quantum wells and separate confinement heterostructures have regretfully been omitted from the body of this monograph due to space constraints. Interested readers can find this work in refs. [72], and [73], as well as keeping an eye out for publication in the near future.

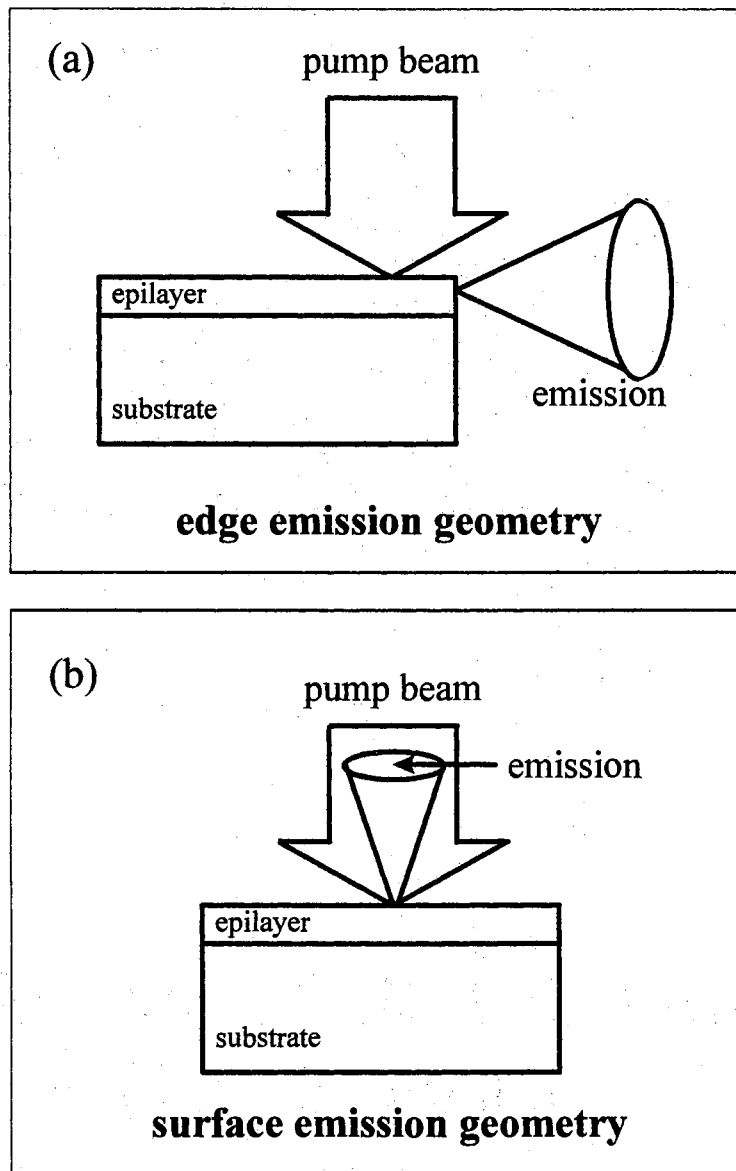


Figure 20. Schematic of (a) edge emission and (b) surface emission pumping geometries. The perspective is such that one is looking at one edge of the sample along the growth plane.

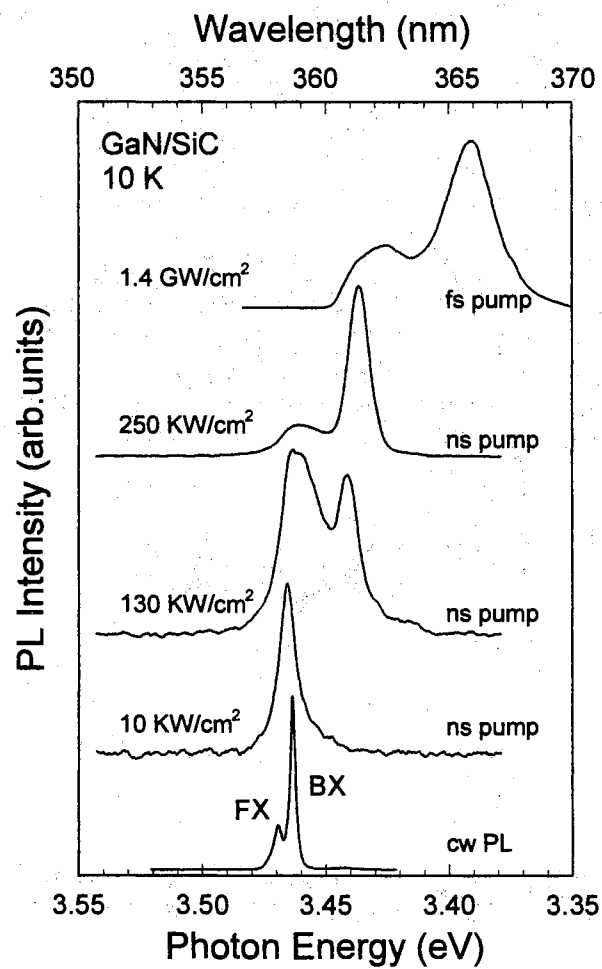


Figure 21. Evolution of band edge emission from MOCVD-grown GaN with increasing optical excitation at 10 K. The spectra have been normalized and displaced for clarity.

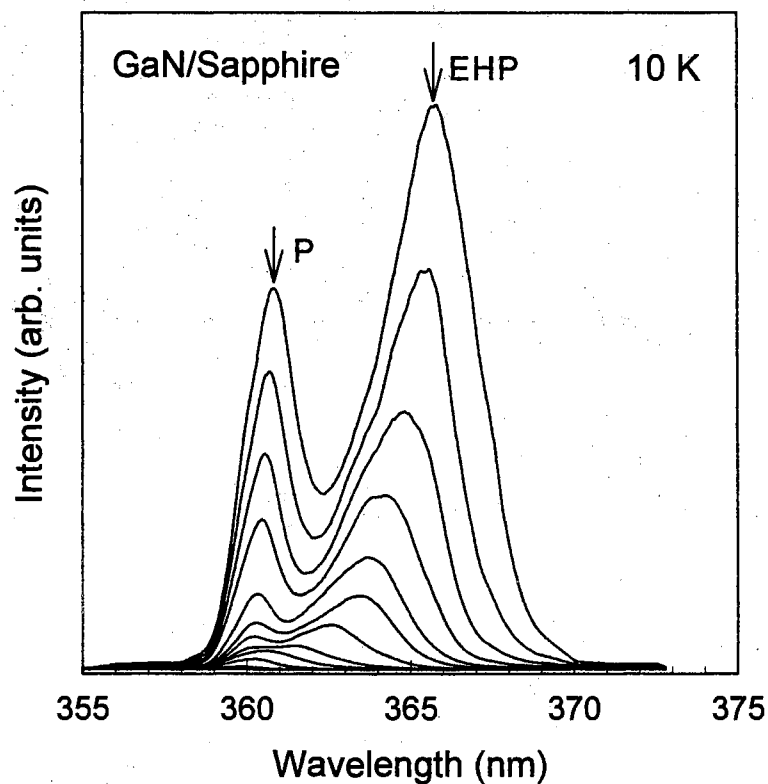


Figure 22. Evolution of the SE from a $4.2\ \mu\text{m}$ MOCVD-grown GaN layer under the conditions of intense femtosecond optical excitation at 10 K. The spectra have been scaled for clarity. A new SE peak is seen to emerge out of the exciton-exciton scattering peak (P-line) with increasing excitation and is attributed to EHP recombination.

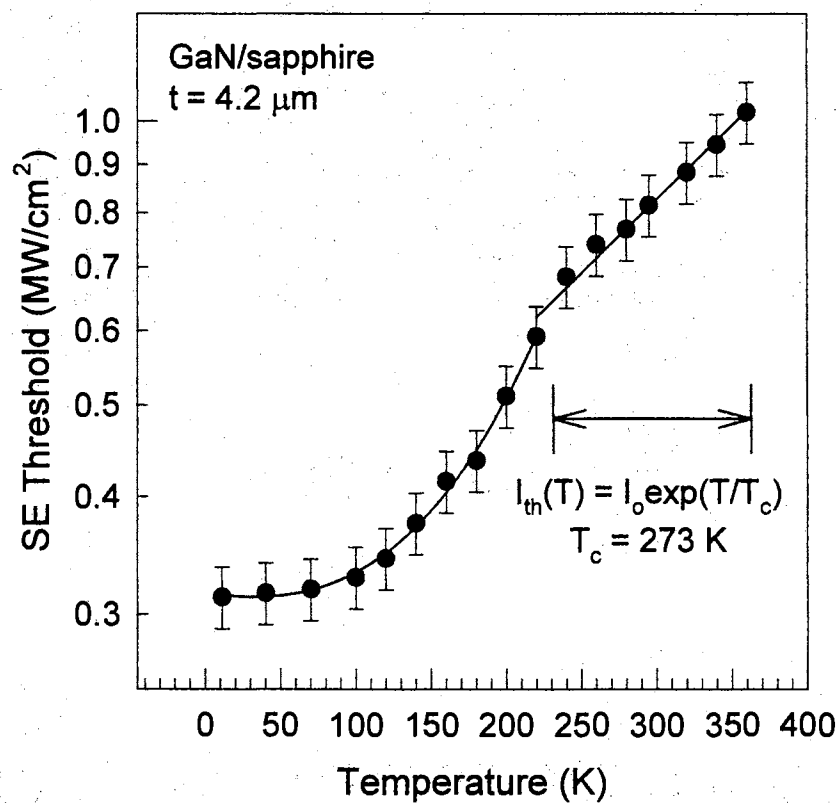


Figure 23. SE threshold as a function of temperature for a 4.2 μm MOCVD-grown GaN layer from 10 K to 375 K. A clear shift in behavior is seen for temperatures exceeding ~ 200 K.

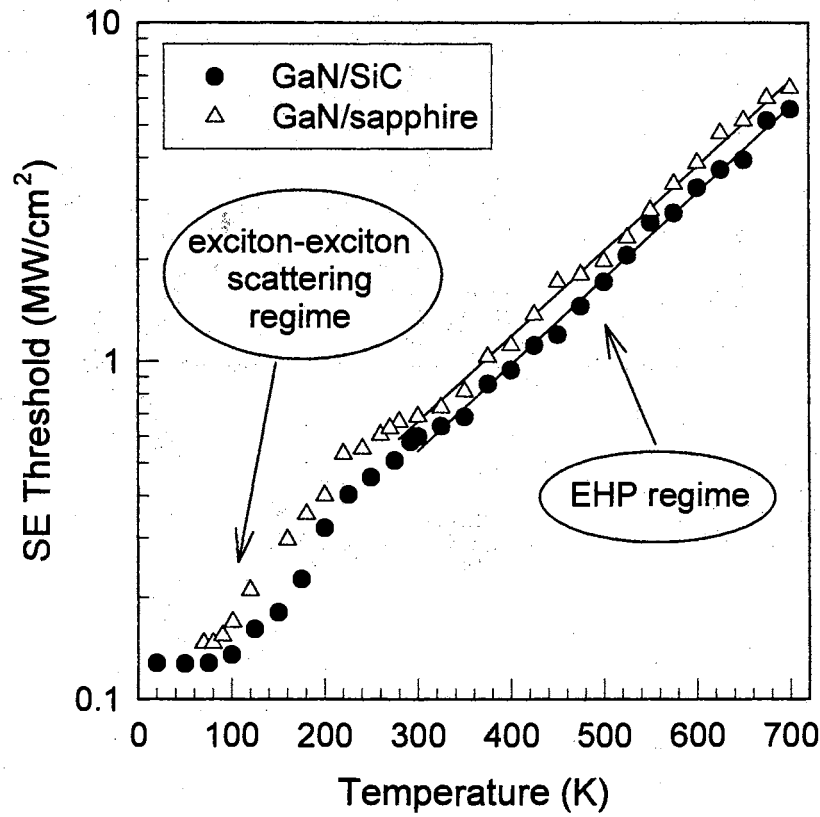


Figure 24. SE threshold as a function of temperature over an extended range for GaN layers grown by MOCVD on 6H-SiC and (0001) oriented sapphire substrates. The solid lines represent a best fit to the experimental data using the empirical formula $I_{th}(T) = I_o \exp(T/T_c)$, yielding characteristic temperatures of $T_c \approx 172$ and 173 K for the GaN/sapphire and GaN/SiC samples, respectively, for $T > 300$ K. Adapted from [63].

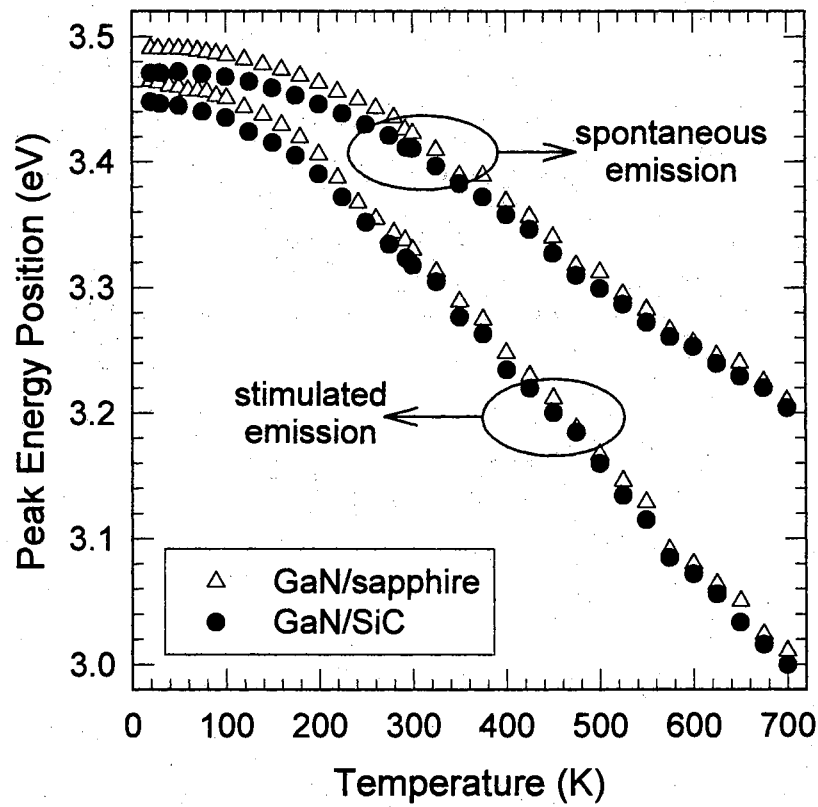
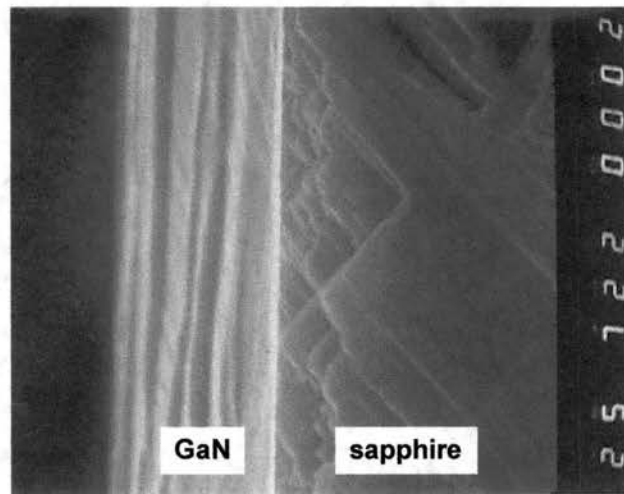
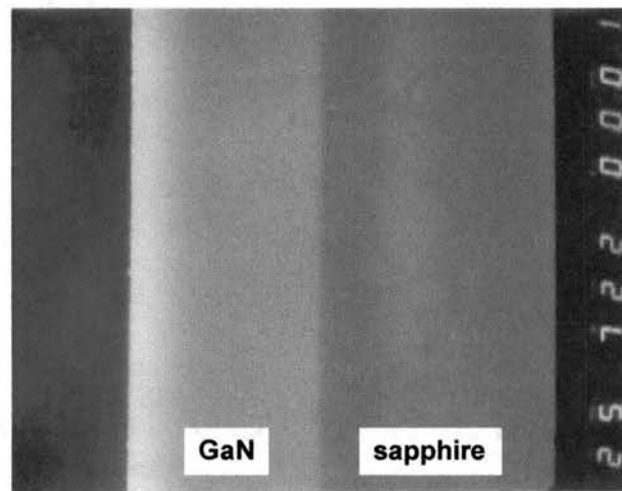


Figure 25. SE peak position near I_{th} as a function of temperature for MOCVD-grown GaN layers on 6H-SiC and (0001) oriented sapphire substrates. The emission energy of the spontaneous emission is included for clarity. From [63].



as cut



polished

Figure 26. SEM micrographs of GaN laser facets before and after mechanical polishing. The GaN layer is $4.2\text{ }\mu\text{m}$ thick and was grown by MOCVD on (0001) oriented sapphire.

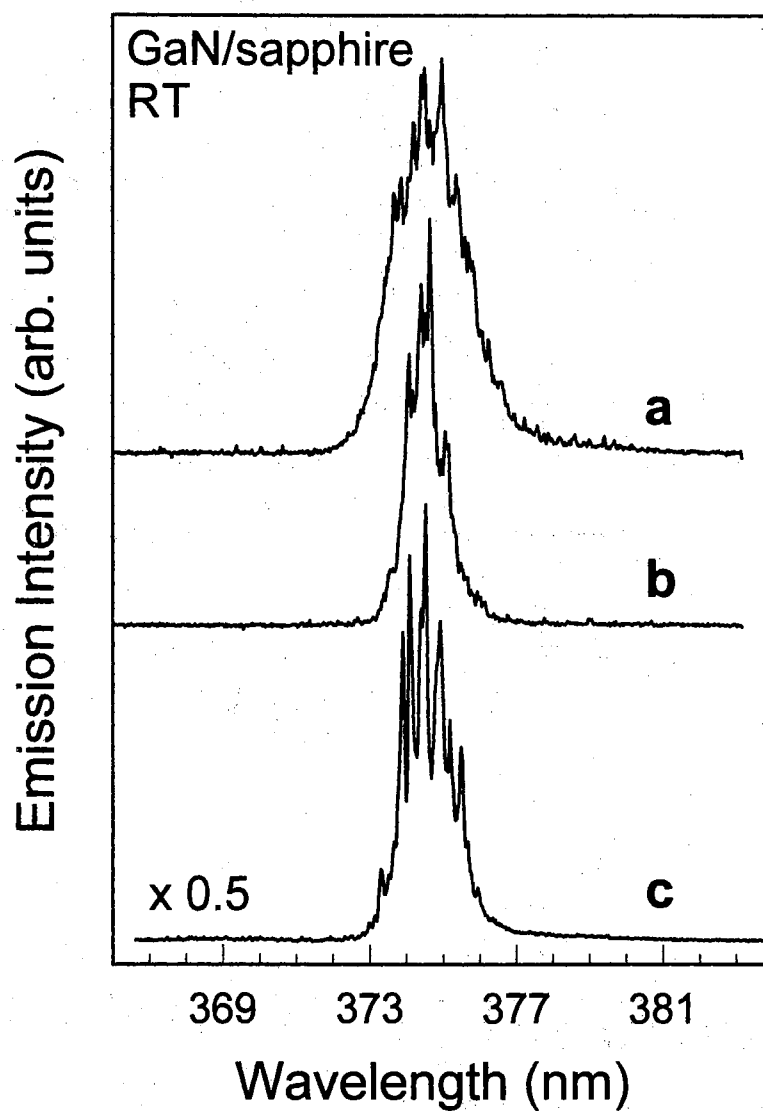


Figure 27. Comparison of RT lasing spectra from optically pumped GaN layers subjected to progressive edge facet treatment: (a) simply cut into bars from the sample wafer; (b) facet surface mechanically fine polished; (c) external mirrors imposed on the facets. The samples were of the same approximate cavity length ($\sim 200 \mu\text{m}$) and were excited under near identical pumping conditions. The spectra have been displaced vertically for clarity.

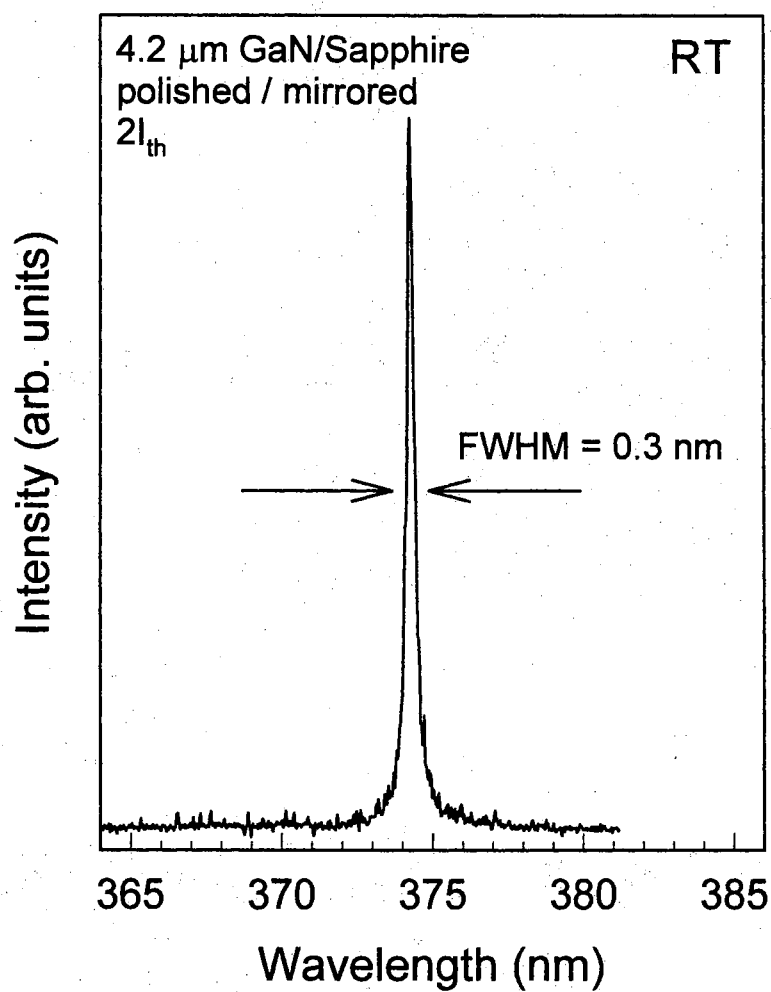


Figure 28. RT lasing spectrum of the 4.2 μm GaN layer with mirrored facets. The emission linewidth is significantly reduced compared to the spectra of Fig. 27.

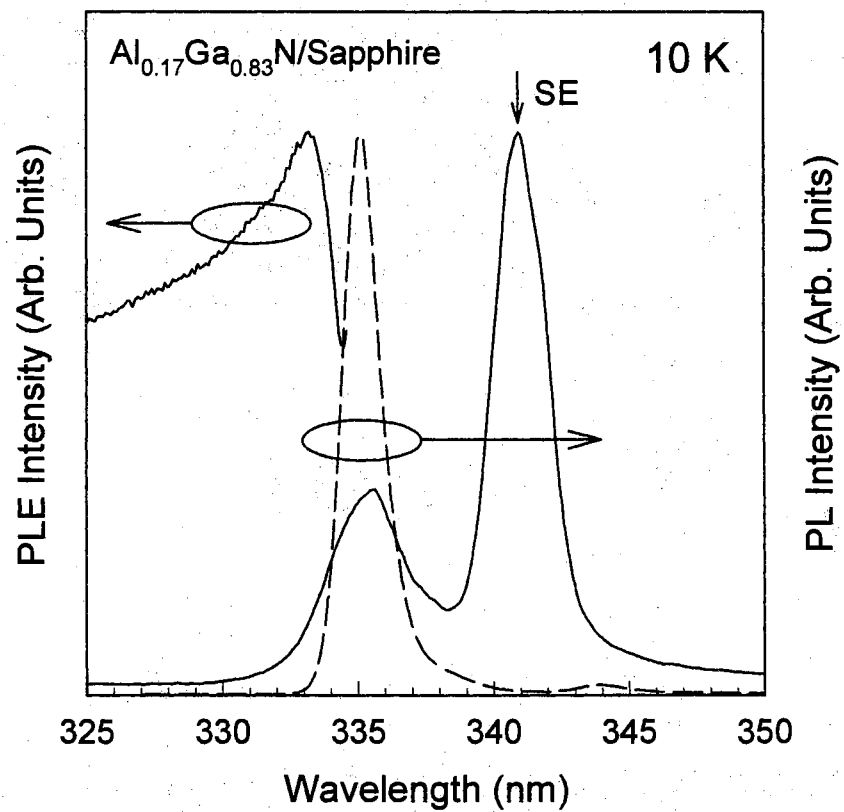


Figure 29. 10 K PLE, PL (dashed line), and SE spectra of an MOCVD-grown $\text{Al}_{0.17}\text{Ga}_{0.83}\text{N}$ thin film. The SE spectrum was taken under the conditions $I_{exc} = 2 \cdot I_{th}$.

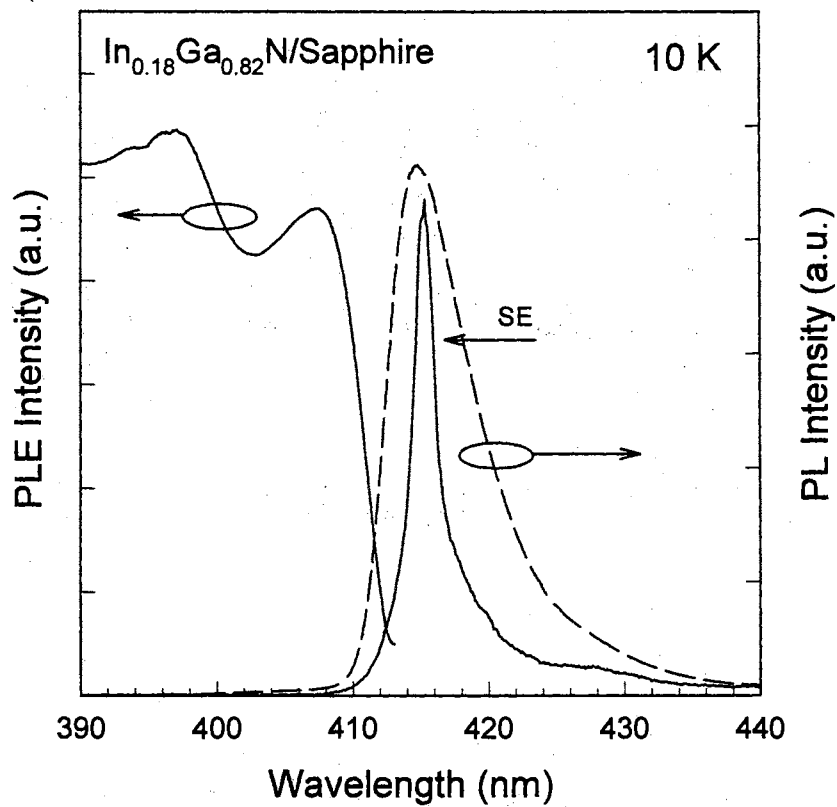


Figure 30. 10 K PLE, PL (dashed line), and SE spectra of an $\text{In}_{0.18}\text{Ga}_{0.82}\text{N}$ layer grown by MOCVD on (0001) oriented sapphire. The SE spectrum was taken under the conditions $I_{exc} = 2 \cdot I_{th}$. Note that the horizontal scale covers twice that of Fig. 29.

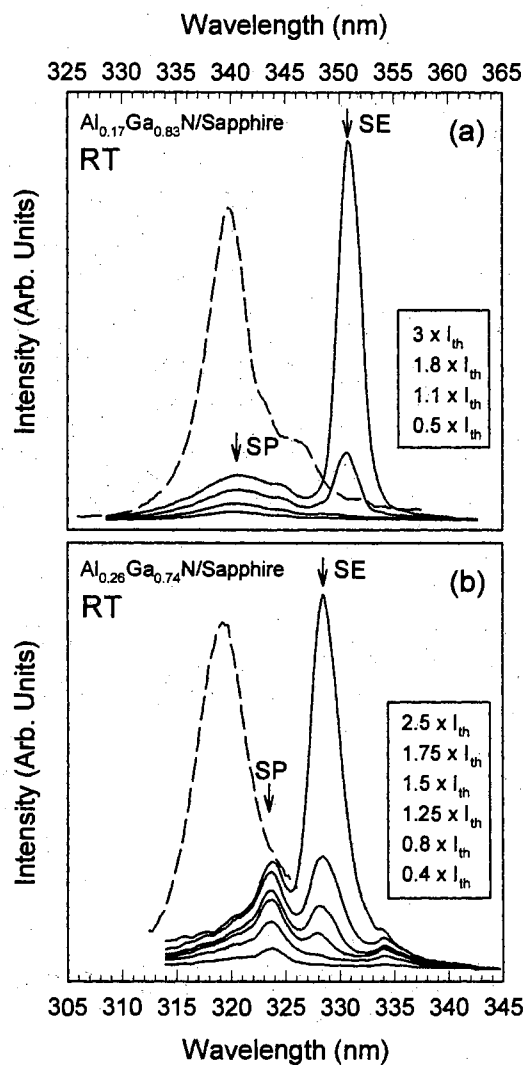


Figure 31. Room temperature emission spectra for several excitation densities below and above the SE threshold (I_{th}) for (1) an $\text{Al}_{0.17}\text{Ga}_{0.83}\text{N}$ and (b) an $\text{Al}_{0.26}\text{Ga}_{0.74}\text{N}$ thin film. The low power cw spontaneous emission spectra are superimposed for completeness (dashed lines). The arrows indicate the spectral regions referred to in Fig 32.

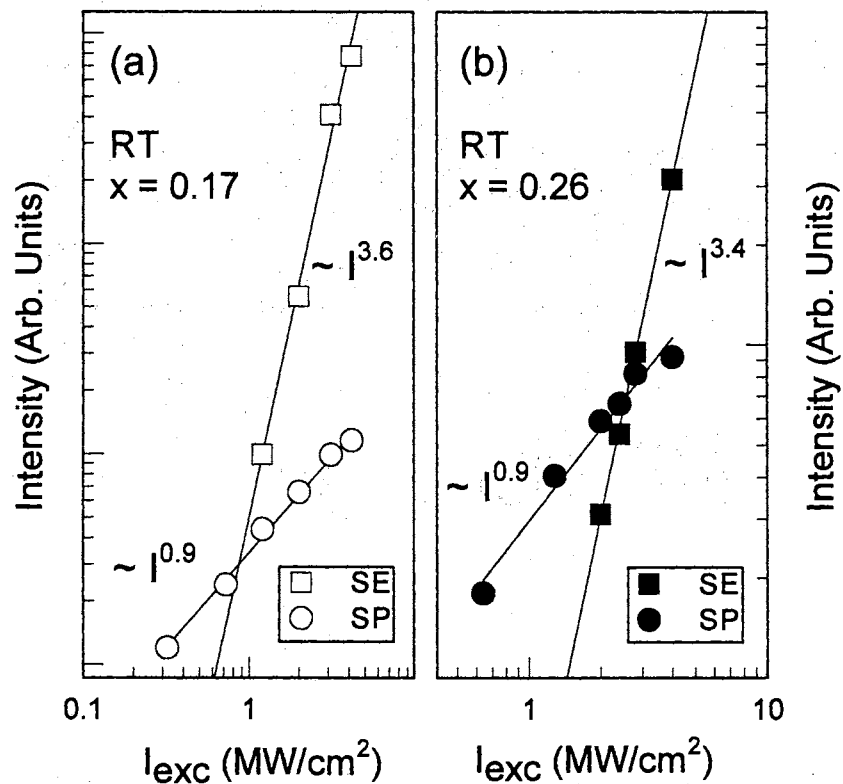


Figure 32. Dependence of emission intensity on excitation density (I_{exc}) for (a) an $\text{Al}_{0.17}\text{Ga}_{0.83}\text{N}$ and (b) an $\text{Al}_{0.26}\text{Ga}_{0.74}\text{N}$ thin film at RT. The spontaneous (SP) and stimulated (SE) emission spectral positions are indicated by the arrows in Fig. 31.

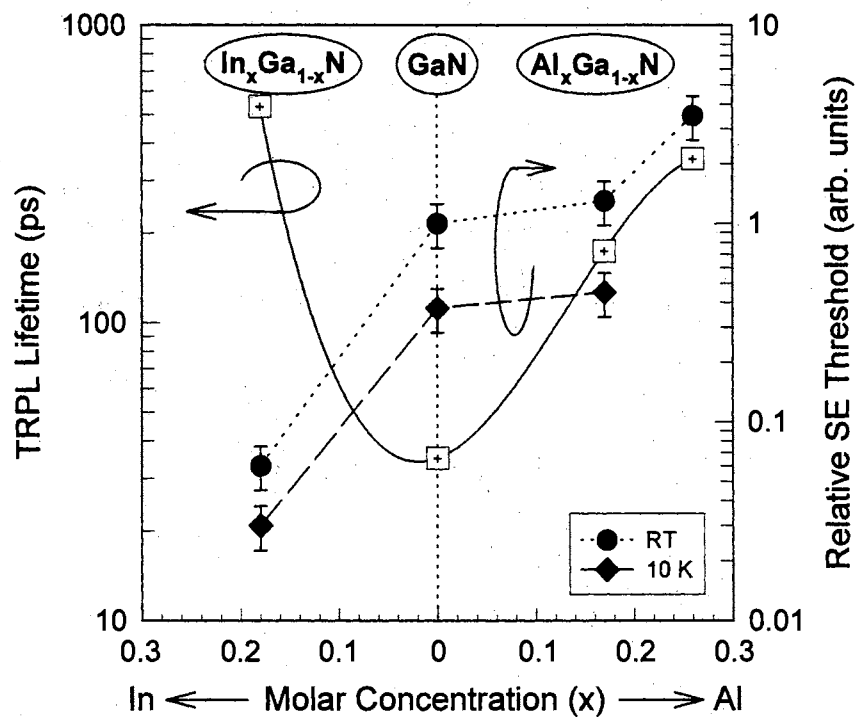


Figure 33. Relative SE thresholds for $\text{In}_{0.18}\text{Ga}_{0.82}\text{N}$, GaN , $\text{Al}_{0.17}\text{Ga}_{0.83}\text{N}$, and $\text{Al}_{0.26}\text{Ga}_{0.74}\text{N}$ thin films. The SE thresholds have been normalized to that of the GaN film at RT ($\sim 800 \text{ kW/cm}^2$). All samples were grown by MOCVD on (0001) oriented sapphire and optically excited under the same experimental conditions ($\lambda_{exc} = 310 \text{ nm}$).

CHAPTER V

PUMP-PROBE SPECTROSCOPY OF GaN THIN FILMS

In this chapter the results of optical pump-probe experiments on GaN thin films are presented. These experiments were undertaken to gain a better understanding of the optical phenomena associated with high carrier concentrations in this material system. In particular, the evolution of the near band edge transitions in GaN was studied as the number of free carriers was increased by direct band to band optical excitation. The experiments were performed under nanosecond optical excitation at excitation densities centered around typical stimulated emission thresholds for GaN epitaxial layers. The experiments were undertaken to provide more insight into the mechanisms responsible for stimulated emission and optical gain than can be extracted from simple optical pumping experiments (the results of which were the subject of the previous chapter). The experiments of this chapter are broken down into four basic categories: (1) Single-beam power dependent absorption experiments, (2) Nondegenerate optical pump-probe absorption experiments at zero time delay between the pump and probe pulses, (3) Nondegenerate optical pump-probe reflection experiments performed on thick (on the order of several μm) GaN layers at zero time delay between the pump and probe pulses, and (4) Nondegenerate optical pump-probe absorption experiments with control of the time delay of the probe pulse with respect to the pump pulse. The first is the simplest of the techniques in that it is a one beam experiment. The laser beam is passed through the GaN layer and spectrally tuned across the near band edge region of interest. The intensity of the laser is varied from scan to scan and the evolution of the band edge transitions can therefore be monitored as a function of the laser intensity. In this experiment,

the transition whose strength is being probed is also being pumped. This allows direct determination of the changes induced in the strength of a given transition by the excitation of that transition. This experiment will be shown to add valuable insight into the behavior observed in the next experiment, nondegenerate optical pump-probe spectroscopy. The second of the above mentioned experiments, nondegenerate optical pump-probe absorption spectroscopy at zero time delay, allows the band edge transitions to be monitored as we increase the number of optically excited free carriers. This experiment allows us to freely change the excitation photon energy (and hence, the excess kinetic energy the photo-excited free carriers possess) and still monitor the band edge transitions. In the case of optically thick GaN samples, we cannot monitor the band edge transitions in absorption (transmission) experiments, so we must do so by monitoring the evolution of the reflection spectra with increasing optical excitation. This experiment is valuable in that it allows us to perform pump-probe experiments on GaN layers of a quality that cannot be matched at this time by thin (on the order of several tenths of a μm) GaN layers. This also allows us to directly compare the strength of a given transition, *i.e.* excitonic, for various excitation densities above and below the stimulated emission threshold, in turn providing great insight into the possible mechanisms responsible for optical gain in these high quality GaN layers. The next nondegenerate optical pump-probe experimental technique allows the probe beam pulse to be delayed with respect to the pump pulse. This experiment provides significant insight into the mechanisms responsible for the large nonlinearities observed in this work.

The experiments of this chapter are presented in an order that best describes the optical characteristics of highly excited GaN, not in the order of their complexity. The chapter starts with the results of nondegenerate optical pump-probe absorption experiments at zero time delay. It then moves on to the results of nondegenerate optical pump-probe experiments with variable time delay (on the order of nanoseconds) between the probe and pump pulses, which help explain the phenomena observed in

the previous section. The results of single-beam power dependent absorption experiments are then presented, providing additional insight into the origin of the phenomena observed in the first section. Nondegenerate optical pump-probe reflection experiments on optically thick GaN layers are then presented to gauge the strength of the excitonic transitions in GaN as the number of free carriers is increased beyond that required to achieve stimulated emission. Using reflection techniques provides a better estimate of the effects of the intense optical pump on the strength of the excitonic transitions by minimizing the effects of the pump beam intensity decrease as it traverses the sample thickness. The last section is devoted to nondegenerate optical pump-probe experiments performed on InGaN thin films. These films exhibit markedly different behavior than GaN thin films, helping to explain the differences in the stimulated emission characteristics of GaN and InGaN thin films. The final section of this chapter summarizes the result of all of the sections and draws conclusions based on the experimental evidence presented.

The works presented in this chapter represent the first of their kind in this material system. The results of several sections (nondegenerate optical pump-probe spectroscopy with time delay and nondegenerate optical pump-probe spectroscopy of InGaN thin films) have not been introduced to the group III nitride scientific community by the time of this writing. They represent a level of understanding of the optical phenomena associated with high carrier concentration in the group III nitrides that is absent at this time in said community. The combined results of this chapter will be summarized in print at a suitable time in the near future.

Nondegenerate Optical Pump-Probe Absorption Spectroscopy

In this section, the results of nanosecond non-degenerate optical pump-probe experiments performed on metalorganic chemical vapor deposition (MOCVD) grown GaN thin films are presented. Changes in the optical transitions near the band gap due to excess photo-generated free carriers were studied as a function of excitation density and time delay after pulsed optical excitation at 10 K and room temperature using pump-probe spectroscopy. At 10 K, strong, well-resolved features are present

in the absorption and reflection spectra corresponding to the 1s A and B free exciton transitions. These features are shown to broaden and decrease in intensity due to the presence of the high densities of photo-excited free carriers generated by the pump beam, resulting in extremely large values of induced transparency, exceeding $4 \times 10^4 \text{ cm}^{-1}$ as the excitation density (I_{exc}) approaches 3 MW/cm^2 . In addition, large values of induced absorption are observed with increasing pump density in the below-gap region where gain is expected. This induced absorption was also found to be extremely large, exceeding $4 \times 10^4 \text{ cm}^{-1}$ as I_{exc} was increased to over 3 MW/cm^2 . At room temperature the resulting induced transparency and induced absorption were found to approach $2 \times 10^4 \text{ cm}^{-1}$ as I_{exc} approached 3 MW/cm^2 . By monitoring the evolution of the band edge transitions as a function of time delay after the pump pulse, we see the below-gap induced absorption is a result of large long-lived band gap renormalization. The renormalization is shown to exhibit rise and decay times consistent with trapping of carriers at deep levels in GaN. The results indicate a complex relationship exists between induced absorption and gain in GaN and help explain the relatively high stimulated emission threshold of GaN compared to other wide (direct) band gap semiconductors. The results of this section will also be shown (in a later section) to provide a partial explanation for the drastic reduction in the stimulated emission threshold that results when indium is incorporated into GaN. The large values of induced transparency/absorption observed in this work and the fact that excitons have been shown to persist to over 450 K in GaN [21] (indicating that the large optical nonlinearities will persist substantially above room temperature) suggest the possibility of new opto-electronic applications for the group III nitrides.

Motivation

GaN and its respective alloys (InGaN and AlGaN) have been attracting an ever increasing amount of attention due to their physical hardness, inert nature, and large direct band gaps, making them promising materials for UV-Blue-Green light emitting devices and detectors [31]. Current technological advances have made high

brightness light-emitting diodes (LEDs) and cw laser diodes based on these materials a reality [74], [75]. Devices based on these materials have advanced quickly over the past several years and now their nonlinear properties are becoming a focus for many research groups. Femtosecond four-wave-mixing (FWM) experiments have been used to study the dephasing times of the A and B free excitons in GaN [20], [76], and femtosecond pump-probe transient transmission experiments have been used to study the ultrafast carrier dynamics in InGaN epitaxial films [77]. Picosecond FWM experiments have shown strong optical nonlinearities below [78] and at the band edge of GaN [79]. However, much information about the optical phenomena associated with the high carrier concentrations at which practical devices operate in these materials is still unknown. Recently, nanosecond pump-probe transmission experiments have shown exciton saturation due to resonant and below resonance optical excitation of the excitonic transitions [79]. Nanosecond nondegenerate pump-probe experiments with optical excitation above the band gap of GaN have also been reported by the author [71], [80] and have shown large values of induced transparency and induced absorption in the band gap region with increasing optical excitation. A better understanding of the optical phenomena associated with high carrier concentrations in this material system is important, not only for general physical insight, but also as an aid in the design and optimization of practical laser diodes. The magnitude of the nonlinearities studied in this work suggest the possibility of new photonic devices based on the group III nitrides as optical switches.

Experimental Technique and Results

The GaN samples used in this work were nominally undoped single-crystal films grown by MOCVD on (0001) oriented sapphire substrates. Thin AlN buffer layers, approximately 50 nm thick, were deposited on the substrate at 775 °C before the growth of the GaN epilayers. The GaN layers were then deposited at 1040 °C directly on the AlN buffer layers. Non-degenerate optical pump-probe experiments were performed using frequency doubled radiation from a nanosecond dye laser as

a UV pumping source and broadband fluorescence from a dye solution as the probe source.

At Zero Time Delay. The experimental system consisted of an amplified dye laser pumped by the second harmonic of an injection seeded Nd:YAG laser operating at 10 Hz. The deep red radiation from the dye laser was frequency doubled in a nonlinear crystal to produce the near UV wavelengths used to synchronously pump the GaN layers above their band gaps and the laser dye solution. The fluorescence from the UV laser dye was collected and focused onto the GaN layer. The broadband transmitted probe was then collected and focused on the slits of a 1 meter spectrometer and spectrally analyzed using a UV enhanced, gated CCD. The pump wavelength was varied from 335 nm (3.700 eV) to 350 nm (3.541 eV), but no noticeable differences in the experimental results were observed for the different pump wavelengths. A pump wavelength of 337 nm (3.678 eV) was used for the data presented in this section. The experimental geometry ensured temporal overlap of the pump and probe, as well as the same temporal profiles of the two (≈ 4 ns FWHM). The probe was kept many orders of magnitude lower (< 200 W/cm²) than the pump beam to avoid any nonlinearities due to the probe, and its spot size was kept at half that of the pump. Special care was taken to monitor the intensity of the probe and pump (separately) from scan to scan to ensure consistent absorption coefficient values and luminescence compensation, when applicable. The sample temperature was varied between 10 K and room temperature through the use of a closed cycle refrigerator. The pump-probe experimental configuration is illustrated in Fig. 35. The experiments were also repeated with a scanned narrowband probe using two synchronously pumped dye lasers, yielding consistent results.

Figure 36(a) shows the 10 K absorption spectra near the band gap for a $0.38 \mu\text{m}$ GaN sample subjected to several different pump power densities. We note here that the unpumped absorption spectra agree very well with published cw absorption values for the same sample, see Fig. 34. Fig. 36(b) shows the measured absorption changes with respect to the unpumped spectra, $\Delta\alpha(I_{exc}) = \alpha(I_{exc}) - \alpha(0)$, for the

pump densities given in Fig. 36(a). Induced transparency ($\Delta\alpha$ negative) in the excitonic region and induced absorption ($\Delta\alpha$ positive) in the below-gap region are clearly seen with increasing pump density. Fig. 37(a) shows room temperature absorption spectra for several different pump densities. We note that at room temperature, the A and B free exciton features seen in Fig. 36(a) have broadened and merged into one and the resulting induced transparency with increasing I_{exc} is about one third that at 10 K. The below-gap induced absorption is seen in Fig. 37(b) to be approximately half that at 10 K. The near symmetry between the induced transparency and induced absorption seen in Fig. 36(b) and Fig. 37(b) appears to be coincidental. For pump densities greater than $\sim 3 \text{ MW/cm}^2$, the induced transparency changes very little while the induced absorption continues to grow with increasing I_{exc} . The origin of the below-gap induced absorption is under continuing investigation (see the next section), but the results of the experiments presented here indicate that it is not due to defects at the GaN-sapphire interface, lattice heating, or excited state absorption. Its presence has been confirmed in a variety of GaN layers of varying thickness, indicating that it is a basic property of state-of-the-art GaN thin films. It is, therefore, deserving of further study. The decrease in the free exciton absorption with increasing I_{exc} is attributed to many body effects, such as exciton screening by free carriers, causing a diminution of their oscillator strength [8]. We note that although the exciton resonances decrease with increasing I_{exc} , their positions remain relatively unchanged. This is due to the decrease in the exciton binding energy being compensated by the red shift of the band edge due to band gap renormalization and is consistent with observations in other materials [8]. For clarity, the dependence of the induced transparency/absorption on I_{exc} for several wavelengths of interest are given in Fig. 38. We note that these samples are still optically thick ($\alpha L \approx 4$ for the pump wavelength and sample thickness, $L = 0.38 \text{ } \mu\text{m}$, used in this study), so the pump intensity is appreciably diminished as it traverses the sample thickness. Therefore, the resulting values of $\Delta\alpha$ presented here are lower limit values of the actual change with pump density. A better gauge of the change in the oscillator strength of the excitonic transitions for a given I_{exc} (*i.e.* the SE threshold) is provided by

pump densities given in Fig. 36(a). Induced transparency ($\Delta\alpha$ negative) in the excitonic region and induced absorption ($\Delta\alpha$ positive) in the below-gap region are clearly seen with increasing pump density. Fig. 37(a) shows room temperature absorption spectra for several different pump densities. We note that at room temperature, the A and B free exciton features seen in Fig. 36(a) have broadened and merged into one and the resulting induced transparency with increasing I_{exc} is about one third that at 10 K. The below-gap induced absorption is seen in Fig. 37(b) to be approximately half that at 10 K. The near symmetry between the induced transparency and induced absorption seen in Fig. 36(b) and Fig. 37(b) appears to be coincidental. For pump densities greater than $\sim 3 \text{ MW/cm}^2$, the induced transparency changes very little while the induced absorption continues to grow with increasing I_{exc} . The origin of the below-gap induced absorption is under continuing investigation (see the next section), but the results of the experiments presented here indicate that it is not due to defects at the GaN-sapphire interface, lattice heating, or excited state absorption. Its presence has been confirmed in a variety of GaN layers of varying thickness, indicating that it is a basic property of state-of-the-art GaN thin films. It is, therefore, deserving of further study. The decrease in the free exciton absorption with increasing I_{exc} is attributed to many body effects, such as exciton screening by free carriers, causing a diminution of their oscillator strength [8]. We note that although the exciton resonances decrease with increasing I_{exc} , their positions remain relatively unchanged. This is due to the decrease in the exciton binding energy being compensated by the red shift of the band edge due to band gap renormalization and is consistent with observations in other materials [8]. For clarity, the dependence of the induced transparency/absorption on I_{exc} for several wavelengths of interest are given in Fig. 38. We note that these samples are still optically thick ($\alpha L \approx 4$ for the pump wavelength and sample thickness, $L = 0.38 \text{ } \mu\text{m}$, used in this study), so the pump intensity is appreciably diminished as it traverses the sample thickness. Therefore, the resulting values of $\Delta\alpha$ presented here are lower limit values of the actual change with pump density. A better gauge of the change in the oscillator strength of the excitonic transitions for a given I_{exc} (*i.e.* the SE threshold) is provided by

nondegenerate optical pump-probe reflection experiments on optically thick (on the order of several μm) GaN layers. This is the subject of a following section and will not be described here.

For the cases of the relatively thin ($< 0.4 \mu\text{m}$) samples used in the above study, as the pump density is increased, there is the possibility that the GaN-sapphire interface of the sample may contribute, under high excitation, to the observed induced absorption due to the presence of a high density of defects and resultant electronic states resulting from the large lattice mismatch between the GaN and the sapphire substrate. In order to clarify the role of the GaN-sapphire interface in these experiments, the experiments were repeated on a high quality thick ($4.2 \mu\text{m}$) GaN sample whose optical properties have been previously reported [56], [70], [81], [49]. While the thickness of the sample precluded the ability to observe excitonic features in transmission experiments, it did allow monitoring of the below-gap absorption changes. Due to the finite penetration depth of the pump beam, only a thin layer of the entire sample thickness was heavily pumped. This was used to study the role of the interface states on the induced absorption. First, the substrate side of the sample was pumped and probed. The resulting (below-gap) absorption changes were then compared to the thin sample case for the same experimental conditions. In this configuration, only a thin region ($< 0.4 \mu\text{m}$) at the GaN-sapphire interface was heavily pumped, maximizing the role of interface states. The experiment was then repeated, except pumping the front surface of the thick sample, and again compared to the thin sample case for the same experimental conditions. This configuration ensured that a negligible amount of interface states were pumped. The results all showed consistently the same induced absorption, qualitatively and quantitatively (when the penetration depth of the pump beam was taken into consideration in the calculations of $\Delta\alpha$). Since there is a negligible amount of the pump beam reaching the GaN-sapphire interface in the second part of the experiment, the possibility of interface states being the origin if the induced below-gap absorption changes is remote.

Another possible origin of the below-gap induced absorption is lattice heating. Since the pump wavelength exceeds the band gap energy, some lattice heating due to the transfer of energy from the photo-generated hot electrons to the lattice is expected. The amount of this heating was estimated to see if the below-gap induced absorption could be attributed to lattice heating. This was done by first comparing the pump-probe absorption spectra at 10 K to the cw absorption spectra for the same sample at different temperatures (see Fig. 34) [21]. It was found that a lattice temperature rise of > 250 K is needed to account for the increased absorption below the band gap for a pump power density of 5 MW/cm^2 . The spontaneous emission emitted from the surface of the sample was then collected for the pump densities of interest, and its spectral redshift with increasing pump density was used to estimate the upper limit of the lattice temperature rise we can expect due to the presence of the pump beam. This estimate was made by comparing the redshift due to pump power to the redshift observed in cw photoluminescence experiments (for the same sample) as the temperature is increased from 10 K [70]. At a pump density of 5 MW/cm^2 , we observe a redshift of $\approx 15 \text{ meV}$ in the pulsed spontaneous emission with respect to the A exciton transition measured in cw photoluminescence experiments. Even if we assume this redshift is due entirely to lattice heating (neglecting all many body effects such as band gap renormalization), we find that this shift can, at maximum, only account for less than a 135 K increase in the lattice temperature, well below that needed to account for the increased below-gap absorption. Another possibility lies in the present crystalline quality of GaN epitaxial film. It is well known that GaN epitaxial films contain a multitude of crystalline defects [82], [83]. There is a possibility that these defects and resultant deep levels in the crystal are a contributing factor to the observed induced absorption. Other possibilities are the presence of two-photon or excited state absorption. Due to the relatively narrow spectral width of the induced absorption, the possibility of excited state absorption being the cause of the below-gap induced absorption seems remote.

The large values of induced transparency and induced absorption observed in this work, and the fact that excitons have been shown to persist in GaN epilayers

well above room temperature (see Fig. 34) [21] (indicating that the large optical nonlinearities observed here will persist to well above room temperature), suggest that these materials may be well suited for optical switching applications. This switching behavior is illustrated in Fig. 39, where the broadband probe has been replaced by a second dye laser tuned to the maximum of the induced absorption, Fig. 39(a), and transparency, Fig. 39(b), at room temperature. The large values of $\Delta\alpha$ are clearly evidenced in the transmitted probe beam as the pump beam is turned on and off. The changes in transmission due to the pump beam agree well with the $\Delta\alpha$ values measured in the broadband probe experiments.

At Non-Zero Time Delay. The previous section showed that in addition to the expected exciton screening with increasing free carrier concentration the emergence of significant below-gap induced absorption in the spectral region optical gain was expected. The below-gap induced absorption was shown to exceed $4 \times 10^4 \text{ cm}^{-1}$ at 10 K and $2 \times 10^4 \text{ cm}^{-1}$ at room temperature. Its presence could not be explained in terms of lattice heating, two-photon absorption, or excited state absorption. It was observed in optically thick samples as well as thin, eliminating the possible role of GaN-sapphire interface states in the process and illustrating that it is a common property of state-of-the-art GaN films. To better understand this behavior and shed light on its origin, the probe pulse was delayed with respect to the pump pulse in the previous experiments, allowing the time evolution (on nanosecond time scales) of the below-gap induced absorption to be studied.

The experimental system consisted of two independent dye laser systems pumped by the second harmonics of separate Q-switched Nd:YAG lasers. The deep red radiation from one of the tunable dye lasers was frequency doubled in a nonlinear crystal to provide the near to deep UV wavelengths needed to optically excite the GaN layers above their fundamental band gap. The red-orange radiation from the other dye laser was also frequency doubled in a nonlinear crystal to generate the deep UV wavelengths needed to pump the dye solution. The near UV broadband fluorescence from the dye solution was collected and focused coincidental (spatially) with

the pump beam on the sample surface. The transmitted broadband probe beam was collected, coupled into a 1/4 meter spectrometer, and spectrally analyzed using a UV enhanced, gated CCD. The two dye laser systems were temporally locked together electronically and a digital delay generator allowed the temporal delay between the two to be precisely varied. A temporal jitter between the pump and probe pulses better than 0.5 ns was achieved through creative use of various signal and delay generators in the process of slaving one Nd:YAG laser to the other. This experimental system provided significant advantages over the previous system in that the laser wavelengths used to pump the sample and the dye solution were now independently variable, allowing optimization of the experimental conditions. The probe intensity was again kept many orders of magnitude lower than the pump intensity and its spot size was kept at approximately 1/2 that of the pump. A pump wavelength of 330 nm (3.756 eV) was used in these experiments. The temperature was varied between 10 K and room temperature through the use of a closed cycle refrigerator. The experimental setup is illustrated in Fig. 40. Both the pump and probe pulses had durations of approximately 4 ns FWHM. the zero of the delay was precisely set using a fast photodiode placed at the sample position and a 1 GHz digital signal analyzer (Tektronix DSA 601). The delay was controlled by a digital delay generator with a better than 10 picosecond resolution for delays from 10 picoseconds to over one second (Stanford Research Systems DG535).

The first thing observed from this experiment is that the below-gap induced absorption is due to a shift in the GaN band gap to lower energies. This is shown in Fig. 41. The band gap is seen to go through a transformation during the pump pulse duration, finally reaching a maximum change at a delay of about 5 ns of the probe with respect to the pump pulse. At this time, the excitonic features that disappeared during the pump pulse duration reappear at a lower energy. The fact that the 1s A and B free excitonic transitions cannot be distinguished in the spectra of Fig. 41 is a result of limited resolution afforded by the use of the 1/4 meter spectrometer and is not due to the changes in the sample itself over what was observed in the previous section. The spectral positions of these transitions are marked in Fig. 41

for completeness. The slight spectral shift in their spectral position with respect to the data presented in the previous section is a result of different residual strain in different areas of this sample (see Chapter 3). An interesting feature of the spectra shown in Fig. 41 is the drastic reduction of the excitonic features in the - 2 ns delay spectrum. This reduction is comparable to that observed in the zero time delay spectrum. The pump density at - 2 ns is by definition approximately 1/2 that at zero delay. This indicates the pump density at which excitons are effectively screened by free carriers is significantly lower than was previously indicated in the zero time delay experiments. A considerable amount of below-gap induced absorption is seen even in the - 2 ns delay spectrum. An interesting feature of Fig. 41 is that the below-gap induced absorption builds up with increasing delay after the peak of the pump pulse, reaching a maximum approximately 5 ns after the peak of the pump pulse. This was observed for all pump densities employed and at both 10 K and room temperature. This is significant in that it provides the following picture for gain development in GaN thin films: Stimulated emission and gain develop on the leading edge of the pump pulse. As the pump pulse continues in duration, gain continues to increase with the increase in the pump pulse. At the same time, the below-gap induced absorption starts to grow. This leads to two competing effects in the below-gap region as the pump pulse continues: induced gain and induced absorption. The induced absorption quickly exceeds the gain and results in only the observation of induced absorption in the probe spectra. This indicates that the stimulated emission threshold of GaN measured in nanosecond experiments significantly overestimates the excitation density needed to achieve population inversion and optical gain. This will be shown in a later section to partly explain the significant reduction of the SE threshold observed for InGaN thin films compared to GaN.

The evolution of the band edge for longer delays is shown in Fig. 42. For delays longer than 5 ns the band edge slowly returns to its pre-pumped position, finally recovering after approximately 100 ns. It is clear from the spectra in Fig. 42 that as the band edge recovers the excitonic resonances also decrease in linewidth. This behavior mimics what is observed in absorption measurements as the temperature

is increased (see Fig. 34), but it will be shown that this behavior is not consistent with lattice heating caused by the intense optical pump. The shift of the band edge to lower energy results in extremely large values of induced absorption in the below-gap spectral region, nearly doubling at 5 ns what was previously observed at zero time delay. This is shown in Fig. 43. It is noted here that this behavior would make an even more effective optical switch than was previously thought (see the preceding section). It is clear from Fig. 43 that the near symmetry between the induced transparency and absorption observed at zero time delay in the previous section is lost as the probe is delayed with respect to the pump. The same behavior is observed at room temperature, as illustrated in Figs. 44 and 45. Of particular interest to optical switching applications is the enhanced induced absorption for a 5 ns delay compared to the previously observed behavior at zero time delay, resulting in a 3 fold increase in the value for $\Delta\alpha$ and a 3 fold reduction in the transmitted light in this spectral region (from approximately 56% to 18% at 3.41 eV). At room temperature the band edge takes longer than 100 ns to completely shift back to its pre-pumped position.

In order to describe the shift in the band edge for various pump densities and probe delays, the effective lattice temperature rise ($T_{eff} - T_o$, where T_o is the ambient temperature) required to shift the band edge the given amount was calculated. This was done using the Varshni equation [84]:

$$E(T) = E(T = 0) - \frac{\alpha T^2}{(\beta + T)} \quad (35)$$

and the best fit values ($\alpha = 11.8 \times 10^{-4}$ eV/K, $\beta = 1414$ K) from ref. [21] for the same GaN thin film. The calculated values for T_{eff} are shown in Figs. 46 and 47 relative to the ambient temperature at 10 K and room temperature for various excitation densities. At 10 K, T_{eff} drops off nearly exponentially for delays less than about 40 ns, with decay times on the order of 40 ns for $I_{exc} = 0.75$ MW/cm², up to approximately 90 ns for $I_{exc} = 3$ MW/cm². For delays longer than approximately 40 ns, T_{eff} exhibits nonexponential decay. At room temperature, T_{eff} decays nonexponentially for all delay ranges and excitation densities, with typical recovery times

on the order of 140 ns. It is interesting to note that the maximum values for T_{eff} (at 5 ns delay) have a sublinear dependence on I_{exc} at both 10K and room temperature (see the insets of Figs. 46 and 47). In fact, if the 0 K rise in T_{eff} for $I_{exc} = 0$ is included in the plot, the rise in $T_{eff} - T_o$ with increasing I_{exc} is seen to exhibit saturation behavior. I point out here that while T_{eff} is being used as a parameter to describe the shift in the band edge with increasing I_{exc} and for various delays, I am not ascribing the behavior to lattice heating. The 5 ns rise time, the recovery time (on the order of 50 to 100 ns), and the saturation behavior of $T_{eff} - T_o$ with increasing I_{exc} suggests a different mechanism for the observed band edge shift.

A well known property of epitaxial GaN films is the presence of a large density of dislocations and other structural defects induced by the large lattice mismatch between the (sapphire) substrate and the GaN layer as well as their differences in thermal expansion coefficients. In addition, the presence of a large concentration of deep levels of (presently) unknown origin exist in this material. These levels give rise to the so-called "yellow-band" luminescence (YBL) that is commonly observed when GaN is excited above its fundamental band gap. The strength of the YBL compared to the band edge luminescence was found to be a strong function of the growth conditions. Samples with the strongest band edge luminescence were typically found to exhibit the least YBL. It was observed by the author that a reduction in the YBL from a GaN layer typically was accompanied by a relative reduction in the stimulated emission threshold. The large concentration of these deep levels responsible for YBL is evidenced by the experiments of Taheri *et al.* [78], where strong laser induced grating production was achieved via two-step single photon absorption of 532 nm (2.33 eV) laser radiation, promoting electrons from the valence band of GaN to the conduction band. The deep levels in GaN provided the mid-gap states required for this process. The large magnitude of the nonlinearities observed in these experiments provides evidence for a considerable concentration of these mid-gap states. Strong band edge (UV) luminescence was also observed in nanosecond optical pumping experiments with 532 nm radiation performed by the author. In the nanosecond experiments, the excitation densities required to observe this luminescence were very

close to the damage threshold of GaN, so a detailed study was not possible at that time. This difficulty would most likely be overcome by using optical pulses with shorter duration to substantially increase the damage threshold. The observation of this luminescence also illustrates the potentially large concentration of these deep levels.

Considering the above observations, a picture emerges for a possible origin of the band edge shift observed in nanosecond optical pump-probe experiments. During the pump pulse duration, the photo-generated free carriers quickly (on the order of a couple hundred picoseconds, or less) relax to deep levels in the crystal. These deep levels are known to radiatively recombine (giving rise to YBL) with effective lifetimes on the order of hundreds of nanoseconds. These deep levels effectively screen the excitons and lead to the observed reduction in the band gap, similar to what has been observed in indirect gap semiconductors while monitoring the direct gap excitonic transitions in nondegenerate optical pump-probe experiments [85]. This screening and band gap reduction decreases as the carriers trapped at these deep levels recombine. This scenario qualitatively explains the experimentally observed phenomena. The near zero time delay behavior is then seen to be a competition between commonly observed changes in the band gap of semiconductors with increasing optical excitation, such as exciton screening by free carriers, band gap renormalization, and formation of optical gain, and the screening behavior described above resulting from carriers trapped at deep levels. The latter dominates after the pump pulse duration (free carriers in GaN recombine on the order of tens of picoseconds) and decays as the trapped carriers recombine (on the order of hundreds of nanoseconds).

In summary, the results of nondegenerate optical pump-probe absorption experiments with variable delay between the pump and probe pulses has been presented for GaN thin films. The below-gap induced absorption observed in the zero delay experiments of the previous section was shown to be due to a large shift in the band gap to lower energy. This shift was observed to be at a maximum within one nanosecond after the end of the pump pulse. The band gap was shown to return to its pre-pumped position on time scales on the order of 100 ns at 10 K and room temperature. The

below-gap induced absorption at 5 ns delay of the probe with respect to the pump was shown to be considerably larger (over three times larger at room temperature) than was previously observed at zero time delay. The large magnitude of this induced absorption makes optical switching and optical bistability applications for GaN look promising. In addition, effective screening of excitons was observed to occur on the leading edge of the pump pulse, indicating the pump (carrier) densities required to effectively screen excitons are considerably less than was previously estimated in the zero time delay nondegenerate optical pump-probe experiments. The long-lived shift in the band gap due to the pump beam is tentatively attributed to screening by carriers trapped at deep levels, in analogy to changes observed in the direct gap transitions of indirect gap semiconductors in this type of experiment. This will, of course, need to be confirmed by theoretical calculations and further experiments, the subjects of which are beyond the scope of present knowledge of this material and the contents of this monograph. The results presented here suggest that induced absorption and gain competition exists in the below-gap spectral region of highly excited GaN. This indicates that the high stimulated emission threshold of GaN can, in part, be attributed to this competition, with gain being overcome by induced absorption on the leading edge of our nanosecond pump pulses. The magnitude of the observed shift in the band gap is expected to be a strong function of the density of these deep levels. As such, the necessity for minimizing (maximizing) these deep levels is clear for the development of GaN based UV laser diodes (optical switches).

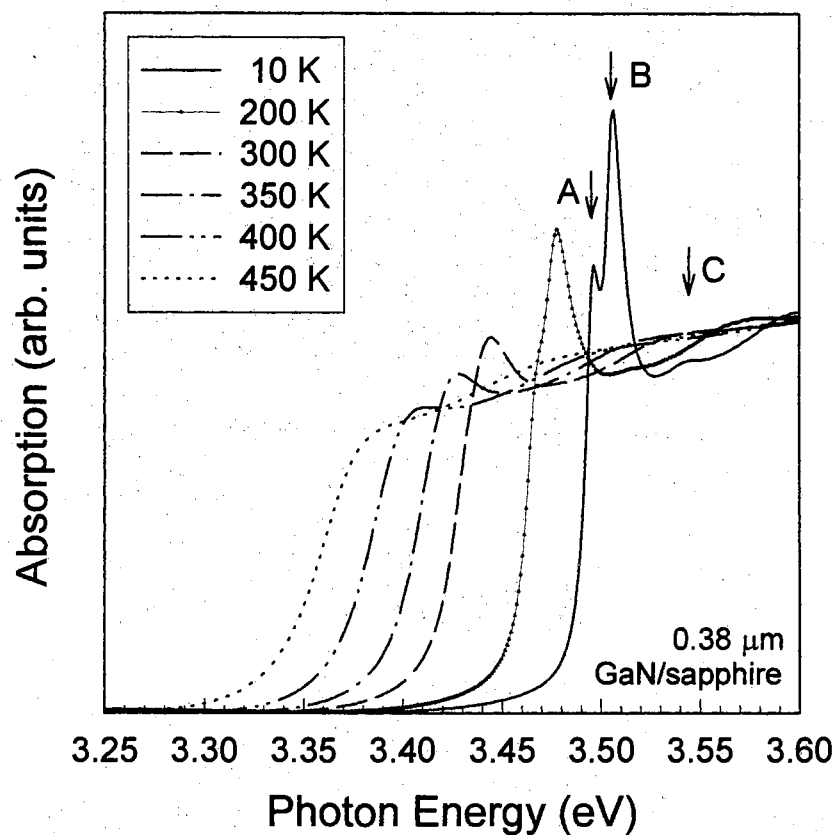


Figure 34. Absorption spectra of a 0.38 μm GaN film near the fundamental band gap as a function of temperature. The A, B, and C free exciton positions (marked by arrows) are clearly seen in the 10 K spectrum. The excitonic features are seen to broaden and merge together with increasing temperature, but are still evident in the 450 K spectrum. Adapted from ref. [21].

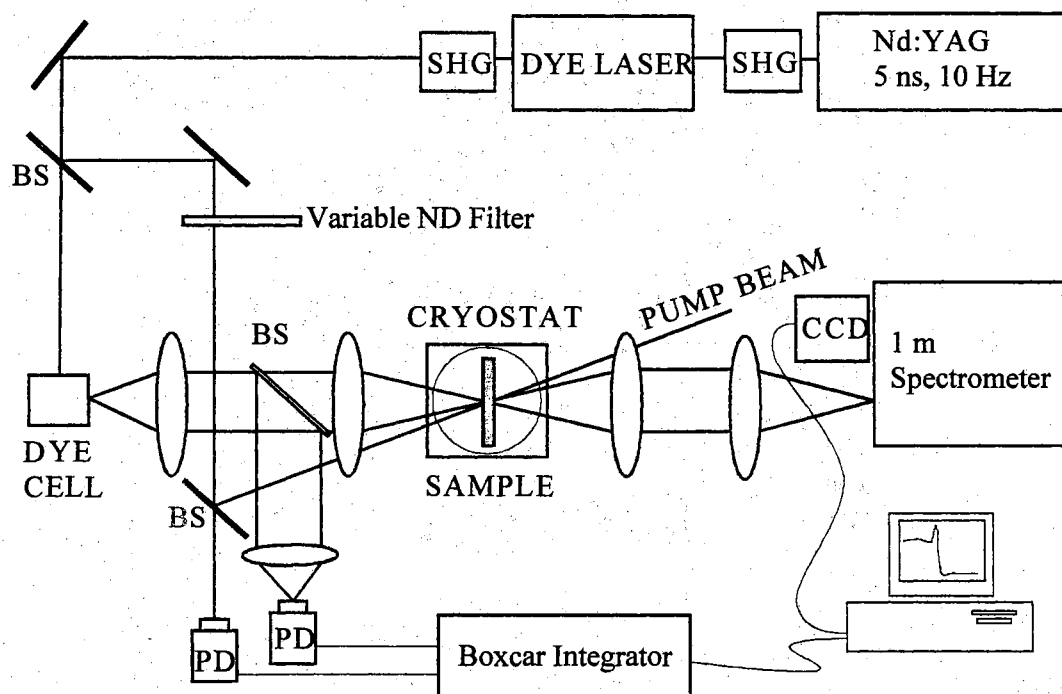


Figure 35. Nanosecond nondegenerate optical pump-probe absorption setup for zero time delay between the pump and probe pulses. SHG, ND, BS, and PD refer to second harmonic generator, neutral density, beam splitter, and photodiode, respectively.

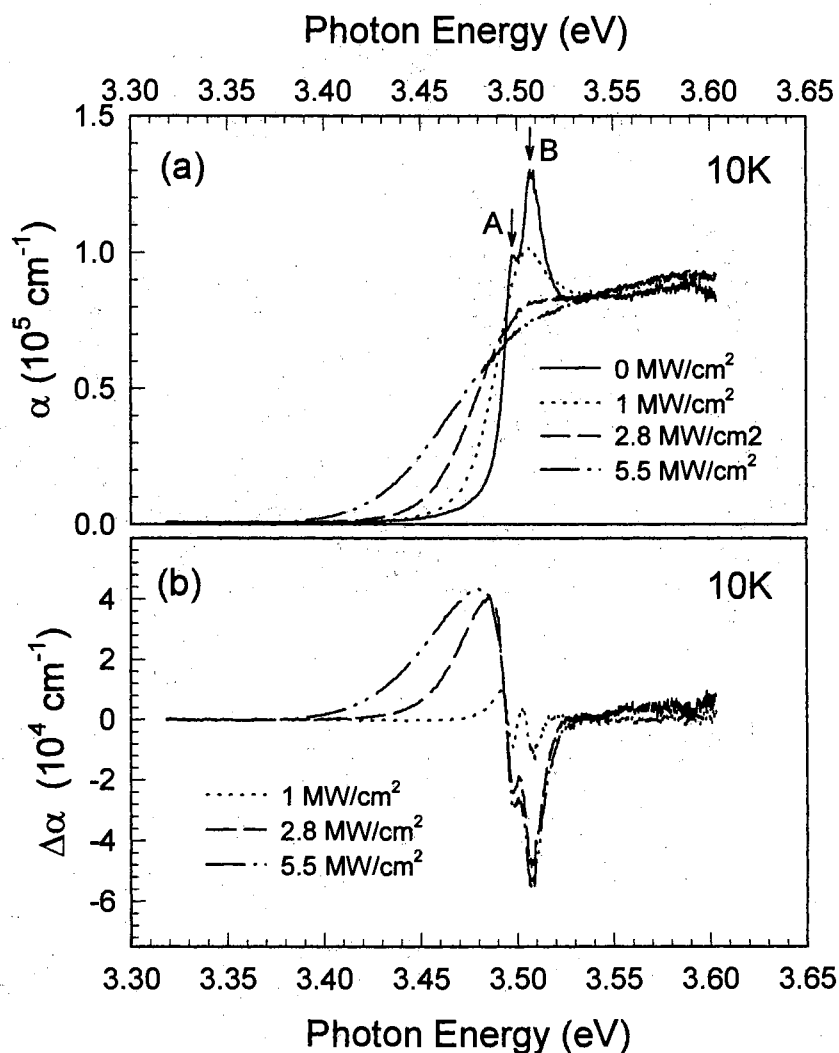


Figure 36. (a) 10 K absorption spectra as a function of I_{exc} for a $0.38 \mu\text{m}$ thick GaN layer grown by MOCVD on (0001) oriented sapphire. (b) Change in absorption spectra as a function of I_{exc} , $\Delta\alpha(I_{exc}) = \alpha(I_{exc}) - \alpha(0)$, for the spectra in (a). The A and B free exciton transitions are clearly seen in the unpumped spectrum. Complete exciton saturation is seen for I_{exc} approaching 3 MW/cm^2 . Induced transparency in the excitonic region and induced absorption in the below-gap region are clearly seen with increasing I_{exc} .

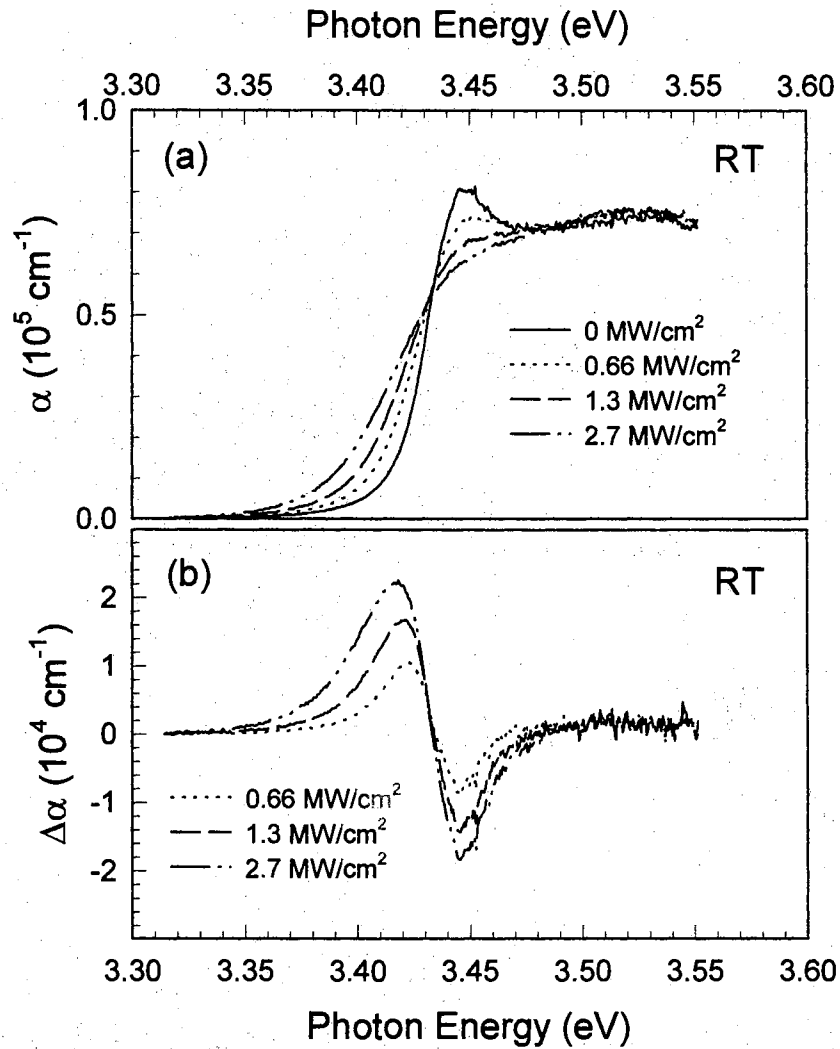


Figure 37. (a) RT absorption spectra as a function of I_{exc} for a $0.38 \mu\text{m}$ thick GaN layer grown by MOCVD on (0001) oriented sapphire. (b) Change in absorption spectra as a function of I_{exc} , $\Delta\alpha(I_{exc}) = \alpha(I_{exc}) - \alpha(0)$, for the spectra in (a). The A and B free exciton transitions have broadened and merged into one feature in the RT spectra. Complete exciton saturation is seen for I_{exc} approaching 3 MW/cm^2 . Induced transparency in the excitonic region and induced absorption in the below-gap region are clearly seen with increasing I_{exc} .

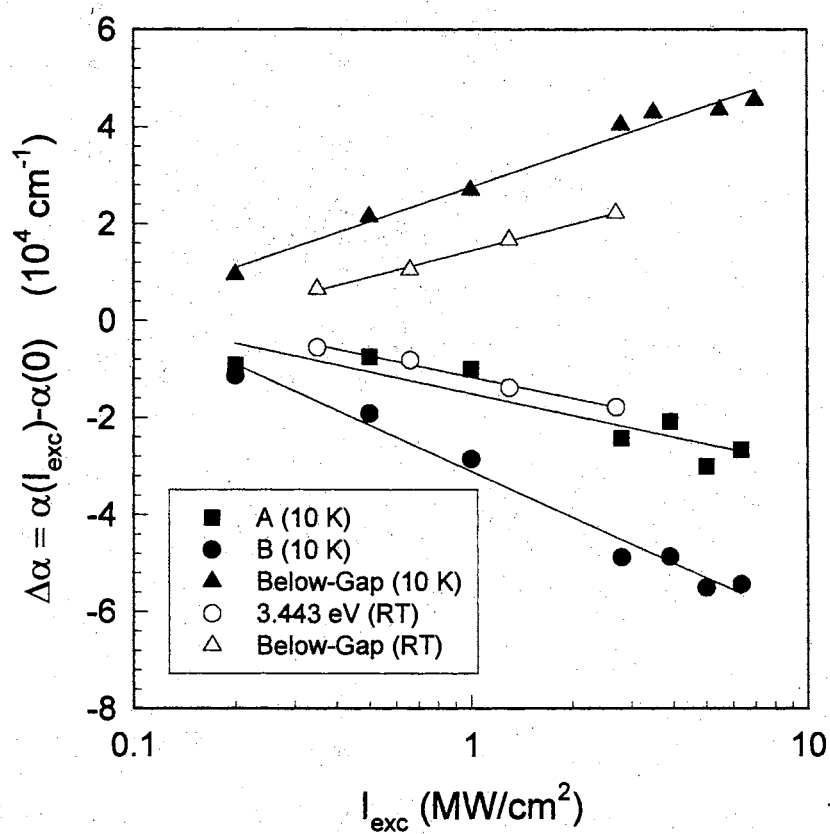


Figure 38. Magnitudes of induced transparency/absorption for the excitonic and below-gap regions at 10 K (solid points) and RT (open points). The given values of the below-gap induced absorption correspond to the maximum absorption change, whereas the values given for the excitonic regions are for the specific energy regions indicated.

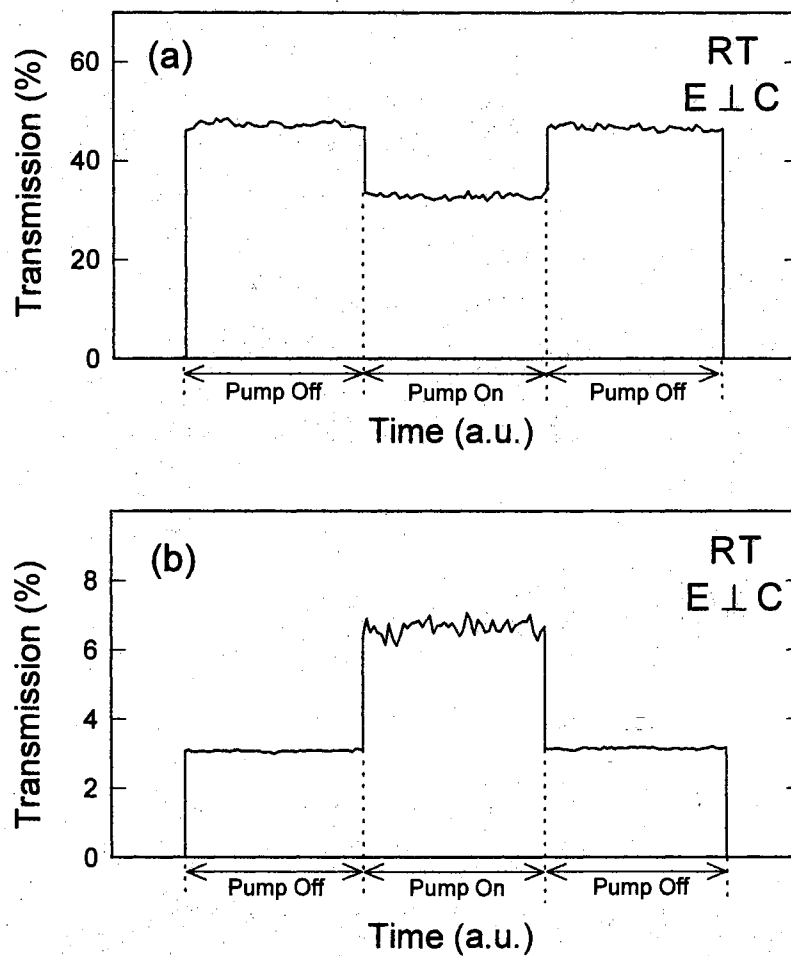


Figure 39. RT transmission values of a second laser beam tuned to the maximum of the induced absorption (a) and transparency (b) for the pump beam off, on, and off again, illustrating the potential of GaN as an optical switch. The GaN thickness is $0.38 \mu\text{m}$, and the pump densities are $\approx 1 \text{ MW}/\text{cm}^2$ and $\approx 3 \text{ MW}/\text{cm}^2$ for (a) and (b), respectively.

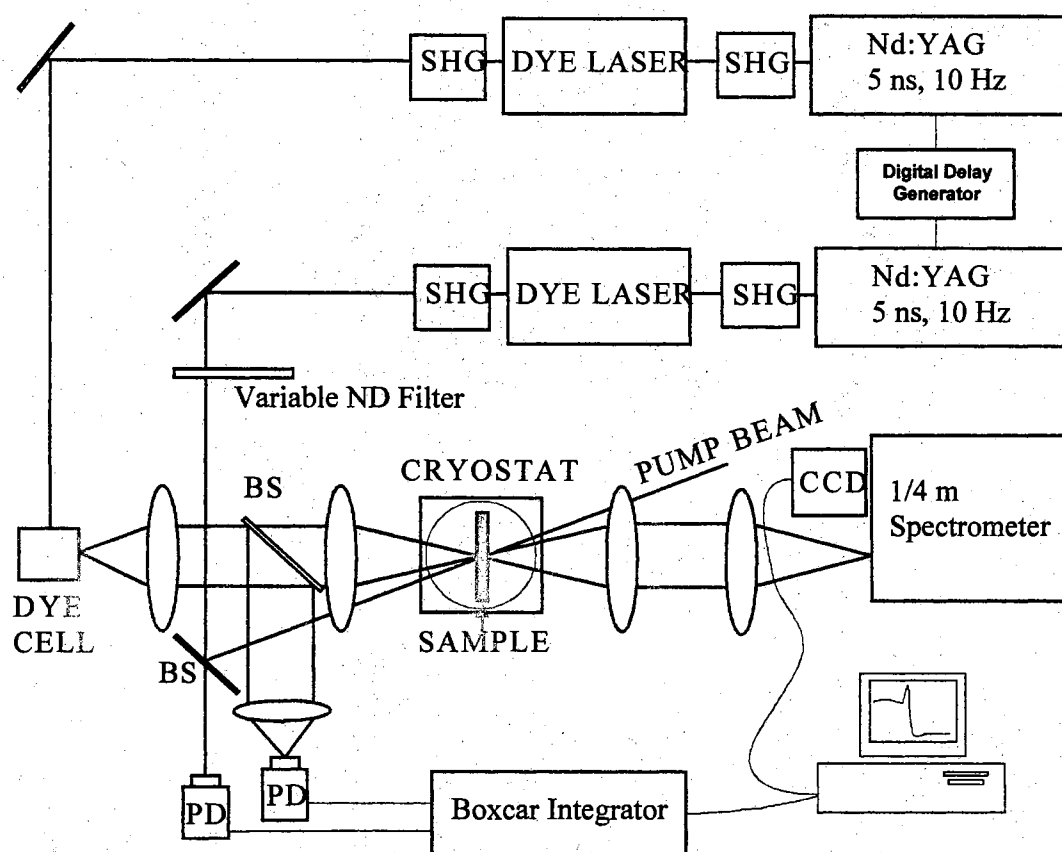


Figure 40. Nanosecond nondegenerate optical pump-probe absorption setup with electronically controlled time delay between the pump and probe pulses. SHG, ND, BS, and PD refer to second harmonic generator, neutral density, beam splitter, and photodiode, respectively.

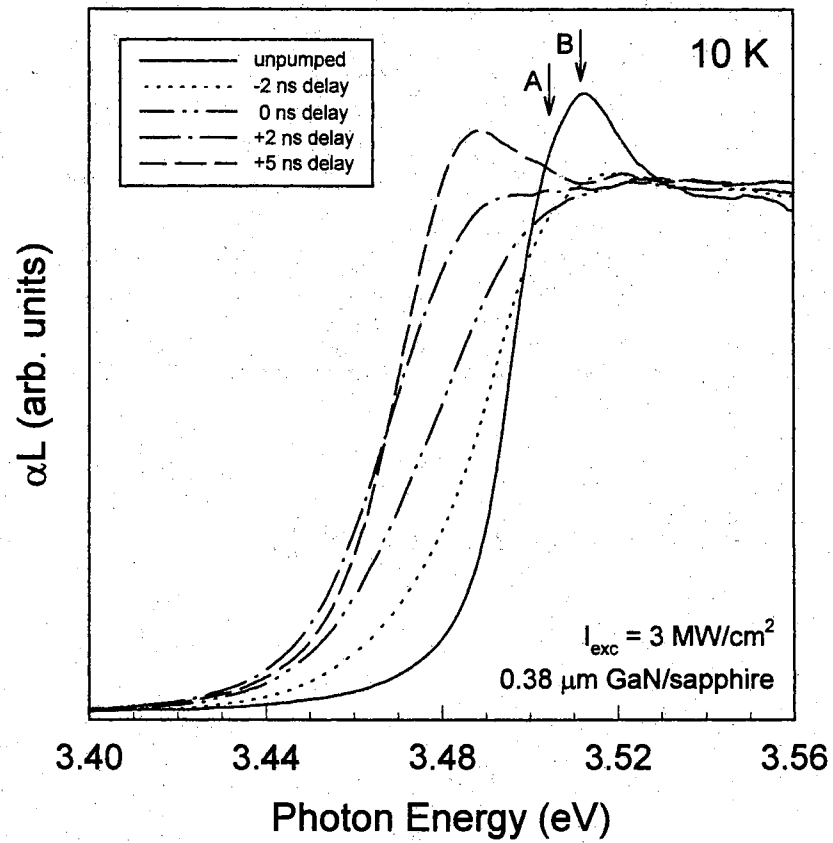


Figure 41. 10 K absorption spectra of a 0.38 μm thick GaN layer near the fundamental band gap as a function of time delay across the pump pulse duration. The 1s A and B free exciton transition energies are indicated for completeness. The spectra show a clear shift in the band gap to lower energy with increasing time delay of the probe across the pump pulse duration.

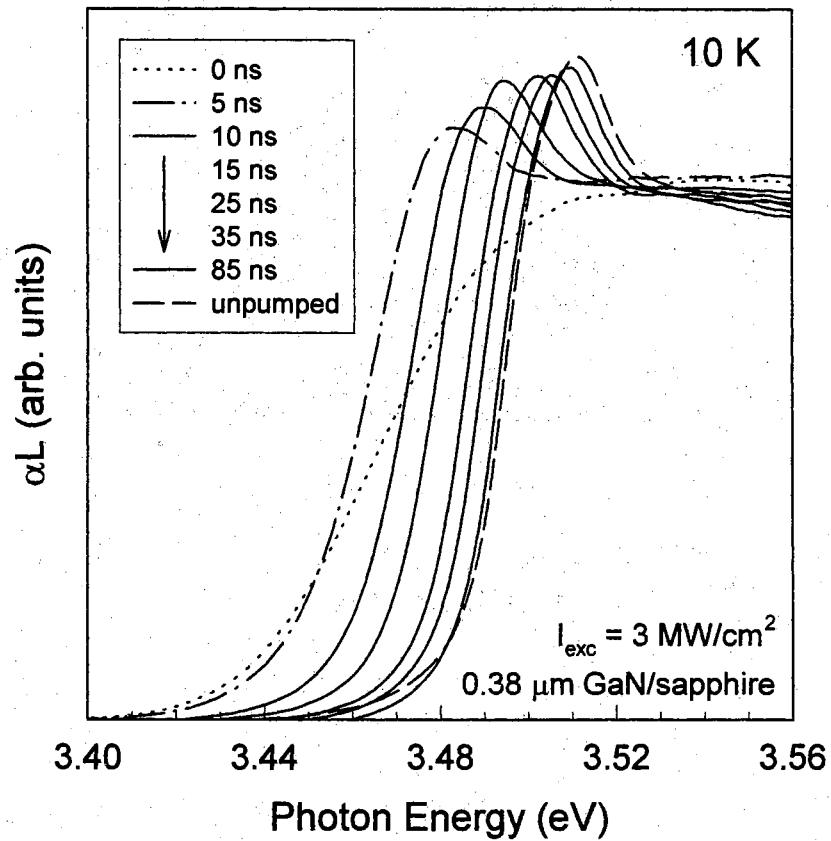


Figure 42. 10 K absorption spectra of a 0.38 μm thick GaN layer near the fundamental band gap as a function of time delay after the pump pulse. The spectra show clear excitonic features that narrow as the band gap returns to its pre-pumped position with increasing delay time. The band gap is seen to almost completely recover within 85 ns after the pump pulse.

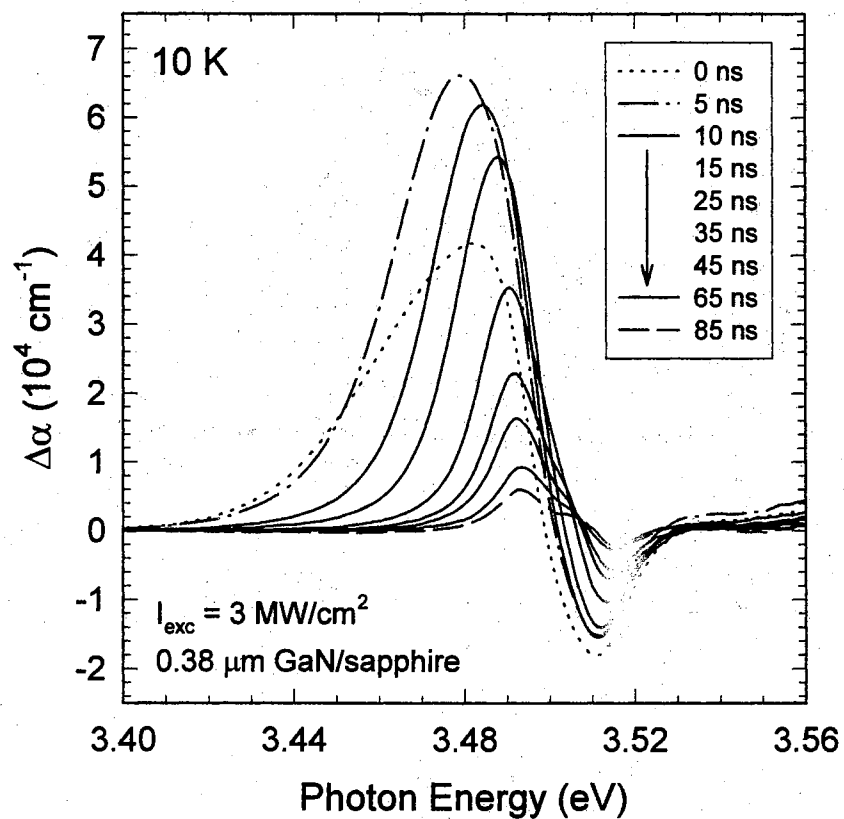


Figure 43. 10 K differential absorption spectra of a 0.38 μm thick GaN layer near the fundamental band gap as a function of time delay after the pump pulse. The spectra at 5 - 15 ns delay show clear enhancement of the below-gap induced absorption compared to the undelayed spectrum. $\Delta\alpha(I_{\text{exc}}) = \alpha(I_{\text{exc}}) - \alpha(0)$.

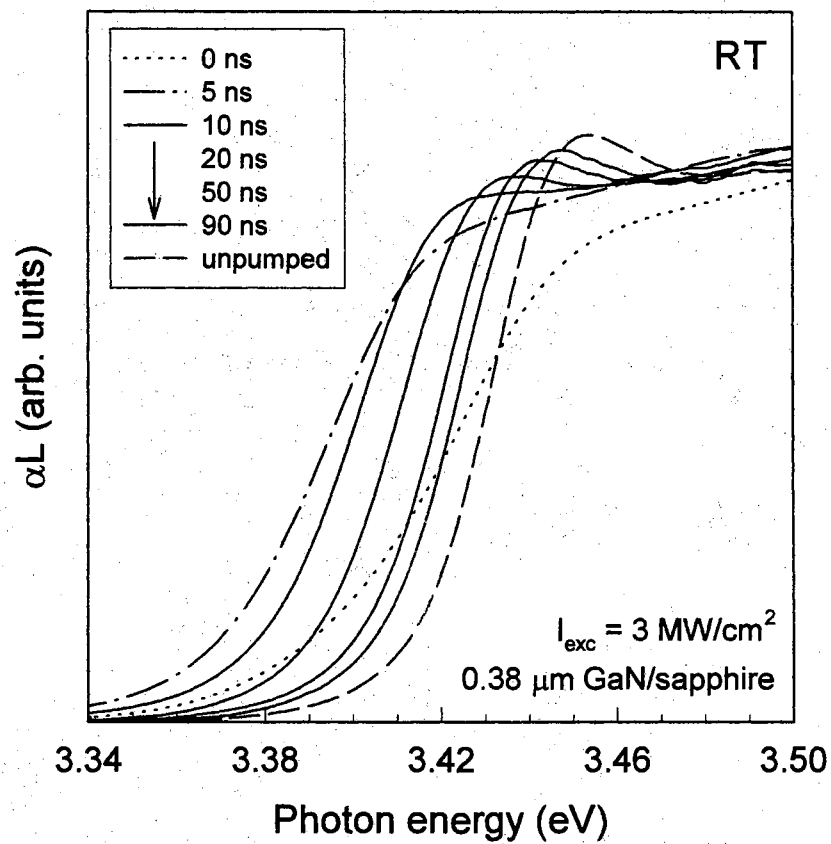


Figure 44. Room temperature absorption spectra of a 0.38 μm thick GaN layer near the fundamental band gap as a function of time delay after the pump pulse. The spectra show clear excitonic features that narrow as the band gap returns to its pre-pumped position with increasing delay time. The band gap is seen to take longer than 90 ns to recover to its pre-pumped position.

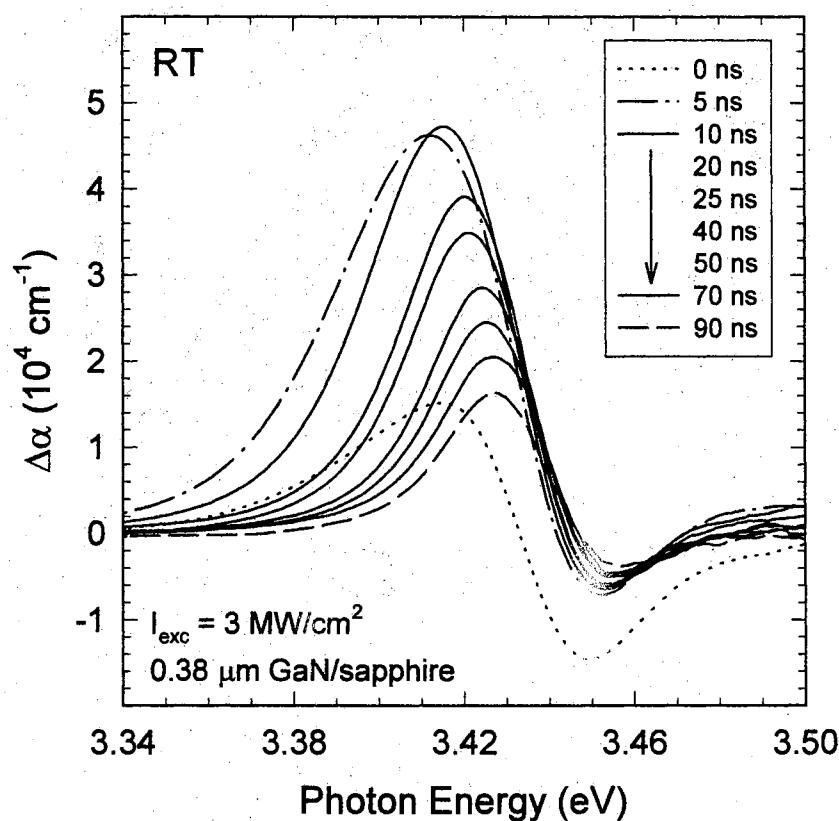


Figure 45. Room temperature differential absorption spectra of a $0.38 \mu\text{m}$ thick GaN layer near the fundamental band gap as a function of time delay after the pump pulse. The time delayed spectra show clear enhancement of the below-gap induced absorption compared to the undelayed spectrum, while the induced transparency in the excitonic region is seen to be significantly reduced in the time delayed spectra. $\Delta\alpha(I_{exc}) = \alpha(I_{exc}) - \alpha(0)$.

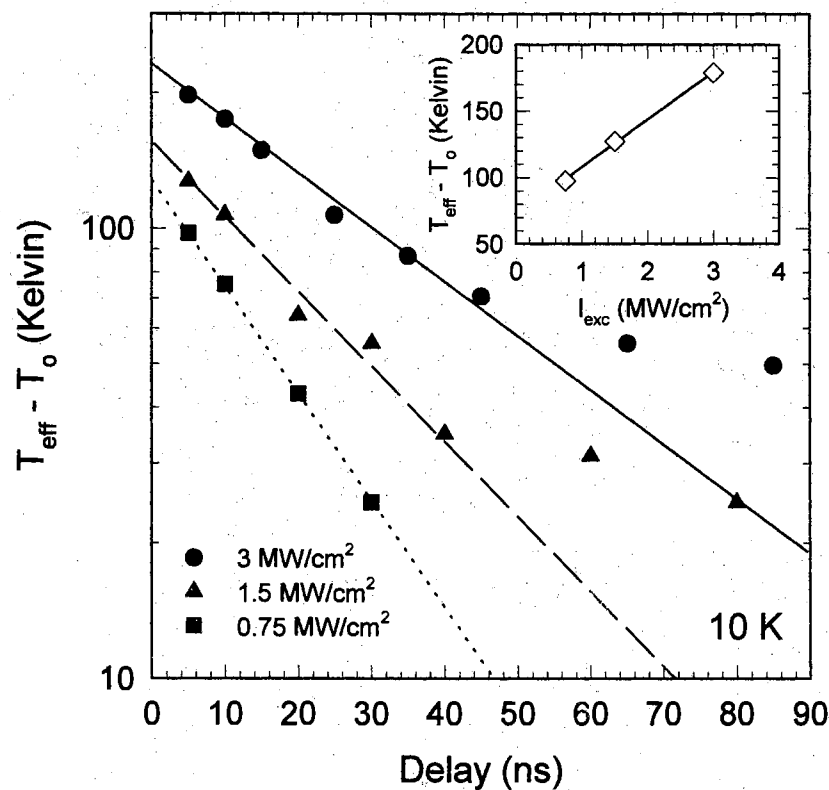


Figure 46. Effective temperature rise in a $0.38 \mu\text{m}$ GaN film ($T_{eff} - T_o$) at $T_o = 10 \text{ K}$ induced by a strong optical pump as a function of time delay after the pump pulse. T_{eff} was calculated using the Varshni equation and the spectral position of the 1s B exciton as a function of delay and excitation density (I_{exc}). The Varshni equation fitting parameters (α , β) were obtained from cw absorption experiments performed on the same sample. The inset shows the maximum effective lattice temperature rise (at 5 ns delay) as a function of I_{exc} . The lines are given only as guides for the eye.

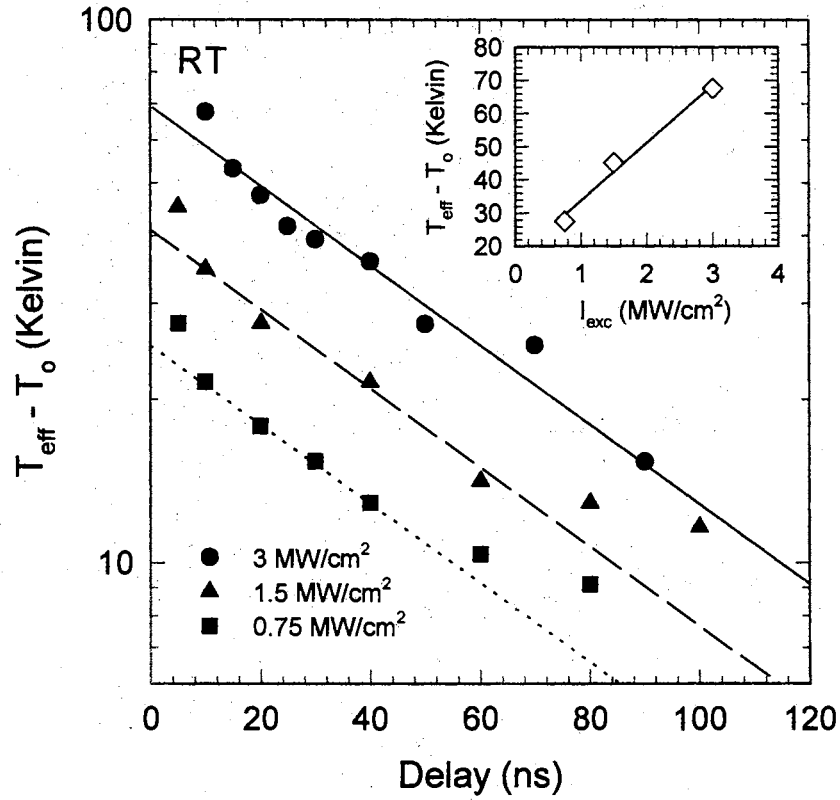


Figure 47. Effective lattice temperature rise in a $0.38 \mu\text{m}$ GaN film ($T_{eff} - T_o$) at $T_o = 300 \text{ K}$ induced by a strong optical pump as a function of time delay after the pump pulse. T_{eff} was calculated using the Varshni equation and the spectral position of the 1s B exciton as a function of delay and excitation density (I_{exc}). The Varshni equation fitting parameters (α, β) were obtained from cw absorption experiments performed on the same sample. The inset shows the maximum effective lattice temperature rise (at 5 ns delay) as a function of I_{exc} . The lines are given only as guides for the eye.

Single-Beam Power Dependent Absorption Spectroscopy

Motivation

In this section the results of single-beam power dependent absorption experiments on GaN thin films are presented. The experiments were performed to better understand the results of the nondegenerate optical pump-probe experiments described above. They differ from the pump-probe experiments in that the excitation photon energy is also the photon energy of the transition being “probed”, making this, in a sense, a form of degenerate pump-probe spectroscopy. From these experiments we obtain a better understanding of how the transition being excited is affected by the excitation, *i.e.* how an excitonic resonance decreases with increasing optical excitation of the resonance. The single-beam experiments provide complimentary information to the nondegenerate pump-probe experiments, where the probe was used to monitor the band edge transitions as the number of photo-excited free carriers was increased by above-gap optical excitation.

Experimental Technique and Results

The single-beam power dependent absorption experiments were performed using the second harmonic of the deep red radiation generated by a dye laser pumped by the second harmonic of an injection seeded Nd:YAG laser (4 ns FWHM pulse width, 10 Hz repetition rate). The phase matching angle for second harmonic generation was maintained using an auto-tracking unit as the dye laser emission wavelength was scanned across the GaN band edge. The intensity of the transmitted beam through the sample was measured using a photodiode and a boxcar integrator. The transmitted signal was compared directly with a split-off portion of the beam not passing through the sample to obtain the absorption spectra. The intensity of the beams was controlled using UV neutral density filters. The single-beam absorption experimental configuration is illustrated in Fig. 48.

The results of the single-beam power dependent absorption experiments are shown in Fig. 49(a) and Fig. 49(b) for the 0.38 μm GaN sample used in the pump-probe experiments described above. No noticeable change in the 10 K absorption spectrum was observed with increasing excitation density (I_{exc}) until I_{exc} exceeded densities on the order of 100 kW/cm². We note that the changes in absorption in the excitonic region are qualitatively consistent with those observed in the pump-probe experiments, but the below-gap induced absorption is, for the most part, absent. The magnitude of the induced transparency in the exciton region is seen to be enhanced in the single-beam experiments compared to the pump-probe experiments for comparable excitation densities. The decreased value of I_{exc} needed to bleach the excitonic transitions a given amount in the single-beam experiments compared to the pump-probe experiment is attributed to enhanced exciton-exciton scattering for the resonant excitation in the single-beam experiments. The drastic reduction in the below-gap induced absorption indicates that the states responsible for it cannot be directly created by below-gap excitation, *i.e.* the states have to first be created by the above-gap excitation of the pump beam. This also explains the observed differences between $\Delta\alpha$ for the A exciton region and the B exciton region seen in Fig. 36(b). In Fig. 49(b) we see the magnitudes of $\Delta\alpha$ for the A and B exciton regions to be approximately equal in magnitude, while in Fig. 36(b), $\Delta\alpha$ in the A exciton region is seen to be approximately half that of the B exciton. Comparing the results in Fig. 49(b) to Fig. 36(b), we see this is most likely due to a superposition of induced transparency and induced absorption in the A exciton region of Fig. 36(b).

Summary

From the single-beam power dependent absorption experiments described above we gain another valuable piece of information concerning the origin of the below-gap induced absorption observed in the nondegenerate optical pump-probe experiments. This is that the states responsible for the below-gap induced absorption must first be created by above-gap excitation and cannot be created by photons of energy less than the fundamental band gap. This is consistent with the concept

that relaxation of free carriers to deep levels in the crystal leads to the below-gap induced absorption. The effective absorption cross sections of these deep levels are considerably smaller than those of the band edge transitions, precluding the ability to directly populate them to sufficient levels with below-gap optical excitation.

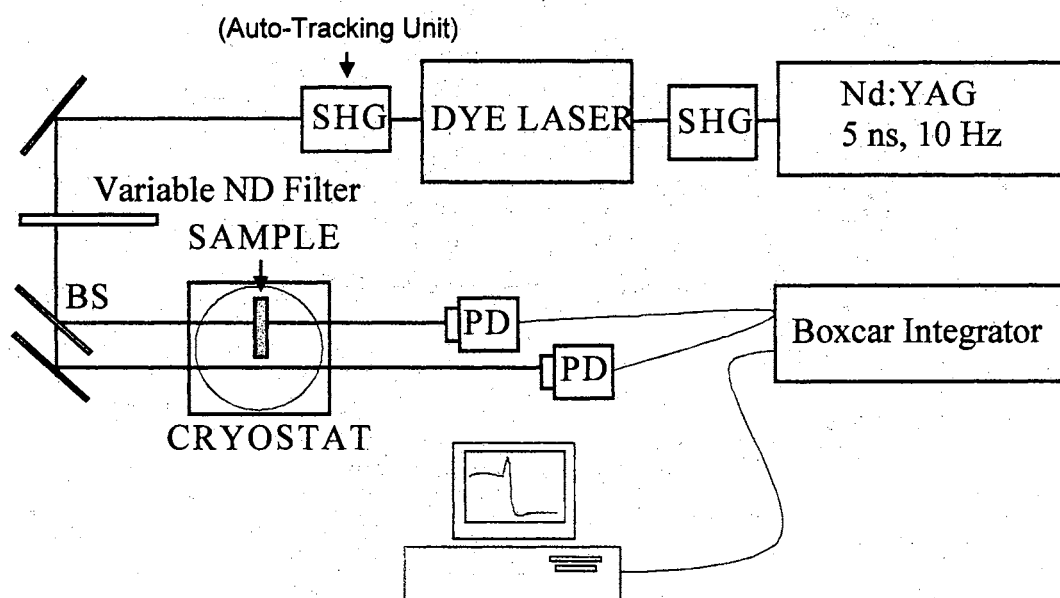


Figure 48. Single-beam power dependent absorption experimental setup. The phase matching condition in the second harmonic generating crystal is maintained by the Auto-Tracking unit as the dye laser is tuned. SHG, ND, BS, and PD refer to second harmonic generator, neutral density, beam splitter, and photodiode, respectively.

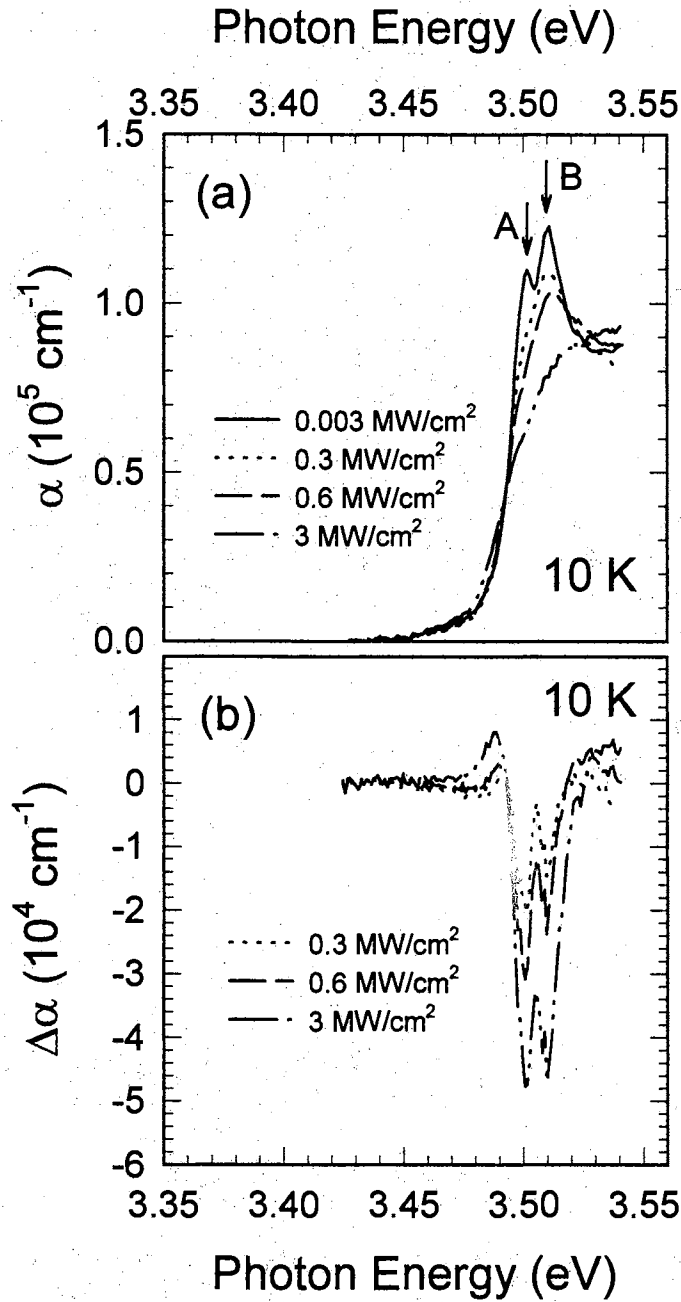


Figure 49. (a) 10 K single-beam power dependent absorption spectra for a $0.38 \mu\text{m}$ GaN thin film grown by MOCVD on (0001) oriented sapphire. (b) Change in absorption, $\Delta\alpha(I_{exc}) = \alpha(I_{exc}) - \alpha(0)$, for the spectra in (a). The 1s A and B free exciton transitions are indicated in (a).

Nondegenerate Optical Pump-Probe Reflection Spectroscopy

Motivation

In this section the results of nanosecond non-degenerate optical pump-probe reflection experiments on GaN thin films are presented. These experiments were performed because the GaN thin films used in the pump-probe absorption experiments presented above are, in fact, optically thick ($\alpha L \approx 4$ for the pump wavelength and sample thickness, $L = 0.38 \mu\text{m}$, used in those studies), so the pump intensity is appreciably diminished as it traverses the sample thickness. Therefore, the resulting values measured for $\Delta\alpha$ are lower limit values of the actual change with pump density. This cannot be avoided, as the samples used in those studies represent the highest quality thin films available at this time. Present efforts are underway to obtain thin ($\approx 1 \mu\text{m}$) GaN layers sandwiched between $\text{Al}_{0.08}\text{Ga}_{0.92}\text{N}$ layers in hopes of obtaining high quality GaN layers of lesser thickness in which to perform additional pump-probe experiments. Since these samples are not presently available, we have switched geometry from transmission to reflection to allow us to perform experiments on high quality thick GaN layers. A more precise measure of the influence of the pump density on the oscillator strength of the excitons is achieved through optical pump-probe reflection measurements. In these measurements, only a thin layer ($\approx 0.1 \mu\text{m}$) at the sample surface is probed for wavelengths at and above the band edge, so the effect of the pump on the band edge is more easily compared to the results of optically pumped stimulated emission (SE) experiments.

Experimental Technique and Results

The experimental configuration is identical to that of Fig. 35 except the reflected instead of transmitted probe is collected, coupled into the spectrometer, and spectrally analyzed using the UV enhanced, gated CCD. An excitation photon energy of 3.676 eV (337 nm) was used in these experiments.

Figure 50 shows the 10 K reflection spectra as a function of I_{exc} for a 4.2 μm thick MOCVD grown GaN layer whose optical properties have been reported previously [56], [70]. The 1s A and B free exciton transitions are clearly seen in the $I_{exc} = 0$ spectra and are shown to be greatly diminished by the time I_{exc} reaches 0.75 MW/cm². They are seen to be absent in the reflection spectra by the time I_{exc} reaches 3 MW/cm². Again, the excitonic features do not noticeably shift in position as I_{exc} is increased. The SE threshold for this sample has been reported earlier [56] as $I_{th} \approx 0.3$ MW/cm² for the same excitation source. The large decrease in the excitonic features at $I_{exc} = 0.75$ MW/cm² indicates that for pump densities a few times threshold, the gain in GaN is likely to arise from an electron-hole plasma rather than exciton related mechanisms, even at 10 K.

Summary

In this section the results of nanosecond nondegenerate optical pump-probe reflection experiments on thick GaN films were presented. Employing a reflection geometry in the pump-probe experiments minimized the effects of the pump density variation problems encountered in transmission experiments. This allowed a more precise determination of the effects of the intense optical pump on the strength of the excitonic transitions and provided a more direct comparison to the results of optically pumped SE experiments. The experimental results indicate that the excitonic resonances are severely diminished for pump densities a few times the SE threshold. This in turn indicates that excitonic gain processes give way to those of an electron-hole plasma for excitation densities a few times the SE threshold, even at 10 K.

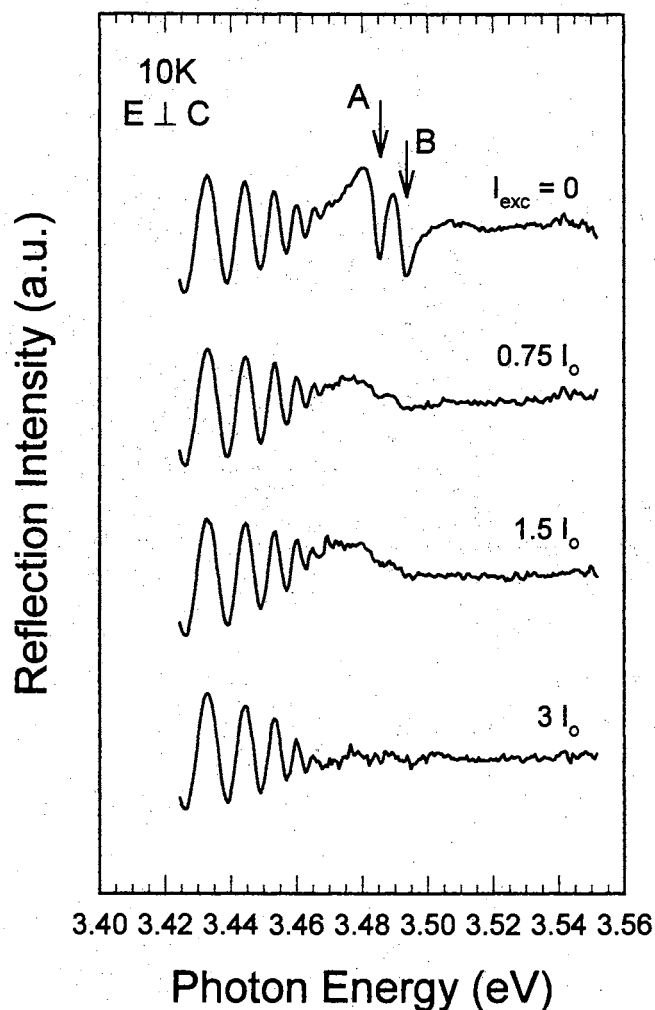


Figure 50. Reflection spectra for a $4.2 \mu\text{m}$ thick GaN epilayer grown by MOCVD on (0001) oriented sapphire as a function of I_{exc} , where $I_0 = 1 \text{ MW/cm}^2$. The 1s A and B free exciton transitions are clearly seen in the $I_{exc} = 0$ spectra (upper curve). The excitonic features are greatly diminished for $I_{exc} = 0.75 \text{ MW/cm}^2$ and are completely indistinguishable from the system noise by 3 MW/cm^2 . No clear redshift is observed in the excitonic positions as I_{exc} is increased from 0 MW/cm^2 . The spectra have been displaced vertically for clarity. The oscillatory structures at longer wavelengths are a result of thin film interference.

Nondegenerate Optical Pump-Probe Spectroscopy of InGaN Thin Films

In this section the results of nanosecond non-degenerate optical pump-probe absorption experiments on InGaN layers at zero time delay are presented. This study was initiated to help explain the drastic reduction of the stimulated emission threshold that results when indium is incorporated into GaN to form InGaN (see the last section of Chapter 4). Considerable differences in the effects of a strong optical pump on the band edge transitions are shown between InGaN and GaN thin films.

Motivation

The ternary group III nitride compound InGaN is of great technological importance for the development of high brightness UV, blue, green, and white light emitting diodes (LEDs) as its fundamental (direct) band gap has the potential to be tuned from that of GaN (in the near UV spectral region) to that of InN (in the red spectral region). It also holds great promise for the development of near UV, violet, and blue laser diodes [31]. Although high brightness LEDs [74] and cw violet laser diodes [75] have been demonstrated and marketed (in the case of LEDs), little is known concerning the effects of high free carrier concentrations on the fundamental band gap transitions of this material system. A fundamental understanding of the processes involved in the highly excited emission phenomena observed in this material is important for the development and optimization of commercial InGaN based blue laser diodes. To date, only femtosecond pump-probe transient transmission experiments studying the ultrafast carrier dynamics in the low excitation density regime (far from that required to achieve stimulated emission) have been performed on this material [77]. For this reason, nanosecond nondegenerate optical pump-probe absorption experiments have been performed on InGaN thin films in order to better understand the optical phenomena associated with high carrier concentrations (enough to result in population inversion and optical gain) in this material. The results of this study will be shown to differ greatly from the behavior observed for

GaN thin films, helping to explain the differences in their stimulated emission (SE) properties.

Experimental Technique and Results

The $\text{In}_{0.18}\text{Ga}_{0.82}\text{N}$ layer used in this study was grown by MOCVD at 800 °C on a 1.8 μm thick GaN layer deposited at 1060 °C on (0001) oriented sapphire. The $\text{In}_{0.18}\text{Ga}_{0.82}\text{N}$ layer was 0.1 μm thick and was capped by a 0.05 μm GaN layer. The average In composition was measured using high-resolution x-ray diffraction and assuming Vegards law. We note that the actual InN fraction could be smaller due to systematic overestimation when assuming Vegards law in this strained material system [86], [87]. The $\text{In}_{0.18}\text{Ga}_{0.82}\text{N}$ layer thickness given above is an estimation from the growth conditions.

The nanosecond nondegenerate optical pump-probe experimental system is illustrated in Fig. 51. The third harmonic (355 nm, 3.492 eV) of an injection seeded Nd:YAG (≈ 5 ns FWHM pulse width, 10 Hz repetition rate) was used to synchronously pump the $\text{In}_{0.18}\text{Ga}_{0.82}\text{N}$ layer and a UV-blue dye solution. The UV-blue fluorescence from the dye solution was collected and focused on the surface of the $\text{In}_{0.18}\text{Ga}_{0.82}\text{N}$ layer coincidental (spatially and temporally) with the pump beam. The broadband transmitted probe was then collected and focused on the slits of a 1/4 meter spectrometer and spectrally analyzed using a UV enhanced, gated CCD.

Figure 52 shows the 10K absorption spectra of the $\text{In}_{0.18}\text{Ga}_{0.82}\text{N}$ subjected to various excitation densities (I_{exc}) below and above the SE threshold (I_{th}). The stimulated emission peak position has been indicated for completeness. We note the absence of clear excitonic features in the unpumped absorption spectrum of the $\text{In}_{0.18}\text{Ga}_{0.82}\text{N}$ film. The absorption edge is seen to be considerable broader than that of the GaN films of the previous sections (~ 50 meV compared to ~ 30 meV for GaN). This is attributed to band tailing resulting from difficulties in uniform indium incorporation. Usually this would lead to a significant increase in the SE threshold. Instead, a reduction of over an order of magnitude in the SE threshold was observed for this film compared to high quality GaN and AlGaIn thin films (see the last section

of Chapter 4). This is a typical result of the incorporation of indium into GaN, the origin of which is still not well understood in the nitride scientific community. Clear bleaching of these band tail states is observed with increasing optical excitation, as shown in Fig. 52. For clarity, the changes in the absorption spectra with respect to the unpumped spectrum, $\Delta\alpha(I_{exc}) = \alpha(I_{exc}) - \alpha(0)$, are shown in Fig. 53 for the spectra given in Fig. 52. The maximum of the observed absorption bleaching occurs on the high energy side of the SE peak, originating approximately 65 meV above the SE peak position and blueshifting slightly with increasing optical excitation. No significant increases in the bleaching spectra were observed for excitation densities exceeding $\sim 2 \text{ MW/cm}^2$. The feature peaked at $\approx 2.955 \text{ eV}$ in the $\Delta\alpha$ spectra coincides spectrally with the SE peak and is attributed to optical gain, the magnitude of which (on the order of 10^3 cm^{-1}) is seen to be more than an order of magnitude smaller than the band edge bleaching. The band edge bleaching of the $\text{In}_{0.18}\text{Ga}_{0.82}\text{N}$ film, exceeding $-3 \times 10^4 \text{ cm}^{-1}$ at $I_{exc} = 2 \text{ MW/cm}^2$, is consistent with the bleaching behavior observed in GaN thin films. The $\text{In}_{0.18}\text{Ga}_{0.82}\text{N}$ film thickness estimated from the growth conditions was used in the calculation of α and $\Delta\alpha$ presented in this section. Some error from this estimation is expected, but the calculated values of $\alpha(0)$ agree well with those of GaN films. Similar behavior was observed at room temperature, as illustrated in Fig. 54 and Fig. 55. Again, no significant increases in the bleaching spectra were observed for excitation densities exceeding $\sim 2 \text{ MW/cm}^2$.

A striking difference between the absorption changes observed for the $\text{In}_{0.18}\text{Ga}_{0.82}\text{N}$ film and those observed for GaN films is the absence of the below-gap induced absorption observed in GaN films with increasing optical excitation. This is significant in that it explains, at least in part, the drastic reduction in the SE threshold observed in InGaN films relative to GaN films. This is explained here as resulting from the lack of induced absorption and gain competition that is exhibited in GaN films (see the first section of this chapter). The incorporation of indium into GaN to form InGaN has been observed by members of this research group and others to typically reduce or eliminate the presence of yellow band luminescence (YBL), and presumably the deep levels giving rise to it. This adds further credence to the theory

of their involvement in the formation of the below gap induced absorption observed in GaN thin films. A detailed study is currently under way to better understand the effects of YBL on the bleaching behavior of highly excited GaN, InGaN, and AlGaIn thin films.

Another difference in the bleaching behavior of the $\text{In}_{0.18}\text{Ga}_{0.82}\text{N}$ film compared to GaN films is the modest reduction in the absorption bleaching maximum as the temperature is increased from 10 K to room temperature. As the temperature is increased from 10 K to room temperature, the maximum in the bleaching spectrum reduces only slightly, from $\Delta\alpha \approx -3.4 \times 10^4 \text{ cm}^{-1}$ at 10K to $\approx -3.1 \times 10^4 \text{ cm}^{-1}$ at room temperature for $I_{exc} = 2 \text{ MW/cm}^2$. This differs greatly from the factor of almost three reduction observed in GaN films. This is attributed to a difference in the bleaching mechanisms between the two materials: excitonic screening for GaN and band tail state filling for InGaN. The bleaching spectra of the $\text{In}_{0.18}\text{Ga}_{0.82}\text{N}$ film at room temperature are significantly broader than those at 10K, showing a 50% increase in FWHM over the 10 K spectra.

Summary

Nanosecond nondegenerate optical pump-probe experiments have been performed at zero time delay on $\text{In}_{0.18}\text{Ga}_{0.82}\text{N}$ thin films to gain a better understanding of the optical phenomena associated with high carrier concentration in this material. Clear band tail state bleaching was observed with increasing optical excitation, reaching a maximum of approximately $3 \times 10^4 \text{ cm}^{-1}$ at 10 K and room temperature for an excitation density of 2 MW/cm^2 . Clear features in the differential absorption spectra are clearly seen in the spectral region stimulated emission is observed. These features are attributed to optical gain and are estimated to reach values as high as $2 \times 10^3 \text{ cm}^{-1}$ at both 10 K and room temperature for an excitation density of 2 MW/cm^2 (which exceeds the stimulated emission threshold by more than an order of magnitude). A striking difference between the evolution of the band edge of these InGaIn films compared to GaN films with increasing optical excitation is the complete absence of the induced absorption in the below-gap spectral region that

is typically observed in GaN thin films. This indicates that the high stimulated emission threshold of GaN films relative to InGaN films is due, at least in part, to competition between induced absorption and gain in the below-gap spectral region of GaN films. The large magnitudes of absorption bleaching observed in this work indicate that InGaN is also a suitable material for use in near UV-blue optical switching applications.

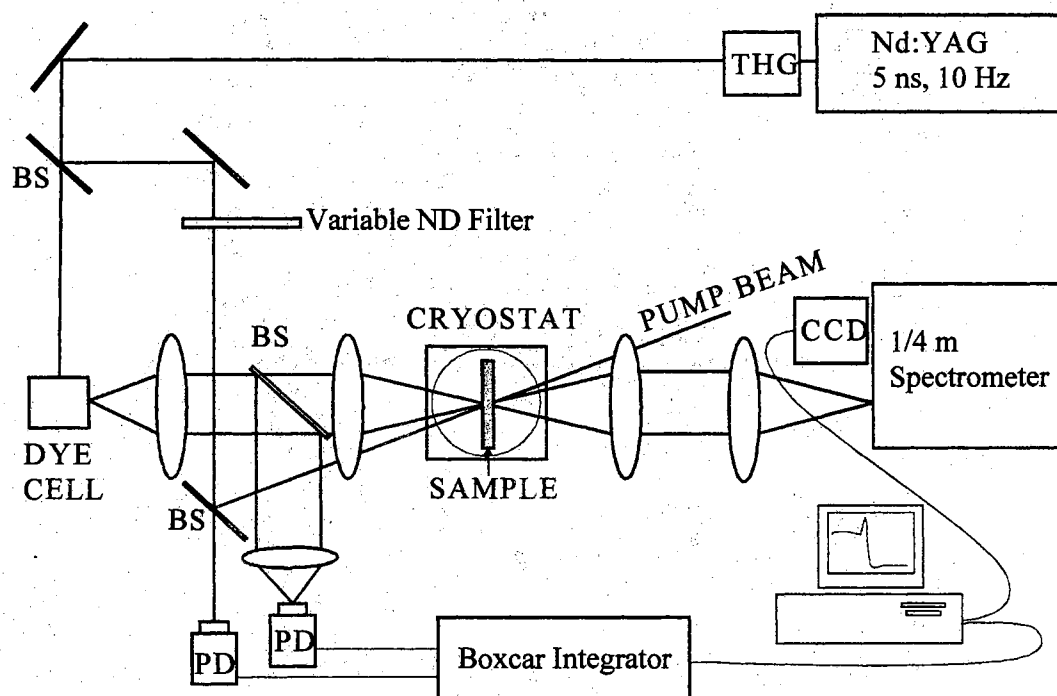


Figure 51. Nanosecond nondegenerate optical pump-probe absorption setup for zero time delay between the pump and probe pulses. THG, ND, BS, and PD refer to third harmonic generator, neutral density, beam splitter, and photodiode, respectively.

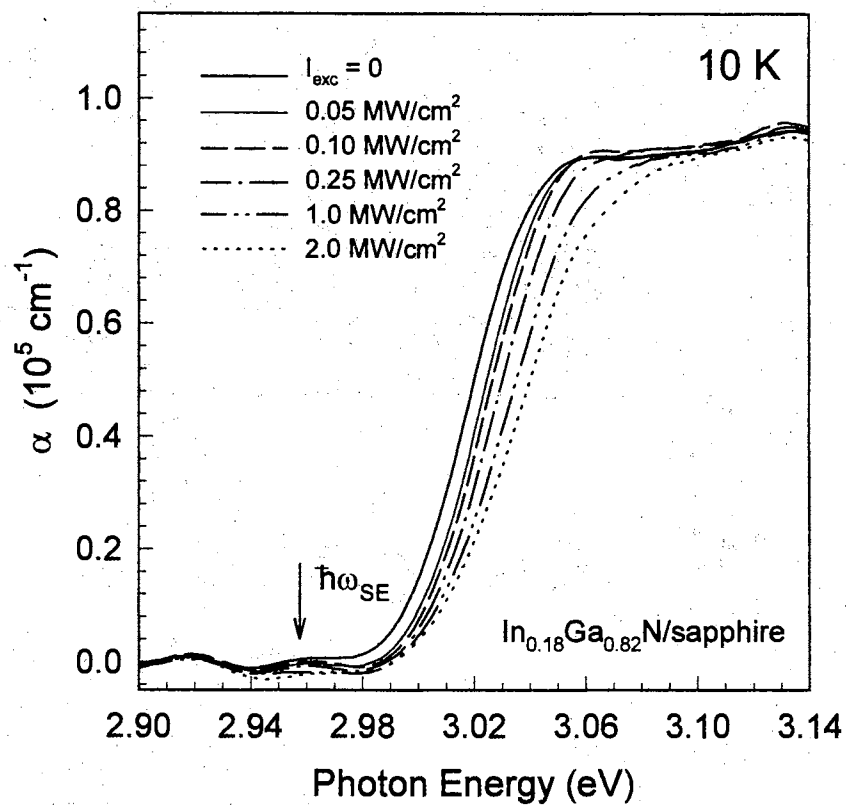


Figure 52. 10 K absorption spectra of a $0.1 \mu\text{m}$ thick $\text{In}_{0.18}\text{Ga}_{0.82}\text{N}$ layer near the fundamental band gap for several excitation densities above and below the stimulated emission threshold. The stimulated emission peak spectral position is indicated by the arrow for completeness.

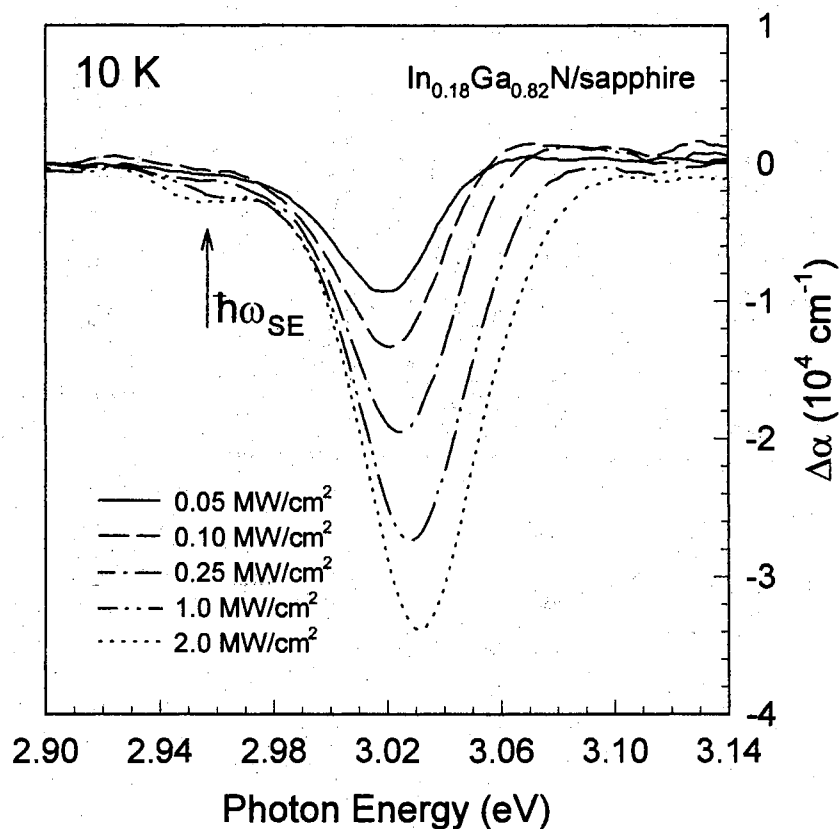


Figure 53. 10 K differential absorption spectra of a 0.1 μm thick $\text{In}_{0.18}\text{Ga}_{0.82}\text{N}$ layer near the fundamental band gap for several excitation densities above and below the stimulated emission threshold. The stimulated emission peak spectral position is indicated by the arrow for completeness. A clear feature attributed to optical gain is seen in the spectral region at which stimulated emission is observed.

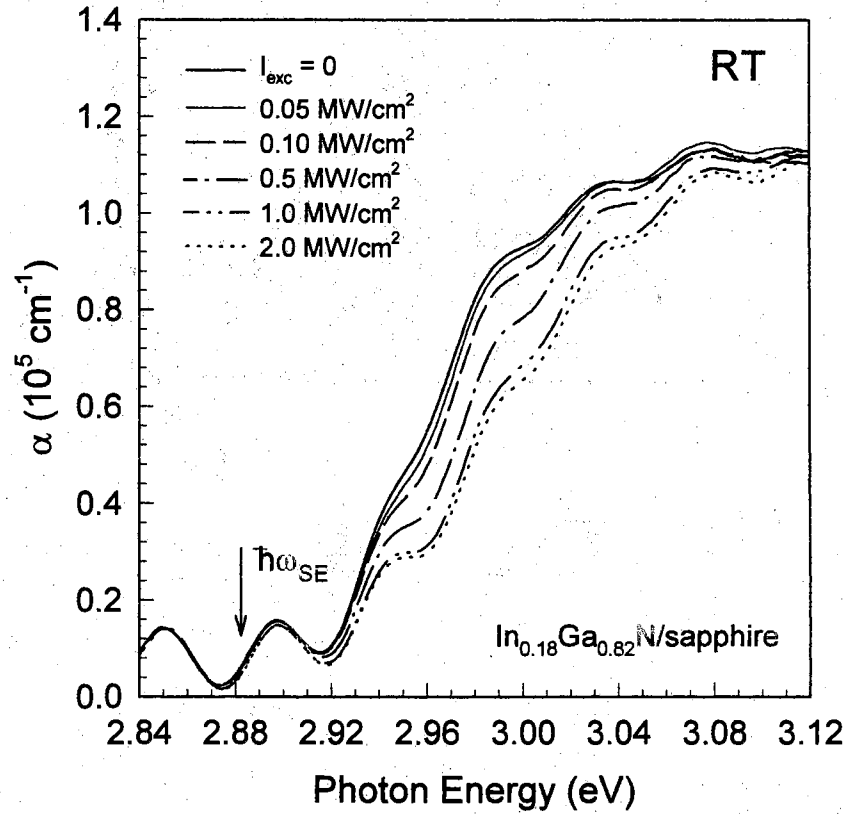


Figure 54. Room temperature absorption spectra of a $0.1 \mu\text{m}$ thick $\text{In}_{0.18}\text{Ga}_{0.82}\text{N}$ layer near the fundamental band gap for several excitation densities above and below the stimulated emission threshold. The stimulated emission peak spectral position is indicated by the arrow for completeness.

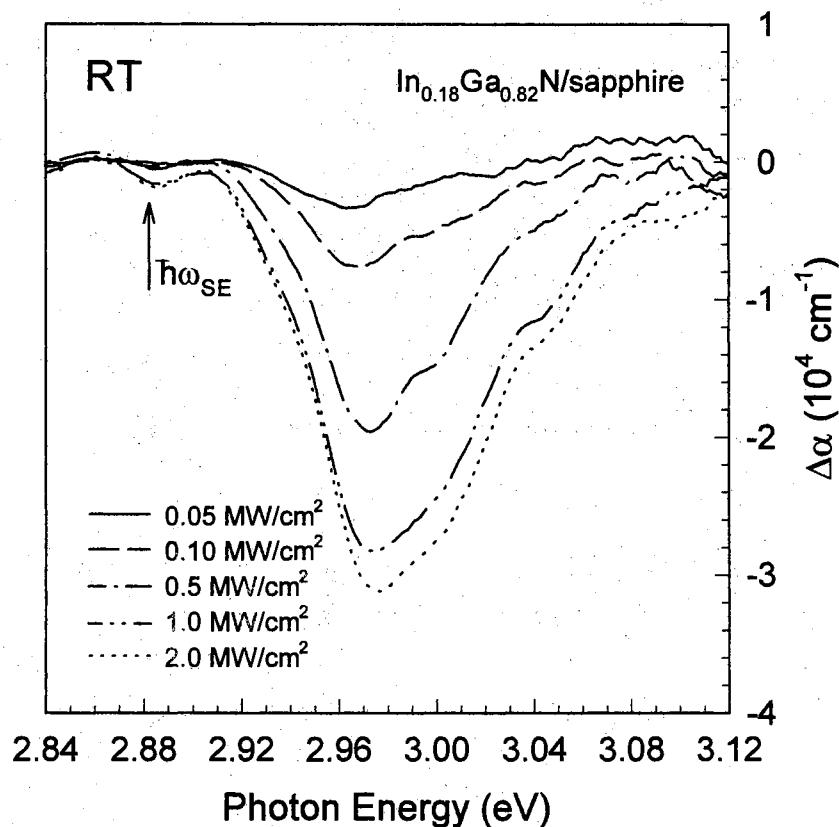


Figure 55. Room temperature differential absorption spectra of a $0.1 \mu\text{m}$ thick $\text{In}_{0.18}\text{Ga}_{0.82}\text{N}$ layer near the fundamental band gap for several excitation densities above and below the stimulated emission threshold. The stimulated emission peak spectral position is indicated by the arrow for completeness. A clear feature attributed to optical gain is seen in the spectral region at which stimulated emission is observed.

Summary

In this chapter the results of nanosecond nondegenerate optical pump-probe and single beam experiments on MOCVD-grown GaN films were presented. The evolution of the band edge was monitored in nondegenerate pump-probe experiments as the number of free carriers was increased by photo-excitation. Large optical nonlinearities in the region of the fundamental band gap were observed as the number of free carriers was increased by optical excitation to densities sufficient to observe stimulated emission. Exciton saturation was observed with increasing carrier concentration, with a resulting decrease in the absorption coefficient (induced transparency) approaching $\Delta\alpha = -4 \times 10^4 \text{ cm}^{-1}$ at 10 K and $-2 \times 10^4 \text{ cm}^{-1}$ at room temperature. In addition, large below-gap induced absorption exceeding $\Delta\alpha = 4 \times 10^4 \text{ cm}^{-1}$ at 10 K and $2 \times 10^4 \text{ cm}^{-1}$ at room temperature was observed as the pump density was increased to over 3 MW/cm^2 . The exciton saturation is explained by many body effects such as screening by excess free carriers. Nanosecond nondegenerate optical pump-probe transmission experiments with variable time delay between the pump and probe pulses showed the below-gap induced absorption to be a result of a large shift in the fundamental band gap to lower energy. This shift was found to increase across the pump pulse duration, reaching a maximum within 1 ns after the end of the pump pulse. The band edge was shown to slowly (on the order of 100 ns) recover to its pre-pumped position. The maximum shift in the band edge (at 5 ns delay) was found to exhibit saturation behavior with increasing optical excitation. Screening due to carriers trapped at deep levels is suggested as the mechanism for the shift in the band edge. Single-beam power dependent absorption experiments show enhanced absorption bleaching of the excitonic transitions for resonant excitation and a drastic reduction in the below-gap induced absorption. The experimental results indicate the states responsible for the induced absorption must first be created by the above-gap excitation of the pump beam and cannot be directly created by below-gap excitation. Nanosecond nondegenerate optical pump-probe absorption experiments were also performed on InGaN films for comparison. Induced transparency in the

band edge region was observed and attributed to the filling of band tail states with increasing optical excitation. The InGaN films did not exhibit induced absorption in the below-gap region. Instead, features in the differential absorption spectra were clearly seen in the spectral region where stimulated emission was observed. These features are attributed to optical gain. The fact that high quality InGaN films typically do not exhibit the yellow band luminescence typically observed from GaN films further suggests the deep levels responsible for yellow band luminescence in GaN contribute to the observed below-gap induced absorption through their screening properties. The work presented here helps explain the significant reduction in stimulated emission threshold that typically accompanies the incorporation of indium into GaN to form InGaN. This is explained here as being, in part, due to the suppression of these deep levels through an as of yet unknown process in InGaN. The high stimulated emission threshold of GaN is attributed to induced absorption and gain competition with increasing free carrier concentration. This work suggests the elimination of these deep levels in GaN is paramount to the development of GaN based near UV laser diodes. Similar problems are expected to plague AlGaN based UV laser diode development. The large values of induced transparency and absorption studied in this work suggest the potential of new optoelectronic applications, such as optical switching, for the group III nitrides.

CHAPTER VI

OPTICAL SPECTROSCOPY OF HIGHLY EXCITED InGaN/GaN MULTIPLE QUANTUM WELLS

Due to their technological relevance in the development of state-of-the-art blue laser diodes, the optical properties of InGaN/GaN multiple quantum wells (MQWs) under the conditions of strong optical pumping have been studied in detail to elucidate the origin(s) of stimulated emission (SE) and lasing in these materials. The SE behavior is shown to differ strongly from that of GaN and AlGaIn thin films. The origin of SE in InGaN/GaN MQWs is explored through the use of temperature dependent SE studies, excitation length dependent SE studies, energy selective optically pumped SE studies, variable-stripe gain spectroscopy, and nanosecond non-degenerate optical pump-probe spectroscopy. By combining the results of the above mentioned studies, we gain a broad overview and understanding of the behavior and origin of SE and lasing in these structures.

The InGaN/GaN MQW samples used in this work were grown by metalorganic chemical vapor deposition (MOCVD) on 1.8 μm thick GaN base layers using the precursors trimethylgallium (TMGa), trimethylindium (TMIn), trimethylaluminum (TMAI), and ammonia. Disilane was used as an n-type dopant. The GaN base layers were grown on (0001) sapphire substrates at a growth temperature of 1050 $^{\circ}\text{C}$. The growth temperature was reduced to 790 $^{\circ}\text{C}$ during the growth of the MQW region. The TMGa and TMIn flows during InGaN well and GaN barrier growth were 5 $\mu\text{mol}/\text{min}$ and 14 $\mu\text{mol}/\text{min}$, respectively. The disilane flow was varied between 0 and 2 nmol/min . The ammonia flow was held constant at 0.35 mol/min . The GaN barriers were doped with Si in the concentration range of 1×10^{17} to $3 \times 10^{19} \text{ cm}^{-3}$ for

the different samples studied. The MQW region consisted of 12 InGaN/GaN quantum wells with 3 nm InGaN wells and 4.5 nm GaN barriers. The MQW structures were capped with 100 nm $\text{Al}_{0.07}\text{Ga}_{0.93}\text{N}$ layers grown at 1040 °C. A detailed description of the growth conditions is given elsewhere [88], [89]. The sample structure is illustrated in Fig. 56. In order to evaluate the interface quality and structural parameters, such as the average In composition of the MQW structure and the period of the superlattice, the samples were analyzed with a 4-crystal high-resolution x-ray diffractometer (HRXRD) using $\text{Cu } K\alpha_1$ radiation. The angular distances between the satellite superlattice diffraction peaks and GaN (0002) reflections were obtained by ω - 2θ scans. The spectra clearly showed higher-order satellite peaks indicating high interface quality and good layer uniformity. The average indium composition in the wells was estimated to be $\approx 20\%$. The details of this x-ray analysis are reported elsewhere [90].

A general property of the MQWs used in this study was a large blueshift of the spontaneous emission with increasing optical excitation (see Fig. 57). This can be due to two different processes, both of which have been reported to be dominant in InGaN MQWs: (1) Bandfilling of localized states, and (2) Screening of the internal piezoelectric field. The latter can be disregarded from future consideration by considering that at the highest Si doping concentration ($3 \times 10^{19} \text{ cm}^{-3}$) of the barriers, the excess carriers should effectively screen the piezoelectric field. If this is the case, a systematic decrease in the excitation density induced blueshift should be observed with increasing Si doping of the barriers. Fig. 57 shows that this is clearly not the case. In fact, the blueshift is seen to be independent of Si doping concentration. This leaves bandfilling of localized states as the dominant mechanism for the blueshifting behavior with increasing optical excitation.

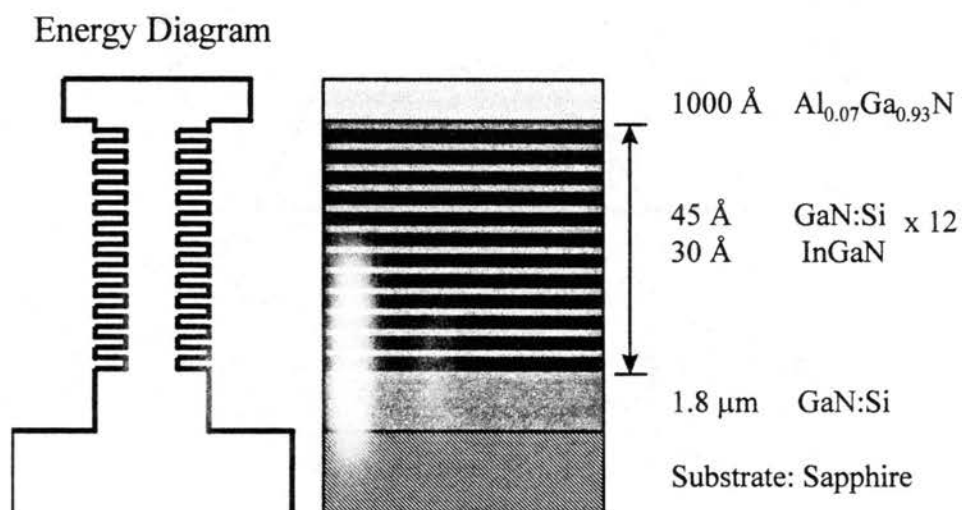


Figure 56. Schematic of the InGaN/GaN MQW structures used in this study.

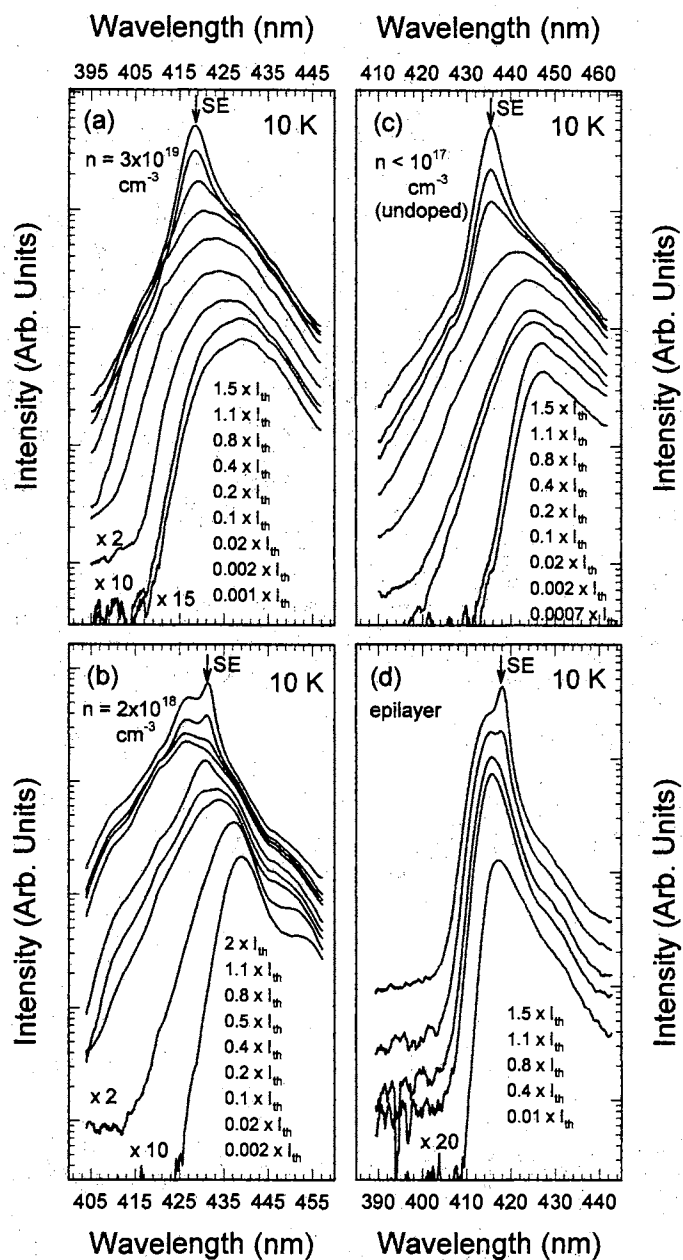


Figure 57. Evolution of emission from InGaN/GaN MQWs with increasing optical excitation for (a) $n = 3 \times 10^{19} \text{ cm}^{-3}$ (b) $n = 2 \times 10^{18} \text{ cm}^{-3}$ (c) $n < 1 \times 10^{17} \text{ cm}^{-3}$ Si doping concentration in the GaN barrier layers. (d) Shows the same for an InGaN reference layer of similar indium concentration. I_{th} is defined as the stimulated emission threshold for the respective samples.

Temperature Dependence of SE from InGaN/GaN MQWs

Stimulated emission (SE) in optically pumped InGaN/GaN multiple quantum well (MQW) structures grown by metalorganic chemical vapor deposition was observed and studied over the temperature range of 10-575 K. The GaN barriers were intentionally doped with different Si concentrations ranging from 1×10^{17} to $3 \times 10^{19} \text{ cm}^{-3}$. The effects of this Si doping on the optical properties of the highly excited InGaN/GaN MQWs were investigated. The SE threshold was measured as a function of temperature and compared with bulk GaN. The SE thresholds were found to be more than an order of magnitude lower than typical high quality MOCVD-grown GaN layers. The low SE thresholds are attributed to high quantum efficiencies of the MQWs due to the suppression of nonradiative channels by the localization of carriers at large potential fluctuations in the InGaN active layers. A characteristic temperature of 162 K was derived from the temperature dependence of the SE threshold. The integrated emission intensity versus pumping density was also examined for the above mentioned temperature range. This study shows that InGaN/GaN MQWs have very different emission mechanisms than GaN films. They are also shown to be suitable for the development of laser diodes and other optoelectronic devices required to operate well above room temperature.

Motivation

The group III-nitrides have attracted considerable interest due to their potential applications for light emitting devices [74], solar-blind detectors [91], and high-power microwave devices [92]. GaN-based structures have been shown to be chemically stable and able to withstand high temperatures [56], [93]. The low temperature sensitivity of the lasing threshold in ridge-geometry InGaN multi-quantum well (MQW) structures [94] near room temperature (RT) compared to conventional III-V [54], [95] and II-VI [55], [96] based structures prompts further research towards high temperature applications for group III nitride MQWs. Some preliminary above room temperature experiments on bulk GaN grown on sapphire and SiC [56], [93],

as well as theoretical predictions of their temperature sensitivity [97], have been published, but, to our knowledge, there are no reported studies on stimulated emission (SE) or lasing in InGaN/GaN/AlGaN-based heterostructures for temperatures above 80 °C. In this section, we report the results of an experimental study on SE in optically pumped InGaN/GaN MQW samples in the temperature range of 10-575 K. Narrow SE peaks with less than 0.1 nm full-width at half maximum (FWHM) were observed throughout the temperature range. The SE threshold was measured as a function of temperature, from which a characteristic temperature of 162 K was derived. The effects of Si doping on the luminescence intensity and SE threshold density of InGaN/GaN MQWs were evaluated experimentally. The dependence of the integrated emission intensity on pumping density for the entire temperature range was also determined. The experimental results presented here show InGaN based MQW structures are particularly well suited for use in opto-electronic devices required to operate at high temperatures.

Experimental Technique and Results

In this study, the third harmonic (355 nm) of an injection-seeded Nd:YAG laser with a pulse width of 6 ns and a repetition rate of 30 Hz was used to optically excite the MQW samples in an edge-emission geometry. The laser beam was focused to a line on the sample surface using a cylindrical lens and the emission was collected from one edge, coupled into a 1-meter spectrometer, and spectrally analyzed using a UV enhanced optical multi-channel analyzer. The laser light intensity was precisely varied using a continuously graded neutral density filter wheel. For the majority of this work, the samples were mounted on a copper heat sink attached to a wide temperature range cryostat/heater system (MMR Technologies Inc., model U220-3), allowing the sample temperature to be varied from 80-575 K. When lower temperatures were required, a conventional closed cycle refrigerator was used.

The effects of Si doping on the optical properties of bulk GaN [98], [99], InGaN/GaN [100], [101] and GaN/AlGaN [102] MQWs have recently been studied in the low excitation regime by a number of authors. In this section, the results of

a study on the effects of Si doping on the optical properties of highly excited InGaN/GaN MQW structures are presented. Only moderate concentrations of Si were observed to lead to an increase the luminescence intensity and a reduction in the SE threshold (I_{th}) for the InGaN/GaN MQWs used in this study. The dependence of the SE threshold (at room temperature) on the Si doping concentration of the MQWs is shown in Fig. 58. The maximum luminescence intensity and lowest SE threshold ($I_{th} = 55 \text{ kW/cm}^2$ at RT) were observed for the sample with a Si concentration of $2 \times 10^{18} \text{ cm}^{-3}$ in the barrier layers. Further increases in Si concentration were observed to result in significant increases in the SE threshold, as shown in Fig. 58. This threshold is more than an order of magnitude lower than that of typical high quality nominally undoped single-crystal GaN films measured under the same experimental conditions. We will concentrate on the emission behavior of this particular MQW sample for the remainder of this section.

Figure 59 shows the emission spectra at various temperatures and excitation powers from the InGaN/GaN MQW sample with a Si doping concentration of $2 \times 10^{18} \text{ cm}^{-3}$ in the GaN barriers. The dotted lines represent the spontaneous emission spectra (also collected from the sample edge) for pumping densities approximately half that of the SE threshold at each respective temperature. Spontaneous emission in InGaN MQWs has recently been attributed to the recombination of carriers localized by large potential fluctuations in the quantum well active regions [66], [67]. We will see in the following sections that SE originates from these localized carriers also. As we raise the excitation power density above the SE threshold, a considerable spectral narrowing occurs (solid lines in Fig. 59). The emission spectra are comprised of many narrow peaks of less than 0.1 nm FWHM, which is on the order of our instrumentation resolution. The major effect of the temperature change from 200 K (Fig. 59a) to 450 K (Fig. 59c) is seen to be a shift in the spontaneous and stimulated emission peaks to lower energy. No noticeable broadening of SE peaks FWHM was observed when the temperature was varied from 10-575 K.

The temperature dependence of SE threshold is shown in Fig. 60 (solid dots) for the temperature range from 175-575 K. SE was observed throughout the entire

temperature range studied, from 10 K to 575 K. The SE threshold was measured to be approximately 25 kW/cm² at 175 K, 55 kW/cm² at 300 K, and 300 kW/cm² at 575 K. It was found to roughly follow an exponential dependence on the excitation density in this temperature range. The low SE thresholds are most likely a result of carrier localization at (large) potential fluctuations in the InGaN active regions. The solid line in Fig. 60 represents the best result of a least-squares fit of the experimental data to the empirical formula:

$$I_{th}(T) = I_0 \exp(T/T_c) \quad (36)$$

for the temperature dependence of the SE threshold. The characteristic temperature (T_c) for this sample was estimated to be 162 K in the temperature range of 175-575 K. This value of T_c is consistent with that of the base material, GaN, in this temperature range (see Chapter 4). A high value of T_c indicates a low temperature sensitivity of the SE threshold. The characteristic temperature measured here is considerably larger than the near RT characteristic temperatures reported for laser structures based on conventional III-V [54], [95] and II-VI [55], [96] materials. This high temperature sensitivity is a strong limiting factor for high temperature operation in conventional III-V and II-VI laser structures. Such a low sensitivity of the SE threshold with increasing temperature in InGaN/GaN MQWs opens up enormous opportunities for high-temperature laser diode applications.

As the temperature was increased from 10 K, the PL intensity was observed to decrease, indicating the increased dominance of nonradiative recombination channels which result in a decrease in the MQWs quantum efficiency. At high temperatures, only a small fraction of the photo-generated free carriers relax to the conduction band minima due to this increasing competition with nonradiative recombination processes. To better understand how nonradiative recombination processes affect the SE process, the integrated photoluminescence intensity was studied as a function of excitation power for different temperatures, as shown in Fig. 61. Under low excitation densities, the integrated intensity (I_{integ}) increases nearly linearly with increasing excitation density, I_{exc} (*i.e.* $I_{integ} \propto I_{exc}^\beta$, where $\beta = 0.8-1.3$). At high

excitation densities, this dependence becomes superlinear (*i.e.* $I_{integ} \propto I_{exc}^\beta$, where $\beta = 2.2-3.0$). The excitation density at which the slope of I_{integ} changes from nearly linear to superlinear corresponds to the SE threshold. Interestingly, the slopes of I_{integ} below and above the stimulated emission threshold do not significantly change over the temperature range involved in this study. This is in contrast to what is observed from GaN layers (see Chapter 4) and indicates that the SE mechanism remains the same for these structures as we raise the temperature from cryogenic temperatures to hundreds of degrees above RT. This is also indicated by the lack of an increase in the FWHM of the SE lines as we increase the temperature over this wide range.

Summary

In conclusion, the effects of Si doping in the GaN barriers on the highly excited optical properties of InGaN/GaN MQWs were characterized. Stimulated emission from optically pumped InGaN/GaN MQWs was studied over the wide temperature range of 10-575 K. The SE threshold was measured as a function of temperature and a characteristic temperature of 162 K was derived for the temperature range from 175-575 K. The integrated emission intensity versus pumping density was also measured at various temperatures in this range. The slopes of the integrated emission intensity below and above the stimulated emission threshold were found to be insensitive to changes in temperature, indicating the SE mechanism does not change with increasing temperature. The general SE behavior (both the FWHM of the SE peaks and the dependence of I_{integ} on I_{exc}) was observed to be independent of temperature from 10 K to 575 K, further indicating the SE mechanism does not change over this wide temperature range. The low stimulated emission threshold and weak temperature sensitivity of the stimulated emission threshold make InGaN/GaN multiple quantum well structures attractive materials for the development of laser diodes that can operate substantially above room temperatures.

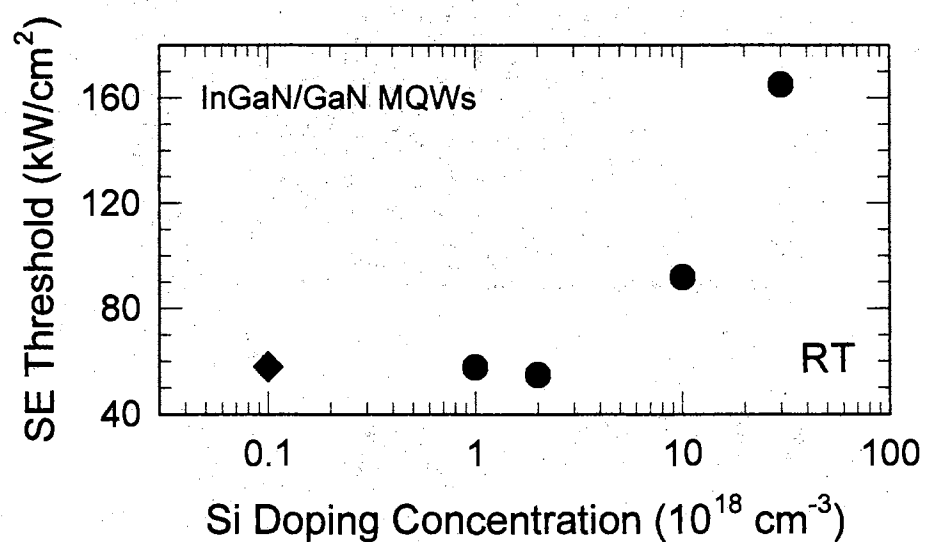


Figure 58. Room temperature stimulated emission threshold as a function of Si doping concentration in the GaN barriers of InGaN/GaN MQWs. The solid circles represent Si concentrations measured by SIMS. The solid diamond represents a Si doping concentration of $< 1 \times 10^{17} \text{ cm}^{-3}$ obtained from Hall measurements.

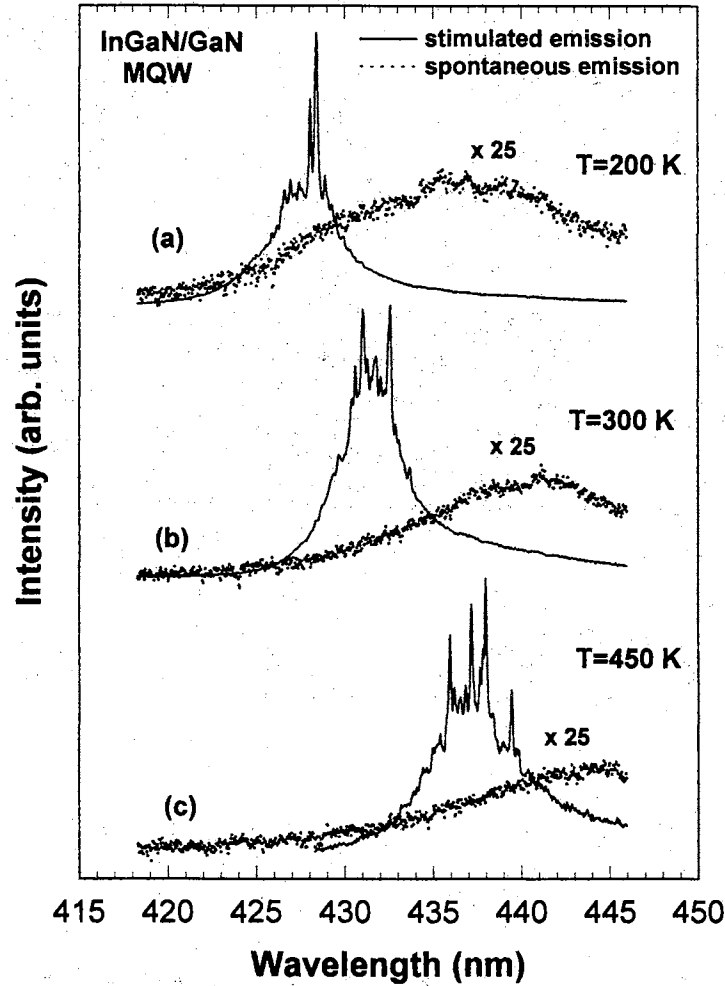


Figure 59. Emission spectra for an InGaN/GaN MQW sample with a Si doping concentration of $2 \times 10^{18} \text{ cm}^{-3}$ in the GaN barriers at: (a) 200 K, (b) 300 K, and (c) 450 K. The spontaneous emission spectra (dotted lines) were taken under an excitation density of $0.5 \cdot I_{th}$. The SE spectra were obtained with a pump density of $2 \cdot I_{th}$, where I_{th} represents the SE threshold for a given temperature. Adapted from [65].

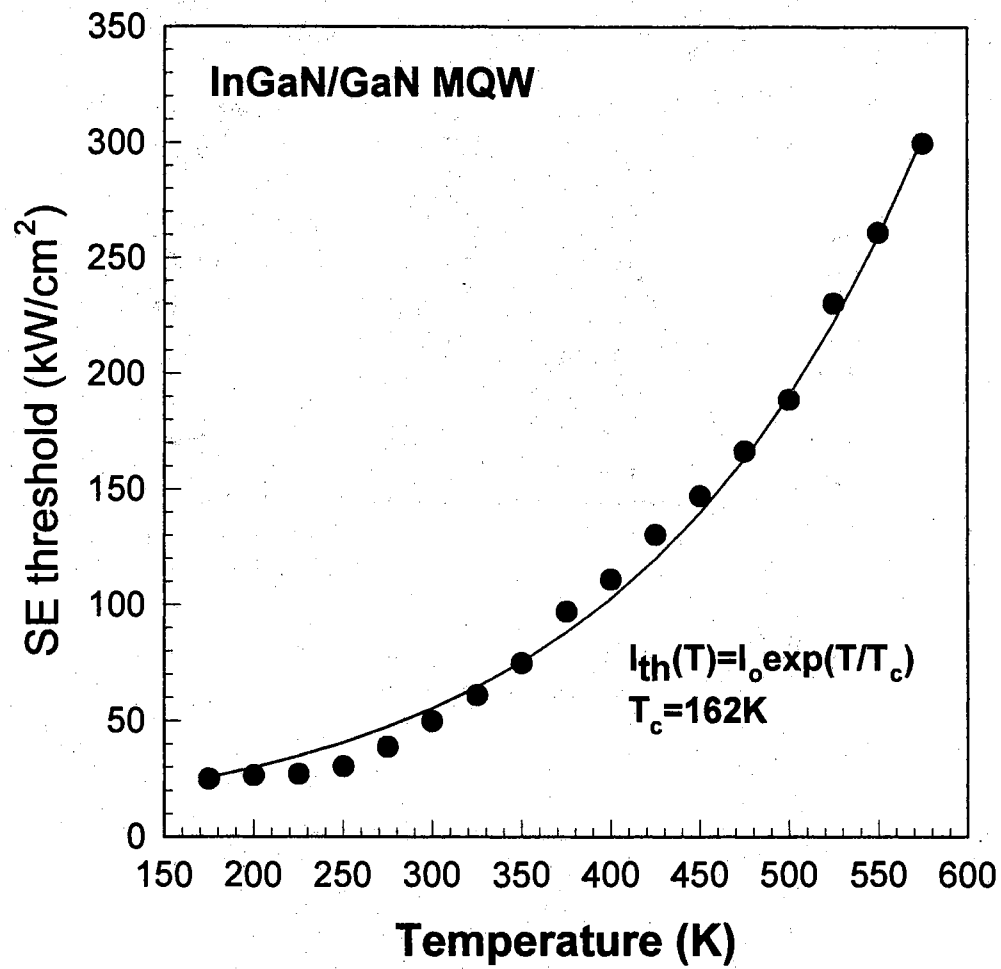


Figure 60. Temperature dependence of the SE threshold in the temperature range of 175-575 K for the InGaN/GaN MQW sample shown in Fig. 59. The solid line represents the best result of a least-squares fit to the experimental data (solid dots). A characteristic temperature of 162 K is derived from the fit. Adapted from [65].

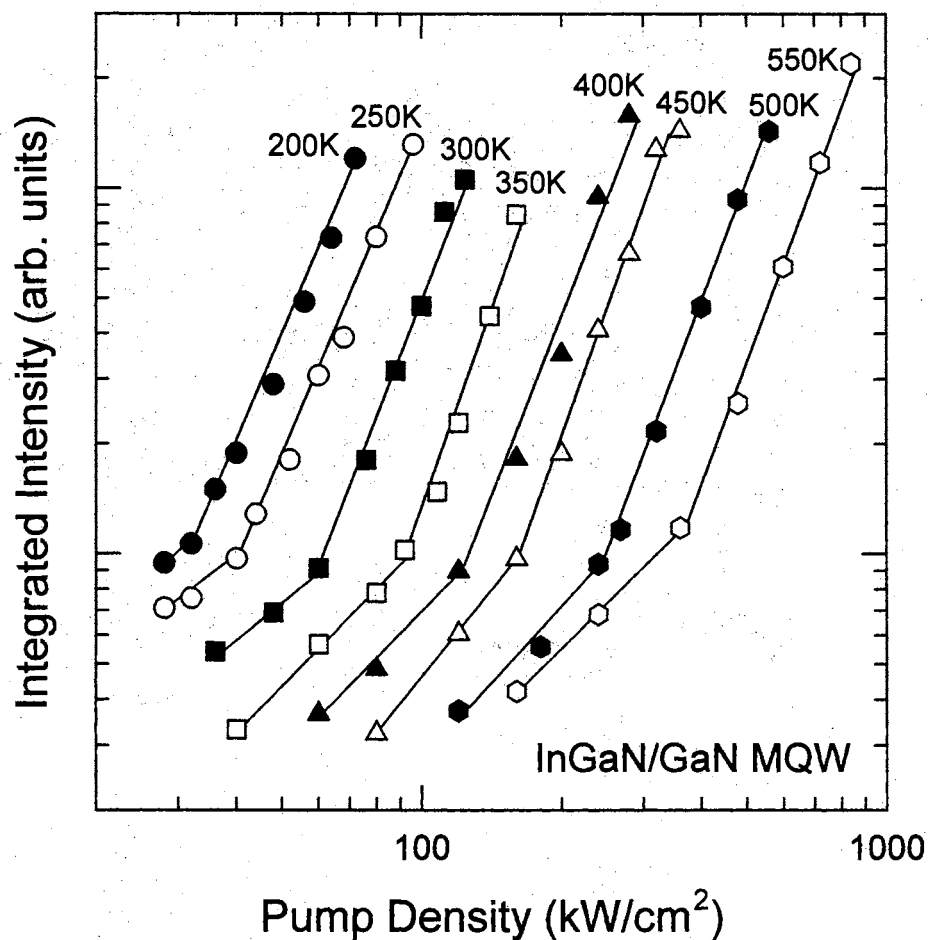


Figure 61. Integrated intensity of InGaN/GaN MQW emission as a function of pump density at various temperatures. The slope change from 0.8-1.3 to 2.2-3.0 indicates the transition from spontaneous emission to stimulated emission. The solid lines are given only as guides for the eye. Adapted from [65].

Excitation Length Dependent Studies of Optically Pumped SE from InGaN/GaN MQWs

Optically pumped stimulated emission (SE) from InGaN/GaN multiple quantum wells (MQWs) grown by metalorganic chemical vapor deposition has been systematically studied as a function of excitation length (L_{exc}). Two distinct SE peaks were observed from these structures: one that originates at 425 nm at 10 K (430 nm at 300 K) and another that originates at 434 nm at 10 K (438 nm at 300 K) for the $n = 2 \times 10^{18} \text{ cm}^{-3}$ MQW sample. The SE threshold for the high energy peak was observed to always be lower than that of the low energy peak, but the difference was found to decrease greatly with increasing L_{exc} . A detailed study of the emission intensity of these two SE peaks as a function of excitation density shows that the two peaks compete for gain in the MQW active region.

Motivation

GaN-based semiconductors and related heterostructures are attracting an ever-increasing amount of attention due to their large direct band gaps, which make them promising materials for UV-blue-green light emitting devices [74], [103], solar-blind UV detectors [91], and high power and high temperature devices [92], [56], [65]. In particular, the realization of high brightness blue and green light emitting diodes [74] and cw blue laser diodes [103] based on InGaN/GaN multiple quantum wells (MQWs) has focused the efforts of many research groups on these structures. Although a considerable amount of research has been conducted on the optical properties of these materials, there is still much left unknown about the optical processes associated with stimulated emission (SE) and lasing. To aid in a fundamental understanding of the processes leading to optical gain in these structures, excitation length dependent studies of optically pumped SE have been performed and illustrate dramatically different SE behavior for changes in the experimental conditions that would typically be insignificant in other semiconductor materials.

Recently, a considerable amount of attention has been given to the potential role of strongly localized band tail states on the SE and lasing processes in InGaN MQWs [104], [105], [66], [106], [107], [108]. Although there exists a sizable amount of data to support localized carrier recombination as the mechanism leading to spontaneous emission in these materials [66], [106], [109], [67], the results for SE behavior in the literature are varied and often contradictory. This has led some research groups to assign the spontaneous emission peak to recombination of localized carriers, and the SE peak to a more traditional recombination mechanism, that of an electron-hole plasma originating from free carriers [110], while others claim that strongly localized carriers are the origin of both spontaneous and stimulated emission [106], [107], [108]. With the recent observation of two different SE peaks from InGaN/GaN MQWs grown by Nichia Chemical Industries [108] we see the possibility that some of the varied results reported in the literature may stem from slightly different experimental conditions, which are shown here to result in significant changes in the SE behavior. We report the results of a detailed study of the SE behavior of these two SE peaks as a function of excitation length (L_{exc}) and excitation density (I_{exc}) and illustrate dramatically different SE behavior in InGaN MQWs for relatively small changes in the experimental conditions. The observation of these two distinct SE peaks from InGaN/GaN MQWs grown under different conditions by separate research groups suggests this SE behavior is a general property of present state-of-the-art InGaN based blue laser diodes. As such, a better understanding of the SE and lasing behavior of these structures is important for the development and optimization of future laser diode structures.

Experimental Technique and Results

In this set of experiments, the InGaN MQWs were again optically pumped in an edge emission geometry by the third harmonic of an injection seeded Nd:YAG (yttrium aluminum garnet) laser (355 nm, 30 Hz, ~ 6 ns pulse width). The excitation beam was focused to a line on the sample using a cylindrical lens and the excitation length was varied using a mask connected to a computer controlled stepper motor.

The emission was collected from one edge of the sample, coupled into a 1-meter spectrometer, and spectrally analyzed using a UV enhanced optical multi-channel analyzer. For clarity, we will concentrate in this section on the optical properties of the InGaN/GaN MQW with $n = 2 \times 10^{18} \text{ cm}^{-3}$ Si doping in the GaN barriers.

Typical power dependent emission spectra at 10 K are shown in Fig. 62 for $L_{exc} = 1,300 \text{ } \mu\text{m}$. At low I_{exc} , we observe a broad spontaneous emission peak peaked at $\approx 441 \text{ nm}$, consistent with low power cw photoluminescence (PL) spectra. As I_{exc} is increased, a new peak emerges at $\approx 428 \text{ nm}$ [designated here as SE peak (1)] and grows superlinearly with increasing I_{exc} . If we continue to increase I_{exc} , we observe another new peak at $\approx 433 \text{ nm}$ [designated here as SE peak (2)] which also grows superlinearly with increasing I_{exc} . SE peak (1) is observed to be the (time averaged) statistical distribution of a multitude of narrow ($< 0.1 \text{ nm FWHM}$) peaks, as illustrated in the inset of Fig. 62. No significant broadening of these narrow emission lines in SE peak (1) was observed as the temperature was tuned from 10 K to over 500 K. The behavior of SE peak (1) was the subject of the previous section. SE peak (2) is observed to always be considerably narrower than (time averaged) SE peak (1). Both SE peaks are seen to originate on the high energy side of the low power spontaneous emission peak (given by the dashed line in Fig. 62). Both SE peaks were found to be highly TE polarized, with a TE to TM ratio of ~ 200 . SE peak (2) has been the subject of extensive experiments performed by the author and has been attributed to stimulated recombination of localized states through the use of energy selective optically pumped SE studies showing “mobility edge” type behavior in the SE spectra as the excitation photon energy is varied [68], and through nanosecond non-degenerate optical pump-probe experiments showing the onset of SE has a direct impact on the bleaching dynamics of the band tail states in these samples [69]. These studies are described in detail in the following sections of this chapter.

Figure 63 shows the SE thresholds (I_{th}) of SE peaks (1) and (2) as a function of L_{exc} . We note that I_{th} for SE peak (2) is larger than that of SE peak (1) for all excitation lengths employed, but approaches that of SE peak (1) with increasing L_{exc} in an asymptotic fashion. The high SE threshold of peak (2) with respect to peak (1)

and its increased presence for longer L_{exc} indicate that it is a lower gain process than that of peak (1).

Figure 64 shows the peak positions of SE peak (1) and SE peak (2) as a function of L_{exc} at 10 K. For L_{exc} less than $\sim 500 \mu\text{m}$, only SE peak (1) is observed. It has a peak emission wavelength of $\approx 425 \text{ nm}$ (430 nm) and a SE threshold of $\approx 100 \text{ kW/cm}^2$ (475 kW/cm^2) at 10 K (300 K). As I_{exc} is increased and/or L_{exc} is increased, a new SE peak [SE peak (2)] at 434 nm (438 nm at RT) emerges. The peak positions were measured for I_{exc} fixed relative to the SE thresholds of the respective peaks; *i.e.* $I_{exc} = 2 \times I_{th}$. As L_{exc} is increased, SE peak (1) shifts to longer wavelengths (due to a re-absorption process), while the peak position of SE peak (2) is observed to be weakly dependent on L_{exc} . The apparent blueshift of SE peak (2) with increasing L_{exc} seen in Fig. 64 is a result of the experimental conditions. Since the SE threshold of SE peak (2) is a strong function of L_{exc} , the peak positions shown for small L_{exc} are for I_{exc} considerably higher than for large L_{exc} . The slight redshift of SE peak (2) with increasing I_{exc} due to many-body effects and lattice heating (see Fig. 62) then manifests itself as the apparent blueshift seen in Fig. 64. The same phenomenon is observed at room temperature, as shown in the inset of Fig. 64. The redshift of SE peak (1) with increasing L_{exc} can be explained by gain and absorption competition in the “soft” absorption edge of the InGaN active regions, where gain saturation with longer L_{exc} combined with the background absorption tail leads to the observed redshift. The fact that SE peak (2) does not experience a re-absorption induced redshift with increasing L_{exc} is explained by the significant reduction of the absorption tail in this spectral region, as shown in the inset of Fig. 65. The gain saturation behavior of SE peak (1) is consistent with the observation of Kuball *et al.* [111] of a high gain mechanism in the band tail region of MQWs with similar active regions. The large spectral range exhibiting gain is explained by compositional fluctuations inside the active region. The redshift of SE peak (1) with increasing L_{exc} is consistent with observations of a redshift in the optical gain spectrum with increasing L_{exc} reported by Mohs *et al.* [112]. It is also consistent with the observation by Nakamura [113] that the external quantum efficiency of

his cw blue laser diodes decreases with increasing cavity length. These similarities, combined with the relatively low SE threshold of SE peak (1) with respect to SE peak (2) and its similar spectral position with laser emission from diodes of similar structure [114], suggests that lasing in current state-of-the-art cw blue laser diodes originates from the gain mechanism responsible for SE peak (1). The microscopic origin of this gain is the subject of continuing research, but is shown here to be different than the localized state recombination responsible for SE peak (2). Its origin may lie in an entirely different degree of carrier localization, such as found in self-formed quantum dots. Further experiments are needed to clarify this issue.

The dependence of the emission intensity of peaks (1) and (2) on I_{exc} is shown in Fig. 65 for $L_{exc} = 1,300 \mu\text{m}$ at 10 K. The emission of peak (1) increases in a strongly superlinear fashion ($\approx I_{exc}^{3.8}$) until the SE threshold of peak (2) is reached, at which point it turns linear, indicating that peak (2) competes for gain with peak (1). This is most likely a result of competition for carriers or re-absorption of the emitted photons. The presence of SE peak (2) is, therefore, seen to be deleterious to SE peak (1). The same process is observed at room temperature and for various excitation lengths. This gain competition may limit this materials performance in high power laser diode applications, where increased driving current and/or longer cavity lengths may result in a shift in the dominant gain mechanism and a drastic change in the emission behavior.

Summary

In summary, the dependence of stimulated emission on excitation length in MOCVD grown InGa_N/Ga_N MQW structures has been studied. Two distinctly different SE peaks were observed with different dependencies on excitation length. The high energy SE peak exhibits a strong redshift with increasing excitation length due to competition between an easily saturable gain mechanism and a background absorption tail. The lower energy SE peak does not exhibit this re-absorption induced redshift with increasing excitation length. The presence of the lower energy SE peak

has been shown to be detrimental to the higher energy SE peak due to gain competition in the InGaN active region. This competition may prove to be an obstacle in the design of InGaN based high power laser diodes, where high current densities and/or long cavity lengths can lead to a shift in the dominant gain mechanism and a change in the emission characteristics.

The previous two sections have demonstrated that the SE behavior of the InGaN/GaN MQWs does not change as a function of temperature, even as we increase the temperature from 10 K to 575 K. We will, therefore, concentrate on experiments performed at 10 K in the following sections. At 10 K the processes involved will be at their clearest due to the minimization of thermal effects on the recombination processes. At higher temperatures (i.e. room temperature), the involved phenomena may be obscured due to the increased presence of thermal effects and related non-radiative recombination processes. The arguments presented at 10 K should directly apply at higher temperatures.

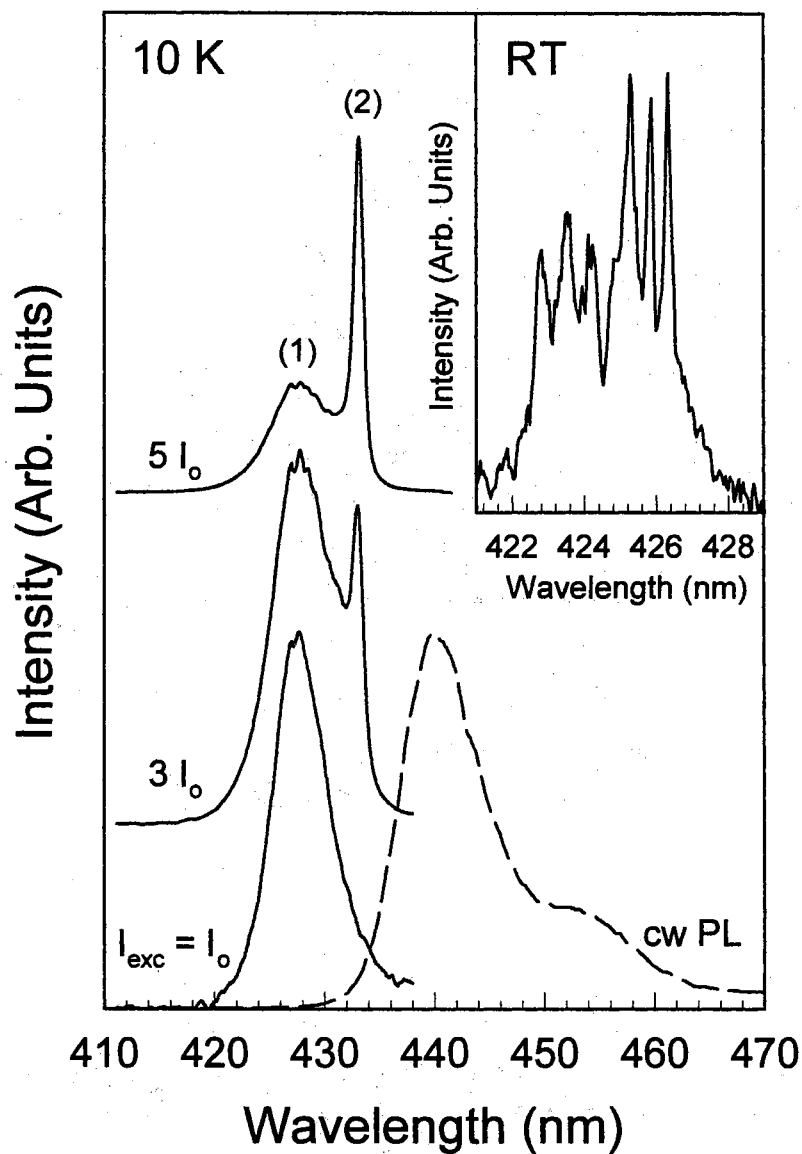


Figure 62. 10 K SE spectra (solid lines) from an InGaN/GaN MQW subjected to several different excitation densities. $I_0 = 100 \text{ kW/cm}^2$. The low power cw spontaneous emission spectrum is also shown (dashed line). The spectra have been normalized and displaced for clarity. The inset shows a short accumulation time spectrum of SE peak (1) at room temperature.

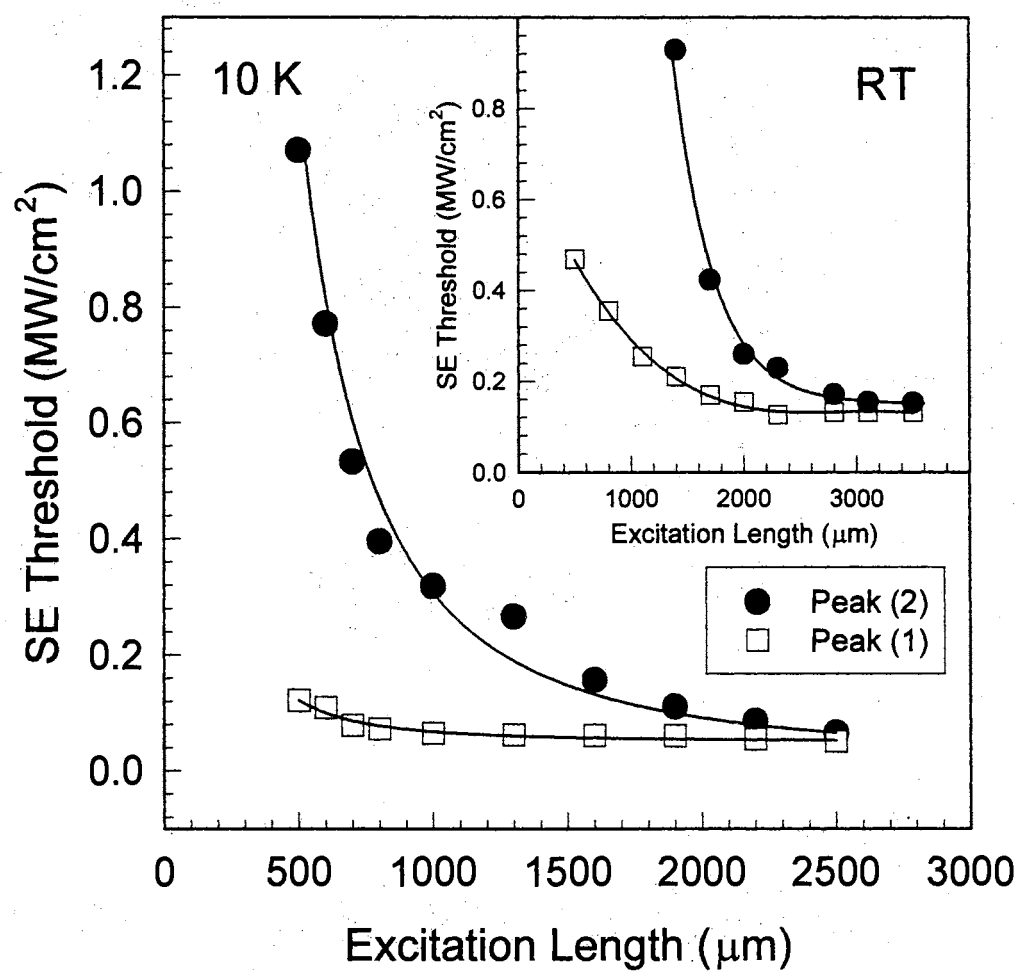


Figure 63. SE threshold as a function of excitation length for SE peaks (1) and (2) at 10 K. The inset gives the values obtained at room temperature. The solid lines are given only as guides for the eye.

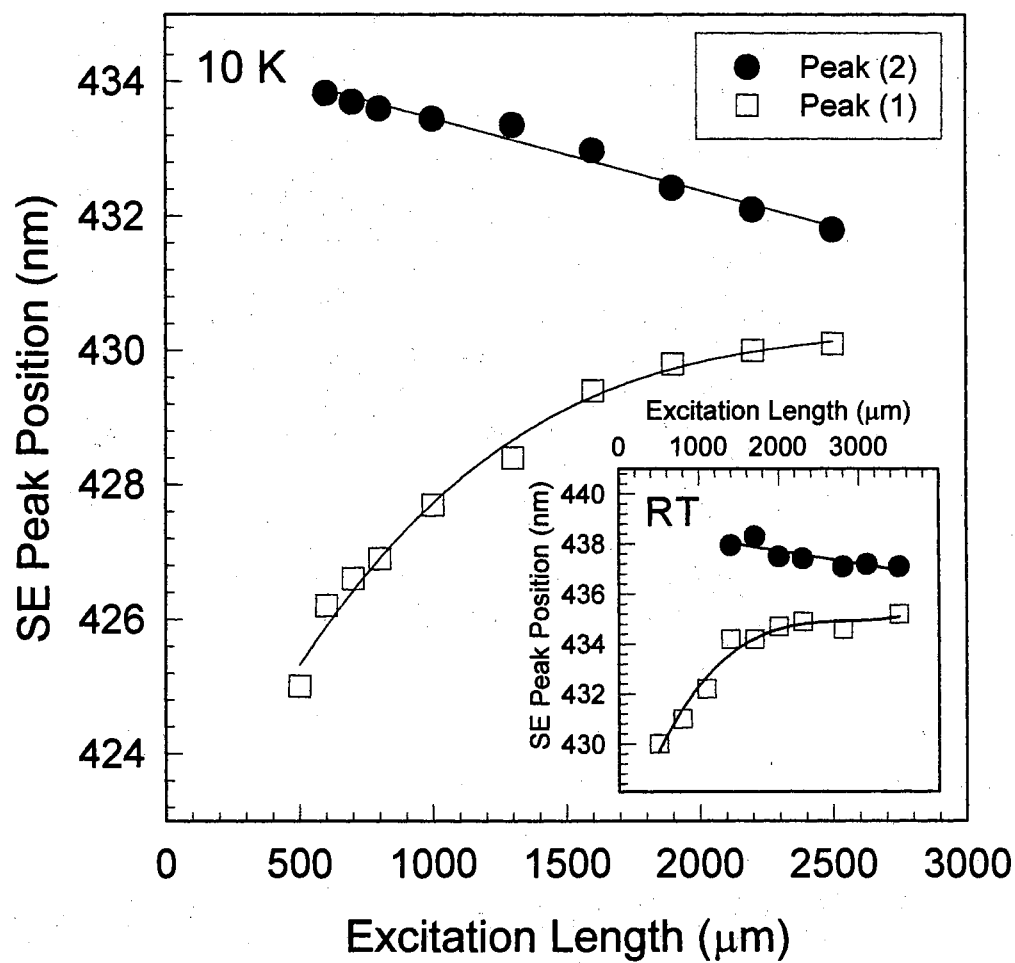


Figure 64. Peak position of SE peaks (1) and (2) as a function of excitation length at 10 K for an InGaN/GaN MQW. The solid lines are given only as guides for the eye. The inset shows the behavior observed at room temperature.

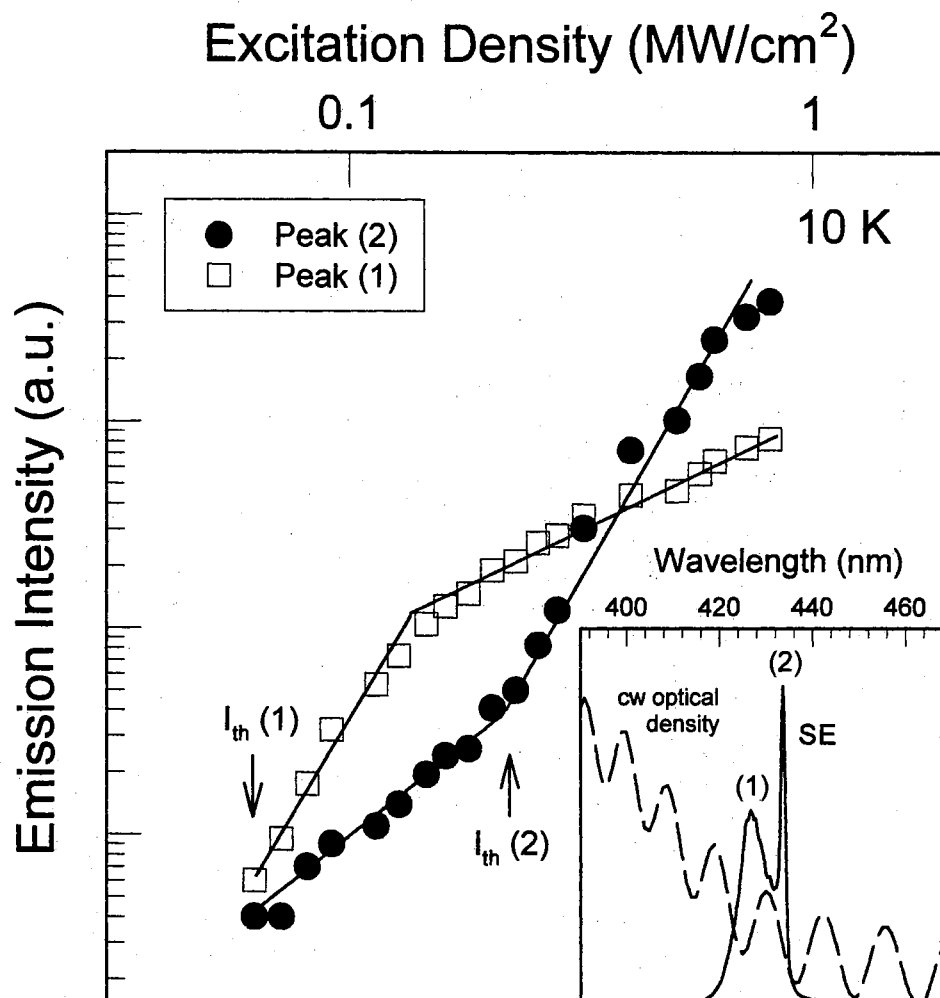


Figure 65. Emission intensity of SE peaks (1) and (2) as a function of optical excitation density at 10 K, illustrating gain competition between SE peaks (1) and (2). The excitation length is $1,300 \mu\text{m}$. The respective SE thresholds, I_{th} , of SE peaks (1) and (2) are indicated for completeness. The solid lines are given only as guides for the eye. The inset shows the optical density (dashed line) given in arbitrary units overlaid on a representative SE spectrum (solid line), illustrating the relative magnitude of the absorption tail in the spectral region of SE peak (1) compared to that of SE peak (2). The oscillatory structure is a result of thin film interference.

Energy Selective Optically Pumped SE Studies of InGaN/GaN MQWs

Optically pumped stimulated emission (SE) from InGaN/GaN multiple quantum wells (MQWs) grown by metalorganic chemical vapor deposition (MOCVD) has been systematically studied as a function of excitation photon energy (E_{exc}) to further understand the origin of SE in these structures. Optically pumped SE was observed for excitation photon energies well below that of the absorption edge of the MQWs, indicating the states responsible for the soft absorption edge in these structures can efficiently couple carriers with the gain region. “Mobility edge” type behavior in the SE peak was observed as E_{exc} was varied. The effective mobility edge measured in these SE experiments lies ~ 110 meV above the main spontaneous emission peak and ~ 62 meV above the SE peak. Tuning the excitation energy below the mobility edge was found to be accompanied by a drastic increase in the SE threshold due to a decrease in the effective absorption cross section. The experimental results indicate that the SE peak observed here has the same microscopic origin as the spontaneous emission peak, *i.e.* radiative recombination of localized states.

Motivation

GaN-based semiconductors and related heterostructures have been attracting an ever-increasing amount of attention due to their large direct band gaps, making them promising materials for UV-blue-green light emitting devices [74], [103], solar-blind ultraviolet detectors [91], and high power and high temperature devices [92], [56], [65]. In particular, the realization of high brightness blue and green light emitting diodes (LEDs) [74] and cw blue laser diodes [103] based on InGaN/GaN multiple quantum well (MQW) structures has focused the efforts of many research groups on these structures. Although a considerable amount of research has been conducted on the optical properties of these materials, there is still much left unknown about the optical processes associated with stimulated emission (SE) and lasing in them. A fundamental understanding of the mechanisms leading to stimulated emission and

lasing in these materials is important, not only for general physical insight, but also as an aid in designing practical devices.

Recently, a considerable amount of attention has been given to the potential role of strongly localized states on the SE and lasing process in InGaN MQWs [104], [105], [106], [107], [108]. Although there exists a sizable amount of data to support localized state recombination as the mechanism leading to spontaneous recombination in these materials [66], [109], [67], the reported results for SE are varied and contradictory. This has led some research groups to assign the spontaneous emission peak to recombination of localized states and the SE peak to recombination of an electron-hole plasma originating from free carriers [110], while others claim strongly localized states to be the origin of both spontaneous and stimulated emission [106], [107], [108]. In this letter, we report the results of excitation energy dependent studies of optically pumped SE from InGaN/GaN MQWs and present evidence that gain originating from localized states exists in this material system, and is responsible for SE peak (2) described in the previous section.

Experimental Technique and Results

The experiments were performed on both MQWs with Si doped ($n \approx 2 \times 10^{18} \text{ cm}^{-3}$) and undoped GaN barriers. The InGaN MQWs were optically pumped in an edge emission geometry under different excitation energies generated by the second harmonic of an amplified dye laser pumped by the second harmonic of an injection seeded Nd:YAG laser (10 Hz, 4 ns FWHM pulse width). The excitation beam was focused into a line on the sample using a cylindrical lens, and the emission was collected from one edge and coupled into a 1-meter spectrometer, then spectrally analyzed using a UV-enhanced gated CCD. The excitation beam spot size was $\approx 100 \times 5,000 \text{ } \mu\text{m}$.

Figure 66 shows the 10 K emission spectra of the doped InGaN/GaN MQW for several excitation densities below and above the SE threshold (I_{th}). As the excitation density (I_{exc}) is increased, the spontaneous emission peak is observed to blue shift until it reaches $\approx 2.875 \text{ eV}$, after this point it is observed to increase only in intensity

until the SE threshold is reached. The SE [SE peak (2)] is seen to develop on the low energy side of the fully blueshifted spontaneous emission peak. The blueshift of the spontaneous emission is attributed to band filling of the localized states due to the intense optical pump. With increasing I_{exc} , the filling level increases and the photoluminescence (PL) maximum shifts to higher energies until sufficient population inversion is achieved and net optical gain results in the observed SE peak. The data presented in Fig. 66 were taken with an excitation energy of 3.49 eV (355 nm) in a surface emitting geometry near the edge of the sample to minimize the role of re-absorption processes in the spontaneous emission spectrum. The SE peak is due to a leak of the in-plane SE at the sample edge. No SE was observed from the middle of the sample in this geometry, indicating the high quality of the sample structure [115]. The spontaneous emission peak has been attributed to radiative recombination of localized states [116] in an analysis along the same vein as Narukawa *et al.* [67]. The effective recombination lifetime as a function of detection energy measured in time-resolved photoluminescence (TRPL) experiments (see [116]), is shown in the inset of Fig. 66 across the 10 K PL spectrum. The large rise in lifetime with decreasing energy across the PL spectrum gives favorable evidence that the PL peak is due to radiative recombination of carriers localized at potential fluctuations. These potential fluctuations can be due to alloy disorder, interface irregularities, and/or self formed “quantum dots” in the quantum well active regions.

To elucidate the origin of the SE peak, we measured the selectively excited SE spectra from the MQWs. Fig. 67 shows the behavior of the SE peak as the excitation photon energy (E_{exc}) is tuned from above the band gap of the AlGaIn cap layer down below the absorption edge of the InGaIn active layers. As E_{exc} is tuned to lower energies, no noticeable change is observed in the SE spectrum until E_{exc} crosses a certain value, at which point the SE spectrum red shifts quickly with decreasing E_{exc} . The inset of Fig. 67 illustrates the SE spectra position change as a function of E_{exc} for the InGaIn/GaN MQW with undoped GaN barrier layers, while the main part of Fig. 67 gives the behavior of the SE peak for the doped MQW whose data is presented in Figs. 66 and 68. The SE peak position is seen to

be relatively insensitive to E_{exc} for energies higher than ≈ 2.925 eV, but as E_{exc} is tuned below this value, the SE peak position is seen to redshift quickly. This red shift of the emission for excitation photon energies below a certain value is consistent with mobility edge behavior. This behavior was also observed in the spontaneous emission spectrum as the excitation photon energy was tuned below ≈ 2.98 eV. The increased presence of lower energy emission compared to the peak emission intensity observed in the spontaneous emission experiments (not shown) is explained as follows: When the excitation photon energy is higher than ≈ 2.98 eV, the photo-generated carriers can easily populate the tail states by their migration, but their lifetimes are relatively short due to the presence non-radiative recombination channels. As E_{exc} is tuned below ≈ 2.98 eV, their relaxation rate is significantly reduced due to the suppression of non-radiative recombination caused by the capture of the carriers in a small volume. This transition energy (≈ 2.98 eV), therefore, defines the transition from extended states to localized states. Note that all states below ≈ 3.1 eV are, in fact, band tail states. This transition is referred to as the mobility edge, as carriers below this energy are not free to migrate, but are instead spatially localized by large potential fluctuation. The increase in lifetime with decreasing E_{exc} results in increased radiative recombination from lower energy states. The behavior of the SE peak is due to enhanced population inversion at lower energies as the carriers are confined more efficiently with decreasing E_{exc} . The “mobility edge” measured in SE experiments lies ~ 110 meV above the spontaneous emission peak, ~ 62 meV above the SE peak, and ~ 185 meV below the absorption edge of the InGaN well regions. The location of the mobility edge with respect to the spontaneous and stimulated emission peaks indicates that large potential fluctuations are present in the InGaN active regions, resulting in strong carrier localization. This explains the efficient radiative recombination (stimulated and spontaneous) observed from these structures as well as the low temperature sensitivity of the SE (see the previous sections) [6].

As a measure of the coupling efficiency of the exciting photons to the gain mechanism responsible for SE peak (2), the SE threshold (I_{th}) was measured as a

function of excitation photon energy. A comparison between this and the coupling efficiency obtained for the spontaneous emission peak measured by photoluminescence excitation (PLE) is given in Fig. 68, where $1/I_{th}$ is plotted as a function of E_{exc} to give a better measure of the coupling efficiency and afford an easier comparison to the results of PLE measurements. The detection energy for the PLE experiments is marked on the inset of Fig. 66. Four distinct slope changes are seen in the PLE spectrum. The first, at ≈ 3.12 eV, marks the beginning of the “soft” absorption edge of the InGaN active region, whereas the other three, located at ≈ 2.96 eV, 2.92 eV, and 2.87 eV suggest varying degrees of localization. The change in $1/I_{th}$ at ≈ 3.1 eV is due to a decrease in the absorption coefficient below the absorption edge, and is an expected result. The change in $1/I_{th}$ at ≈ 2.92 eV (indicated by the dotted line) is coincident with a slope change in the PLE spectrum and is attributed to a significant decrease in the effective absorption cross section for excitation photon energies below the mobility edge (indicated by the dashed-dotted line). The band filling maximum (shown by a dashed line in Figs. 66 and 68) is seen to correspond to the slope change at 2.875 eV in the PLE spectrum in Fig. 68. The inset of Fig. 68 shows the same comparison over a wider energy range for both the Si doped and undoped MQWs. A strong correlation between the SE threshold and PLE measurements is clearly seen over the entire range for both samples. The correlation between the high density behavior presented here and the cw PLE results indicates that carrier localization plays a significant role in both the spontaneous and stimulated emission processes.

Summary

In summary, energy selective optically pumped stimulated emission from InGaN/GaN MQW structures has been studied for the first time to gain further insight into the gain mechanisms responsible for lasing in state-of-the-art blue laser diodes. A strong correlation was observed between the stimulated and spontaneous emission peaks studied. Mobility edge type behavior was observed with decreasing excitation photon energy for both the spontaneous and stimulated emission peaks. The “mobility edge” measured in SE experiments was found to lie ≈ 110 meV and ≈ 62 meV

above the spontaneous and stimulated emission peaks, respectively, indicating the presence of large potential fluctuations in the QW active regions. The excitation energies at which significant changes are observed in the SE behavior are closely linked to features observed in the PLE spectrum of the main spontaneous emission peak, indicating that the recombination mechanisms are strongly related. The observed bandfilling effects with increasing excitation density, the observation of mobility edge type behavior, and the strong correlation between the spontaneous and stimulated emission behavior as the excitation photon energy is varied provide strong evidence that localized carriers are responsible for the gain associated with SE peak (2).

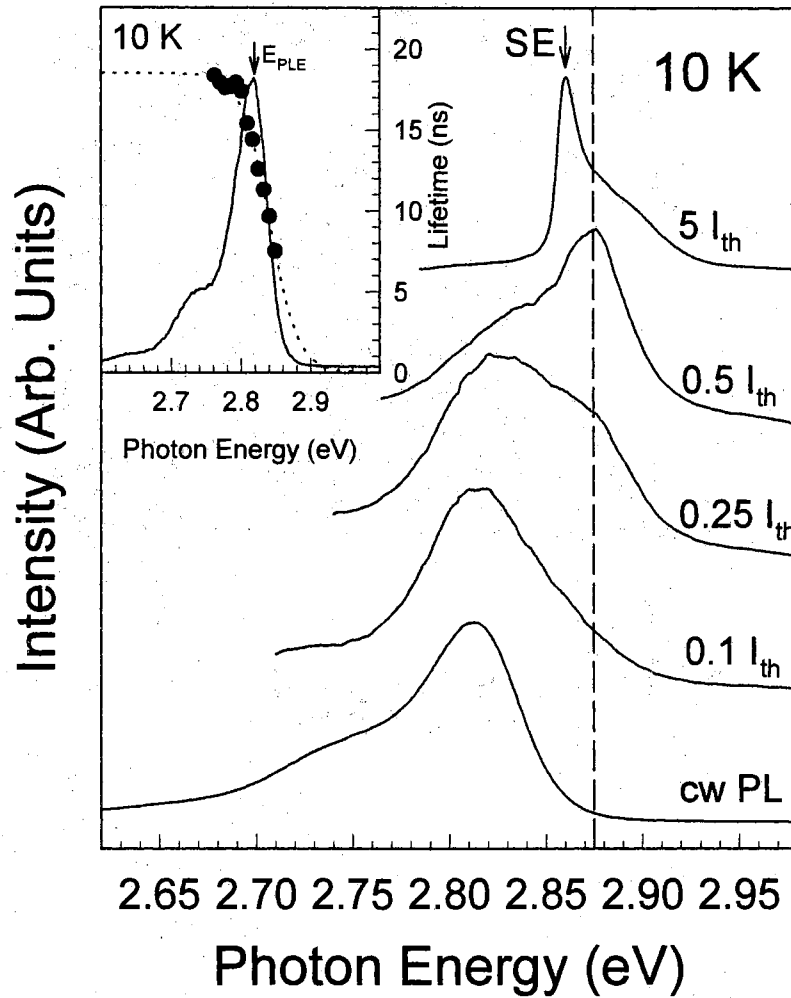


Figure 66. 10 K emission spectra for several excitation densities below and above the SE threshold. The spectra were collected in a surface emission geometry from an InGaN/GaN MQW with a Si doping concentration of $2 \times 10^{18} \text{ cm}^{-3}$ in the GaN barriers. The spectra have been normalized and displaced for clarity. The inset shows the effective recombination lifetime across the 10 K spontaneous emission spectrum. The dotted line is given only as a guide for the eye. The PLE detection energy is also given in the inset.

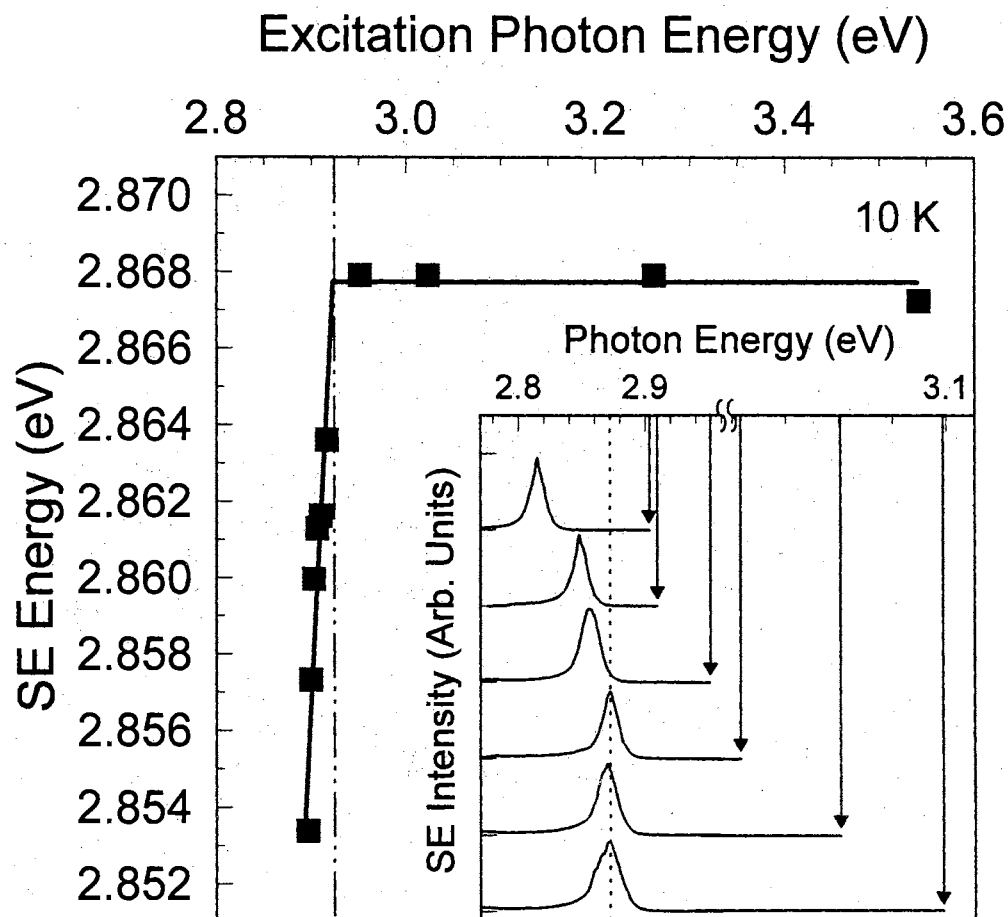


Figure 67. SE peak position as a function of excitation photon energy, E_{exc} , for the InGaN/GaN MQW with a $2 \times 10^{18} \text{ cm}^{-3}$ Si doping concentration in the GaN barriers. “Mobility edge” type behavior is clearly seen with decreasing excitation photon energy. The solid lines are given only as a guide for the eye. The inset shows the redshift of the SE peak with decreasing E_{exc} as E_{exc} is tuned below the “mobility edge” for an InGaN/GaN MQW with undoped GaN barriers. The excitation photon energies for the given SE spectra are represented by the arrows in the inset. The dotted line in the inset is given as a reference for the unshifted SE peak position. The SE spectra have been normalized and displaced vertically for clarity.

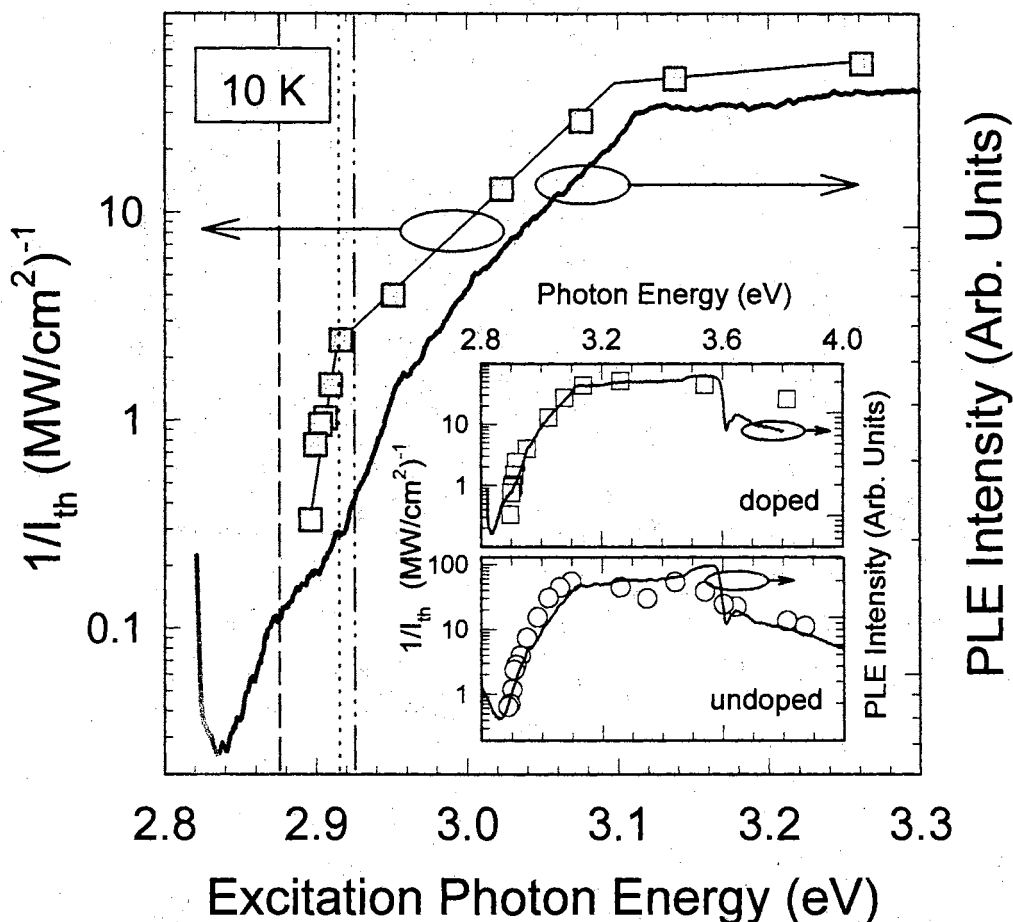


Figure 68. Inverse SE threshold as a function of excitation photon energy (solid squares) shown in comparison with the results of low power PLE experiments (solid lines) for the Si doped ($n = 2 \times 10^{18} \text{ cm}^{-3}$) InGaN/GaN MQW. The band filling maximum (dashed line) and "mobility edge" (dashed-dotted line) from the previous two plots are indicated for completeness. The dotted line shows the excitation photon energy at which the SE threshold is found to increase quickly with decreasing photon energy. The inset shows the same comparison over a wider energy range for both the undoped and Si doped InGaN/GaN MQWs, illustrating the similarities over the entire energy range.

Variable-Stripe Gain Spectroscopy of InGaN/GaN MQWs

One of the best ways to understand the optical processes leading to SE and lasing in a semiconductor is to directly measure the spectral region in which gain exists and how it evolves as a function of excitation density. There are several experimental methods to measure this behavior. They include direct observation of net amplification in pump-probe experiments, extracting the gain curve from the luminescence as a function of excitation density [117], and extracting the gain curve by measuring the edge emitted amplified spontaneous emission as a function of amplification path length at a given excitation density [118], to name a few. We will see a little later in the text that the first option, while providing a lot of insight into the optical processes exhibited by these materials when highly excited, is not conducive to the observation and description of optical gain. The second option, while easily performed experimentally, relies on some basic assumptions (that will be shown later in the text to be invalid) about the behavior of the band edge in order to extract gain curves. The later method, the variable-stripe method developed by Shaklee and Leheny [118], turns out to be a good choice for the measurement of optical gain in this material system, as it relies on nothing but the observation of amplification in the material with no initial assumptions about origin.

Experimental Technique and Results

In these experiments, the MQWs were optically excited in an edge emission geometry by the third harmonic of a Q-switched, injection seeded Nd:YAG laser (355 nm) operating at 10 Hz with a 4 ns FWHM pulse width. The excitation length of the pump beam was varied precisely using a mask connected to a computer controlled stepper motor with better than 0.5 μm linear resolution. The spontaneous luminescence is amplified (stimulated luminescence) as it passes through the crystal volume excited by the pump beam. The emission is collected from the edge of the sample and coupled into either a 1/4 meter or a one meter spectrometer (depending on the resolution and spectral range required) and spectrally analyzed using a UV

enhanced, gated CCD. If the net gain, $g(\lambda)$, experienced by the light in the crystal for a certain photon energy is given by:

$$g(\lambda) = g'(\lambda) - \alpha(\lambda) \quad (\text{given in cm}^{-1}) \quad (37)$$

where $\alpha(\lambda)$ is the background absorption coefficient and $g'(\lambda)$ is the absolute gain for the given spectral region, then the intensity of the light emitted from the sample edge is given by:

$$I(l, \lambda) = \frac{C(\lambda)}{g(\lambda)} [\exp \{g(\lambda) \cdot l\} - 1] \quad (38)$$

where $C(\lambda)$ is a constant that takes into account the cross sectional area of the excited volume and the spontaneous emission rate per volume, and l is the excitation (amplification) length. Of particular interest is the situation in which l is varied from L to $2L$ (where L is typically on the order of several 100's of μm). In this case, the gain coefficient is given by:

$$g(\lambda) = \ln \left[\frac{I(2L, \lambda)}{I(L, \lambda)} - 1 \right] / L \quad (39)$$

This technique is particularly conducive to extracting the gain spectrum when using an array-type detector. By accumulating a spectrum at L and $2L$ and analyzing the data using equation. 39, we immediately obtain the gain spectrum for a given excitation density. We note that the experiment requires that the emission not be significantly spectrally narrowed, as occurs for I_{exc} above I_{th} at long excitation lengths. We want to be in the experimental region where gain and amplification exists in the material, but the photons are not amplified along a long enough path to significantly narrow the spectra. For these conditions we observe amplified spontaneous emission (ASE) from the edge of the sample. These conditions occur in these materials for L on the order of a few 100's of μm . To get a feel for how heavily the samples were being pumped, the SE threshold was measured for long excitation lengths ($L \simeq 1 \text{ mm}$). This value was used as a reference pumping level, of course, keeping in mind that I_{th} is a strong function of excitation length (see previous sections).

The modal gain curves measured in these experiments are shown in Fig. 69 for $L = 100 \mu\text{m}$. We see that the crossover from gain to absorption blueshifts significantly with increasing I_{exc} . This can be understood by considering the model

introduced in Chapter 2 for gain originating from EHP recombination. With increasing optical excitation, the level of filled states in the conduction band increases and the number of empty states in the valence band increases, leading to an increase in the quasi-Fermi level separation. This directly leads to a blueshift in the crossover point with increasing I_{exc} . While the EHP model presented in Chapter 2 was for an EHP originating from free carriers and for parabolic bands, the concepts for gain curve construction can still be used even though the gain we observe originates from carriers localized at potential fluctuations (band tail states). The origin of gain is seen more clearly in Fig. 70, where the modal gain has been superimposed on the band edge measured by PLE. We see the peak of the gain curve is redshifted by more than 25 nm ($\simeq 182$ meV) with respect to the band edge of the InGaN active layers. This, combined with the other experimental observations discussed in this chapter, gives compelling evidence for gain arising from localized states in this material system.

Summary

In summary, variable stripe gain measurements have been performed on InGaN/GaN MQWs. The gain spectra for various optical excitation densities were obtained. The gain spectra show clear spectral broadening to higher energy with increasing optical excitation. This behavior is attributed to filling of localized states with increasing optical excitation and indicates that optical gain originates from localized states in these materials.

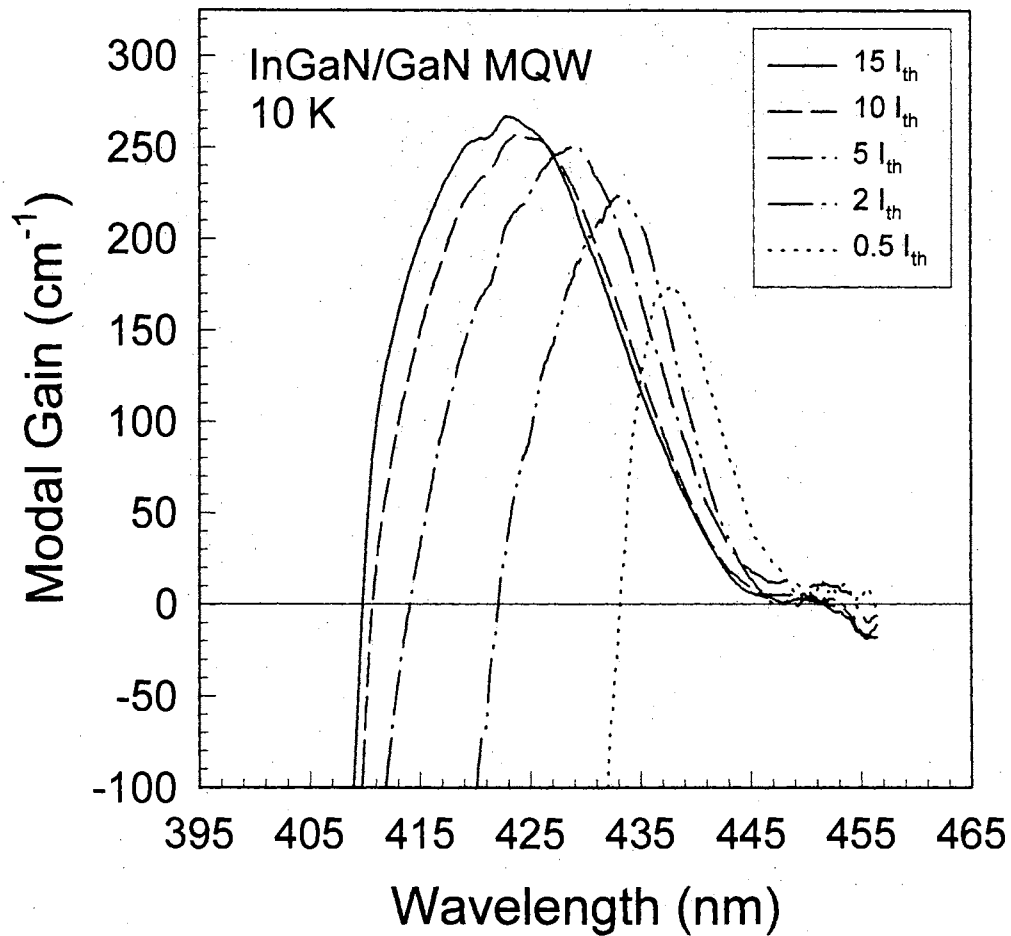


Figure 69. 10 K modal gain spectra of an MOCVD-grown InGa_N/Ga_N MQW measured using the variable-stripe method of Shaklee and Leheny [118]. Large broadening to higher energy resulting from increased quasi-Fermi level separation is seen with increasing optical excitation. The excitation densities are given with respect to the SE threshold, I_{th} , measured for long excitation lengths.

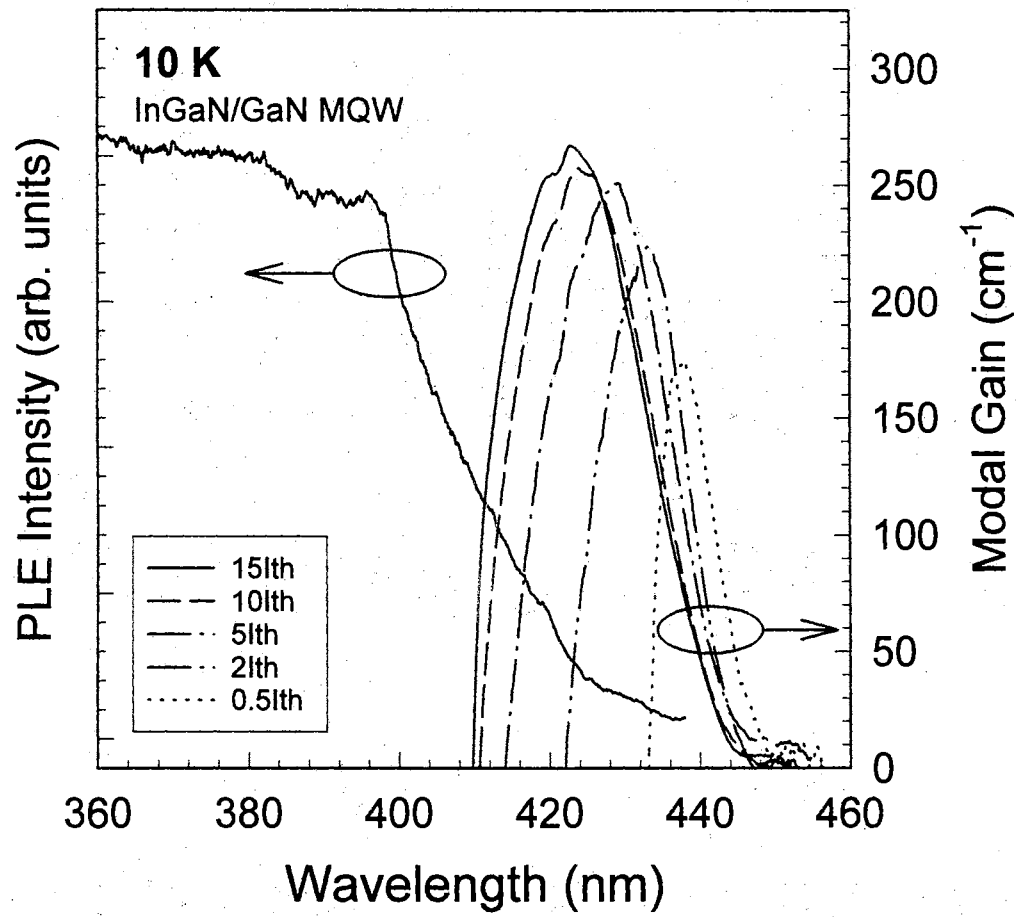


Figure 70. 10 K modal gain spectra overlaid on the band edge of the InGaN active region measured by PLE for an MOCVD-grown InGaN/GaN MQW. The excitation densities are given with respect to the SE threshold, I_{th} , measured for long excitation lengths.

Nondegenerate Optical Pump-Probe Spectroscopy of InGaN/GaN MQWs

Nanosecond non-degenerate optical pump-probe experiments have been performed on InGaN thin films and InGaN/GaN multiple quantum wells. Bleaching of band tail state absorption was observed with increasing excitation density (I_{exc}) of the pump pulse. The dynamics of the bleaching was found to depend on the localization depth of the band tail states and on I_{exc} . With high I_{exc} , large blueshifts in the spontaneous emission luminescence peaks were also observed, the magnitude of which was again found to depend on the localization depth of the band tail states. Stimulated emission is observed from the samples with increasing I_{exc} and correlates with significant changes in the behavior of the absorption bleaching. The observed bleaching dynamics of the band tail states are well explained by considering the effective lifetime of the band tail states as measured by time-resolved photoluminescence experiments.

Motivation

The ternary compound InGaN is of great scientific interest for its applications in UV-blue-green and white light emitting diodes [74] and UV-blue laser diodes [103]. The difficulties associated with indium incorporation in these materials results in a non-random alloy [119] and the presence of potential fluctuations. This, in turn, results in carrier localization, which has been studied in the low excitation density regime by a number of authors in a variety of InGaN based structures [66], [106], [120], [121], [122], [123], [124], [125], [126], [107], [67]. Experiments performed at carrier densities at which working devices operate have predominantly been concerned with the observation and characterization of stimulated emission (SE) [127], [108] and optical gain [108], [128], [61], [111], [127], [110], [113], [112] as a function of excitation and/or temperature. Other types of experiments performed at these carrier densities, though, are few [68], [129], [103]. In this section, we present the results of a systematic study of InGaN/GaN multiple quantum wells (MQWs) under the conditions of strong optical pumping and have compared the results to those obtained

from a thin InGaN layer of comparable average indium composition. The results of nanosecond non-degenerate optical pump-probe experiments, gain spectroscopy, and excitation density dependent emission studies have been combined with the results of low power photoluminescence (PL), PL excitation (PLE), and time-resolved PL (TRPL) experiments to gain a better understanding of the recombination mechanisms of this material.

Experimental Technique and Results

The InGaN/GaN MQW used in this study had $n = 2 \times 10^{18} \text{ cm}^{-3}$ Si doping in the GaN barrier layers. The $\text{In}_{0.18}\text{Ga}_{0.82}\text{N}$ layer used for comparison in this study was grown by MOCVD at 800 °C on a 1.8 μm thick GaN layer deposited at 1060 °C on c-plane sapphire. The $\text{In}_{0.18}\text{Ga}_{0.82}\text{N}$ layer was 0.1 μm thick and was capped by a 0.05 μm GaN layer. The average In composition was measured using high-resolution x-ray diffraction and assuming Vegards law. We note that the actual InN fraction could be smaller due to systematic overestimation when assuming Vegards law in this strained material system [86], [87].

Figure 71 shows the relevant 10 K spectra for (a) the InGaN/GaN MQW and (b) the InGaN epilayer. Note that the x-axis of (b) covers half that of (a). We see the low power spontaneous emission peak (dashed line) is significantly Stokes shifted for both samples with respect to the absorption edge measured by low power PLE spectroscopy (solid line). The band tail states responsible for the “soft” absorption edge are seen to be significantly larger in the MQW than in the epilayer, as is the resulting Stokes shift of the spontaneous emission peaks. Representative SE spectra are also given in Fig. 71 (solid line) for $I_{exc} = 1.5 I_{th}$ (I_{th} is defined here as the SE threshold) and an excitation spot size of $\approx 100 \times 5,000 \mu\text{m}$. We see that the SE peak is situated at the end of the absorption tail for both samples. The SE is seen to occur on the high energy side of the low power spontaneous emission peak for the MQW and on the low energy side for the epilayer. The modal gain measured using the variable stripe excitation method of Shaklee and Leheny [118] (see the previous section) is also shown in Fig. 71 (dotted line) for excitation lengths less

than $200\ \mu\text{m}$ and $I_{exc} \gg I_{th}$. The 3rd harmonic (355 nm) of an injection seeded Nd:YAG (yttrium aluminum garnet) laser was used as the excitation source ($\approx 5\ \text{ns}$ FWHM, 10 Hz repetition rate). The modal gain maxima are 250 and $150\ \text{cm}^{-1}$ for the MQW and epilayer, respectively. We see that the SE peak for long excitation lengths ($> 5,000\ \mu\text{m}$) is situated on the low energy tail of the gain curve measured for small excitation lengths ($< 200\ \mu\text{m}$). This is explained by gain and absorption competition in the band tail region of this alloy, where gain saturation with longer excitation lengths combined with the background absorption tail leads to a redshift of the SE peak with increasing excitation length. This effect has been observed by other research groups [128], [61], [111], [127], [110], [113] and has been studied in detail by the author [64] (see Section 2 of this chapter). The modal gain spectrum for the MQW is seen to be significantly broader ($\approx 24\ \text{nm}$ FWHM) than that of the epilayer ($\approx 7\ \text{nm}$ FWHM), although both are peaked significantly below the onset of the "soft" absorption edge.

Figure 72 shows the results of TRPL experiments. A rise in effective recombination lifetime (τ) with increasing temperature from 10 K to $\approx 50\ \text{K}$, rising from $14.4\ \text{ns}$ ($0.8\ \text{ns}$) at 10 K to $18.8\ \text{ns}$ ($0.88\ \text{ns}$) at 50 K for the MQW (epilayer), is clearly seen, indicative of recombination dominated by radiative recombination channels. For $T > 50\ \text{K}$, τ decreases with increasing temperature, from $18.8\ \text{ns}$ ($0.88\ \text{ns}$) at 50 K to $\approx 11.7\ \text{ns}$ ($\approx 0.16\ \text{ns}$) for temperatures exceeding $\sim 175\ \text{K}$, indicating the increasing dominance of non-radiative channels in the recombination process [130]. The lifetimes given above are for the peak wavelength of the spontaneous emission spectrum. We note that the MQW has a significantly larger τ than the epilayer for all temperatures studied (10 K to 300 K), and the lifetimes of both are significantly larger than that of GaN epilayers and heterostructures [131], [35]. This is attributed to suppression of non-radiative recombination by the localization of carriers at spatial alloy composition fluctuations. This localization is evidenced in the rise of the effective lifetime with increasing emission wavelength across the 10 K PL spectrum, from $7.5\ \text{ns}$ at 436 nm to $18\ \text{ns}$ at 446 nm for the MQW, and from $0.62\ \text{ns}$ at 410 nm to $1.0\ \text{ns}$ at 424 nm for the epilayer. The differences in τ between

the two samples indicate that the potential fluctuations localizing the carriers are significantly smaller in the epilayer than in the MQW.

Figure 73 shows the evolution of the spontaneous emission with increasing pump density for (a) the MQW and (b) the epilayer. Note that the horizontal scales are different for (a) and (b) but cover the same spectral width (60 nm). The spectra shown in Fig. 73 were collected in a surface emission geometry to minimize the effects of re-absorption on the emission spectra. The pump spot size was $\sim 1 \text{ mm}^2$ and the excitation wavelength was the 3rd harmonic of the Nd:YAG laser described above (355 nm). The blueshift of the spontaneous emission with increasing I_{exc} is attributed to band filling of localized states. We see the I_{exc} induced blueshift is significantly larger for the MQW than the epilayer ($\approx 12 \text{ nm}$ for the MQW compared to $\approx 2 \text{ nm}$ for the epilayer), further indicating that the potential fluctuations are significantly larger in the MQW than in the epilayer. For large enough I_{exc} , we observe that the blueshift of the spontaneous emission with increasing I_{exc} stops, and that further increases in I_{exc} result in the observation of SE, indicated by the arrows in Fig. 73. The SE peak is seen to grow out of the low-energy wing of the fully blueshifted spontaneous emission peak for both samples.

Figure 74 shows the results of nanosecond non-degenerate optical pump-probe experiments performed on (a) the InGaN/GaN MQW and (b) the InGaN epilayer. In these experiments, the 3rd harmonic of the Nd:YAG laser described above (355 nm) was used to synchronously pump the individual samples and a dye solution. The superradiant emission from the dye solution (covering the entire spectral range of the localized states) was collected and focused onto the samples, coincidental with the pump beam. The intensity of the probe was kept several orders of magnitude lower than the pump beam to avoid any nonlinear effects due to the probe. The spot size of the probe was kept at $\sim 1/3$ that of the pump to minimize the role of variations in the pump intensity across the excitation spot. The transmitted (broadband) probe (with and without the pump beam) was then collected and coupled into a 1/4-meter spectrometer and spectrally analyzed using a UV enhanced, gated CCD. Absorption bleaching of band tail states is clearly seen in Fig. 74 for (a) the MQW

and (b) the epilayer with increasing excitation density, where the bleaching is seen to cover the entire spectral range of the absorption tails of the samples. The bleaching is peaked at ~ 410 nm for both samples, but is spectrally much broader for the MQW, consistent with its increased absorption tail. We note that the maximum in the absorption bleaching is significantly blueshifted with respect to the luminescence maximum for both samples. This is explained by the intraband relaxation of the localized carriers, where the carriers are created with energies above the mobility edge (see the preceding section), but are quickly caught in the potential wells and localized. Further intraband relaxation at low temperatures can now only occur by means of phonon-assisted tunneling to a (deeper) neighboring potential well or by further relaxation to lower energy states within the same well until the potential minima are reached. The radiative recombination of these localized states is expected to be mainly from these potential minima. An interesting difference between the two samples is the behavior of the absorption bleaching as the SE threshold is exceeded. As the pump density is increased, the bleaching is observed to increase for both samples, but as the SE threshold is exceeded, the bleaching of the MQW tail states is seen to decrease significantly with increasing excitation, while the bleaching of the epilayer tail states continues to increase with increasing excitation density. This is shown in Figs. 74(a) and 74(b), where the dotted and dashed lines show the bleaching spectra for excitation densities below the SE threshold and the solid lines show the bleaching spectra for excitation densities above the SE threshold. The differences in behavior are explained by considering the recombination lifetimes given above. Although radiative recombination from these samples occurs from the potential well minima, localized states of higher energy are temporarily occupied as the carriers excited by the pump beam relax, resulting in the observed bleaching peaked at higher energy than the luminescence maximums. The bleaching of the In-GaN/GaN MQW decreases for excitation densities above the SE threshold because of the fast depopulation of the states from which the SE originates. This results in the localized carriers with energies above the SE peak now having a much greater number of available lower energy states, this in turn results in a decrease in the localized

states occupied at higher energies and therefore a decrease in the observed bleaching for excitation densities above the SE threshold. This behavior has been previously observed in other materials where intrinsic disorder through compositional fluctuations has lead to the same carrier localization observed here [132]. The absence of the absorption bleaching decrease for excitation densities above the SE threshold in the InGaN epilayer results from its short recombination lifetime (≈ 0.8 ns) with respect to the pump pulse (≈ 5 ns FWHM). Therefore, the recombination lifetime for the epilayer is always significantly shorter than the pump pulse, leading to no noticeable reduction in the relaxation dynamics of the higher energy localized states as the SE threshold is exceeded, and, therefore, no noticeable change in the bleaching behavior is observed. The modal gain shown in Figs. 71(a) and 71(b) (dotted lines) is seen to correspond spectrally with the low energy tail of the localized state absorption bleaching, with the crossover from absorption to gain corresponding approximately with the maximum in the observed bleaching for both samples, indicating that the gain originates from the localized states.

Summary

In summary, nanosecond non-degenerate optical pump-probe experiments have been performed for the first time on InGaN/GaN MQWs and InGaN epilayers and the results have been combined with the results of low power PL and PLE experiments, TRPL studies, modal gain studies, and excitation density dependent studies of the spontaneous and stimulated emission. The experimental results show that the carriers responsible for spontaneous and stimulated emission share the same relaxation channels and illustrates the dominance of localized state recombination, both stimulated and spontaneous, in the low temperature emission spectra of InGaN based systems.

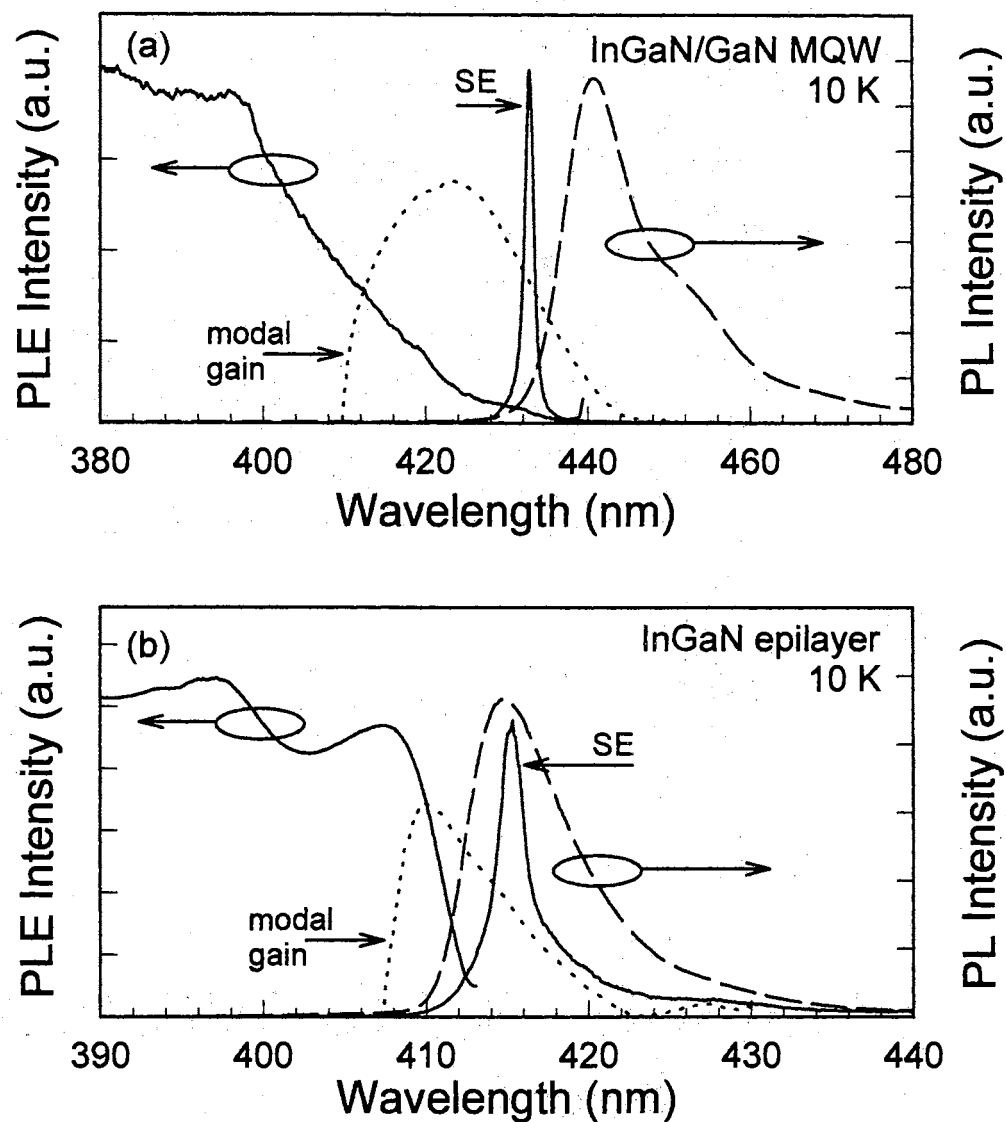


Figure 71. 10 K PLE (solid lines) and PL (dashed lines) spectra from (a) an InGaN/GaN MQW and (b) an InGaN epilayer. Both were grown by MOCVD on (0001) oriented sapphire. The SE spectra for long excitation lengths have been superimposed, as have the modal gain spectra (dotted lines). The maximum modal gain is 250 and 150 cm^{-1} for the MQW and epilayer, respectively.

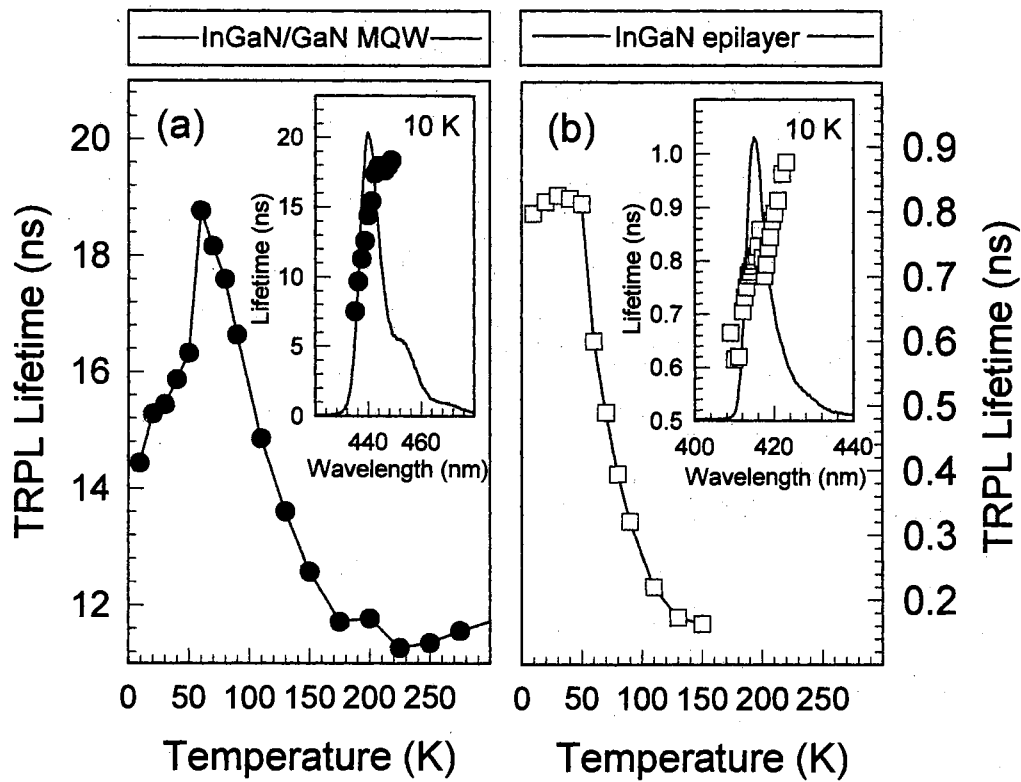


Figure 72. Effective recombination lifetime as a function of temperature for (a) an InGaN MQW and (b) an InGaN epilayer, as measured by TRPL. The insets show the rise in the effective recombination lifetime across the 10 K spontaneous emission spectra.

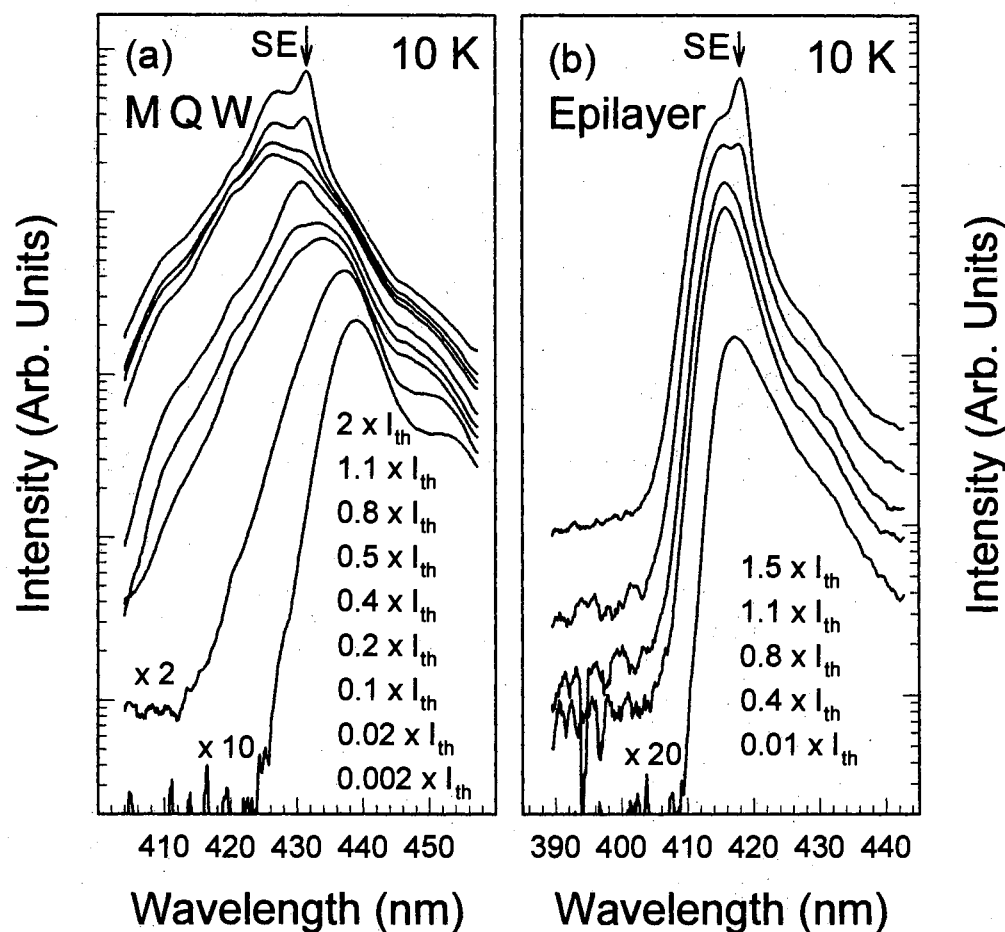


Figure 73. 10 K emission spectra as a function of excitation density for (a) an InGaN/GaN MQW and (b) an InGaN epilayer showing band filling of localized states with increasing optical excitation. The emission was collected in a surface emission geometry. The SE threshold, I_{th} , for the MQW and epilayer was measured to be ≈ 170 and 130 kW/cm^2 , respectively, for the experimental conditions.

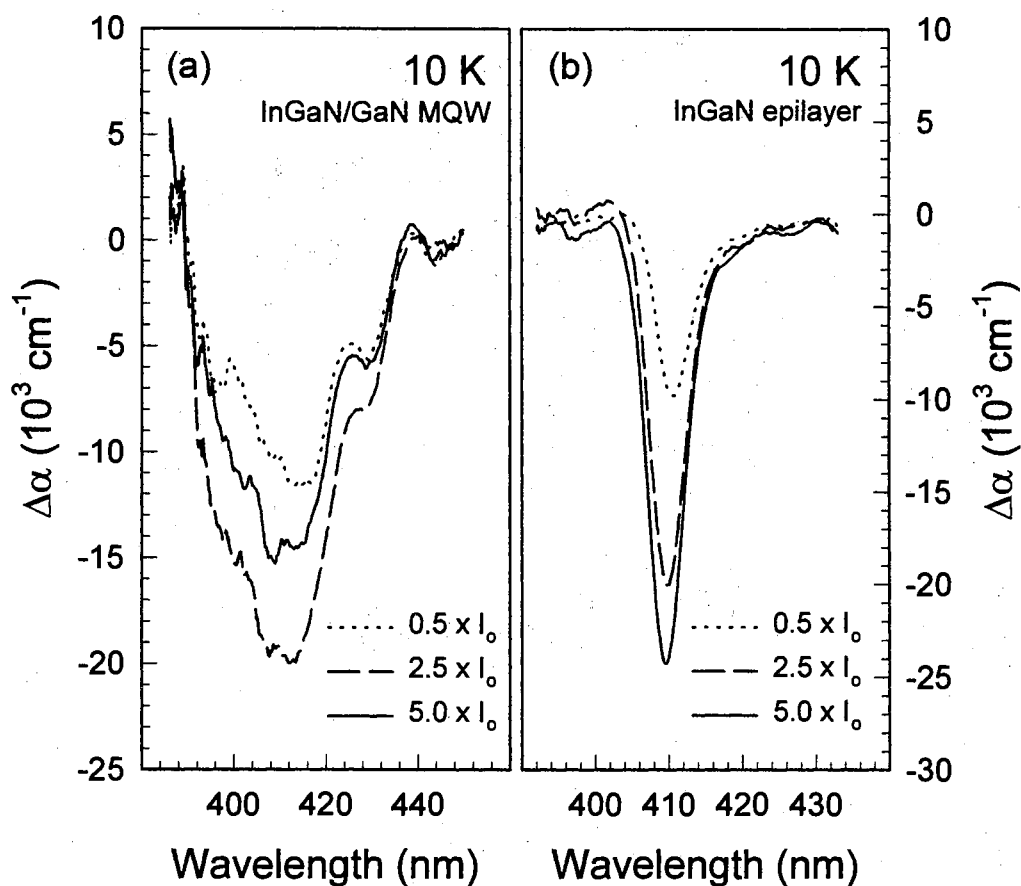


Figure 74. 10 K nanosecond nondegenerate optical pump-probe differential absorption spectra for an InGaN/GaN MQW and (b) and InGaN epilayer as a function of excitation density, I_{exc} . Absorption bleaching ($\Delta\alpha$ negative) of band tail states is clearly seen with increasing I_{exc} . $\Delta\alpha(I_{exc}) = \alpha(I_{exc}) - \alpha(0)$ and $I_0 = 100 \text{ kW/cm}^2$.

Summary

We have seen in the previous sections that SE from InGaN/GaN MQWs differs significantly from that of GaN and AlGaIn thin films. The emission was shown to be strongly dependent on the experimental conditions (*i.e.* on excitation length) and two different SE peaks were observed with very different characteristics. These two SE peaks were shown to compete for gain in the material. The higher energy SE peak was shown to actually be the statistical average of a multitude of spectrally narrow (<0.1 nm FWHM) SE peaks. These emission peaks were shown not to spectrally broaden as the temperature was raised from 10 K to 575 K. The average peak position of this higher energy SE peak was shown to redshift greatly (≈ 5 nm) with increasing excitation length. This redshifting behavior was attributed to gain and absorption competition in the band tail region of these materials, where gain saturation at longer excitation lengths combined with the background absorption tail leads to the observed redshift with increasing excitation length. The temperature dependence of the SE threshold of this higher energy SE peak was shown to be consistent with that of GaN, indicating that the rise in the SE threshold with increasing temperature is dictated by the (nonradiative) recombination mechanisms of the base material, GaN. The SE threshold was shown to be significantly lower for InGaIn MQWs (typically by more than an order of magnitude) than GaN films, but of the same order as that of InGaIn films. The above behavior is consistent with stimulated recombination of highly localized carriers, such as is found in self formed quantum dots. This localization is attributed to difficulties in uniform indium incorporation leading to large potential fluctuations in InGaIn epilayers and MQWs. The degree of localization is, of course, dependent on the sample growth conditions and sample structure..

The lower energy SE peak observed for longer excitation lengths and/or higher excitation densities was shown to exhibit "mobility edge" type behavior with decreasing excitation photon energy. This SE peak was also shown to affect the relaxation dynamics of band tail states as observed in nanosecond non-degenerate optical pump-probe experiments. The above behavior indicates this lower energy SE peak

originates from stimulated recombination of localized band tail states in the InGaN active regions. As such, both SE peaks are attributed to stimulated recombination of localized carriers. The localization of the carriers responsible for the lower energy SE peak is most likely smaller compared to that responsible for the higher energy SE peak. The onset of the lower energy SE peak was shown to affect the SE behavior of the higher energy SE peak, indicating the two SE peaks compete for gain in the InGaN active regions.

The results of this chapter are summarized in Fig. 75. We see that the crossover from absorption to gain in the fully blueshifted modal gain spectrum corresponds spectrally to the maximum in the band tail state bleaching. The mobility edge measured in quasi-cw PL experiments is also seen to roughly correspond to the maximum of the band tail state bleaching. The “mobility edge” measured in SE experiments on the lower energy SE peak is seen to correspond spectrally to the maximum of the fully blueshifted modal gain spectrum. SE, shown to occur over a wide spectral region, is seen to start at the maximum of the fully blueshifted modal gain spectrum and extend over a large region of the low energy tail of the spectrum. The mobility edge measured in the quasi-cw experiments locates, by definition, the crossover point from extended to localized band tail states. The correlation between this point and the maximum of the band tail state bleaching adds further evidence for this model. The correlation between the gain spectrum and the low energy tail of the band tail state bleaching indicates the optical gain originates from localized band tail states. The large spectral width of the gain and band tail state bleaching spectra, and the wide range of photon energies at which SE is observed indicate a large variance in the degree of localization present in the InGaN active regions. The fact that the “mobility edge” measured for the lower energy SE peak corresponds to the maximum of the modal gain spectrum further indicates the two separate SE peaks are related in their origin.

The results presented here give strong evidence that gain arising from localized states is present in this material system and is responsible for the observed SE peaks

and their behavior. The carrier localization arises from difficulties in uniform indium incorporation and is a result of large potential fluctuation in the InGaN active layers.

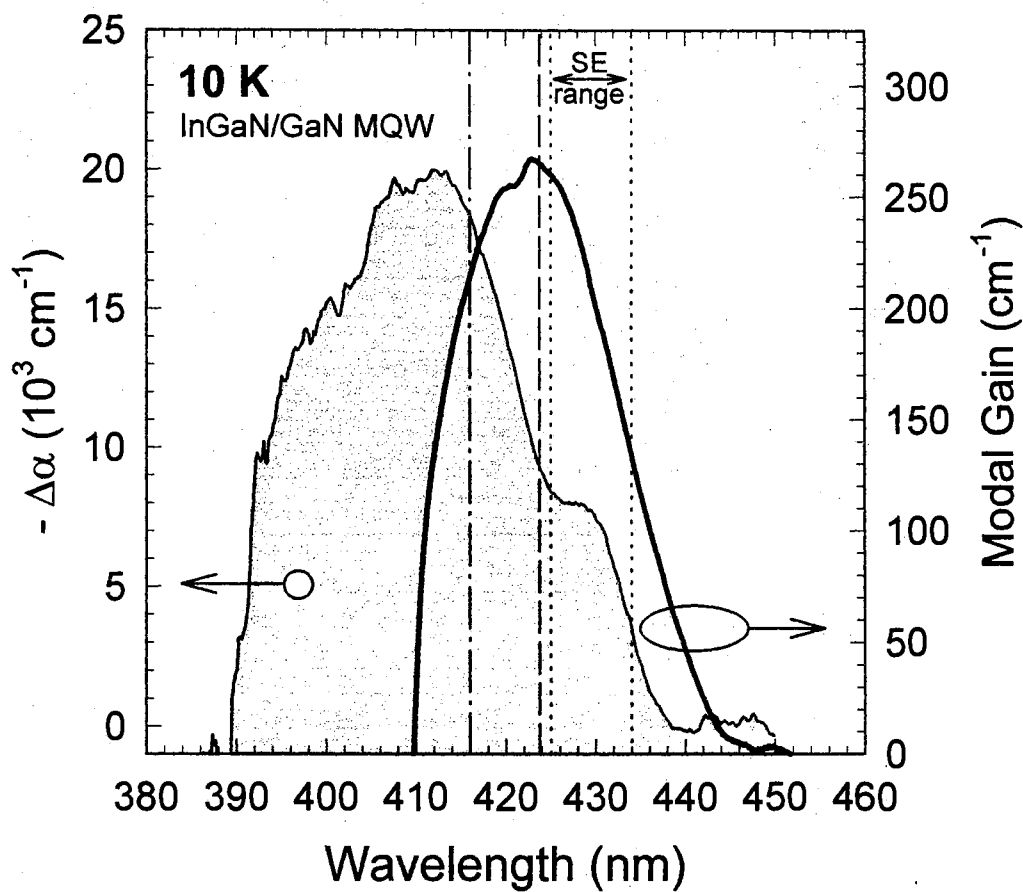


Figure 75. Summary of observed behavior of highly excited InGaN/GaN MQWs. The modal gain spectrum (heavy solid line) for $I_{exc} \simeq 15 \cdot I_{th}$ is overlaid on the band tail state bleaching spectrum measured in pump-probe experiments. The crossover from absorption to gain is seen to correspond to the maximum in the absorption bleaching spectrum. The mobility edge measured in quasi-cw PL measurements (dashed-dotted line) and SE experiments (dashed line) are given for reference, as is the spectral range over which SE was observed (dotted lines).

CHAPTER VII

SUMMARY

The wide band gap group III nitride semiconductors are technologically important materials due to their applications in UV-blue light emitting devices and detectors. Although commercialization of blue laser diodes based on the ternary nitride compound InGaN is predicted to occur in the very near future, very little information exists on the high excitation optical properties of this material system. This thesis serves to considerably extend the knowledge base of the optical properties of these materials in their highly excited state. This thesis contains the first high temperature stimulated emission (SE) and lasing studies of GaN and the follow-up work that demonstrated SE in GaN up to 700 K without noticeable sample degradation. This is the highest temperature for SE ever reported in a semiconductor system, and opens up the door for novel high temperature optoelectronic devices based on the group III nitrides. It also includes the first demonstration of extremely large band gap nonlinearities in GaN, including the observation of extremely large band gap renormalization and a resulting large increase in the below-gap absorption coefficient with increasing photo-generated free carrier concentration. It goes on to fully describe the optical phenomena associated with this renormalization, illustrating the potential uses of GaN in optical switching applications. The contents of this thesis also include the first observation of deep UV SE from AlGaN, with a room temperature SE wavelength as low as 327 nm, the shortest room temperature SE wavelength ever reported from a semiconductor. The potential applications for deep UV lasers based on this material include a myriad of medical applications, where a compact short wavelength laser would satisfy the needs of many applications, both known and presently unrealized.

This thesis, after some general background information, started with a complete description of SE from GaN over the temperature range from 10-700 K. It included a designation of the gain mechanisms responsible for SE in this material and the temperature range in which they exist. It has shown exciton-exciton scattering to be the dominant near threshold gain mechanism for the temperature range from 10 K to approximately 175 K and electron-hole plasma recombination to be the dominant gain mechanism for temperatures above approximately 175 K as well as for higher excitation densities at the lower temperatures. It also contains a comparison of the SE properties of AlGa_N and InGa_N with GaN. It shows that AlGa_N has very similar SE behavior to GaN, although exciton-exciton scattering was shown not to be a dominant gain mechanism for any temperature. The SE properties of InGa_N were shown to be markedly different than GaN and AlGa_N. The emission from InGa_N, both spontaneous and stimulated, is shown to result from radiative recombination of carriers localized at potential fluctuations in the InGa_N layers. This results from difficulties in achieving uniform In incorporation during the growth process.

This thesis then went on to describe how the near band edge optical transitions in GaN and InGa_N evolve with increasing concentrations of photo-generated free carriers through nondegenerate optical pump-probe spectroscopy. The band gap of GaN was shown to shift to lower energy with increasing optical excitation, resulting in extremely large values of induced absorption in the spectral region in which gain was expected. This band gap renormalization was shown to exhibit a characteristic build up and decay time consistent with screening by carriers trapped at deep levels. This renormalization was shown to only be induced by above gap optical excitation. It was also shown to be absent in InGa_N thin films, explaining, in part, why InGa_N typically exhibits a markedly lower stimulated emission threshold than GaN and AlGa_N. The results of this study shows that a complex relationship exists between gain and induced absorption in GaN thin films and suggests new uses for GaN in optical switching applications. Pump-probe spectroscopy was also used to show at what optical excitation densities excitons were dissociated due to scattering and screening by free carriers. The results indicate that excitons are no longer present

in highly excited GaN for excitation densities a few times the SE threshold at 10 K, indicating that EHP recombination dominates at these high excitation densities, even at cryogenic temperatures.

The most extensive chapter of this thesis is concerned with the optical properties of highly excited InGaN/GaN multiple quantum well blue laser structures. This work was undertaken to substantially add to the knowledge base of the high excitation density optical properties of these technologically important structures. This chapter included the results of several unique studies, including “energy selective” optically pumped SE studies, excitation length dependent SE studies, and nondegenerate optical pump-probe studies, combined with traditional temperature dependent SE and variable-stripe modal gain studies. These studies, when combined, provide a unique and extensive overview of the optical processes leading to SE and gain in these structures. The observed behavior is shown to differ greatly from traditional gain mechanism in direct gap semiconductors and is attributed to stimulated recombination of carriers localized at potential fluctuations in the InGaN active layers.

There are, of course, many things that are still unknown about the optical properties of the group III nitrides, but this work has served to chip away at some of the unknowns. This is evidenced by the number of publications and presentations that have grown out of these studies over the past several years. With a little luck, this will continue to be the case in the future. Better insight into the optical phenomena associated with SE and lasing in the group III nitrides is important, not only for general physical insight, but also (and most immediately) as an aid in designing viable laser devices. With this said, I end this chapter in my life.

BIBLIOGRAPHY

1. J.I. Pankove, E.A. Miller, and J.E. Berkeyheiser, RCA Review **32**, 383 (1971).
2. J.I. Pankove and J.A. Hutchby, Appl. Phys. Lett. **24**, 281 (1974).
3. H. Amano, M. Kito, K. Hiramatsu, and I. Akasaki, Jpn. J. Appl. Phys. **28**, L2112 (1989).
4. S. Nakamura, M. Senoh, S.I. Nagahama, N. Iwasa, T. Yamada, T. Matsushita, H. Kiyoku, Y. Sugimoto, T. Kozaki, H. Umemoto, M. Sano, and K. Chocho, Jpn. J. Appl. Phys. **36**, L1568 (1997).
5. R. Szweda and K. Gurnett, *Gallium Nitride Related Wide Bandgap Materials*, Elsevier, Oxford, 1997.
6. S. Nakamura and G. Fasol, *The Blue Laser Diode*, Springer, New York, 1997.
7. J. Duboz and M. Khan, in, *Group III Nitride Semiconductor Compounds: Physics and Applications*, Oxford Univ. Press, New York, 1998.
8. C. Klingshirn and H. Haug, Phys. Rep. **70**, 315 (1981).
9. H. Schrey and C. Klingshirn, Phys. Stat. Sol. b **90**, 67 (1978).
10. R. de Laer Kronig and W.J. Penney, Proc. Roy. Soc. London A **130**, 499 (1930).
11. J.I. Frenkel, Phys. Rev. **37**, 17 (1931).
12. J. Dimmock, *Semiconductors and Semimetals*, volume 3, Academic Press, New York, 1967.
13. G.H. Wannier, Phys. Rev. **52**, 191 (1937).
14. R.J. Elliot, Phys. Rev. **108**, 1384 (1957).
15. H. Frohlich, in, *Polarons and Excitons*, Plenum Press, New York, 1963.
16. K.J. Nash and D.J. Mowbray, J. of Lumin. **44**, 315 (1989).
17. A.J. Fischer, D.S. Kim, J. Hays, W. Shan, J.J. Song, D.B. Eason, J. Ren, J.F. Schetzina, H. Luo, Z.Q. Zhu, T. Yao, J.F. Klem, and W. Schaefer, Phys. Rev. Lett. **73**, 2368 (1994).

18. D.S. Kim, J. Shaw, J.E. Cunningham, T.C. Damen, W. Schaefer, M. Hartmann, and S. Schmitt-Rink, *Phys. Rev. Lett.* **69**, 1008 (1992).
19. S. Rudin, T. Reinecke, and B. Segall, *Phys. Rev. B* **42**, 11218 (1992).
20. A.J. Fischer, W. Shan, G.H. Park, J.J. Song, D.S. Kim, D.S. Yee, R. Horning, B. Goldenberg, *Phys. Rev. B* **56**, 1077 (1997).
21. A.J. Fischer, W. Shan, J.J. Song, Y.C. Chang, R. Horning, and B. Goldenberg, *Appl. Phys. Lett.* **71**, 1981 (1997).
22. C. Benoit a la Guillaume, J.M. Debever, and F. Salvan, *Phys. Rev.* **177**, 567 (1969).
23. R. Levy and J.B. Grun, *Phys. Stat. Sol. a* **22**, 11 (1974).
24. H. Buttner, *Phys. Stat. Sol* **42**, 775 (1970).
25. A. Yariv, *Quantum Electronics*, Wiley, New York, 1989.
26. G.E. Kimball, *J. Chem Phys.* **3**, 560 (1935).
27. E. Kuphal, *Solid State Electron.* **24**, 69 (1981).
28. J.M. Hvam and E. Ejder, *J. of Lumin.* **12/13**, 611 (1976).
29. H. Haug and S.W. Koch, *Phys. Stat. Sol. b* **82**, 531 (1977).
30. A. Yariv, *Optical Electronics*, Saunders College Publishing, San Francisco, 1991.
31. S.N. Mohammad and H. Morkoc, *Prog. Quant. Electr.* **20**, 361 (1996).
32. B. Gil, editor, *Group III Nitride Semiconductor Compounds: Physics and Applications*, Oxford Univ. Press, New York, 1998.
33. R. Dingle and M. Ilegems, *Solid State Commun.* **9**, 175 (1971).
34. R. Dingle, D.D. Sell, S.E. Stokowski, and M. Ilegems, *Phys. Rev. B* **4**, 1211 (1971).
35. W. Shan, X.C. Xie, J.J. Song, and B. Goldenberg, *Appl. Phys. Lett.* **67**, 2512 (1995).
36. W. Shan, B.D. Little, A.J. Fischer, J.J. Song, B. Goldenberg, W.G. Perry, M.D. Bremser, and R.F. Davis, *Phys. Rev. B* **54**, 16369 (1996).
37. S. Chichibu, A. Shikanai, T. Azuhata, T. Sota, A. Kuramata, K. Horino, and S. Nakamura, *Appl. Phys. Lett.* **68**, 3766 (1996).
38. M. Tcholinkeu, O. Briot, B. Gil, J.P. Alexis, and R.L. Aulombard, *J. Appl. Phys.* **80**, 5352 (1996).

39. B. Gil, O. Briot, and R.L. Aulombard, *Phys. Rev. B* **52** (1995).
40. W. Reiger, T. Metzger, H. Angerer, R. Dimitrov, O. Ambacher, and M. Sturtzmann, *Appl. Phys. Lett.* **68**, 970 (1996).
41. W. Shan, A.J. Fischer, J.J. Song, G. Bulman, H.S. Kong, M.T. Leonard, W.C. Perry, M.D. Bremser, and R.F. Davis, *Appl. Phys. Lett.* **69**, 740 (1996).
42. D. Volm, K. Oettinger, T. Streibl, D. Kovakev, M. Ben-Chorin, J. Diener, B.K. Meyer, J. Majewski, L. Eckey, A. Koffmann, H. Amano, I. Akasaki, K. Hiramatsu, and T. Detchprohm, *Phys. Rev. B* **53**, 16543 (1996).
43. H. Amano, K. Hiramatsu, and I. Akasaki, *Jpn. J. Appl. Phys.* **27**, L1384 (1988).
44. K. Osamura, S. Naka, and Y. Murakami, *J. Appl. Phys.* **46**, 3432 (1975).
45. S. Sze, *Physics of Semiconductor Devices*, Wiley, New York, 1981.
46. F. Ponce, in, *Group III Nitride Semiconductor Compounds: Physics and Applications*, Oxford Univ. Press, New York, 1998.
47. W. Lambrecht and B. Segall, *Proc. of Mater. Res. Soc. Symp. on Wide Bandgap Semicond.*, Philadelphia: Elsevier Science, 1992.
48. J. Song and W. Shan, in, *Group III Nitride Semiconductor Compounds: Physics and Applications*, Oxford Univ. Press, New York, 1998.
49. W. Shan, T.J. Schmidt, X.H. Yang, J.J. Song, and B. Goldenberg, *J. Appl. Phys.* **79**, 3691 (1996).
50. R. Dingle, K.L. Shaklee, and R.B. Zetterstrom, *Appl. Phys. Lett.* **19**, 5 (1971).
51. B. Goldenberg, J.D. Zook, and R.J. Ulmer, *Appl. Phys. Lett.* **62**, 381 (1993).
52. T.W. Weeks, Jr., M.D. Bremser, K.S. Ailey, E. Carlson, W.G. Perry, and R.F. Davis, *Appl. Phys. Lett.* **67**, 401 (1995).
53. Saito and E. Goebel, *Phys. Rev. B* **31**, 2360 (1982).
54. H. Shoji, Y. Nakata, K. Mukai, Y. Sugiyama, M. Sugawara, N. Yokoyama, and H. Ishikawa, *Appl. Phys. Lett.* **71**, 193 (1997).
55. H. Jeon, J. Ding, A.V. Nurmikko, W. Xie, D.C. Grillo, M. Kobayashi, R.L. Gunshor, G.C. Hua, and N. Otsuka, *Appl. Phys. Lett.* **60**, 2045 (1992).
56. X.H. Yang, T.J. Schmidt, W. Shan, J.J. Song, and B. Goldenberg, *Appl. Phys. Lett.* **66**, 1 (1995).
57. S. Nakamura, M. Senoh, S.I. Nagahama, N. Iwasa, T. Yamada, T. Matsushita, H. Kiyoku, and Y. Sugimoto, *Appl. Phys. Lett.* **68**, 3269 (1996).

58. J.J Song and W.C. Wang, J. Appl. Phys. **55**, 660 (1984).
59. R. L. M. Voos and J. Shah, *Optical Properties of Solids*, North-Holland, Amsterdam, 1980.
60. A.I. Dirochka, M.N. Zargar'yants, A.A. Kiselev, and E.V. Sinitsyn, Sov. Phys. Semicond. **13**, 113 (1979).
61. D. Wiesmann, I. Brener, L. Pfeiffer, M.A. Khan, and C.J. Sun, Appl. Phys. Lett. **69**, 3384 (1996).
62. J. Holst, L. Eckey, A. Hoffmann, I. Broser, B. Schottker, D.J. As, D. Schikora, and L. Lischka, Appl. Phys. Lett. **72**, 1998 (1998).
63. S. Bidnyk, T.J. Schmidt, B.D. Little, J.J. Song, B. Goldenberg, W.G. Perry, M.D. Bremser, and R.F. Davis, Submitted to Appl. Phys. Lett. (1998).
64. T.J. Schmidt, S. Bidnyk, Y.H. Cho, A.J. Fischer, J.J. Song, S. Keller, U.K. Mishra, and S.P. DenBaars, Submitted to Appl. Phys. Lett. (1998).
65. S. Bidnyk, T.J. Schmidt, Y.H. Cho, G.H. Gainer, J.J. Song, S. Keller, U.K. Mishra, and S.P. DenBaars, Appl. Phys. Lett. **72**, 1623 (1998).
66. S. Chichibu, T. Azuhata, T. Sota, and S. Nakamura, Appl. Phys. Lett. **69**, 4188 (1996).
67. Y. Narakawa, Y. Kuwakima, S. Fujita, and S. Nakamura, Phys. Rev. B. **55**, R1938 (1997).
68. T.J. Schmidt, Y.H. Cho, G.H. Gainer, J.J. Song, S. Keller, U.K. Mishra, and S.P. DenBaars, Appl. Phys. Lett. **73**, 560 (1998).
69. T.J. Schmidt, Y.H. Cho, G.H. Gainer, J.J. Song, S. Keller, U.K. Mishra, and S.P. DenBaars, Appl. Phys. Lett. **73**, 1892 (1998).
70. W. Shan, T.J. Schmidt, X.H. Yang, S.J. Hwang, J.J. song, and B. Goldenberg, Appl. Phys. Lett. **66**, 985 (1995).
71. T.J. Schmidt, J.J. Song, Y.C. Chang, R. Horning, and B. Goldenberg, Appl. Phys. Lett. **72**, 1504 (1998).
72. J.J. Song, W. Shan, T.J. Schmidt, X.H. Yang, A.J. Fischer, S.J. Hwang, B. Taheri, B. Goldenberg, R. Horning, A. Salvador, W. Kim, O. Aktas, A. Botchkarev, and H. Morkoc, SPIE Conf. Proceed. **2693**, 86 (1996).
73. T.J. Schmidt, X.H. Yang, W. Shan, J.J. Song, A. Salvador, W. Kim, O. Aktas, A. Botchkarev, and H. Morkoc, Appl. Phys. Lett. **68**, 1820 (1996).
74. S. Nakamura, M. Senoh, N. Iwasa, S. Nagahama, T. Yamada, and T. Mukai, Jpn. J. Appl. Phys. **34**, L1332 (1995).

75. S. Nakamura, M. Senoh, S. Nagahama, N. Iwasa, T. Yamada, T. Matsushita, Y. Sugimoto, and H. Kiyoku, *Appl. Phys. Lett.* **70**, 868 (1997).
76. R. Zimmermann, M. Hofmann, D. Weber, J. Mobius, A. Euteneuer, W.W. Ruhle, E.O. Goebel, B.K. Meyer, H. Amano, and I. Akasaki, *MRS Internet J. Nitride Semicond. Res.* **2**, Art. 24 (1997).
77. C. K. Sun, F. Vallee, S. Keller, J.E. Bowers, and S.P. Denbaars, *Appl. Phys. Lett.* **70**, 2004 (1997).
78. B. Taheri, J. Hays, and J.J. Song, *Appl. Phys. Lett.* **68**, 587 (1996).
79. H. Haag, P. Gilliot, D. Ohlmann, R. Levy, O. Briot, and R.L. Aulombard, *MRS Internet J. Nitride Semicond. Res.* **2**, Art. 21 (1997).
80. T.J. Schmidt, Y.C. Chang, and J.J. Song, *Proc. SPIE* **3419**, 61 (1998).
81. W. Shan, T.J. Schmidt, R.J. Hauenstein, J.J. song, and B. Goldenberg, *Appl. Phys. Lett.* **66**, 3492 (1995).
82. S.D. Lester, F.A. Ponce, M.G. Craford, and D.A. Steigerwald, *Appl. Phys. Lett.* **66**, 1249 (1995).
83. S.D. Hersee, J.C. Ramer, and K.J. Malloy, *Mater. Res. Bull.* **22**, 45 (1997).
84. Y. Varshni, *Physica* **34**, 149 (1967).
85. H. Haug and S. Schmitt-Rink, *J. Opt. Soc. Am. B* **2**, 1135 (1985).
86. T. Takeuchi, H. Takeuchi, S. Sota, H. Sakai, H. Amano, and I. Akasaki, *Jpn. J. Appl. Phys.* **36**, L177 (1997).
87. M.D. McCluskey, C.G. Van deWalle, C.P. Master, L.T. Romano, and N.M. Johnson, *Appl. Phys. Lett.* **72**, 2725 (1998).
88. S. Keller, A.C. Abare, M.S. Minsky, X.H. Wu, M.P. Mack, J.S. Speck, E. Hu, L.A. Coldren, U.K. Mishra, and S.P. DenBaars, *Materials Science Forum* **264-268**, 1157 (1998).
89. B.P. Keller, S. Keller, D. Kapolnek, W.N. Jiang, X.F. Wu, H. Masui, X.H. Wu, B. Heying, J.S. Speck, U.K. Mishra, and S.P. DenBaars, *J. Electron. Mater.* **24**, 1707 (1995).
90. Y.H. Cho, J.J. Song, S. Keller, M.S. Minsky, E. Hu, U.K. Mishra, and S.P. DenBaars, *Appl. Phys. Lett.* **73**, 1128 (1998).
91. B.W. Lim, Q.C. Chen, J.Y. Yang, and M.A. Khan, *Appl. Phys. Lett.* **68**, 3761 (1996).
92. Y.F. Wu, B.P. Keller, S. Keller, D. Kapolnek, P. Kozodoy, S.P. DenBaars, and U.K. Mishra, *Appl. Phys. Lett.* **69**, 1438 (1996).

93. A.S. Zubrilov, V.I. Nikolaev, D.V. Tsvetkov, V.A. Dmitriev, K.G. Irvine, J.A. Edmond, and C.H. Carter, Jr., *Appl. Phys. Lett.* **67**, 533 (1995).
94. S. Nakamura, M. Senoh, S.I. Nagahama, N. Iwasa, T. Yamada, T. Matsushita, Y. Sugimoto, and H. Kiyoku, *Appl. Phys. Lett.* **69**, 1477 (1996).
95. P.D. Floyd and D.W. Treat, *Appl. Phys. Lett.* **70**, 2493 (1997).
96. J.M. Gaines, R.R. Drenten, K.W. Haberern, T. Marshall, P. Mensz, and J. Petruzzello, *Appl. Phys. Lett.* **62**, 2462 (1993).
97. W. Fang and S.L. Chuang, *Appl. Phys. Lett.* **67**, 751 (1995).
98. S. Ruvimov, Z. Liliental-Weber, T. Suski, J.W. Ager III, J. Washburn, J. Kreuger, C. Kisielowski, E.R. Weber, H. Amano, and I. Akasaki, *Appl. Phys. Lett.* **69**, 990 (1996).
99. E.F. Schubert, I.D. Geopfert, W. Grieshaber, and J.M. Redwing, *Appl. Phys. Lett.* **71**, 921 (1997).
100. S. Keller, A.C. Abare, M.S. Minski, X.H. Wu, M.P. Mack, J.S. Speck, E. Hu, L.A. Coldren, U.K. Mishra, and S.P. DenBaars, *Proc. of International Conference on Silicon Carbide, III-Nitrides, and Related Materials*, Stockholm, Sweden, 1997.
101. P.A. Grudowski, C.J. Eiting, J. Park, B.S. Shelton, D.J.H. Lambert, and R.D. Dupuis, *Appl. Phys. Lett.* **71**, 1537 (1997).
102. K.C. Zeng, J.Y. Lin, X.H. Jiang, A. Salvador, G. Popovici, H. Tang, W. Kim, and H. Morkoc, *Appl. Phys. Lett.* **71**, 1368 (1997).
103. S. Nakamura, M. Senoh, S. Nagahama, N. Iwasa, T. Yamada, T. Matsushita, Y. Sugimoto, and H. Kiyoku, *Appl. Phys. Lett.* **69**, 4056 (1996).
104. S. Nakamura, M. Senoh, S.I. Nagahama, N. Iwasa, T. Yamada, T. Matsushita, Y. Sugimoto, and H. Kiyoku, *Appl. Phys. Lett.* **70**, 1417 (1997).
105. S. Nakamura, M. Senoh, S.I. Nagahama, N. Iwasa, T. Yamada, T. Matsushita, Y. Sugimoto, and H. Kiyoku, *Appl. Phys. Lett.* **70**, 2753 (1997).
106. Y. Narukawa, Y. Kawakami, M. Funato, S. Fujita, and S. Nakamura, *Appl. Phys. Lett.* **70**, 981 (1997).
107. A. Satake, Y. Masumoto, T. Miyajima, T. Asatsuma, F. Nakamura, and M. Ikeda, *Phys. Rev. B* **57**, R2041 (1998).
108. T. Deguchi, T. Azuhata, T. Sota, S. Chichibu, M. Arita, H. Nakanishi, and S. Nakamura, *Semicond. Sci. Technol.* **13**, 97 (1998).

109. E.S. Jeon, V. Kozlov, Y.K. Song, A. Vertikov, M. Kuball, A.V. Nurmikko, H. Liu, C. Chen, R.S. Kern, C.P. Kuo, and M.G. Craford, *Appl. Phys. Lett.* **69**, 4194 (1996).
110. J.S. Im, S. Heppel, H. Kollmer, A. Sohmer, J. Off, F. Scholz, and A. Hangleiter, *Proceed. 2nd International Conference Nitride Semicond.*, Tokushima, Japan, 1997.
111. M. Kuball, E.S. Jeon, Y.K. Song, A.V. Nurmikko, P. Kozodoy, A. Abare, S. Keller, L.A. Coldren, U.K. Mishra, S.P. DenBaars, and D.A. Steigerwald, *Appl. Phys. Lett.* **70**, 2580 (1997).
112. G. Mohs, T. Aoki, M. Nagai, R. Shimano, M. Kuwata-Gonokami, and S. Nakamura, *Proceed. 2nd International Conference Nitride Semicond.*, Tokushima, Japan, 1997.
113. S. Nakamura, *MRS Internet J. Nitride Semicond. Res.* **2**, Art. 5 (1997).
114. M.P. Mack, A. Abare, M. Aizcorbe, P. Kozodoy, S. Keller, U.K. Mishra, L. Coldren, and S.P. DenBaars, *MRS Internet J. Nitride Semicond. Res.* **2**, Art. 41 (1997).
115. S. Bidnyk, T.J. Schmidt, G.H. Park, and J.J. Song, *Appl. Phys. Lett.* **71**, 729 (1997).
116. Y.H. Cho, G.H. Gainer, A.J. Fischer, J.J. Song, S. Keller, U.K. Mishra, and S.P. DenBaars, *Appl. Phys. Lett.* **73**, 1370 (1998).
117. C.H. Henry, R.A. Logan, and F.R. Merritt, *J. Appl. Phys.* **51**, 3042 (1980).
118. K.L. Shaklee and R.F. Leheny, *Appl. Phys. Lett.* **18**, 475 (1971).
119. I.-Hisu Ho and G.B. Stringfellow, *Appl. Phys. Lett.* **69**, 2701 (1996).
120. K.P. O'Donnell, T. Breitkopf, H. Kalt, W. Van der Stricht, I. Moerman, P. Demeester, and P.G. Middleton, *Appl. Phys. Lett.* **70**, 1843 (1997).
121. P.G. Eliseev, P. Perlin, J. Lee, and M. Osinski, *Appl. Phys. Lett.* **71**, 569 (1997).
122. S. Shichibu, K. Wada, and S. Nakamura, *Appl. Phys. Lett.* **71**, 2346 (1997).
123. M.B. Nardelli, K. Rapcewicz, and J. Bernholc, *Appl. Phys. Lett.* **71**, 3135 (1997).
124. S. Chichibu, T. Azuhata, T. Sota, and S. Nakamura, *Proceed. 2nd International Conference Nitride Semicond.*, Tokushima, Japan, 1997.
125. A. Satake, Y. Masumoto, T. Miyajima, T. Asatsuma, and M. Ikeda, *Proceed. 2nd International Conference Nitride Semicond.*, Tokushima, Japan, 1997.

126. T. Taguchi, Y. Yamada, F. Sasaki, S. Kobayashi, and T. Tani, *Proceed. 2nd International Conference Nitride Semicond.*, Tokushima, Japan, 1997.
127. Y.K. Song, M. Kuball, A.V. Nurmikko, G.E. Bulman, K. Doverspike, S.T. Shepard, T.W. Weeks, M. Leonard, H.S. Kong, H. Dieringer, and J. Edmond, *Appl. Phys. Lett.* **72**, 1418 (1998).
128. G. Frankowski, F. Steuber, V. Harle, F. Scholz, and A. Hangleiter, *Appl. Phys. Lett.* **68**, 3746 (1996).
129. S. Nakamura, M. Senoh, S.I. Nagahama, N. Iwasa, T. Yamada, T. Matsushita, Y. Sugimoto, and H. Kiyoku, *Appl. Phys. Lett.* **69**, 1568 (1996).
130. J. Feldmann, G. Peter, E.O. Gobel, P. Dawson, K. Moore, C. Foxon, and R.J. Elliott, *Phys. Rev. Lett.* **59**, 2337 (1987).
131. C.I. Harris, B. Monemar, H. Amano, and I. Akasaki, *Appl. Phys. Lett.* **67**, 840 (1995).
132. T. Breitkopf, H. Kalt, C. Klingshirn, and A. Reznitsky, *J. Opt. Soc. Am. B.* **13**, 1251 (1996).
133. W.C. Johnson, J.B. Parson, and M.C. Crew, *J. Phys. Chem.* **36**, 2561 (1932).
134. R. de Laer Kronig, *J. Opt. Soc. Am.* **12**, 547 (1926).
135. E. Ejder, *Phys. Stat. Sol.* **6**, 445 (1971).
136. M.E. Lin, B.N. Sverdlov, S. Strite, H. Morkoc, and A.E. Drakin, *Electron. Lett.* **29**, 1759 (1993).
137. G. Yu, G. Wang, H. Ishikawa, M. Umeno, T. Soga, T. Egawa, J. Watanabe, and T. Jimbo, *Appl. Phys. Lett.* **70**, 3209 (1997).
138. T. Moss, *Optical Properties of Semiconductors*, London, 1959.

APPENDICES

APPENDIX A

POLISHING CAVITY FACETS FOR GROUP-III NITRIDE LASER STRUCTURES

Since Johnson *et al.* first synthesized GaN in 1928 [133], a great variety of experiments have repeatedly indicated that GaN is an exceedingly stable compound of significant hardness. In fact, this chemical stability at elevated temperatures and hardness have made GaN an attractive material for protective coatings. However, due to its wide band gap, it is also an excellent candidate as a material for devices required to operate at elevated temperatures and/or in caustic environments. In fact, the majority of research conducted on GaN is aimed towards its semiconductor device applications, as is the subject of this monograph. While the thermal stability of GaN may aid in freedom in high temperature processing, its chemical stability and hardness present a technological challenge for device processing and fabrication. Conventional wet etching techniques typically used in semiconductor processing are not successful for GaN device fabrication. In particular, when GaN is grown on (0001) oriented sapphire, it is not cleavable. This, combined with a lack of convenient etching procedures and GaN's great hardness make facet formation for laser diodes difficult. To aid in our studies on the lasing properties of the group III nitrides, a mechanical polishing technique was developed to obtain good quality, repeatable, facets in laser structures.

Before You Begin

The following procedure assumes that you have sectioned the epilayers into suitable sizes for polishing of the edge facets. This is typically accomplished using a

diamond saw (such as Buehler Isomet[©] or equivalent). Typical sample sizes after sectioning are 2 x 5 x 0.4 mm, where the 0.4 mm dimension is the thickness of the substrate and the 2 mm dimension is the cavity thickness you will start with before reducing this dimension through polishing. Typical final cavity lengths after polishing are around 0.4 mm, so the 2 mm starting thickness allows us to remove enough material so that we are past the region of cutting induced damage and stress. Sectioning itself requires a little practice, but with a little practice and a steady hand acceptable results can be obtained. The cutting procedure is not given here because of length considerations, and a suitable technique is left as an exercise for the reader. As for polishing, the quality that most leads to success when preparing these cavity facets is patience, the more of it the better.

Squeaks

If at any point during the polishing procedure you hear a squeak, stop polishing immediately and check the samples (preferably under a microscope)! Squeaks are most often caused by pieces of sample or braces that have chipped off and are scratching the sample surface. Wash the samples, polishing setup, and polishing disk before resuming polishing. Squeaks are also on occasion caused by the rollers that keep the polishing jig on the polishing plate. If you determine this to be the case, a little lubricant applied to the wheel's axle will remedy the situation. Throughout the following procedure, your best chance for success is to be careful and patient.

Adjusting the Guide Roller Position

Every time a different polishing plate is used, the height of the guide rollers will have to be adjusted to guide the polishing jig on the polishing plate correctly. Use the two allen bolts on the left side of the polishing rig to adjust the rollers' height and azimuthal angle. Adjust the position at which the jig is held on the polishing plate by loosening and retightening the pivot bolt above the rollers (not their axle bolts). When properly positioned, the rollers should hold the jig so that its outer

edge lines up with the outer edge of the polishing plate. This ensures that the plate does not become concave as it wears. These adjustments are necessary because the polishing plates were custom made to our specifications by the Physics and Chemistry Instrument Shop at OSU. They tend to differ in height and diameter (slightly) from plate to plate, especially when going from one plate material to another (*i.e.* from a copper plate to a tin plate).

Adjusting the Polishing Pressure

Through trial and error, we have arrived at an optimal polishing pressure of approximately 300 g/cm^2 . Sapphire is typically polished at 100 g/cm^2 , so our value is in reasonable agreement. We are, of course, polishing a thin layer (on the order of several μm) grown on sapphire (or SiC), so our conditions are a little different. To adjust the pressure exerted on the samples by the polishing jig, turn the load adjustment screw on the polishing jig, see Fig. 76. Turning the ring clockwise to increase pressure and counter-clockwise to decrease pressure. To get the right pressure, first turn the adjustment screw all the way clockwise until the full weight of the polishing jig is on the sample (approximately 1,500 g). Then, loosen the shaft set screw and re-tighten it when the collar that compresses the spring just barely rests on the spring. The pressure is then adjusted by turning the spring adjustment screw up N turns, where N is given by $(6-N)(1500 \text{ g})/A = 300 \text{ g/cm}^2$, where A is the combined area of the samples and braces (in cm^2) to be polished. It takes 6 turns up on the spring adjustment to lift the samples off of the polishing disk (zero pressure), and zero turns leaves the full 1500 g on the samples. If the samples (including braces) seem brittle and are chipping off at an unacceptable rate, decrease the pressure to around 200 g/cm^2 .

Monitoring the Sample Thickness

The best way to monitor the thickness of the samples is to use the depth of focus of an optical microscope. Position and align the sample the same way on

the microscope each time to ensure a consistent thickness measurement. Do not rely on the stock removal indicator on the polishing jig to monitor the thickness accurately. It is good for an estimate of stock removal during grinding and the first steps of polishing, but becomes increasingly less accurate as the surface finish of the samples improves. This is because it measures the thickness relative to the feet of the polishing jig, which polish at about the same rate as the samples during the later stages of polishing.

Calculating Particle Size From Mesh

Often the diamond particle size is given in mesh, not in μm . To convert from mesh to μm , use the following formula:

$$\text{Diameter (in } \mu\text{m)} = \left(\frac{2.54}{\text{mesh}} \right) 10^4$$

(mesh is defined as the reciprocal of the particle diameter in inches). Dissolve the diamond paste in OptiClear[©] solvent (water will not dissolve the paste to an acceptable uniformity). We have found that about 1 gram of diamond paste dissolved in 500 ml of OptiClear[©] gives optimal results.

Avoiding Cross-Contamination

Cross-contamination of the polishing plates is potentially the biggest source of poor polishing results. This occurs when larger diamond particles are transferred to a polishing plate of smaller diamond size due to improper cleaning of the equipment between polishing steps. This contamination is often irreversible and only the introduction of a new, clean polishing plate can remedy the situation. This is obviously a situation one wants to avoid, especially since the plates are often custom made. To ensure no cross-contamination occurs, clean all equipment well when switching polishing plates. This includes the sample surface, the polishing jig itself (being especially careful about cleaning the conditioning ring), all materials that come in contact with the diamond/OptiClear[©] solution, and any other equipment/surfaces that may come in contact with the polishing plate. It is equally important not to

contaminate the diamond/OptiClear[©] solution itself when mixing it up by making sure the container (squeeze bottle) is clean and does not come in contact with larger diamond particles. On a related note, make sure all bottles of diamond/OptiClear[©] solution are well marked.

Mounting Samples for Polishing

The following procedures are the end result of a lot of trial and error experiments on sample mounting. Since we are polishing the edge facets of thin films (on the order of several μm) to a high degree of parallel and surface quality, we do not want to damage the resulting facets when dismounting the samples from the polishing mount. This requires that the glue used to bond the samples to the mount be dissolvable in a common (and preferably relatively safe) solvent, such as acetone. There are plenty of acetone based glues on the market, but none were found to adhere the samples to the mount adequately during the polishing routine. For this reason, we were forced to use two types of glue to bond the samples to the mount: an acetone based one to bond the samples to the mount, and a 2-Ton epoxy overlaid on the other for all around bonding of the sample and support braces to the mount. When done properly, only a thin region where the samples contact the mount and support braces is bonded with the acetone based glue while the support braces are bonded with the 2-Ton epoxy. We found Duco[©] cement served our purpose best of all the acetone-dissolvable glues we tried.

The samples and support braces are mounted on a porous substrate to ensure the samples lie parallel with the polishing jig surface. The porous substrate allows the glue to seep into the pores of the substrate and the sample to fit flush with the substrate surface, allowing a high degree of facet parallelness in the resulting laser cavity.

Grinding the Porous Substrate Flat

With hot wax (Crystal Bond[©] from Buehler), glue a 25 x 25 mm porous substrate slab to the polishing jig. Adjust the load adjustment screw to provide the maximum load (1500 g) on the porous substrate slab. Grind the porous substrate flat and parallel to the polishing jig surface using first the 70 μm diamond embedded steel disk and then the 30 μm diamond embedded steel disk. This is a very important step in that it ensures the sample will be polished flat with parallel facets required for lasing. After the grinding, the pores in the substrate should still be open so the samples to be mounted will adhere well and sit flat. Do not grind so much that the pores are mostly filled with the mounting wax. After grinding, clean the jig and substrate well with water. Dry thoroughly using compressed air. This will also force the water out of the pores of the substrate.

Gluing the Samples to the Braces

The samples to be polished must be held tightly between sapphire (quartz can be substituted with acceptable results) braces so the diamond polishing particles will not impact the edges of the sample, but will instead roll over the edges. The braces must have flat surfaces to contact well with and protect the GaN layer(s). They should also be at least as thick as the starting cavity length to provide protection during the initial grinding process. Use the clamping equipment to tightly press the braces together with the samples in between, as illustrated in Fig. 77(a). It works well to do this step on a glass microscope slide. Smearing the glass slide with a very thin films of grease will ensure the pieces do not stick to it during the glue-up process. You should use a thin film of Duco[©] cement to join the sample surfaces to the braces. After the Duco[©] cement has set up, the samples and braces (still clamped together) can be glued to the porous substrate from the previous step using the Duco[©] cement and the 2-Ton epoxy. The Duco[©] cement is used in the region in contact with the samples and the 2-Ton epoxy is used everywhere else, as shown in Fig. 77(b). Use a very thin layer of the Duco[©] cement so it isn't squeezed into

other areas when the porous substrate is pressed on the samples/braces. Press the clamped braces and samples into the porous substrate. Press them straight down to avoid smearing and mixing the two different glues. Use a very slight side to side motion to seat the samples/braces firmly against the porous substrate. You will know they are seated well when it becomes very difficult to slide the samples along the substrate surface and you can feel the abrasiveness of the substrate. Orient the samples on the jig mount as shown in Fig. 78. This will allow the braces to optimally protect the GaN facets by being the first to contact each diamond particle as the jig spins on the polishing plate. The porous substrate should be mounted towards the outer edge of the jig mount to allow for the most distance traveled per rotation of the jig on the polishing plate. The gluing procedure must be completed quickly because the Duco[®] cement dries in a few minutes. If the cement sets up before you complete the procedure, you can dissolve it in acetone and start over. After gluing the samples, let the glues harden up overnight. The amount and degree of success experienced during the polishing procedure depends directly on how well the samples are glued and protected by the braces, so attention to details must be paid in the preceding steps. A properly glued and braced sample is shown in Fig. 79 under 600X magnification of an optical microscope. The picture was taken near the completion of the polishing procedure. Note that the brace is seated closely to the GaN layer surface (within a μm).

Polishing

With the samples glued correctly, the polishing procedure itself can begin. It will start with rough grinding to remove excess thickness and to level the samples with the braces. It is composed of two steps. Polishing will then start. It is composed of three steps of varying length.

Rough Grinding

70 μm diamond on steel. Begin by grinding with the 70 μm diamond imbedded steel disk. Grind at 120 revolutions per minute (rpm) and a pressure of 300 g/cm². Keep the polishing wheel wet with water to provide the best cutting action and to remove the ground off material from the disk. The depth gauge can be used as an indicator of material removal during this stage. Grind until the braces are flush with the sample surfaces and the large chips induced by the cutting and sectioning procedure are removed. This usually takes less than 20 minutes to complete, but it may take considerably less or more time, depending on the substrate and brace material. Be careful not to grind the samples away completely. Clean the jig, mount, and samples thoroughly before proceeding to the next step.

30 μm diamond on steel. Next, grind with the 30 μm diamond imbedded steel disk using water to lubricate and remove waste. Remove at least 50 μm to erase the damage produced by the previous step. Again, use 300 g/cm² pressure and a polishing plate speed of 120 rpm. This step will typically take about a half hour. The amount of material removed can again be measured (roughly) using the stock removal indicator on the polishing jig. Clean the jig, mount, and samples thoroughly before proceeding to the next step.

Polishing

8.5 μm diamond on copper. Next, polish on a copper disk at 120 rpm and 300 g/cm² using a suspension of 8.5 μm diamond particles in OptiClear[®] solvent. Use the concentration given previously (1 g of paste in 500 ml of solvent). Be sure to use the copper disk designated for this step to avoid cross-contamination. Use a squirt bottle to dispense the polishing solution on the copper plate, making sure to keep the plate wet with solution at all times or the samples will be damaged. Remove at least 30 μm to erase the damage produced by the previous step. Material should be removed at about 10 μm per minute during this step, so this is a good time

to achieve the desired sample thickness. At this point, the stock removal indicator accuracy starts to deteriorate, so don't rely on it completely for sample thickness and do not polish for more than 2 hours without checking the sample thickness under a microscope. Typical surface quality after this step is illustrated in Fig. 80(b) and Fig. 82(b) for GaN grown on SiC and sapphire substrates, respectively. The GaN layer, substrate, and brace areas are indicated in Figs. 80(a) and 82(a) for the respective samples. Clean the jig, mount, and samples thoroughly before proceeding to the next step.

3.2 μm diamond on copper. This step is the same as the previous step, except using 3.2 μm diamond in OptiClear[©] solvent. Use the copper disk designated for 3.2 μm diamond particles. Remove at least 10 μm to remove damage produced by the previous step. This step typically removes about 0.5 μm per minute. Since this step can take a relatively long time, use the automatic drip setup with the magnetic stirrer. Adjust the drip rate to about 6 to 8 drops per minute. Note that the drip rate can change over time as diamond particles and paste clog up the drip tube, so don't leave the polishing setup unattended for extended periods of time. Typical surface quality after this step is illustrated in Fig. 81(a) and Fig. 83(a) for a GaN layer grown on SiC and sapphire, respectively. Clean the jig, mount, and samples thoroughly before proceeding to the next step.

MasterPolish2[©] on tin. This step is the same as the previous step, except using MasterPolish2[©] on the designated tin disk. MasterPolish2[©] from Buehler is 0.06 μm Fe_2O_3 and SiO_2 particles in water at a pH of 10. The particles would normally be too soft to polish the hard crystals we are polishing here, but, with pH 10, very effective mechanochemical polishing is achieved. Use the designated automatic drip setup to dispense the solution at a rate of 6 to 8 drops per minute (or a squeeze bottle can be used). Use the magnetic stirrer to keep the particles suspended well. Do not let the drops of MasterPolish2[©] fall near the polishing jig because the solution will accumulate on the drive/conditioning ring and can lead to

vibrations and skipping as the accumulated solution dries and flakes off. Do this step in no longer than 15 minute intervals, since the solution will build up on the polishing jig. Wash the samples, jig, and tin polishing plate between intervals and check the surface quality and thickness of the samples under a microscope. This step will typically remove 0.3-1 μm per minute, and four 15 minute intervals or less will typically result in the desired cavity facet quality. Typical surface quality after this final step is illustrated in Fig. 81(b) and Fig. 83(b) for a GaN layer grown on SiC and sapphire, respectively. Clean the jig, mount, and samples thoroughly before proceeding to the next step.

Polishing the Second Cavity Facet

Remove the porous substrate from the jig mount by carefully melting the hot wax using a hot plate. Do not heat the jig mount more than necessary, as excess heat can destroy the integrity of the glues used to mount the samples and braces to the porous substrate. After the porous substrate has been removed from the jig mount, clean the sample and brace surface using methanol and lens paper. Be careful not to drag particles from the outer edges to the sample surface. Work from the inside (sample area) outward. Next, mount a new piece of porous substrate to the jig mount and grind it flat, as was done previously. Clean it with water and dry thoroughly with compressed air when completed. Next, glue the polished sample/brace assembly (polished face to the newly ground porous substrate) to the new porous substrate as was done before polishing the first side. Be sure to use Duco[®] cement in the sample region and 2-Ton epoxy in the brace and outer region, as was done before (see Fig. 77(b)). Be sure the polished faces seat flat against the new porous substrate to ensure the two polished facets will be parallel to each other. Allow the glues to dry overnight (at least 12 hours). Repeat the grinding and polishing steps performed on the first side (the original porous substrate will grind away quickly using the 70 μm diamond in steel disk, so be sure to monitor the progress carefully).

Dismounting and Cleaning Polished Samples

Remove the porous substrate from the jig mount using a hot plate to soften the hot wax. Do not use excessive heat to melt the wax, as excess heat can destroy the integrity of the glues used to mount the samples and braces to the porous substrate, making it difficult (or impossible) to remove completely from the sample surface. Wrap the porous substrate (with the samples and braces still glued to it) in lens paper and soak in acetone for several hours to soften the Duco[®] cement. After soaking, carefully pry away the braces (they will still be attached by the 2-Ton epoxy to the porous substrate) from the samples. The Duco[®] cement should have dissolved by this point and the samples (bars) should dislodge easily from the braces and porous substrate. Individually wrap the samples in lens paper and soak in acetone for a few hours to thoroughly remove the Duco[®] cement. Handle the polished samples only by the unpolished edges. Any contact with tweezers (especially metal tweezers) will chip the polished facets, so keep the damage to a minimum on the edges of the polished bars. After soaking a second time, ultrasonically clean the samples using acetone, trichloroethylene, and methanol, in that order.

Typical facet quality achieved using the preceding polishing procedure is illustrated in Fig. 84 for a GaN layer grown on sapphire.

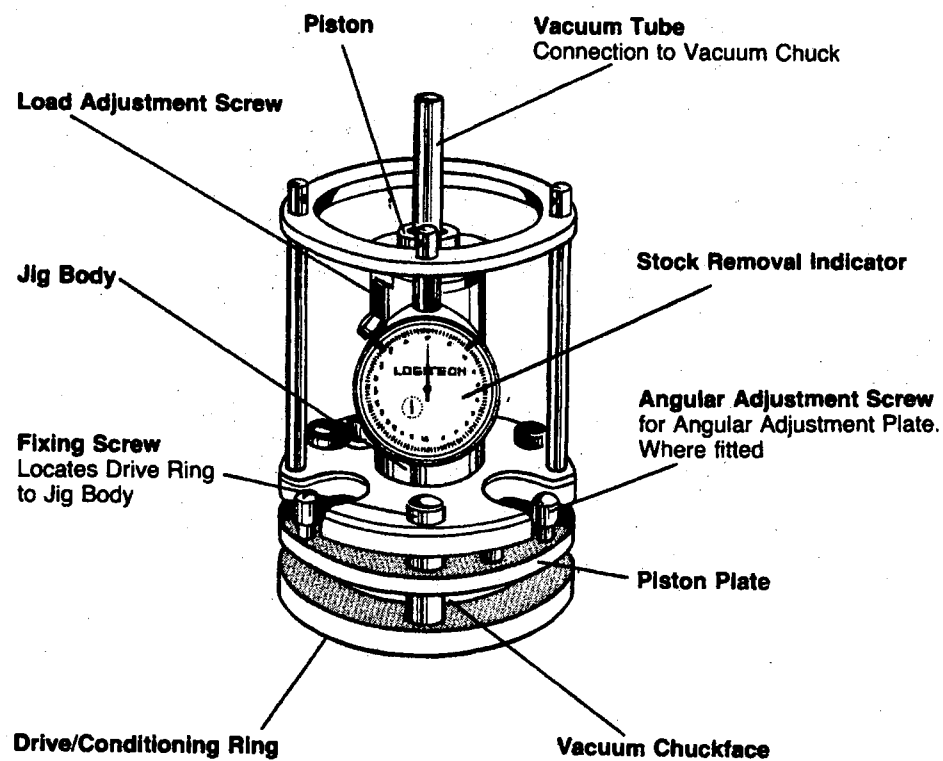


Figure 76. Schematic of the Logitech PP5D precision polishing jig.

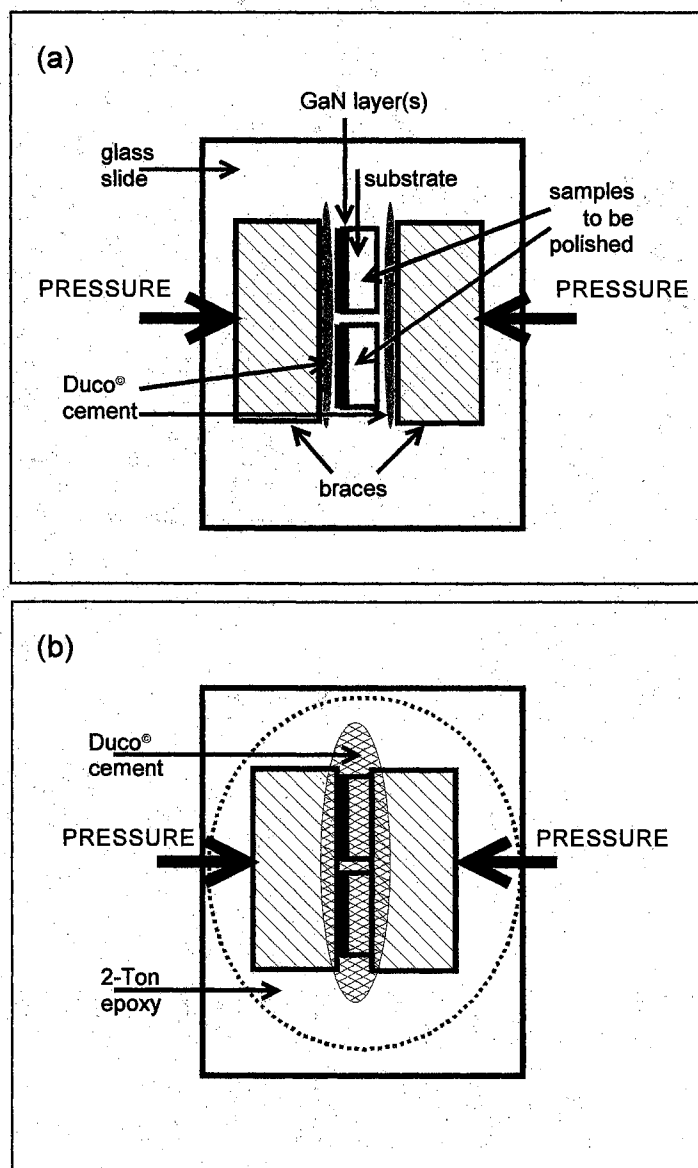


Figure 77. Glue-up schematic of GaN thin films prior to mechanical polishing. (a) Diagram of sample placement and orientation prior to clamping between support braces. (b) Sample orientation and glue location immediately prior to gluing entire assembly to the porous substrate.

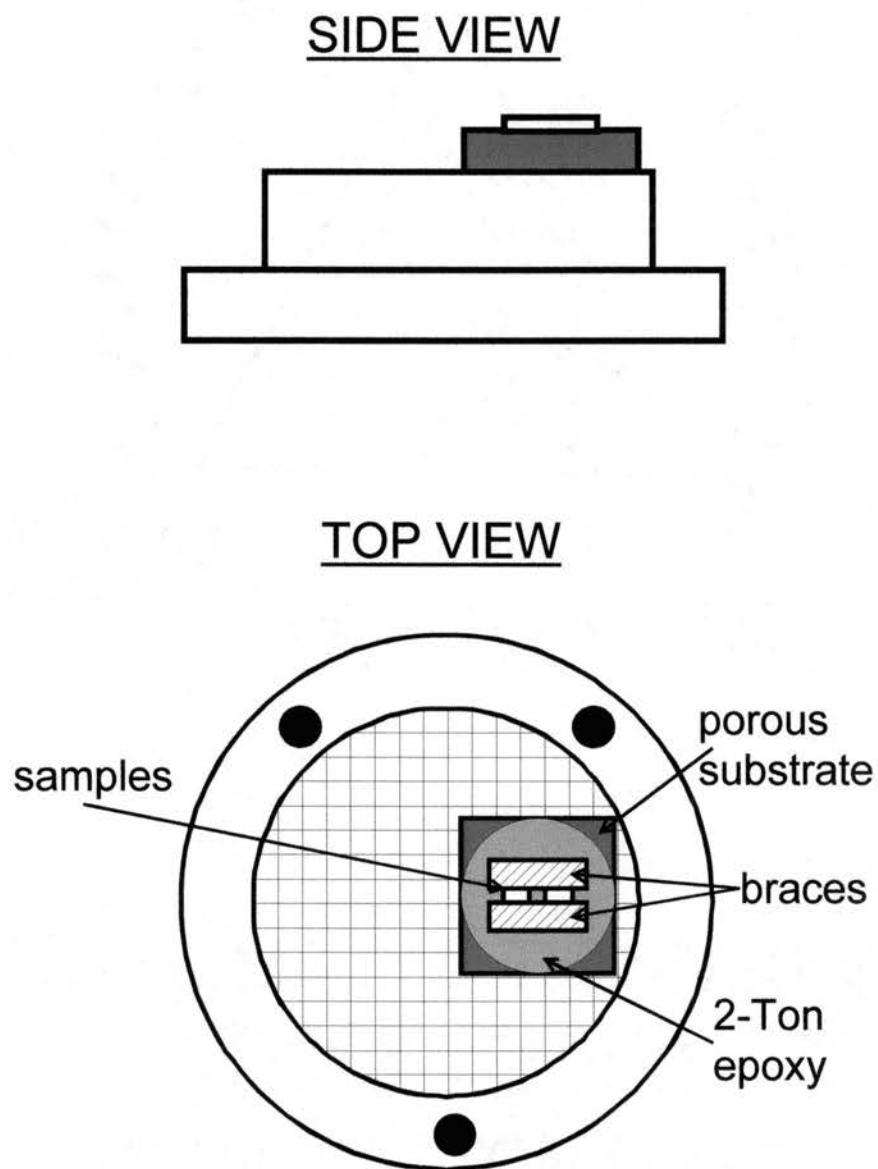


Figure 78. Side and top view of polishing jig mount for Logitech PP5D precision polishing jig and proper sample orientation on the jig mount.

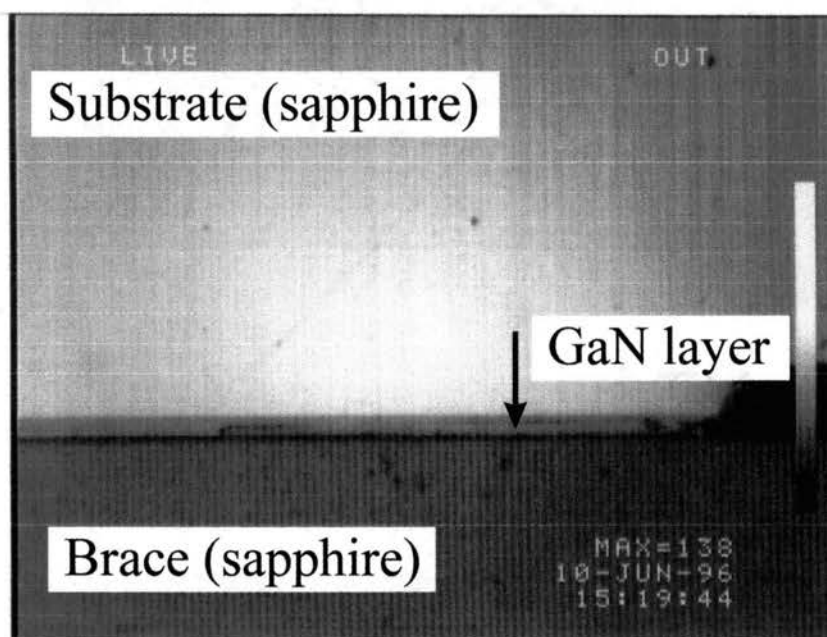


Figure 79. Optical microscope photo showing proper sample bracing. The GaN layer thickness is approximately $4\text{ }\mu\text{m}$. The sapphire brace is seen to be in close contact with the GaN surface, providing maximum protection during polishing. Magnification = 600X.

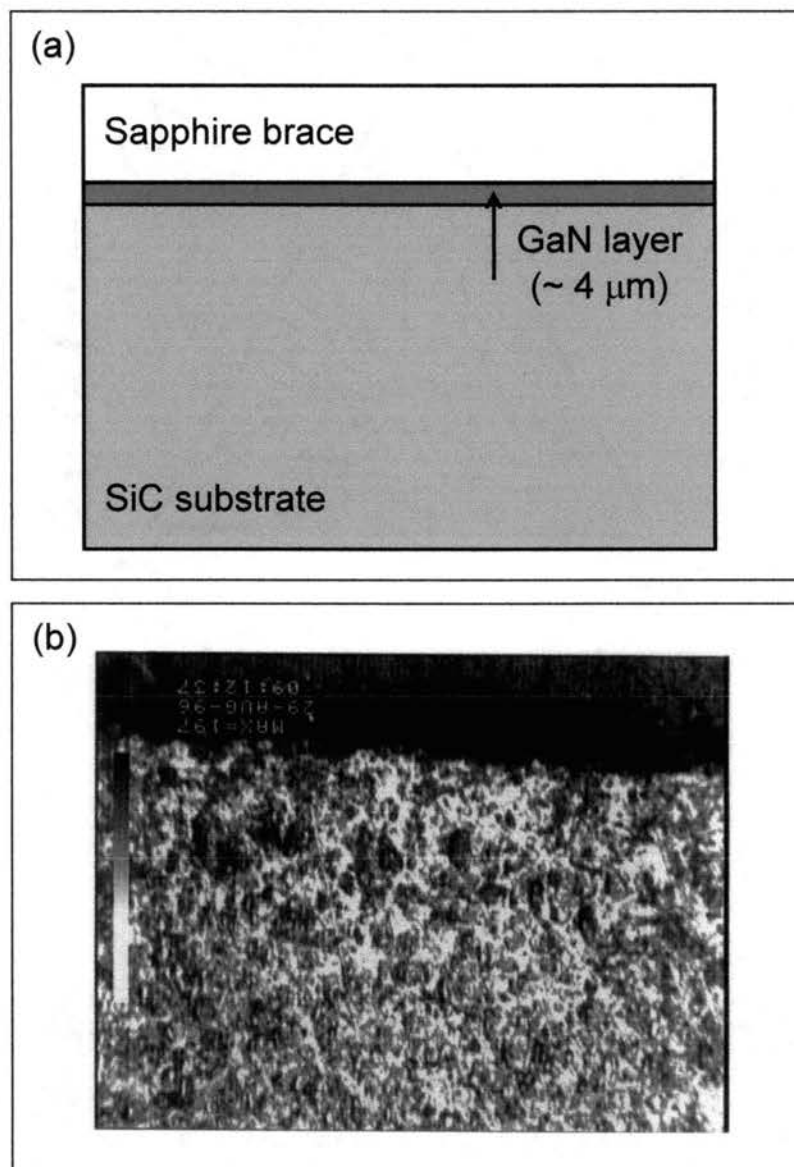


Figure 80. (a) Schematic of GaN/SiC sample showing location of sapphire brace, GaN layer, and SiC substrate. (b) Optical microscope photo showing GaN/SiC surface quality after completion of 8.5 μm diamond on copper polishing step. Magnification = 400X.

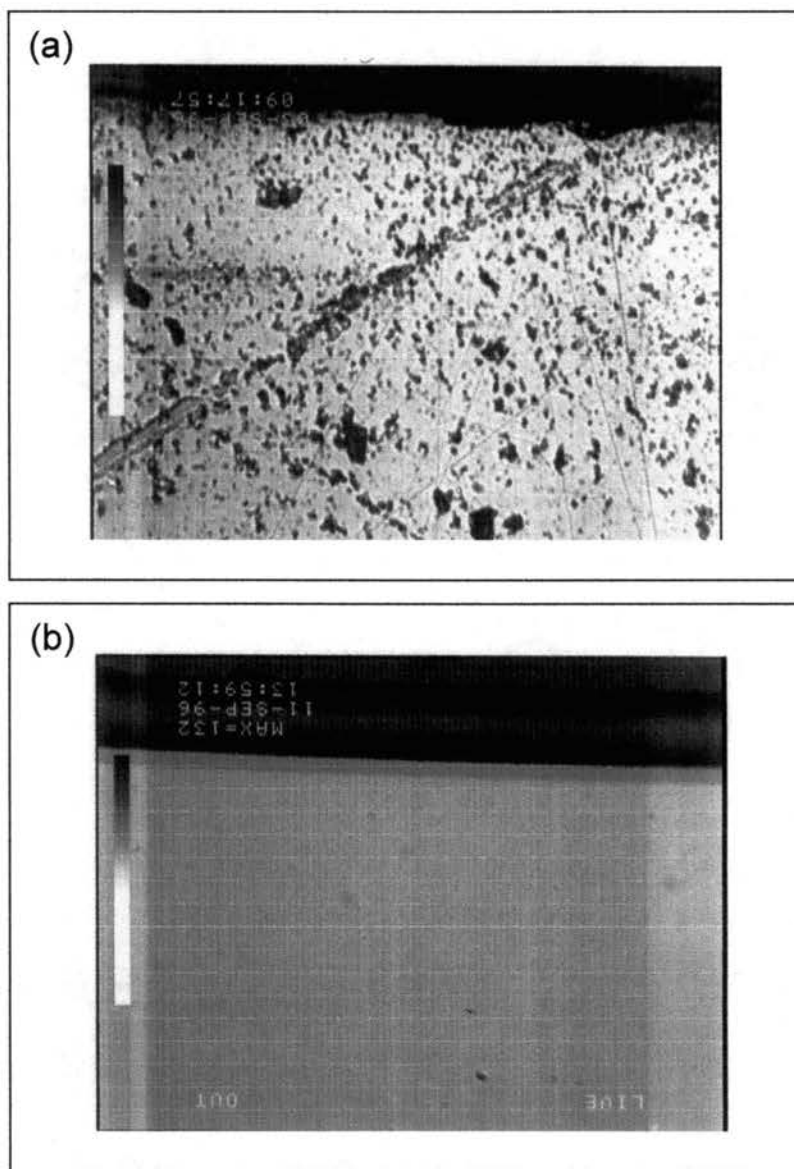


Figure 81. Optical microscope photos showing GaN/SiC surface quality after (a) 3.2 μm diamond on copper, and (b) MasterPolish2[©] on tin polishing steps. Magnification = 400X.

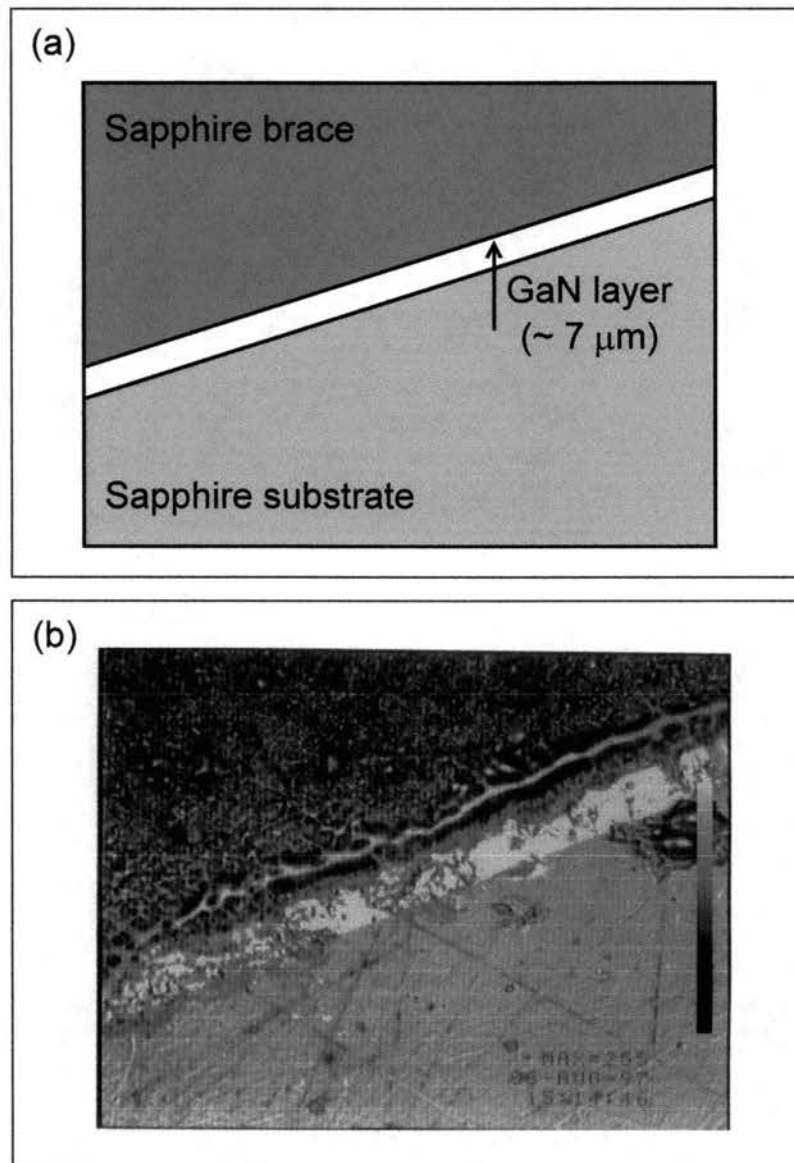


Figure 82. (a) Schematic of GaN/sapphire sample showing location of sapphire brace, GaN layer, and sapphire substrate. (b) Optical microscope photo showing GaN/sapphire surface quality after completion of 8.5 μm diamond on copper polishing step. Magnification = 600X.

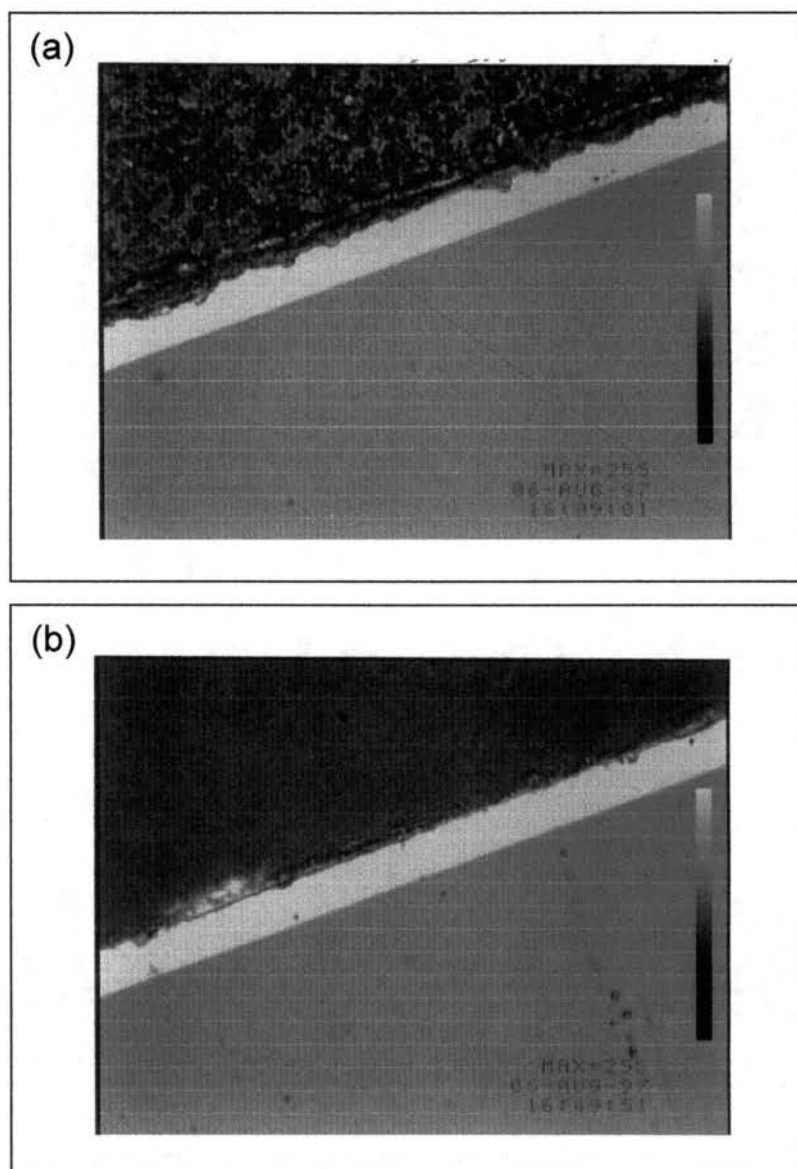


Figure 83. Optical microscope photos showing GaN/sapphire surface quality after (a) 3.2 μm diamond on copper, and (b) MasterPolish2[©] on tin polishing steps. Magnification = 600X.

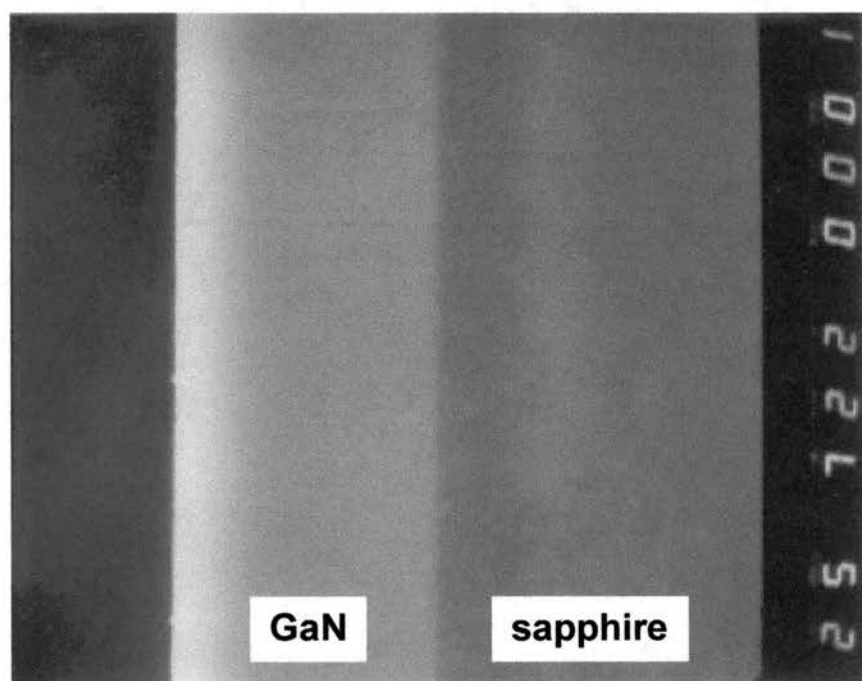


Figure 84. SEM image of GaN/sapphire laser facet after mechanical polishing. The GaN layer shown is $\approx 4.2 \mu\text{m}$ in thickness. Magnification = 15300X.

APPENDIX B

REFRACTIVE INDEX OF WURTZITE GaN

In general, the index of refraction, n , depends directly on the absorption coefficient, α , through the Kramers-Kronig relation [134]. Due to the present quality of state-of-the-art GaN thin films, there can be a great deal of variance in the band edge properties of GaN thin films when comparing films grown in different reactors and even between samples grown in the same reactor. The presence of impurities and defects can lead to band tailing and a significant increase in below-gap absorption. This in turn leads to variance in the index of refraction in the band edge region from sample to sample. It has been observed by the authors that index of refraction values reported in the literature vary by several percentage points in the long wavelength region (> 600 nm). This discrepancy was larger than 5 % in the band edge region [135], [136], [137]. Of significant importance to the contents of this monograph, the rate of increase of the index as we approach the band edge can vary significantly from sample to sample. This can significantly affect calculations relying on the index of refraction dispersion curve values, where a 5 % difference quickly becomes a 10 % error in, for example, a calculation of the reflection coefficient. For this reason, the index of refraction dispersion curve has been measured for a variety of GaN layers whose optical properties are a good percentage of this text. This allows us to confidently calculate reflection coefficients, Fabry-Pérot fringe spacings, etc., that rely on the index of refraction near the GaN band edge.

The modulation of the reflectivity and transmission spectra due to thin film interference was used to determine the refractive index of GaN films. In the reflectance experiments, the quasi-monochromatic light of a tungsten halogen lamp dispersed by a 1/2 meter monochromator was reflected off of the GaN surface at an angle if

incidence close to 90° . The reflected beam was collected and its intensity was monitored using a photomultiplier tube (PMT). In the transmission measurements, the transmitted signal was instead collected. The measurements were performed over the wavelength range of 300 to 3000 nm. The amplitude of the reflected/transmitted signal was wavelength modulated due to the interference of the beams reflected from the air/GaN interface and the GaN/sapphire interface. The refractive index was then calculated from the relation [138]:

$$2nd = N\lambda$$

which holds for the reflectivity minima and transmittivity maxima, where n is the refractive index, d is the sample thickness, and N is the interference order. The reflection and transmission signals for the $4.2 \mu\text{m}$ GaN layer are shown in Fig. 85 for reference. The interference order was determined graphically using the region where the refractive index is weakly dependent on λ ($\lambda > 600 \text{ nm}$). In this region, the dependence of N on $1/\lambda$ is near linear and N could be determined precisely from the intersection of this line with the y-axis. The plot of the refractive index for three GaN layers grown by MOCVD on (0001) oriented sapphire using the above equation are given in Fig. 86, where the inset shows the index of refraction dispersion curve for the spectral region of interest to this monograph.. Good agreement between the values obtained for the different GaN layers is clearly seen. All experiments were carried out with the electric field perpendicular to the GaN c-axis ($E \perp c$), which is the same condition for which the TE polarized SE/lasing is incident on the GaN/air interface of the laser cavity facets.

It is well known that the accuracy of the above method for determining the index of refraction dispersion curve is principally determined by the accuracy of the film thickness measurement. To measure the GaN film thickness, we fine polished the sample edges and measured their thickness using a SEM and a $0.5 \mu\text{m}$ calibration grid. The consistency between calculated index of refraction for the various samples (ranging in thickness from 2.5 to $7.2 \mu\text{m}$) is evidence of the validity of our technique.

The slight deviation of the index for the $7.2\text{ }\mu\text{m}$ layer with respect to the other two is most likely a result of layer thickness fluctuations present in the thicker sample.

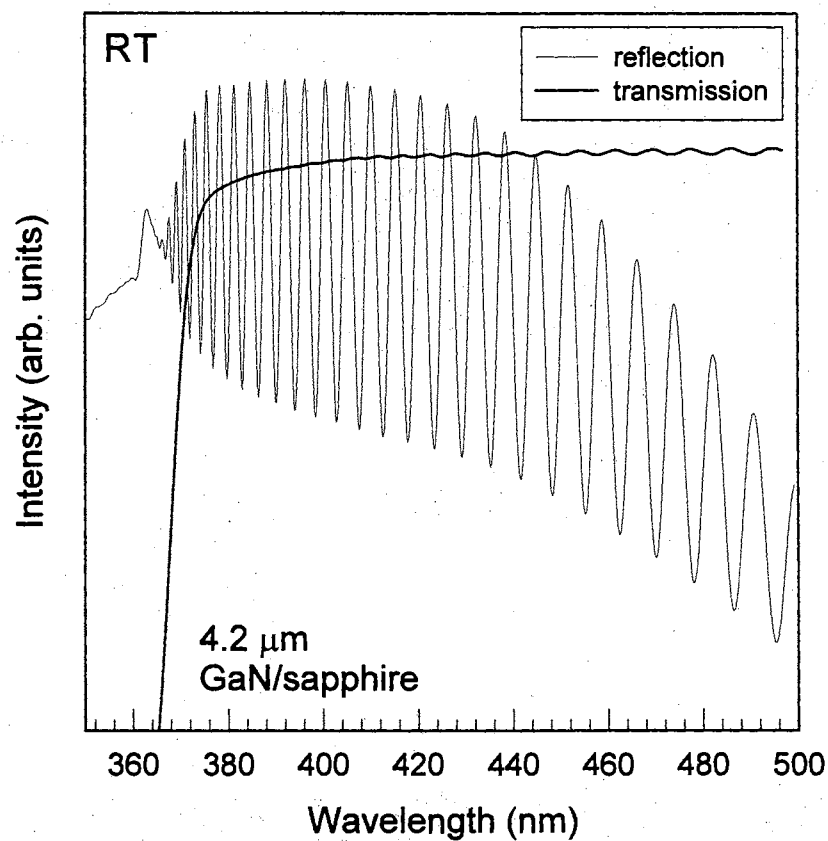


Figure 85. RT reflection and transmission spectra for a 4.2 μm MOCVD-grown GaN layer on (0001) oriented sapphire.

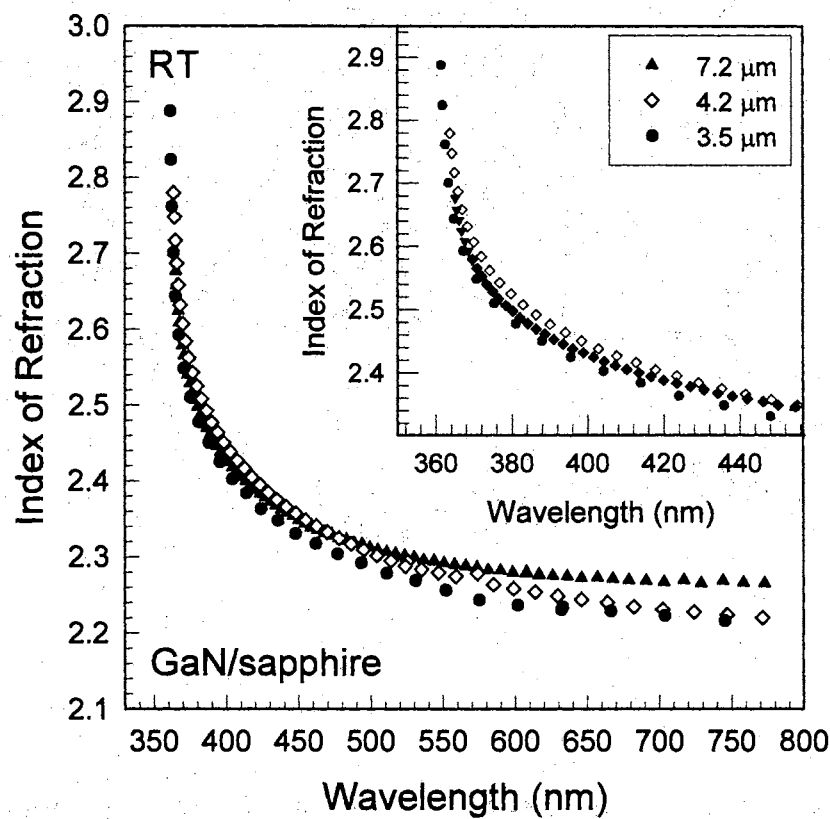


Figure 86. RT index of refraction dispersion curves for MOCVD-grown GaN thin films of various thicknesses on (0001) oriented sapphire. The inset shows the same for a narrower spectral region near the GaN band edge.

✓
VITA

Theodore J. Schmidt

Candidate for the Degree of

Doctor of Philosophy

Thesis: OPTICAL SPECTROSCOPY OF HIGHLY EXCITED GROUP III
NITRIDES

Major Field: Physics

Biographical:

Personal Data: Born in Fargo, North Dakota, on May 22, 1969, the son of Herbert J. and Bonita Rae Schmidt.

Education: Graduated from West Fargo High School, West Fargo, North Dakota in May 1987; received Bachelor of Science Degree in Engineering Physics from North Dakota State University, Fargo, North Dakota in May 1992. Completed requirements for the Doctor of Philosophy Degree at Oklahoma State University in December 1998.

Professional Experience: Research Assistant, Department of Physics and Center for Laser and Photonics Research, Oklahoma State University, from August 1992 to present.

Professional Memberships: American Physical Society, Optical Society of America, Materials Research Society, SPIE, Phi Kappa Phi, Tau Beta Pi.